Environmental-(S)TEM of Dynamic Catalyst Nanostructures

David Carlos Lloyd

PhD

University of York

Physics

September 2018

Abstract

The production of intelligently designed catalysts requires an understanding of, not only the specific reaction pathways, but also the effects of reactive species on catalyst materials. Gas composition, temperature and pressure can alter the physical characteristics of a catalyst material. The size, shape, crystallographic topography, chemical state and material composition of catalytic nanostructures can be highly dynamic under reaction conditions. E(S)TEM is uniquely suited to observe the structure of nanomaterials in real time under simulated reaction conditions.

The oxidation of Ni nanoparticles was investigated using dynamic in-situ imaging in ETEM. These observations show a change in reaction mechanism as the Ni-NiO structure evolves over the course of the reaction. Initially, pyramidal NiO crystals grow on the Ni surface. The overlap and outward growth of these crystallites leads to an oxide shell around a metallic core. At a critical oxide thickness, the mechanism switches and further structural transformations are observed due to differential diffusion. Fast diffusion of cation vacancies lead to the formation of Kirkendall voids and ultimately hollow NiO structures.

Nanoparticle based catalysts for industrial methanation reactions were studied using ESTEM. The study focuses on the origin of enhanced catalytic activity via the addition of a ceria promoter. Oxygen vacancies at the ceria surface were found to be active sites for the activation of carbon oxides. A correlation was found between decreasing promoter crystallite size and the enhancement of catalytic activity. The best promotional effect was observed when the ceria takes the form of a highly dispersed atomic-scale species.

E(S)TEM was used to observe the evolution of Pd nanoparticles under redox conditions. Pd model systems utilising carbon, silica and alumina supports were tested. The amount of sintering was found to be determined by both: gas environment and the support material.

Contents

List of Tables

List of Figures

Acknowledgements

This thesis represents more to me than simply a body of scientific work; it is a reminder of an incredible adventure and the people who I have had the enormous pleasure of meeting along the way.

Firstly, I would like to thank my supervisors, Prof. Edward Boyes and Prof. Pratibha Gai. The past four years would not have been what they were, if not for their kindness, scientific insight and overall support. I am truly grateful for everything they have done for me, and for encouraging me to attempt any experiment that peaked my curiosity.

Secondly, I would like to thank my industrial supervisor Dr. Leon van de Water and Johnson Matthey as a whole for the provision of catalyst samples and associated XRD and activity data. Leon has been incredibly accommodating, both with his time and in sharing his vast catalysis/industrial knowledge. Thanks to Johnson Matthey and the EPSRC, for providing this studentship and ensuring that, at the very least, this thesis has some practical utility.

The nanocentre has been a fantastic place to work and the people who lurk within its walls have been like an extended family during my time there. Thanks go to Drs. Gnanavel Thirunavukkarasu, Robert Mitchell, Thomas Martin, Leonardo Lari and Ian Wright. I'd like to give special thanks to Dr. Michael Ward for training, support and motivation from my first day in HXH/001D. Special credit must go to Dr. Alec LaGrow for being such a great research partner and quasi-boss. I am also especially grateful to Dr. Jon Barnard for being my TEM guru. Thanks go to Mr. P. Bentley and Dr. A. Pratt for XPS testing.

Finally, I would like to thank my mother for being a constant source of love and support throughout my PhD, I could not have done it without you. Apologies for the stress, although you should know by now- *Mala hierba nunca muere!*

Declaration

I declare that this thesis is a presentation of original work. I am the sole author, with the following exceptions: 1) methanation activity measurements in chapter 6 were performed by Dr. Leon van de Water, 2) XRD measurements in chapters 6 and 7 were provided by JM and 3) XPS measurements in chapter 6 were performed by Mr. P. Bentley and Dr. A. Pratt. This work has not previously been presented for an award at this, or any other, University. All sources are acknowledged as references.

Contributions to Other Published Work

R.W. Mitchell, **D.C. Lloyd**, L.G.A. van de Water, P.R. Ellis, K.A. Metcalfe, C. Sibbald, L.H. Davies, D.I. Enache, G.J. Kelly, E.D. Boyes, P.L. Gai, Effect of Pretreatment Method on the Nanostructure and Performance of Supported Co Catalysts in Fischer–Tropsch Synthesis, *ACS Catalysis*, 2018, **8**, 8816-8829.

A. P. LaGrow, **D. C. Lloyd**, P. L. Gai, E. D. Boyes, In-Situ Scanning Transmission Electron Microscopy of Ni Nanoparticle Redispersion via the Reduction of Hollow NiO, *Chemistry of Materials*. 2018, ***30***, 197-203.

A. P. LaGrow, N. M. AlYami, **D. C. Lloyd**, O. M. Bakr, E. D. Boyes, P. L. Gai, In-Situ Oxidation and Reduction of Triangular Nickel Nanoplates via Environmental Transmission Electron Microscopy, *Journal of Microscopy*. 2018, ***269***, 161-167.

A. P. LaGrow, M. R. Ward, **D. C. Lloyd**, P. L. Gai, E. D. Boyes. Visualizing the Cu/Cu_2O Interface Transition in Nanoparticles with Environmental STEM, *Journal of the American Chemical Society*, 2017, ***139***, 179-185.

Chapter 1

Introduction

A catalyst is a substance that can increase the rate (activity) and targeting (selectivity) of the output of a chemical reaction. Catalysts can be used to perform industrial reactions at lower temperatures and pressures; they can also increase activity or selectivity for a given reaction. This allows for more efficient use of chemical feedstocks, increased yield and decreased environmental impact in both waste streams and energy requirements. Many catalytically active materials involve precious metals (Pd, Ir, Pt, Au, etc.); and as such there are complex financial, political and supply issues that surround the production of catalysts. Due to the industrial, economic and environmental ramifications of catalytic materials, there has been heavy investment into creating efficient, cheaper and more active catalysts; and this is an important driver for this thesis work.

It is known that the general mechanism by which a catalyst works is that reactants are adsorbed onto the catalytically active surface, where they undergo dissociation, bond breaking/forming events followed by desorption of the products. Since it is the catalyst surface that promotes this enhanced activity the goal of research has been to increase the effective surface area. The primary way of doing this is to shrink the catalyst particles down so that the surface-area to volume ratio increases. With a higher surface-area to volume ratio more surface area is exposed per unit volume, or more importantly per unit mass and therefore, general materials cost of the catalyst. Today catalysts are better described as nanocatalysts, which typically consist of a precious metal in the form of nanoparticles dispersed on a high surface-area ceramic support [1], the function of which is to prevent nanoparticle sintering and deactivation. Nanocatalysts are used in key applications including: industrial chemistry [2], advanced chemical synthesis [3],

photocatalysis [4], the production of pharmaceuticals [5] and increasingly in emission control and remediation measures [6, 7].

The use of nanoparticles as the provider of the active catalyst sites is a great opportunity for material scientists. At the nanoscale the properties of materials can differ dramatically from their bulk counterparts. By altering the synthesis conditions the nanoscale character can be tailored to alter both the physical and chemical properties of the nanoparticles [8].

However, correlating the structure-property relationships of nanometer size materials is still an ongoing area of research. While there have been many advances in the fields of chemistry, physics and nanotechnology, including nanocatalysis, there is still much work to be done. It is obvious that in order to manipulate the features of these materials at the nanoscale, it is of paramount importance to be able to observe these materials at the molecular, nano and even atomic level in order to understand more fully their properties. One technique that is particularly pertinent to nanomaterials is (scanning) transmission electron microscopy ((S)TEM) [9-12] as it allows for direct observation of the structure and chemistry of the materials. This has been made more so by developments in atomic resolution environmental TEM (ETEM) [13] in which samples can be exposed to reaction conditions relevant to industrial processes and observed in-situ. Thus, one can not only see how the catalysts behave under reaction conditions but how the very reactions that are being catalyzed affect the structure of the catalysts themselves. The application of ETEM specifically for the purposes of intelligent catalyst design has seen increasing interest in recent years [14-19].

It is the aim of this thesis to leverage the power of the atomic-resolution environmental (S)TEM to try and elucidate the atomic scale processes and mechanisms that lead to the dynamic behavior of catalysts under reaction conditions.

1.1 Thesis Overview

An overview of nanoparticle based catalysts is given in chapter 2, beginning with the enhancement of catalytic activity and the physico-chemical properties that lead to such enhancements. Particular attention is paid to the processes relevant to industrial catalysts, namely the treatments that are involved in the precursor to active-phase transition and the mechanisms of deactivation and reactivation. Since electron

microscopy is the primary experimental technique used in this thesis, chapter 3 is dedicated to the concept of transmission electron microscopy (TEM). The basic design of the TEM is presented and techniques used herein are explained. An introduction to environmental (scanning) transmission electron microscopy (E(S)TEM) is provided along with a discussion of the experimental artifacts, i.e. beam induced reactions, which need to be considered when using the E(S)TEM. Supplementary experimental techniques are also briefly discussed in this chapter. Chapter 4 gives an overview of the experimental procedures and analysis tools used in this thesis.

In chapter 5 the oxidation of Ni nanoparticles is investigated using in-situ E(S)TEM. The dynamics of the oxidation are discussed in the context of both the standard theory of metal oxidation, and the diffusion limited ionic transport of material during the reaction. Chapter 6 inter-compares the nanostructure of a number of Ni-based supported catalysts relevant to methanation reactions. Chapter 7 explores the effect of support material on the nanostructure and stability of a model system of Pd nanoparticles. Finally, concluding remarks are given in chapter 8 along with suggestions for future work on these topics.

Chapter 2

Nanoparticle Catalysis

The focus of this chapter is the discussion of nanoparticle based systems for applications in heterogeneous catalysis. The aim is to discuss the origin of catalytic activity in nanoparticulate systems and to describe the interconnected parameters that result in the final activity profile of a catalyst. The lifetime of a catalyst is discussed from its formation and activation to its deactivation and possible recovery. Literature and insights specific to the nanoparticle systems used in the experimental sections of this thesis can be found at the start of chapters 5, 6 and 7.

Heterogeneous catalysis represents an exciting sector of scientific exploration in which there is a rapid and significant interplay between industrial application and fundamental research in the sciences. Around 90% of the chemical manufacturing processes in the world today utilise catalysts [20]. As such, catalysis is intrinsically linked to the world economy and advances in this area can have a dramatic impact. Even small advances at the research level can become significant when applied to the scale of commercial industry. In addition to their economic and industrial values, catalysts are essential from an environmental stand point. Not only do they promote cleaner chemical processing, they are essential for the conversion of hazardous waste materials from existing processes.

It should be of considerable surprise then, that until recently the main approach for the development of new catalysts were trial and error based methodologies. This philosophy has been superseded by rational design methods; the shift caused by the interest of the chemical and material physics communities as well as advances in nanoscience.

2.1 Introduction to Heterogeneous Catalysis

Classically a catalyst is any substance that increases the rate of a chemical reaction without being consumed in the process. However, the second part of that definition is not always true. Under harsh reaction conditions such as increased temperature and pressure, or in the presence of strongly oxidising, reducing or acidic environments the structure or chemical composition of a catalyst can undergo significant change.

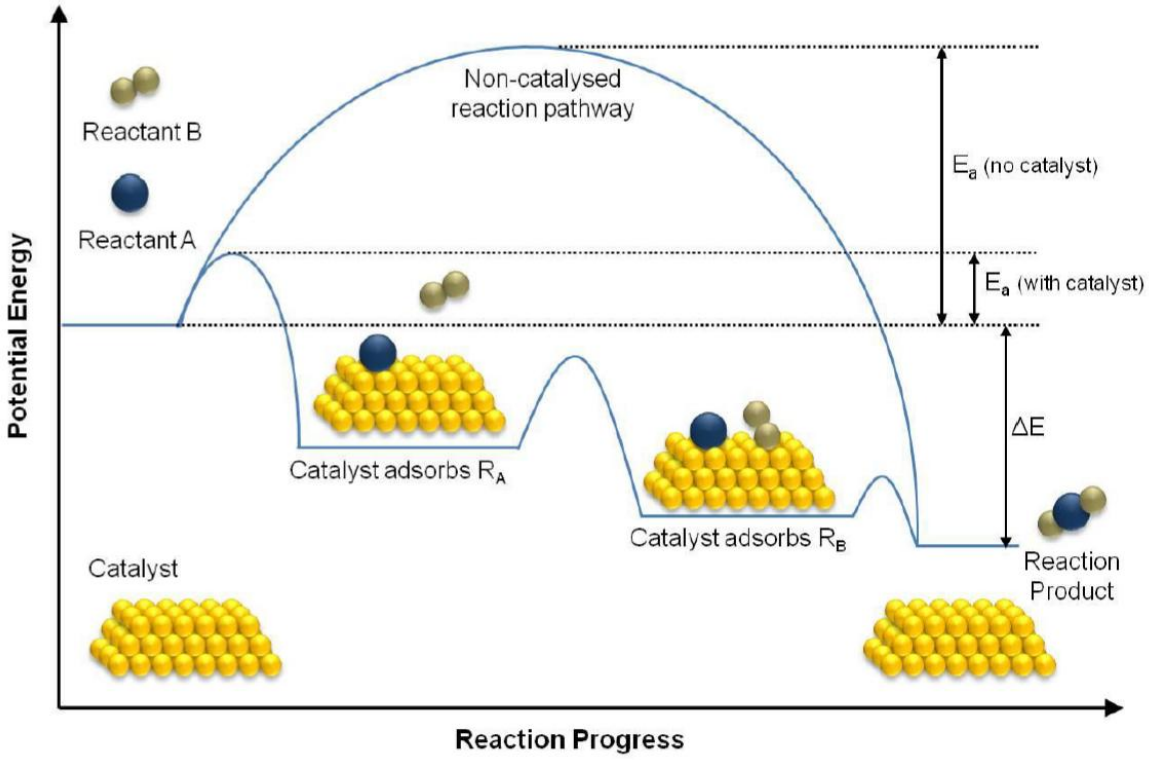

Figure 2. 1: Schematic energy diagrams of simple catalytic and non-catalytic reaction pathways. Reproduced from [21].

In a typical chemical reaction, reactants combine to form single or multiple products (some of which may be useful or detrimental by-products). For a reaction to occur, the reacting species need to come into close proximity to each other and interact with sufficient energy. This energy is known as the activation energy. Catalyst materials function by providing a common surface for reactant molecules to adsorb onto, such that their probability of interaction increases. Secondly, adsorption of reactant molecules on to the catalyst allow for the dissociation of these molecules and the formation of intermediate species which have a lower activation energy than the uncatalysed reaction [22]. The intermediate chemical reactions on the surface of a catalyst can represent multiple reaction steps and multiple adsorption/desorption events. All of which have an

associated energy barrier. The reduced activation energy barrier for the catalysed reaction versus the uncatalysed reaction sometimes means that reactions can take place at lower temperatures. This has significant consequence for industrial chemical reactions where lower temperatures reduce the cost of maintaining such a reaction environment, thus maximising profits. A general schematic of the catalytic process is given in figure 2.1.

All chemical reactions obey Le Chatelier's principle. This principle states that when a system at equilibrium is subject to a change (in temperature, volume or pressure) the system will readjust to oppose the change and establish a new equilibrium. By this principle and with the use of a catalyst certain reactions can be driven (made more favourable) at the expense of others in order to maximise the yield of a particular product.

Catalysts can usually be split into two groups: homogeneous and heterogeneous catalysts. Homogeneous catalysis is when the catalyst and the reactants are in the same phase. For example, the two components can be mixed together in a solvent (liquid phase reaction). Heterogeneous catalysis is where the catalyst and reactants are in different phases, for example, solid-liquid or solid-gas. The catalysts discussed in this thesis are heterogeneous catalysts for industrial gas phase reactions.

The effect of the chemical and physical environment on a catalyst can lead to degradation of the catalytic activity over time. This is known as deactivation and can occur by a number of routes. For example, reaction by-products can cover the surface of the catalyst (i.e. coking), catalytically active sites may be blocked by strongly adsorbed molecular species (i.e. poisoning), and at high temperatures loss of surface area can occur (i.e. sintering). The performance of catalysts, for a given chemical reaction, under pre-defined conditions is usually described in terms of its turn over frequency (ToF), given by equation 2.1.

$$ToF = \frac{1}{S_n}\left(\frac{dn}{dt}\right) \tag{2.1}$$

Where S_n is the number of catalytically active sites, n is the number of times that a reaction event takes place at an active site in time, t.

Most materials used in heterogeneous catalysts are precious metals, such as Au and Pt. Therefore, substantial effort is put into finding ways to reduce the amount of catalytic material used and to combat the deactivation of catalysts over time.

2.2 Introduction to Nanocatalysis

Nanoparticle (NP) based catalysts show enhanced reactivities and selectivities compared to bulk [23, 24]. One of the most striking examples of this phenomenon are gold NPs. Gold is catalytically inert in bulk but systems of dispersed gold NPs have been shown to be highly active catalysts for a number of reactions. These include the low-temperature oxidation of CO [25] and the reduction of nitrogen oxides [26].

Supported gold clusters are a dramatic example of the novel nanocatalytic phenomenon and are well studied. Many transition metal NPs exhibit high catalytic activity, in particular the platinum group metals show remarkable promise. Oxide supported platinum and palladium catalysts show much promise and are an active area of research. The nanoscale structure of nanocatalysts and their interaction with the gas reaction environment is the focus of this work.

It would be natural to assume that the enhanced reactivity observed in NP catalysts is due to the greatly reduced size of the metal clusters. While this is true for the most part, particle size is not the only contributing factor. The particle shape, the composition of the material, the metal-support interaction and the reaction environment all play a role in determining the final reactivity and selectivity of the catalyst. Furthermore, these parameters are interdependent and contribute to different degrees depending of the reaction/system being catalysed. This section aims to give an overview of such contributing factors. Knowledge of these factors is crucial when investigating NP systems and is useful for the design of model systems.

2.2.1 Size Effects

Investigations into the effect of particle size on the enhanced activity of NP catalysts are diverse to say the least. In the case of Au NPs, several investigations have been performed to correlate the particle size with the origin of the enhancement. Correlations of chemical

activity have been attempted with regard to: modified electronic structure, band gap modification and binding energy shifts. In such cases there is enough literature in support and opposition that a fundamental understanding of the dependency of activity on NP size has not been obtained to date. One feature prevalent to smaller NPs is the increased number of low-coordinated atoms. Chemisorption experiments show that the highly stepped surfaces of certain NP can contribute significantly to the catalytic activity. Density functional theory (DFT) calculations support this conclusion [27]. Figure 2.2 highlights some of the features of NPs that are thought to play a significant role in determining the catalytic activity.

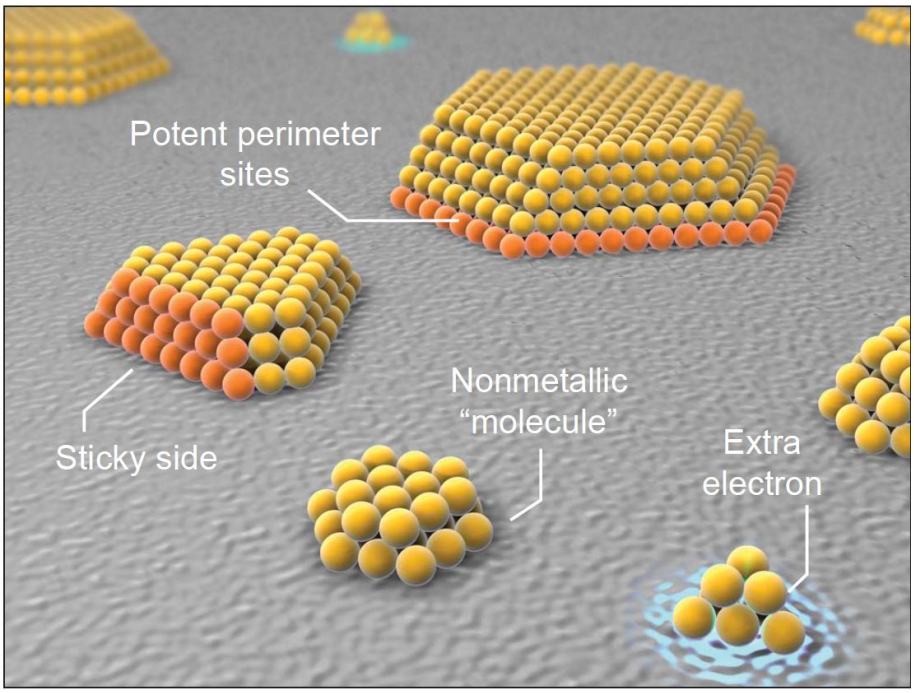

Figure 2. 2: Features potentially responsible for the enhanced activity of NPs [28]. From [A. Cho, Connecting the dots to custom catalysts, Science, 299 (2003) 1684-1685]. Reprinted with permission from AAAS.

A key feature of reduced particle size is the enhancement of effective surface area. As the particle size decreases the surface area to volume ratio increases, as shown by equations 2.2 and 2.3 below (approximating spherical NPs).

$$\frac{Surface\ area}{Volume} = \frac{4\pi r^2}{\frac{4}{3}\pi r^3} \tag{2.2}$$

$$\frac{Surface\ area}{Volume} = \frac{6}{D} \tag{2.3}$$

Where r is radius and D is the particle diameter. This is important in terms of catalyst efficiency since the material at the core of the NP is shielded and does not contribute to catalysis.

2.2.2 Shape Effects

As it will be shown in the sections below, the NP-support interaction is a contributing factor to the activity of certain catalysts. However, the contact between the NP and the supporting oxide is determined by the shape of the NP. Different NP shapes have different stabilities [29] and the shapes that occur are a result of both the crystal growth route and deposition method. Additionally, the shape determines the surface features present, like those shown in the previous section, which can contribute to the activity of the catalyst.

The shape of the nanocrystal determines which crystal facets are exposed to the reaction environment. Figure 2.3 demonstrates how the presence of different crystal facets on Ag NPs can affect the reactivity of the catalyst. In this case, the increase in the number of exposed (100) facets resulted in a striking increase in reaction rate. Furthermore, crystal facets will promote the adsorption, stability and desorption of reactants and intermediates to different degrees. These results highlight a fundamental need to understand catalysis in terms of the nanoscale crystal structure. Furthermore, different sizes/shapes can promote crystal features such as steps, kinks and edges to different degrees. These sites are energetically favourable adsorption sites for certain reactant molecules. Thus, it may be said that smaller is not always better, for certain reactions. An example would be spherical Pd NPs with low symmetry facets containing kink sites. These sites show higher CO oxidation rates than cubes or polyhedra [31].

Having highlighted the need for initial understanding of the crystallography of the nanocatalyst the effect of the dynamic reaction environment must be considered. For example, dynamic shape changes have been observed in Pd nanocatalysts when exposed to repeated CO/NO cycles [32]. This means that the density of catalytically active surface facets can decrease as a result of chemical environment and reaction parameters such as temperature and pressure. In-situ experiments are needed to chart the crystal changes

induced by chemical environment. Indeed these experiments are paramount if long term catalytic stability is to be the end goal.

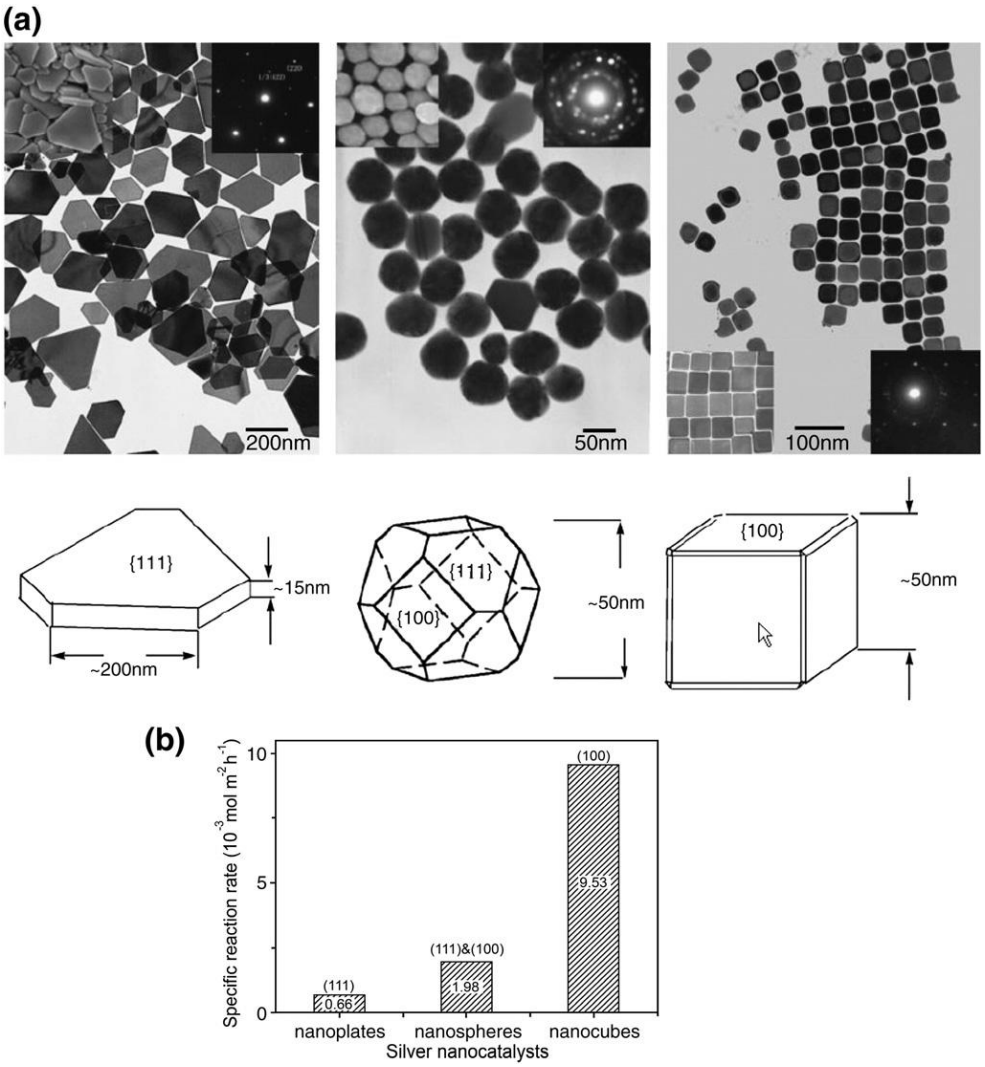

Figure 2. 3: Different shapes of Ag NPs reveal crystal facets with different catalytic activities. a) Shows TEM images (with inset diffraction patterns and SEM images) and models while b) demonstrates reactivities for a styrene conversion reaction. Reprinted from [30] with permission (2006 Wiley-VCH Verlag GmbH & Co. KGaA, Weinheim).

2.2.3 Support Effects

The performance of a catalyst system depends not only on the material and features of the metal nanoclusters but on the support material. Metal-oxides are the most common type of support due to their stabilising effect on the NPs. A catalyst support must perform two key roles: the first is to anchor the metal clusters such that they remain intact on the catalyst macro-structure under reaction conditions. The second is to stop or inhibit the mobility of the metal NPs so that the particles do not coalesce leading to a loss of surface

area [33]. From this definition it would seem that the support is of secondary importance but studies have shown that the interaction between catalyst and support plays a role in the activity of the catalyst. However, there is significant debate as to the exact nature of the contribution from the support to the enhanced activity.

One feature of the metal-oxide support that has gained a significant interest is the presence of oxygen vacancies. DFT calculations have suggested that electron transfer from O-vacancies at the metal-support interface facilitates oxidation reactions over Au NPs [34]. In reducible supports such as TiO_2 the presence of O-vacancies drastically alters the adsorption profile of the supported NPs [35].

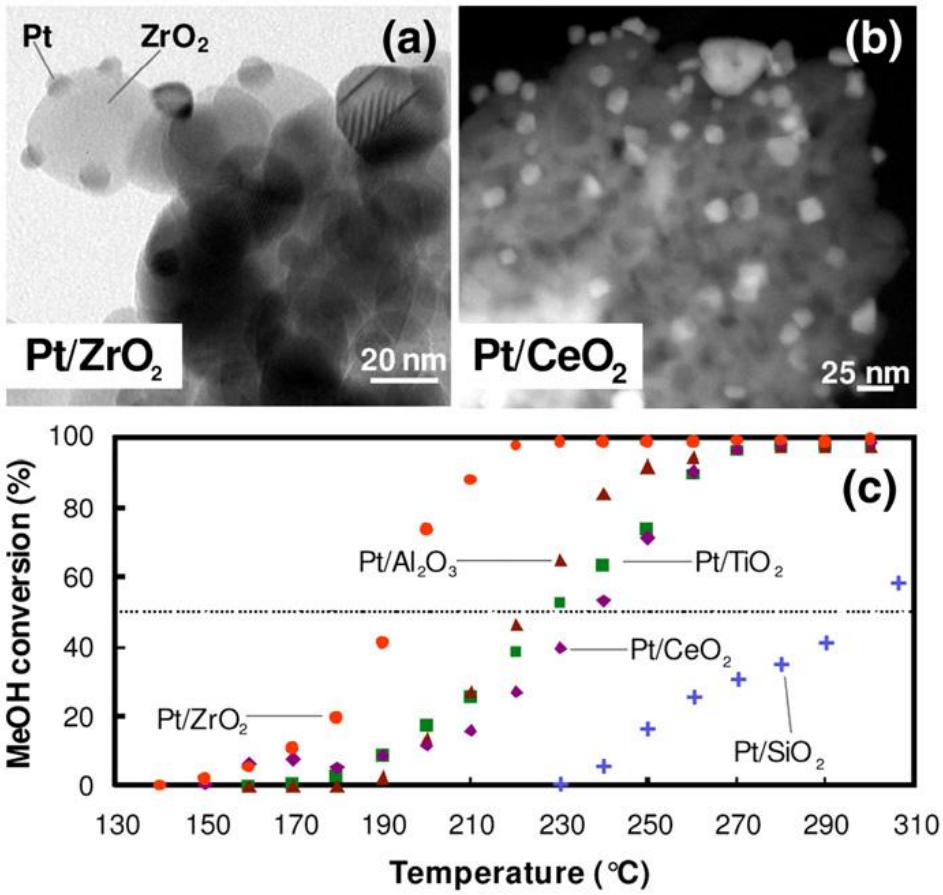

Figure 2. 4: a) TEM of Pt NPs supported on ZrO_2, b) HAADF-STEM of Pt/CeO_2 catalyst and c) the effect of supporting oxide on catalytic performance during methanol decomposition [36]. Reprinted by permission from Springer Nature: Springer, Catalysis Letters, Support Dependence of MeOH Decomposition Over Size-Selected Pt Nanoparticles, J.R. Croy, S. Mostafa, J. Liu, Y. Sohn, H. Heinrich, B.R. Cuenya, Springer Science+Business Media, LLC (2007).

The choice of support material can also have a bearing on the performance of a catalyst. An example is the decomposition of methanol (CH_3OH) for H_2 synthesis. This reaction is catalysed by the presence of supported Pt NPs. In this case the reaction is shown to be

support dependent. Figure 2.4 shows the results of a study in which SiO_2, Al_2O_3, ZrO_2, TiO_2 and CeO_2 supports were investigated for the methanol conversion. Figure 2.4c demonstrates that the choice of NP support can cause a reaction to be catalysed at lower temperatures; the consequence of this observation is extremely attractive in an industrial setting. In that study, Croy et al [36] showed that the support material has its own stability profile under reaction conditions. For example, the CeO_2 support can become less disperse over the course of a reaction. Therefore, the impact of the reaction environment must be considered with regard to the catalyst support as well as the catalytic NPs.

In summary, the support affects the stability, shape, structure and routes to deactivation of the NPs and provide its own contributions of active sites and charge transfer. While there is still debate in the literature as to the importance of the NP support, it should be clear from the comments made so far that the support requires serious consideration for the intelligent design of future catalysts. This statement is by no means trivial; as such considerations may not be possible in any general sense, thus requiring reaction-specific catalyst-support design.

2.3 Activation- Formation of the Active Phase

Catalysts are synthesised using chemical methods to produce catalyst precursors. The catalyst synthesis method has a large impact on the characteristics, structure and composition of the final catalyst. The catalyst manufacturing facilities are usually far from the sites where they will eventually be used. This means that catalysts are exposed to ambient conditions during transport i.e. air and humidity. For this reason, most catalysts require some form of activation process to be performed before they are brought online.

In many cases, the activation is a reduction at elevated temperatures to reduce an oxidic precursor or remove surface oxide species. A common example of this is the reduction of NiO to Ni. Other examples include, the chemical leaching with NaOH on Ni-Al alloys to produce Raney-nickel catalysts [37], extended reduction of Co_3O_4 to Co through an intermediate CoO phase [38] and calcination treatments when a metal oxide is the active species. As previously discussed, the size and shape of the catalyst material can affect the

activity of the catalyst. Thus, investigations into possible changes induced by the activation process are required.

2.4 Metal-Support Interactions

Nanoparticles rarely exist in isolation; nanoparticles are usually loaded onto an oxide support. The support has the effect of providing an increased surface area for the catalyst system and stabilising the nanoparticles. Since the catalyst material and the oxide support are in contact with each other, chemical bonds are formed between them. The term metal-support interaction is used to express the chemical and physical changes induced by the support on the nanoparticles. Interaction with the support can influence morphology, activity and ageing [39, 40].

The oxide support is exposed to the same reaction environment as the active phase and so may transform, either by itself or via interaction with the metal. An example is the covering of active metal surfaces by silica [41]. Supports such as TiO_2, ZrO_2 and CeO_2 are reducible supports, unlike Al_2O_3 and SiO_2. Some such supports may contain acidic sites on their surface. When a metallic nanoparticle is in contact with an acid site, electrons are removed from the metal. In some cases the lack of electrons mean that oxygen cannot adsorb easily on the surface, inhibiting oxidation in small nanoparticles [42].

The stabilising effect of the metal-support interaction can be pushed all the way down to the single atom level. For example, under-coordinated anion sites in γ-Al_2O_3 [42] and cation vacancies in FeO_x [43, 44] can be used to anchor Pt atoms.

2.5 Deactivation Mechanisms

Unfortunately nanocatalysts do not retain their catalytic activity indefinitely. Mechanisms such as: covering of the nanoparticle surface, blocking of adsorption sites and loss of total surface area by sintering reduce the efficacy of the catalyst. Since catalysis is a surface reaction, loss of surface area directly impacts the catalytic activity of the system. Deactivation fundamentally changes the surface structure of an active catalyst destroying sites such as highly active crystal facets or desirable under-coordinated atomic sites. Blocking of surface sites, together with changes to morphology or size, can also mean a

loss of nanoscale features that the system was originally designed to promote. In some cases the metal-support interaction may be sensitive to the nanoparticle size distribution and may be affected by changes to either material at the interface.

As the surfaces of catalysts become blocked, there is less surface area on which chemical reactions can take place. This may mean that, when possible, non-catalytic reactions can take place in the gas phase, this leads to a reduction in selectivity to the reaction of interest, potentially leading to increased concentrations of undesired products from competing reactions.

The most significant deactivation mechanism, due to its irreversible nature, is sintering. Sintering is the process in which particles migrate across the support surface forming larger particles, leading to reduced surface area of the catalyst. Two sintering mechanisms are known: Ostwald ripening and particle migration and coalescence, which are explained below.

2.5.1 Ostwald Ripening

Ostwald ripening is the process in which small nanoparticles lose atoms to the surrounding support. These atoms then migrate to large particles, as illustrated by figure 2.5. This results in the growth of larger nanoparticles at the expense of the smaller ones [45, 46]. Ostwald ripening is driven by energy minimisation. Atoms migrate from regions of high chemical potential to sites of low potential, e.g. from unstable nanoparticle surfaces to low energy positions on the support. The chemical potential of an atom on the surface of a spherical nanoparticle can be described by equation 2.4, known as the Gibbs-Thomson relation [47].

$$\mu(r) = \mu_0 + \frac{2\gamma_m \Omega}{r} \tag{2.4}$$

Where μ is the chemical potential at a radius r, μ_0 is the bulk chemical potential, γ_m is the surface free energy and Ω is the atomic volume of the bulk metal.

The ease with which atoms migrate during Ostwald ripening is affected by the ability of atoms to detach from the nanoparticle surface (material and size dependent) and the ability of atoms to diffuse along support surfaces (dependent on the support material, the

presence of defects and the support surface roughness). Each of these processes has its own associated energy barrier. The energy associated with a metal atom diffusing along the surface of a support is given by equation 2.5.

$$E_{Tot} = \Delta H_{sub} - \left(E_{ad} + E_{diff}\right) \quad (2.5)$$

Where ΔH_{sub} is the sublimation energy of the metal, E_{ad} is the adsorption energy of an atom on the support surface and E_{diff} is the diffusion activation energy of an atom on the support.

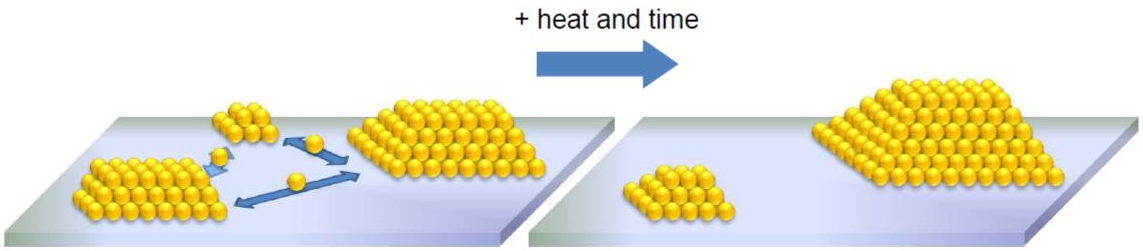

Figure 2. 5: Sintering by Ostwald ripening in which atomic or cluster transport occurs between particles, leading to the growth of larger particles at the expense of others. Reproduced from [21].

Since the Ostwald ripening process would theoretically mean a decreasing number of smaller particles in favour of larger ones, a particle size distribution based solely on Ostwald ripening would give an asymmetric distribution with a long tail pointing to smaller sizes. This is usually modelled by the Lifshitz-Slyozov-Wagner model [48]. However, observations of practical catalyst systems show that this model, along with Gaussian and lognormal distributions, can occur [49]. Therefore, nanoparticle size distributions cannot be used in isolation to identify the dominant sintering mechanism within a catalyst system. Indeed it is unlikely that Ostwald ripening will be the sole mechanism at play in the deactivation of a catalyst.

2.5.2 Particle Migration and Coalescence

In particle migration and coalescence (see figure 2.6), mobile species at the nanoparticle surface allow movement of the entire nanoparticle and a Brownian type motion. The nanoparticle migration proceeds like a random walk until two particles collide and interact. When this happens they merge to become a single nanoparticle, usually with the formation of a neck or bridge which facilitates the transfer of mass between the two

entities [50]. The neck structure also helps to facilitate the reorientation of crystal planes during the coalescence. Once the particles are joined together, restructuring can follow leading to low index, low energy surface facets. Most systems which form by particle migration and coalescence generate a lognormal particle size distribution.

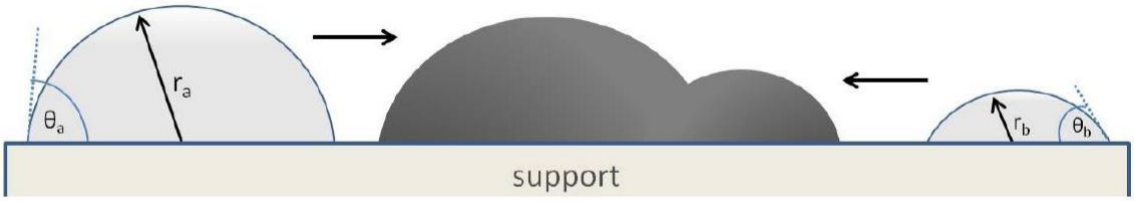

Figure 2. 6: Schematic representation of sintering via particle migration and coalescence. Reproduced from [21].

2.6 Reactivation

While deactivation due to sintering is an irreversible process, the effects of coking, poisoning and surface oxidation may be reversible with an appropriate reactivation procedure [51]. These can be performed online and do not require removal of the catalyst from the reactor. Carbonaceous contamination and strong adsorbed surface species can be removed by annealing treatments and oxidation of metallic catalysts can be reversed via reduction at high temperatures. Certain nanoparticles can restore themselves over progressive redox cycles. For example, small Ni nanoparticles can eject NiO crystallites preserving the original size distribution [52].

Chapter 3

Electron Microscopy

The experimental focus of this thesis is the utilization of environmental (scanning) transmission electron microscopy (E(S)TEM) to nanoparticle systems for catalysis applications. As such, this chapter will give a brief overview of TEM and STEM techniques relevant to this work. This discussion is by no means exhaustive and there are many excellent texts that describe the numerous techniques and theoretical understanding generated by decades of (ongoing) TEM development [11, 53-56]. This chapter will also present an introduction to the ETEM along with some possible detrimental effects that need to be considered when using the technique. Finally, a discussion will be given of supplementary techniques which provided data for the experimental work presented here.

3.1 The Transmission Electron Microscope

For the purposes of improving nanoparticle catalysts -and for nanoscience in general- material scientists aim to find a correlation between macroscopic behaviour and nanoscale structure. While there are many techniques available to materials scientists that can infer the fine structure of materials, microscopy is unique in that it provides real space images of the materials. However, the Rayleigh criterion (equation 3.1) states that the resolution of a microscope is dependent on the wavelength of the radiation used.

$$\delta = \frac{0.61\lambda}{\mu \sin \beta} \tag{3.1}$$

Where δ is the smallest object that can be resolved, λ is the wavelength of radiation, μ is the refractive index of the viewing medium and β is the collection semi-angle of the magnifying lens.

In a visible light microscope (VLM) photons of wavelength λ=400-700 nm are used. This gives a resolution of approximately 200 nm. While this is technically on the nanoscale, the nano-structures used in catalysis are much smaller than this. Moreover, the features which most heavily impact activity of a catalyst are well below this size.

In order to increase the resolution of a microscope, the wavelength of the radiation used (which can be focused and deflected with precision) needs to be decreased. The de Broglie wavelength [57] of a high energy electron (with relativistic correction) is given by equation 3.2.

$$\lambda = \frac{h}{\left[2m_0 eV\left(1+\frac{eV}{2m_0c^2}\right)\right]^{1/2}} \tag{3.2}$$

Where h is the Planck constant, m_0 is the electron rest mass, e is the charge on an electron, V is the potential difference that causes the electron acceleration and c is the speed of light. For an electron accelerated through a potential difference of 200 KV the relativistic wavelength is 0.00251 nm. This is much shorter than the wavelength of visible light and is much smaller than the distance between atoms in crystals.

Knoll and Ruska [58] invented the first electron microscope [59-61] in 1931. The advantage of using high energy electrons, as opposed to short wavelength photons, is that electrons have a fundamental charge which allows them to be controlled by electric and magnetic fields. Additionally, they interact strongly with matter; figure 3.1 shows some of the signals produced when a high energy beam of electrons interact with a thin specimen. Indeed the usefulness of the transmission electron microscope is not only the high resolution but its propensity for generating secondary signals from the specimen. Furthermore, the small wavelength of electrons opens up the possibility for these signals to be recorded on an atomic scale.

Electrons incident on a thin specimen can be transmitted through the specimen without deviation (and the majority are). However, for a given material a number interaction cross-sections exist. Elastically scattered electrons lose negligible energy during their

interaction within the specimen and can be forward or back-scattered by interaction with atomic nuclei. These elastically scattered electrons and their interactions with each other upon leaving the sample are used for imaging and diffraction. Inelastically scattered electrons lose energy to the specimen and can be used in electron energy loss spectroscopy (EELS) to give chemical and bonding information. Inelastically scattered electrons lose their initial kinetic energy by interaction with the electrons within the sample. Inner shell electrons can be scattered away from atoms, ionizing them. The relaxation of these atoms to lower energy states can release Auger electrons or characteristic X-rays which are used in energy dispersive X-ray spectroscopy (EDS or EDX) to give composition information. Energy loss events can trigger phonon or plasmon excitations within the sample. Finally, weakly bound electrons can be released from near the surface as secondary electrons, although these are utilized mostly in scanning electron microscopy (SEM).

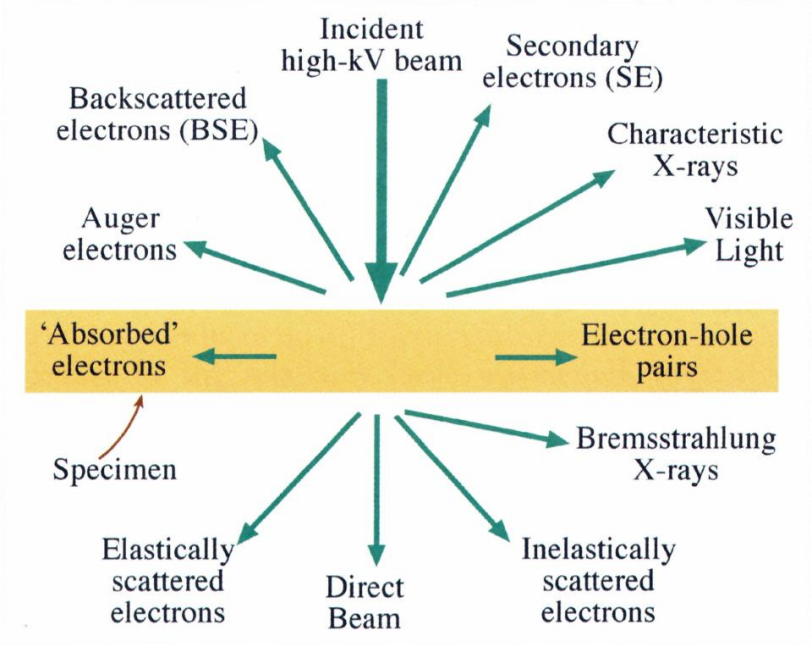

Figure 3. 1: Diagram illustrating the major signals generated by the interaction of high-energy electrons with a thin specimen [56]. Reprinted by permission from Springer Nature: Springer, Transmission Electron Microscopy by D.B. Williams and C.B. Carter, Springer Science+Business Media, LLC (2009).

3.1.1 Electron Optics

The most useful property of electrons is their intrinsic charge, this allows them in interact strongly with the electrostatic potential created by the atoms within a specimen.

However, this charge also allows a beam of electrons to be deflected by electric and magnetic fields. A beam of electrons can thus be focused using magnetic lenses. The force exerted on a beam of electrons under the action of a magnetic field (and electric field) is called the Lorentz force, shown in equation 3.3.

$$\boldsymbol{F} = -e(\boldsymbol{E} + \boldsymbol{v} \times \boldsymbol{B}) \tag{3.3}$$

Where **F** is the Lorentz force, **E** is the electrostatic field vector, **v** is the velocity of the electrons and **B** is the magnetostatic field vector. The Lorentz force allows the trajectories of a beam of electrons to be influenced using the relative strength of the magnetic field. It is this fact that allowed for the invention of the magnetic lens [62, 63]. A magnetic lens is formed from turns of copper wire, through which a current is passed, this creates a magnetic field. The coils of wire are wound around a magnetically permeable material such as soft iron which is shaped to be cylindrically symmetric. The piece of soft iron is called the lens pole piece. Through the centre of the lens there is a hole through which the beam of electrons can travel. The size and shape of the pole piece gap effects the relative strength and homogeneity of the magnetic field. An illustration of a simple magnetic lens is shown in figure 3.2.

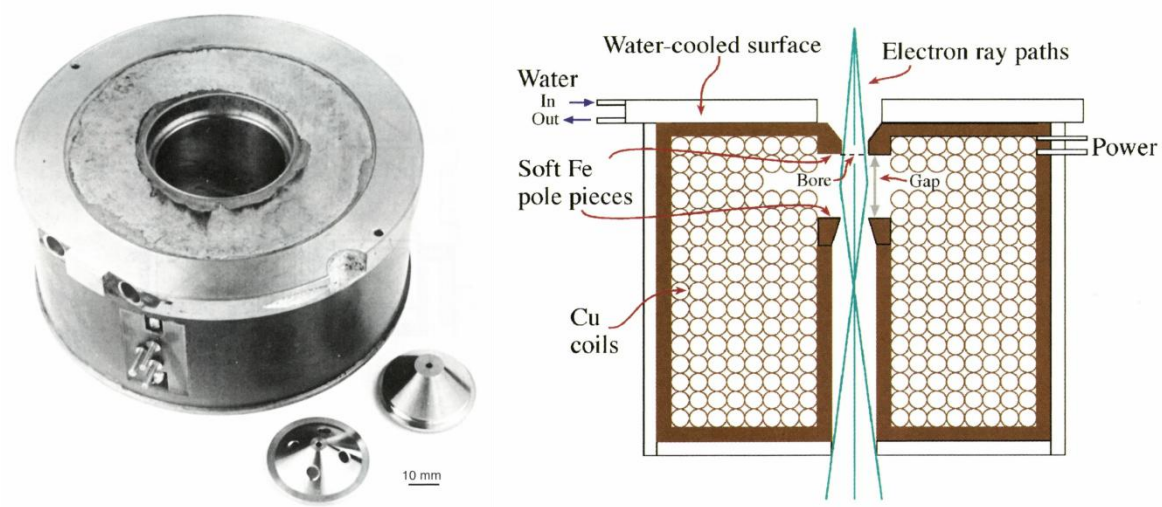

Figure 3. 2: Photograph of a TEM magnetic lens body and shaped pole pieces. A simple schematic of the internal components is also shown [56]. Reprinted by permission from Springer Nature: Springer, Transmission Electron Microscopy by D.B. Williams and C.B. Carter, Springer Science+Business Media, LLC (2009).

Since the force exerted on the electrons and by extension the amount by which their paths are deflected depends on the strength of the magnetic field, the focal length of the lens is related to the current passing through the coils and the geometry of the pole pieces. The focal length of a magnetic lens is given by equation 3.4. Where f is the focal

length, K is a constant based on the number of turns in the coil and the shape of the pole piece and I is the current through the coil.

$$f = K\left(\frac{V}{I^2}\right) \tag{3.4}$$

This change in focal length gives magnetic lenses a high degree of flexibility compared to glass lenses in a VLM. However, to generate the fields needed to deflect a high energy beam of electrons: large electrical currents are needed which lead to resistive heating within the copper coil. Therefore, water cooling is needed in all lenses used in the TEM.

For high resolution imaging in TEM the objective lens focal length needs to be kept short. This puts constraints on the geometry of the pole piece gap needed to create a magnetic field with relative homogeneity. This makes the shaping of the magnetic lens quite complex. The shape of the pole piece (as related by equation 3.4) has a large influence on the power of the lens. A number of designs of magnetic lens exist, especially where the objective lens is concerned; this lens focuses the incident beam of electrons onto the sample. The focal length of a typical objective lens is ~1.5 mm meaning that the sample must be immersed in the field. The most common objective lens design is the split pole piece objective. In this design the upper and lower pole pieces are separated allowing the specimen to be inserted from the side. This design accommodates specimen holders which allow for greater degrees of tilting or hot-stage capability. Apertures and detectors such as EDS detectors can be placed near the specimen within the split pole piece design.

The pole piece gaps in a magnetic lens are very small (on the order of mm) and the pole pieces themselves are shaped to concentrate the magnetic field. This means that magnetic lenses can be approximated as thin lenses. However, they are far from perfect and aberrations appear which lower the resolution of the microscope. Lens aberrations can be corrected for with an aberration corrector (see section 3.3).

3.1.2 Design

Figure 3.3 shows the basic arrangement of lenses, apertures and specimen in a conventional TEM (CTEM), note that deflector/alignment coils are not shown in this diagram for simplicity. The first element of the TEM is the electron gun [64]. The electron gun consists of a filament, from the surface of which electrons are released. This can be

done via thermionic emission using a W (Tungsten) or LaB_6 (Lanthanum Hexaboride) [65] filament through which a current is passed to raise its temperature providing energy to overcome the work function of the material. Alternatively, electrons can be emitted via a field emission gun (FEG) [66-68] in which case a strong electrostatic field is applied across the tip of a fine needle mounted on the aforesaid filament. The tip is normally made of single crystal W, where the field enables electron tunnelling through the surface energy barrier. A combination of these effects can be used in the case of the Schottky-emitter used in the present work. In either case electrons are released from the surface of the filament. An electrostatic lens is then used to bring the electrons to a cross-over, creating a virtual source. These electrons are then accelerated by electric potentials usually in the range of 100-300 KV for intermediate voltage electron microscopes (IVEM). However, larger acceleration voltages are used for certain materials and earlier in TEM development as a way of decreasing the wavelength of the electrons to gain high resolutions. Low acceleration voltages are used in biology as well as materials science where the sample can be very sensitive to beam damage by displacement.

The first magnetic lenses that the electrons encounter are the condenser lenses, traditionally two or three. The key role of the condenser lenses is to illuminate the specimen. They are used to collimate the electrons and provide the TEM operator control over the spot size, convergence angle and illumination spread at the sample.

The sample sits in the field of the objective lens, usually a split pole piece objective lens with both pre and post-specimen fields. The objective lens pre-field alters the convergence of the beam and for CTEM imaging illuminates the specimen with a near-parallel beam of electrons. This field can be changed to give a narrower beam with a larger convergence angle for alternate TEM modes such as convergent beam electron diffraction (CBED) and nano-beam diffraction (NBD). The electrons then interact with the specimen. For the TEM the specimen is required to be thin enough that electrons can be transmitted through the specimen (thickness <100 nm). It is common adage that for TEM the thinner the specimen the better. Specimens are usually loaded onto TEM grids approximately 3 mm in diameter. The general region of the specimen illuminated by the electron beam is controlled by the sample stage or goniometer, which can move the sample laterally and vertically respectively in x, y and z directions as well as tilt the

specimen in two axes. Next, an image of the specimen is formed by the objective lens, albeit not at a high magnification.

The final lenses in the TEM are the intermediate and projector lenses, these take the image of the specimen formed by the objective lens and magnify it many times. CTEMs can have a number of intermediate and projector lenses which sequentially magnify the image presented at their object plane by the previous lens (compound magnification). The projector lens projectors the final image onto a phosphorescent screen or a CCD (charge-coupled device) camera [69] (historically photographic film). Today images are collected and processed digitally [70].

In the TEM there are a number of alignment coils which act to deflect the beam such that the electron beam travels directly down the optical axis of each of the lenses and arrives normal to the sample. These coils also correct for astigmatism caused by inhomogeneous magnetic fields in the lenses. The stability (current-voltage) of these coils and lenses are not constant and the alignment of the electron beam at the start of a TEM experiment is essential [72] for high resolution imaging and for avoiding artefacts in the images or diffraction patterns. In this thesis an alignment procedure was performed at the start of every experiment; an overview of which is described in the following monograph [73]. The final component of the transmission electron microscope is that electrons are easily scattered by gases. Therefore, the microscope column needs to be kept under high vacuum conditions by the use of vacuum pumps including backing pumps (rotary or scroll) and high vacuum pumps such as diffusion and turbo.

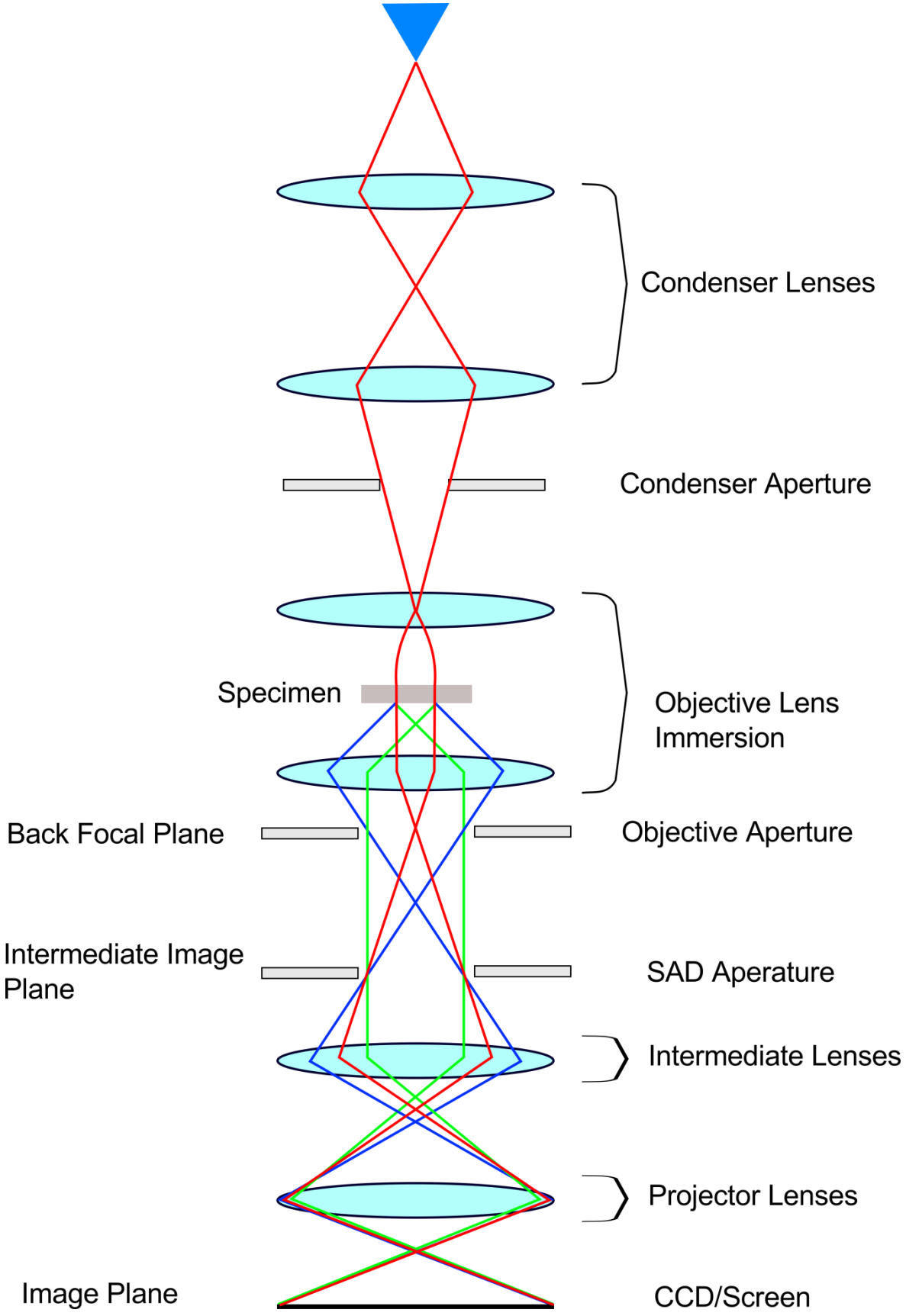

Figure 3. 3: Schematic of the main lenses in a TEM used for imaging [71]. Note that for simplicity the blue triangle represents the electron gun.

3.1.3 Electron Diffraction

Crystalline solids are made up of repeating arrays of atoms at set distances from each other. This translational symmetry of crystals is defined in terms of the crystal lattice, where lattice points are occupied by a motif of atoms in the crystal. The smallest repeating unit within a crystal is called the primitive unit cell. Any unit cell (primitive or non-primitive) can be described mathematically by three unit cell vectors **a, b** and **c**. The form of the crystal lattice that a material takes dictates the relative sizes and angles between these lattice vectors. This allows any point within a crystal to be described in terms of these vectors and is useful for the modelling of crystalline solids.

Crystal System	No. of Bravais Lattices in System	Axial and Angular Relationships
Cubic	3 (P, I, F)	a=b=c α=β=γ=90°
Tetragonal	2 (P, I)	a=b≠c α=β=γ=90°
Orthorhombic	4 (P, C, I, F)	a≠b≠c α=β=γ=90°
Monoclinic	2 (P, C)	a≠c α=γ=90°, β≠90°
Triclinic	1 (P)	a≠b≠c α≠β≠γ≠90°
Trigonal	1 (P)	a=b=c α=β=γ≠90°
Hexagonal	1 (P)	a=b α=β=90°, γ=120°

Table 3. 1: Summary the 14 Bravais lattices. P= primitive, C= base-centred, I= body-centred and F= face-centred. a, b and c define the axes of the crystal and α, β and γ are the corresponding angles.

As one would expect many elements and chemical compounds show similar atomic arrangements which share a common translational symmetry. The majority of these translational unit cells are described by the 14 Bravais lattices [74]. The 14 Bravais lattices are summarised in table 3.1. With repeating motifs of atoms, repeating atomic planes can be seen in crystals. Atomic planes are described by Miller indices (hkl), these planes are

described by the lowest fraction intersections of the planes with the axes defined by the unit cell vectors **a**, **b** and **c**. The Miller notation uses circular brackets, i.e. (hkl), to describe specific atomic planes and curly brackets to describe families of planes that have equivalent crystallographic symmetry. Crystallographic directions are notated by square brackets, for cubic systems these directions are orthogonal to the planes by (hkl). The distances between repeating atomic planes (hkl) are called inter-planar distances and are shown in table 3.2 [75].

Louis de Broglie hypothesised that electrons can behave as waves (proved by Davisson and Germer), as already discussed the wavelength of a high energy beam of electrons is much smaller than the distance between atoms in a crystal. When the specimen is placed far from the electron source (as it is in the TEM) the electron wave that arrives at the sample can be thought of as a coherent plane wave. With a suitably orientated crystal, the periodic arrangement of the atoms acts like a diffraction grating. Bragg provided the famous model for X-rays diffracting through a crystal [76, 77] and the same laws apply for electron diffraction. Constructive interference of electrons after passing through a crystal is described by the Bragg equation (equation 3.5).

$$n\lambda = 2d \sin\theta_B \tag{3.5}$$

Where n is the diffraction order and θ_B is the Bragg angle. Since the wavelength of the electron in a TEM is fixed by the microscope and d is determined by the material of the specimen, the resulting diffraction pattern can yield information about the crystal specimen.

Electrons incident upon a crystal at an angle that satisfies the Bragg condition, exit the specimen parallel to, and in phase with each other. In an optical system (like the TEM), the point at which initially parallel rays come to a focus is called the back focal plane of the imaging lens. In a TEM the strength of the first intermediate lens can be set to image the back focal plane of the objective lens. This allows the operator to acquire a magnified diffraction pattern of a crystal, which can be captured by the CCD for analysis. The physical size of the projected diffraction pattern [53] is given by equation 3.6.

$$rd = L\lambda \tag{3.6}$$

Where r is the measured distance from the centre of the diffraction pattern (direct beam or zero-angle scattered/transmitted beam) to the diffracted beam caused by scattering from crystal planes a distance d apart. L is called the camera length and is the effective

distance between the specimen plane and the recording plane. Note that the physical distance between these planes is fixed in a TEM column, but the effective distance travelled is determined by the excitation of the intermediate and projector lenses. This relates the distance in reciprocal space of a diffracting element in the crystal to the physical size of the diffraction pattern. This is determined by the product Lλ (called the camera constant) which can be thought of as the magnification of the diffraction pattern. This can be altered for greater sampling of the diffracted special frequencies or for a wider angular range for the higher order diffracting elements.

Crystal System	Inter-planar Distances, d_{hkl}
Cubic	$\frac{1}{d^2} = \frac{h^2 + k^2 + l^2}{a^2}$
Tetragonal	$\frac{1}{d^2} = \frac{h^2 + k^2}{a^2} + \frac{l^2}{c^2}$
Orthorhombic	$\frac{1}{d^2} = \frac{h^2}{a^2} + \frac{k^2}{b^2} + \frac{l^2}{c^2}$
Monoclinic	$\frac{1}{d^2} = \left(\frac{h^2}{a^2} + \frac{k^2 \sin^2\beta}{b^2} + \frac{l^2}{c^2} - \frac{2hl\cos\beta}{ac}\right)\csc^2\beta$
Triclinic	$\frac{1}{d^2} = \frac{\frac{h^2}{a^2}\sin^2\alpha + \frac{k^2}{b^2}\sin^2\beta + \frac{l^2}{c^2}\sin^2\gamma + \frac{2kl}{bc}\cos\alpha + \frac{2hl}{ac}\cos\beta + \frac{2hk}{ac}\cos\gamma}{1 - \cos^2\alpha - \cos^2\beta - \cos^2\gamma + 2\cos\alpha\cos\beta\cos\gamma}$
Trigonal	$\frac{1}{d^2} = \frac{(h^2 + k^2 + l^2)\sin^2\alpha + 2(hk + kl + hl)(\cos^2\alpha - \cos\alpha)}{\alpha^2(1 - 3\cos^2\alpha + 2\cos^3\alpha)}$
Hexagonal	$\frac{1}{d^2} = \frac{4}{3}\left(\frac{h^2 + hk + k^2}{a^2}\right) + \frac{l^2}{c^2}$

Table 3. 2: Inter-planar distances, d, for given (hkl) planes in the Bravais lattices.

Since not all crystal planes diffract in the same way, diffraction from different crystal planes within a sample can interfere with each other and lead to destructive interference. This is described mathematically by the structure factor, given by equation 3.7. The intensity of a diffracted beam is equal to the modulus squared of the structure factor. The structure factor can be solved for individual crystal planes (hkl) to give a scattering intensity of zero, this leads to certain reflections in the diffraction pattern being forbidden (total destructive interference).

$$F(\theta) = \sum_{i}^{\infty} f_i(\theta) exp(2\pi i[hx_i + ky_i + lz_i]) \tag{3.7}$$

Where F is the structure factor, θ is the scattering angle, f is the atomic scattering factor and x, y, z are coordinates such that i atoms have coordinates x_i, y_i and z_i.

For practical purposes in the TEM, it is useful to collect a diffraction pattern from one part of the specimen rather than every object under the beam. In order to do this an aperture is used to select a region of interest on the specimen, this is called the selected area diffraction (SAD) aperture. Due to the lack of room around the sample (inside of the objective lens pole piece) the SAD aperture is placed at the image plane of the first intermediate lens which is projected back to the specimen plane. Due to the physical distance between these two planes and the optical conditions (defocus and spherical aberration) involved there is a lateral displacement error between the area observed to be selected by the aperture and the true selected area [78]. This is given by equation 3.8 [79], this displacement error can be on the order of micrometres, but can be significantly reduced by correcting the spherical aberrations of the objective lens.

$$y = C_s(2\theta_B)^3 + 2\theta_B\Delta f \tag{3.8}$$

Where y is the lateral displacement, C_s is the spherical aberration coefficient and Δf is the defocus.

3.1.4 Imaging

So far the TEM has been discussed as a diffraction instrument; however, like any microscope it can provide real space images of the sample. Upon leaving the specimen the electrons are collected by the post-specimen field of the objective lens. The image of the sample is then magnified further by the intermediate lenses to produce a highly magnified image at the CCD/detector. Based on the imaging conditions and apertures used, a number of different images can be produced, dominated by different contrast mechanisms. Most relevant to this thesis are amplitude contrast and phase contrast in high-resolution TEM (HRTEM).

Amplitude contrast images (or bright field (BF) and dark field (DF)) are formed by the insertion of an aperture into the back focal plane of the objective lens (figure 3.3). This aperture can be used to select either the direct beam or one of the many diffracted beams from the sample. By selecting only the central (direct beam) a BF image is formed, in which the vacuum is white and objects are dark due to mass-thickness contrast. Alternatively, a specific diffracted beam can be selected and all contrast within the image comes from that beam. In other words, objects within a specified range of scattering

angles appear bright, while everything else is black. The range of spatial frequencies that can be selected in this way depend purely on the size of the objective apertures in the TEM. Additionally, large objective apertures can be used to filter out high order diffracted beams to enhance contrast in HRTEM images or in energy filtered TEM (EFTEM).

Phase contrast arises when the direct beam and the diffracted beams are both allowed to be imaged by the intermediate lens. In the image plane these beams interfere with each other and produce contrast in the image due to phase differences. Details of the formation of phase contrast images can be found elsewhere, what is important is that the electron wave exiting the sample is a product of the incident electron wave function and the projected periodic potential of the sample [80]. This interaction gives rise to complex images feature such as: lattice fringes which are related to atomic planes in the sample and can give information about the crystal planes present [81] and Moiré fringes which arise from overlap of two crystal planes (similar or different) which are translated or rotated with respect to each other. Subtle features in phase contrast images can be used to identify crystal attributes such as grain boundaries, dislocations and extended defects.

3.2 The Scanning Transmission Electron Microscope

The scanning transmission electron microscope (STEM) was invented by Albert Crewe [9, 82]; unlike the TEM where a parallel beam is used, the STEM relies on a highly converged electron beam. The point at which the electrons come to a focus is called the probe and is made to appear at the specimen plane. The highly converged beam is achieved using the TEM condenser lenses, in STEM the condenser lenses are collectively referred to as the probe forming lens. A schematic diagram of the STEM is shown in figure 3.4.

In the STEM instrument the electron probe is too small to form an image, instead, a set of scan coils are used to raster the beam across a small region of the sample. The electrons transmitted through the sample are collected by various detectors and integrated for each probe position and together form the final image. Simply, TEM is a parallel technique where the entire image is collected at once whereas STEM is a serial technique where each pixel of the image is collected individually. The localisation of the electron probe allows for composite images to be created (from different signals); energy loss

(EELS) and X-ray (EDS) signals are acquired in parallel with the image to produce spectral images or composition maps of specimens [83, 84].

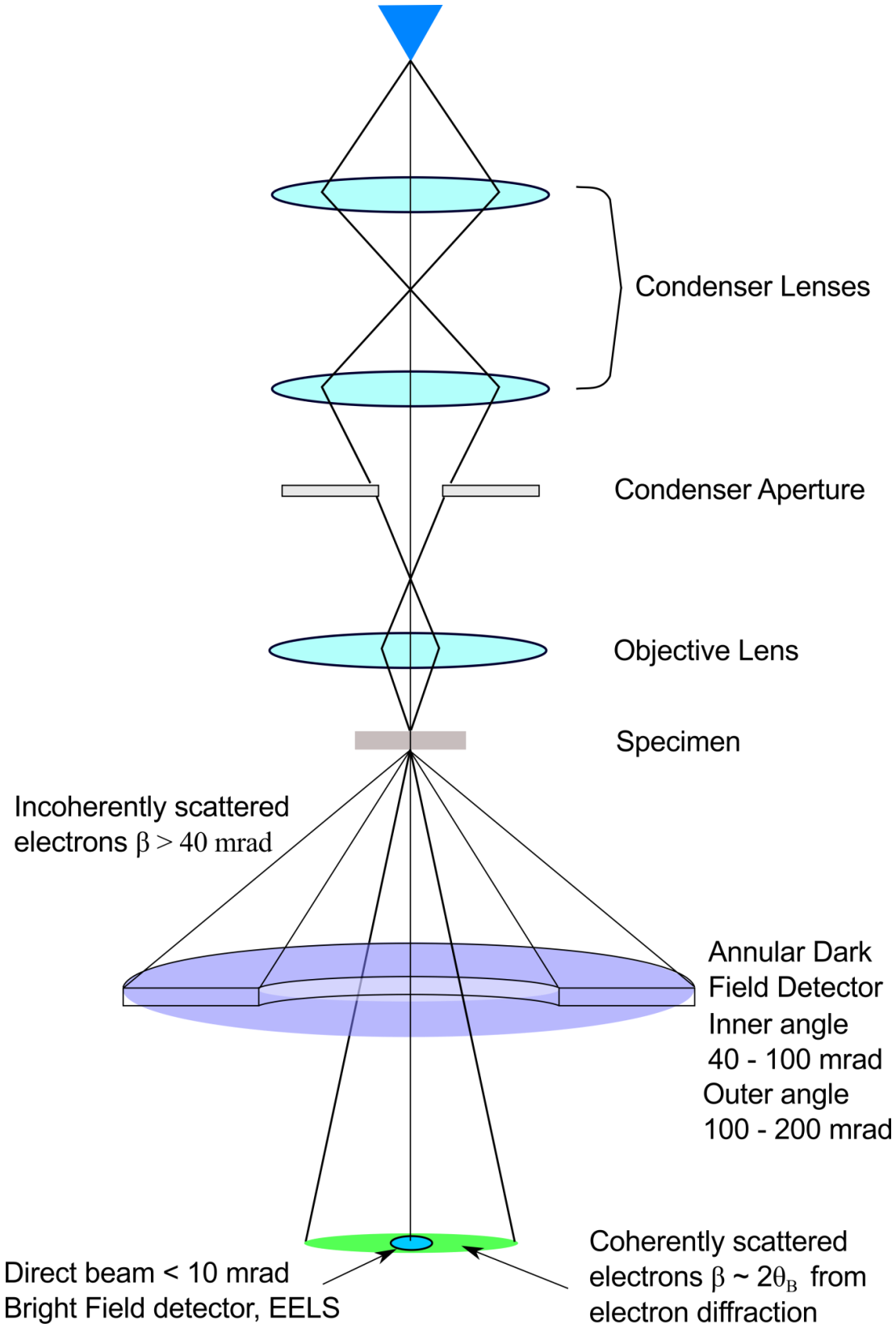

Figure 3. 4: Schematic of the STEM showing the probe forming system and the geometry of the detectors [71]. The scan coils (not shown) are located above the objective lens.

STEM is a high resolution technique and was one of the first to be able to resolve single atoms [85, 86]. In a STEM the resolution is determined by the size of the probe. The magnification is determined by the area of the specimen scanned and the number of points that the area is divided into. This process is not dependent on the lenses but on the electronic signals sent to the scan coils and the integration time of the detectors.

The type of image formed by the STEM depends upon which electrons are being collected. In STEM the only lenses that matter are those above the specimen which form the electron probe. Below the specimen the lenses only act to project the electrons further down the column to the detectors. The most common STEM detectors are the on-axis detector and the annular dark field (ADF) detector. When electrons from the direct beam or with small scattering angles are collected (by the in-line detector) they form a bright field STEM (BF-STEM) image. This technique is similar to a BF TEM image however, as elastically scattered electrons are dominant, the image contains diffraction contrast [87] as well as absorption contrast. For the high angle scattered electrons, an annular detector is used. Depending on the collection angles of the detector the image formed is a DF image with some diffraction contrast [10]. However, when very highly scattered (~100 mrad) electrons are collected, with a high angle annular dark field (HAADF) detector, the electrons are scattered primarily by the nuclei of the specimen via Rutherford scattering. The collection angles for a HAADF-STEM detector are usually >40 mrad (inner) and <200 mrad (outer). For Rutherford scattering the intensity in the image is related to the atomic number (Z) of the specimen and so is commonly referred to as Z–contrast imaging. The intensity is proportional to Z^n where $1.5<n<2$ [88, 89]. The discrepancy between the predicted value of n=2 and the experimentally observed values (closer to n=1.7) is known as the Stobbs factor [90, 91]. STEM is an appropriate technique in the study of catalysts since, in many cases, heavy metals are dispersed on a low-Z supports. The detector signal for HAADF-STEM can be boosted by the electronics to pick out various features. A quantitative interpretation of the image intensity requires a well characterised detector and an accurate model of the initial probe intensity [92] or advanced image simulations of the sample [93] to account for the possible contributions to the final image intensity [94].

An interesting feature of the STEM is the electron Ronchigram [95, 96]. The Ronchigram is a far-field Fraunhofer diffraction pattern and can be used for alignment of the STEM

instrument [97]. At high levels of defocus this forms a shadow image of the specimen useful for finding a region of interest. Since the Ronchigram is a far-field diffraction image, small apertures can be introduced into the condenser system to create convergent beam diffraction patterns of the specimen at the probe position. This has been utilized more recently as a way of collecting diffraction patterns and images simultaneously and in precession diffraction techniques [98].

3.3 Limits to Resolution

Decades of (S)TEM development have seen great improvements to factors such as mechanical and thermal stability of the microscope column and reduction in instabilities in voltage supplies for both lenses and electron sources. Nevertheless, the resolution achieved by (S)TEM is still not in line with that predicted by the Rayleigh criterion. The main limiting mechanism for (S)TEM resolution is aberrations in the magnetic lenses. The two main types of lens aberrations are spherical aberrations and chromatic aberrations. Photonic lenses in VLMs can limit these using shaped (concave) lenses and optical elements and by chemical coatings. The reduction of aberrations in the cylindrically symmetric magnetic lenses of the (S)TEM is more of a challenge.

Spherical aberration is caused when electrons entering the lens close to the optical axis are brought to a focus at a different point to those that enter further from the optical axis. This is shown schematically in figure 3.5 where a point in the specimen appears as a disc in the image.

Chromatic aberration occurs when electrons of different wavelengths are brought to a focus at different points by the lens. This has a similar effect as spherical aberrations in that point objects are spread out into discs; the radii of the discs caused by spherical and chromatic aberrations are given by equations 3.9 and 3.10 respectively. Seeing as the wavelength of electron is related to their energy, chromatic aberrations can be caused by the initial energy spread produced by the electron gun or by the specimen via inelastic scattering. While inelastic scattering is useful for EELS and EFTEM, a large energy spread in the electron source is invariably a drawback. This has been greatly reduced with the introduction of the FEG and sometimes (usually on analytical instruments) by the use of a monochromator.

$$r_{sph} = C_s\beta^3 \tag{3.9}$$

$$r_{chr} = C_c\frac{\Delta E}{E_0}\beta \tag{3.10}$$

Where C_s and C_c are the spherical and chromatic aberration coefficients respectively, ΔE is the energy spread of the beam, E_0 is the initial (or modal) beam energy and β is the collection semi-angle of the lens.

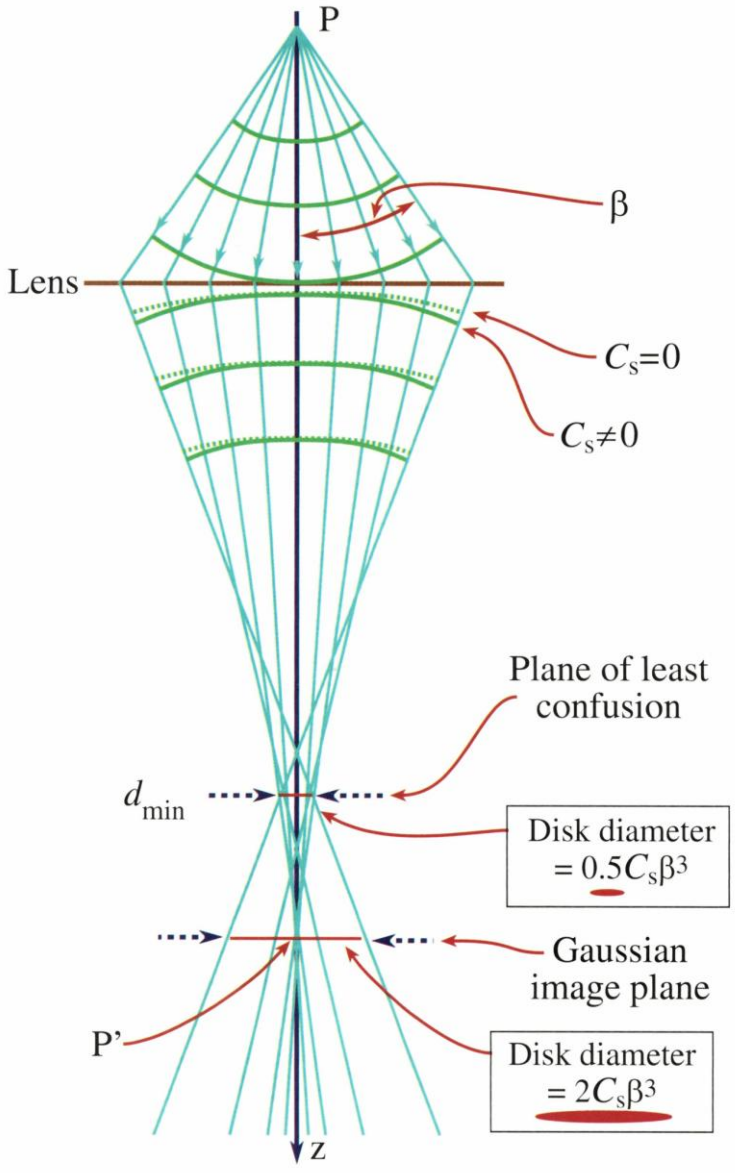

Figure 3. 5: Ray diagram showing the effect of spherical aberration. A point P is imaged as a disc at the Gaussian image plane [56]. Reprinted by permission from Springer Nature: Springer, Transmission Electron Microscopy by D.B. Williams and C.B. Carter, Springer Science+Business Media, LLC (2009). Originally printed in Springer, Transmission Electron Microscopy by L. Reimer, Springer-Verlag Berlin Heidelberg (1993).

3.3.1 The Contrast Transfer Function

The way in which information (or contrast) transferred from the specimen to the image [99] is described by the contrast transfer function (CTF), H(**u**), where **u** is a spatial frequency (Fourier transform of a real space vector). The CTF is given by equation 3.11.

$$H(\boldsymbol{u}) = A(\boldsymbol{u})E(\boldsymbol{u})B(\boldsymbol{u}) \tag{3.11}$$

The CTF is a product of the aperture function A(**u**), the envelope function E(**u**) and the aberration function B(**u**). The first two terms describe a cut off for **u** by the apertures and the lens respectively. By considering the specimen as a weak phase object the CTF can be rewritten as the intensity transfer function, T(**u**), which is given by equation 3.12.

$$T(\boldsymbol{u}) = A(\boldsymbol{u})E(\boldsymbol{u})2\sin\chi(\boldsymbol{u}) \tag{3.12}$$

$$\chi = \pi\Delta f\lambda u^2 + \frac{1}{2}\pi C_s\lambda^3 u^4 \tag{3.13}$$

Where χ(**u**) is the phase distortion function (equation 3.13) which describes the phase shift of the electrons affected by spherical aberration and defocus. The form of equation 3.13 assumes that 2-fold astigmatism, caused by imperfections in the shape of the lens pole piece, has been corrected for (TEMs ubiquitously have corrector coils for this). Figure 3.6 shows a plot of T(**u**) for a C_s corrected and uncorrected microscope.

Figure 3.6 shows that the contrast oscillates (switches from light to dark contrast and back again) many times over the range of spatial frequencies commensurate with the atomic features of most materials. This oscillation in contrast makes HRTEM phase contrast images difficult to interpret. Furthermore, there are specific spatial frequencies where the contrast transfer is zero resulting in no contrast in the image for those frequencies. The region of figure 3.6 of interest to most microscopists is the initial part of the curve before it intersects with the x-axis. This region marks the range of spatial frequencies for which the contrast is continuous (no inversion) and the image contrast is directly interpretable. The first point of intersection with the x-axis is known as the first zero or the point resolution after which phase inversions make the contrast information hard to translate. The point at the right of the diagram is called the information limit and is when no information is transferred at all; mathematically this is not zero but a rapid oscillation with low amplitude (below the noise level).

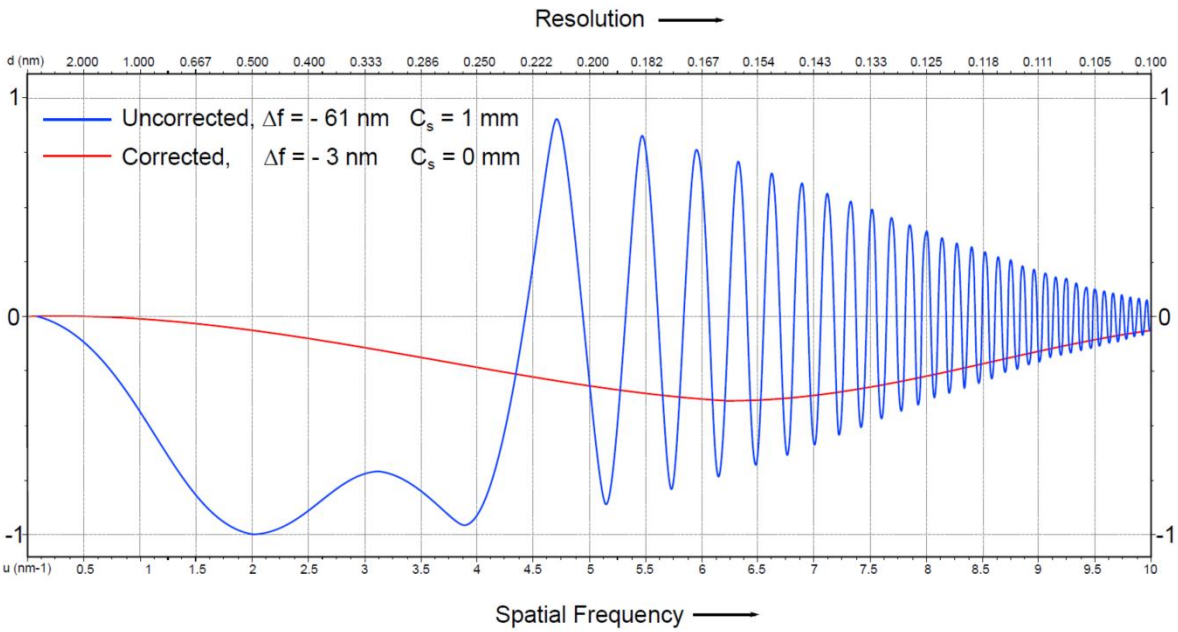

Figure 3. 6: Typical intensity CTF for a modern C_s corrected and uncorrected microscope with representative E(**u**). Defocus is set at the optimum (extended Scherzer) defocus [71].

Owing to the fact that T(**u**) depends on the defocus value, it can be shown that for any given value of C_s there is an optimum value of defocus for which the spatial range before the onset of the first zero is maximised [100]. This value is known as the Scherzer defocus and is given by equation 3.14. Note that the 1.2 term is for the "extended" Scherzer defocus shown in figure 3.6 which gives a slight inflection on the contrast transfer, values of 0, 0.5, 1, 2, etc. can be used to remove this inflection at the cost of moving the first zero to lower spatial frequencies.

$$\Delta f_{Sch} = -1.2(C_s\lambda)^{1/2} \tag{3.14}$$

The C_s corrected example in figure 3.6 shows that by minimising the spherical aberrations a continuous transfer of contrast information can be generated across the entire range of spatial frequencies down to the information limit. Thus aberration correction can lead to the acquisition of readily interpretable phase contrast images with small values of defocus (reducing delocalisation effects).

3.3.2 The Aberration Corrector

In 1936 Scherzer [101] showed that any electron optical system will present spherical and chromatic aberrations if the following criteria are met simultaneously [102].

1) The optical system is rotationally symmetric.
2) The system produces a real image of the object.

3) The fields of the system do not vary with time.
4) There is no charge present on the electron-optical axis.

The basis for the current commercial aberration correctors relies on breaking the rotational symmetry of the optical system [103]. This is achieved using magnetic multipole lenses which produce non-circular fields. Dipole lenses impose a uniaxial force on electrons. Quadrupole, sextupole (hexapole) and octupole produce 2-fold, 3-fold and 4-fold symmetries respectively.

Name	Krivanek notation	Rose notation	Target values
Defocus	$C_{1,0}$	C_1	<2 nm
2-fold astigmatism	$C_{1,2}$	A_1	<2 nm
3-fold astigmatism	$C_{2,3}$	A_2	<10 nm
Coma	$C_{2,1}$	B_2	<10 nm
Spherical aberration	$C_{3,0}$	C_3 (C_s)	<500 nm
4-fold astigmatism	$C_{3,4}$	A_3	<1000 nm
Star aberration	$C_{3,2}$	S_3	<1000 nm
5-fold astigmatism	$C_{4,5}$	A_4	Cannot be corrected

Table 3. 3: Table of the common lens aberrations corrected for with an aberration corrector [102]. The target values were considered optimal and correction was performed to achieve this (for 0.1 nm resolution).

Theoretical designs for the aberration corrector came about very early on [104, 105] but there was a long delay before the creation of the first working corrector. The delay was due to the lack (at the time) of advanced computing power that is needed to control the parameters of the corrector simultaneously while modelling and interpreting the complex series equations that describe the relationship between the aberrations of differing order. The problem with using multipole lenses is that their own symmetries and in-homogeneities induce additional parasitic aberrations [106-108]. Examples of common aberrations are shown in table 3.3 along with the values of the aberration coefficients that were aimed for during the correction phase of the alignments used for this thesis.

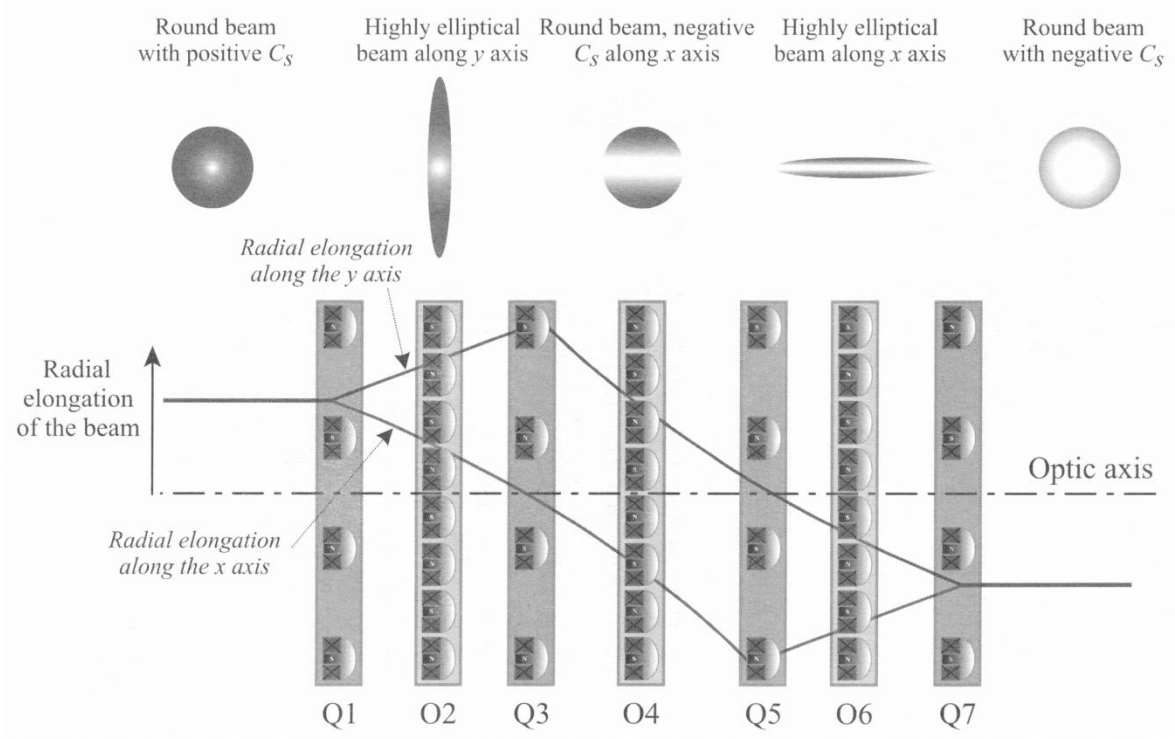

Figure 3. 7: The quadrupole-octupole corrector schematic. The corrector consists of three octupoles and four quadrupoles. Reprinted from [102] with permission (2011 John Wiley & Sons, Ltd).

In TEM the aberration corrector is placed after the specimen to correct for the aberrations in the objective lens [109]. The TEM corrector is known as an image corrector [110, 111]. In STEM mode the resolution is determined by the shape and size of the probe. Therefore, the STEM corrector, called a probe corrector, is placed before the specimen to correct for aberrations in the probe forming lens [112]. Correcting the aberrations in STEM creates a narrower and more intense probe. Aberration correction has enabled STEM to achieve a sub-angstrom level of resolution [113-115]. The two commercial designs of aberration correctors are the quadrupole-octupole corrector [116] (figure 3.7) and the double hexapole corrector [117-119] (figure 3.8).

Aside from the increase in resolution and the greater interpretability of contrast in images there are a couple of additional benefits to aberration correction. Firstly, the C_s of a lens is no longer fixed and can be controlled to produce new imaging regimes [120] such as negative C_s imaging (NCSI) [121] which can invert the contrast of atomic positions in TEM. Secondly, wider gap pole pieces can be utilized without fear of incurring additional C_s. This is particularly advantageous for in-situ experiments as a wider gap in the objective lens means that specialised holders (heating, gas, liquid, tilt-tomography, etc.) can be introduced.

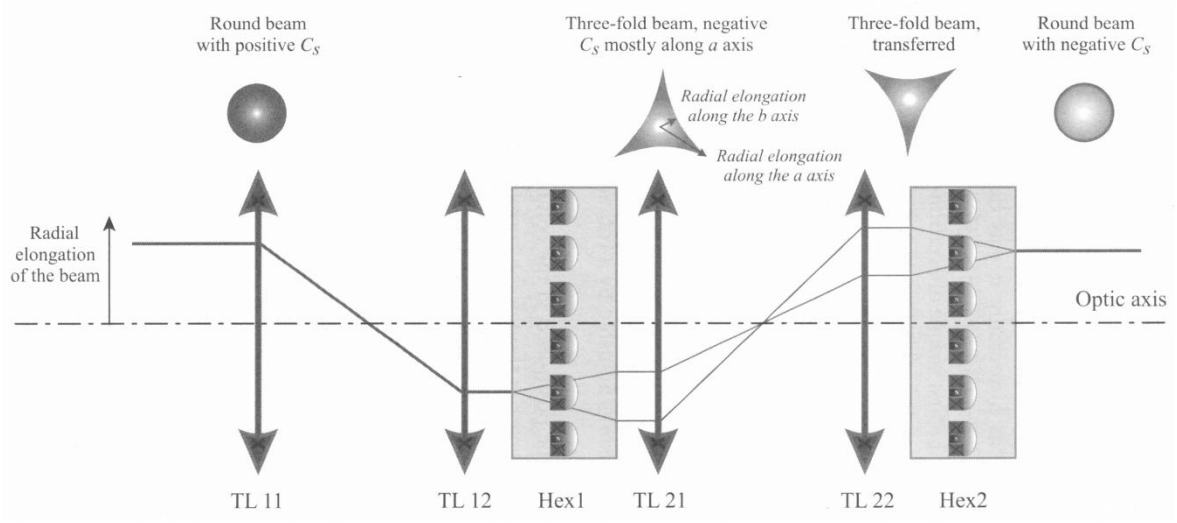

Figure 3. 8: The double hexapole corrector schematic. The corrector consists of two hexapoles and two transfer lenses. Reprinted from [102] with permission (2011 John Wiley & Sons, Ltd).

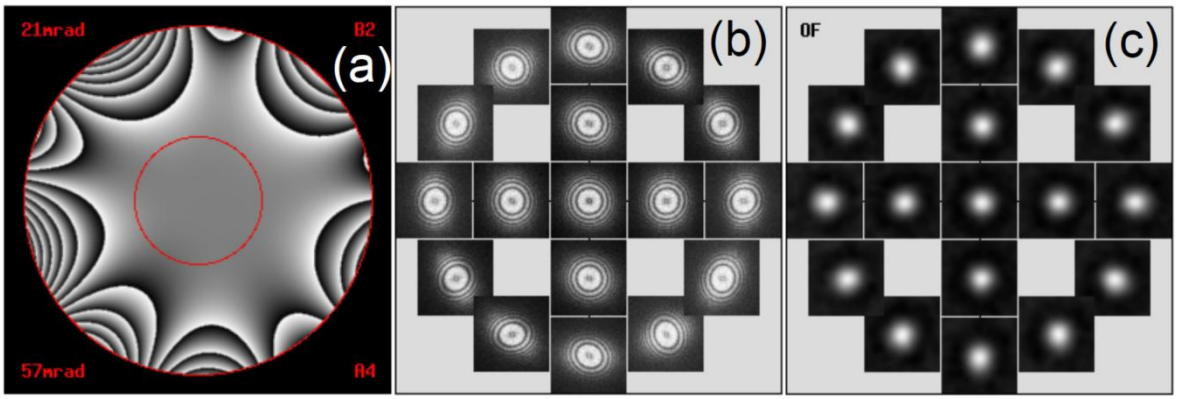

Figure 3. 9: CEOS aberration correction software showing a) electron phase plate, b) TEM Zemlin tableau and c) HAADF-STEM probe image tableau. The angle at the top of a) is the calculated angle over which a constant phase, within π/4, is preserved. The lower value represents the 12π limit. Reproduced from [71].

The correction of the microscope is done via a software interface. For TEM correction a specimen made from thin amorphous carbon film is used. A fast Fourier transform (FFT) of this type of sample produces a series of high contrast Thon rings when displaced from the electron optical eucentric position. The software interprets the shape of these rings and calculates the defocus and 2-fold astigmatism in the image. This is done numerous times as a function of beam tilt to create a Zemlin tableau [122]. The software uses this to construct a model (or phase plate) of the electron wave front and suggests corrections to the user. A similar method is employed for STEM, except that a specimen of heavy nanoparticles (usually Au) is used instead. This produces a HAADF-STEM image with high contrast. A deconvolution algorithm is used to construct an under and over-focused image of the probe which is used to calculate the defocus and 2-fold astigmatism. A

similar set of tableaus are then constructed as a function of beam tilt. Examples of the software interface are shown in figure 3.9.

3.4 Beam Damage

So far, only the benefits of TEM have been discussed, however there are drawbacks to the technique. As already discussed electrons can be involved in inelastic collisions and thereby deposit energy within a thin sample. This is referred to as beam damage [123]. Beam damage is a major issue for electron microscopists as there is no single step that can be taken to reduce this as the susceptibility to beam damage is sample dependent. For the most part beam damage is irreversible and once the structure of the specimen has been changed, it is no longer representative of the rest of the specimen or the bulk from which the sample was taken.

There are three types of beam damage. First, radiolysis caused by electron-electron interactions, for example, ionization which breaks chemical bonds in materials such as polymers. Since this is an electron-electron interaction radiolysis can be minimised by using higher beam energies. Second is knock-on damage, produced when a large amount of energy and momentum from the incident beam of electrons is transferred to the nuclei of atoms within the specimen. This causes atoms to be either moved from their equilibrium positions or ejected from the specimen all-together. This type of beam damage can be reduced by lowering the beam energy; ideally below the threshold critical onset voltage for displacement damage. The final type of beam damage is heating; as electrons travel through the specimen they cause phonon excitations. The phonons produce heat which can damage soft materials such as biological samples. Cooling of the sample mitigates heat damage.

In this thesis the materials investigated are metals. For metals the major type of beam damage is knock-on damage. By displacing atoms from their original lattice sites, defects can be introduced into the material. If care is not taken these defects may be interpreted as being part of the original structure. The threshold energy for knock-on damage is determined by how atoms within the crystal lattice are bonded to their neighbours. An expression for this was conceived by Hobbs [124] and is shown in equation 3.15.

$$E_t = \frac{\left(\frac{100 + AE_d}{5}\right)^{1/2} - 10}{20} \quad (3.15)$$

Where E_t is the threshold energy required for displacement of atoms, A is the atomic weight of those atoms and E_d is the displacement energy and depends on the type of chemical bonding in the crystal.

The main way of telling whether knock-on damage has occurred in a specimen is to take images before and after long exposures to the electron beam. These so-called calibration experiments are needed to gauge the imaging conditions necessary for the acquisition of representative data by the TEM.

Beam damage is compounded during in-situ experiments. When hot-stages are used for investigating thermally driven transformations, calibrations have to be made for the heating caused by the beam versus by the stage. Environmental (gas) in-situ experiments can be impacted by gas ionisation. Additionally, under oxidising or reducing conditions the electron can add energy to the reaction. This is theoretically more pronounced during reduction as the beam itself is adding electrons to the sample. Furthermore, reference images should be taken periodically during in-situ studies to check that the current state of the specimen is the same for the imaged areas and the non-imaged areas. Beam damage is more easily identified in STEM as the beam raster is confined across a specific area and difference between the imaged and “untouched” area is usually more striking than in TEM.

3.5 In-Situ Electron Microscopy

Conventional TEM and STEM experiments are performed under high or ultra-high vacuum conditions and structural details of the sample are observed. For catalysis research the structure is used to infer the origin of the catalytic activity. This approach provides an incomplete picture of catalytic reactions and of catalysts themselves. Catalysis can involve a number of intermediate reaction steps and the formation of metastable structures within the sample. These are unobservable using ex-situ methodologies which only show the start and end points of a reaction. Furthermore, an aged catalyst sample may be changed by exposure to ambient conditions on the way to the TEM. It is obvious then that in-situ (S)TEM techniques are needed.

In regard to electron microscopy the term “in-situ” is rather broad and can describe simple heating of the specimen to the full complement of in-situ techniques. Although many forms of in-situ TEM exist including cryo-TEM and wet cell TEM, this thesis focuses on the in-situ reproduction of conditions relevant to heterogeneous catalysis using heating and gaseous environments. In-situ TEM using gas injection is referred to as environmental TEM (ETEM).

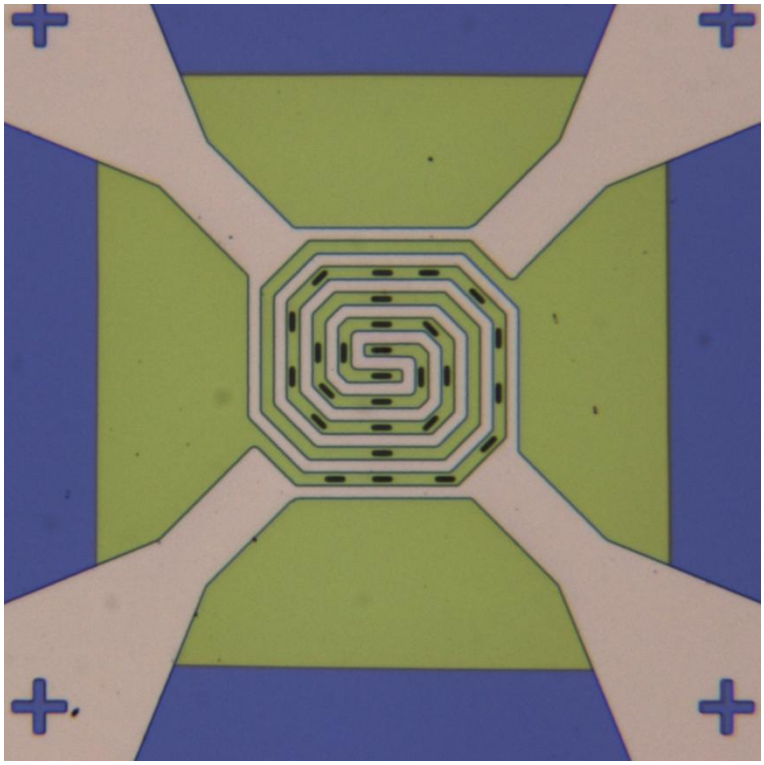

Figure 3. 10: Optical micrograph of the central heating element of a MEMS heating chip used in this thesis. The green area is a thinned central region and the black slits are holes through the SiN_x (Si_3N_4 related) chip and covered by an amorphous support film for TEM observations (~20 μm across).

As discussed earlier in this chapter, aberration correction allows wider gap objective lens pole pieces to be used without impact to the TEM resolution. The wider gap allows specimen heating stages (hot stages) to be used. Until recently these involved a specimen stage with an integrated resistive heating element. These holders suffered from instabilities from power supplies and from large thermal expansions/contractions that would displace the specimen by micrometres and induce sample drift. Today MEMS technology has advanced to the stage where “heating chips” can be used for in-situ heating [125]. The MEMS heating stage used in this thesis was made by Dens Solutions and an image of the heating element of a MEMS chip is shown is figure 3.10. The small area of the heating element leads to much greater stability and faster sensing of the

temperature which (via a feedback loop) leads to stable temperatures and positionality compared to the old style hot-stages.

The earliest ETEM experiments involved separate chemical reaction chamber that was physically added to the TEM column [126, 127]. This cell featured electron transparent windows at the top and bottom for the electron beam and provided ports for gas injection. Certain modern environmental cells incorporate a miniaturised gas reactor into a MEMS design such that the environmental cell is simply part of the specimen holder [128-131]. This design allows for high gas pressure to be reached, but at the expense of TEM resolution due to the thick windows that are in the beam path. Additionally, EDS is complicated due to shadowing of the specimen by the environmental cell.

An alternate approach has been to incorporate the reaction chamber into the existing specimen chamber of the microscope i.e. a true environmental TEM. In this design gases are injected into the specimen chamber of the TEM to interact with the specimen. A series of limiting apertures and a differential pumping system is used to continually pump gas out of the TEM [13]. This results in a step wise reduction in the gas pressure as the distance from the specimen increases. In this way gases are prevented from damaging the electron gun. This design preserves the resolution of the TEM [132-135], but requires that a lower gas pressure is used and puts restriction on the gas compositions that can be injected. The general range of pressures applicable by ETEM cover the pressure gap between surface science techniques (P= <1 Pa) and industrial catalyst testing (P≈ 1-100 bar).

A modification of this design (originally developed for the Philips (later named Fei/Thermo) CM-series instruments by the thesis supervisors in the USA [13]) has been incorporated into a double aberration corrected JEOL 2200FS STEM-TEM at York. It is this microscope that is used for the in-situ experiments presented in the later chapters of this thesis. A schematic diagram of this design is shown in figure 3.11. Improvements over the original design along with the aberration correctors enable 0.1 nm resolution environmental STEM (ESTEM) HAADF imaging [136-139].

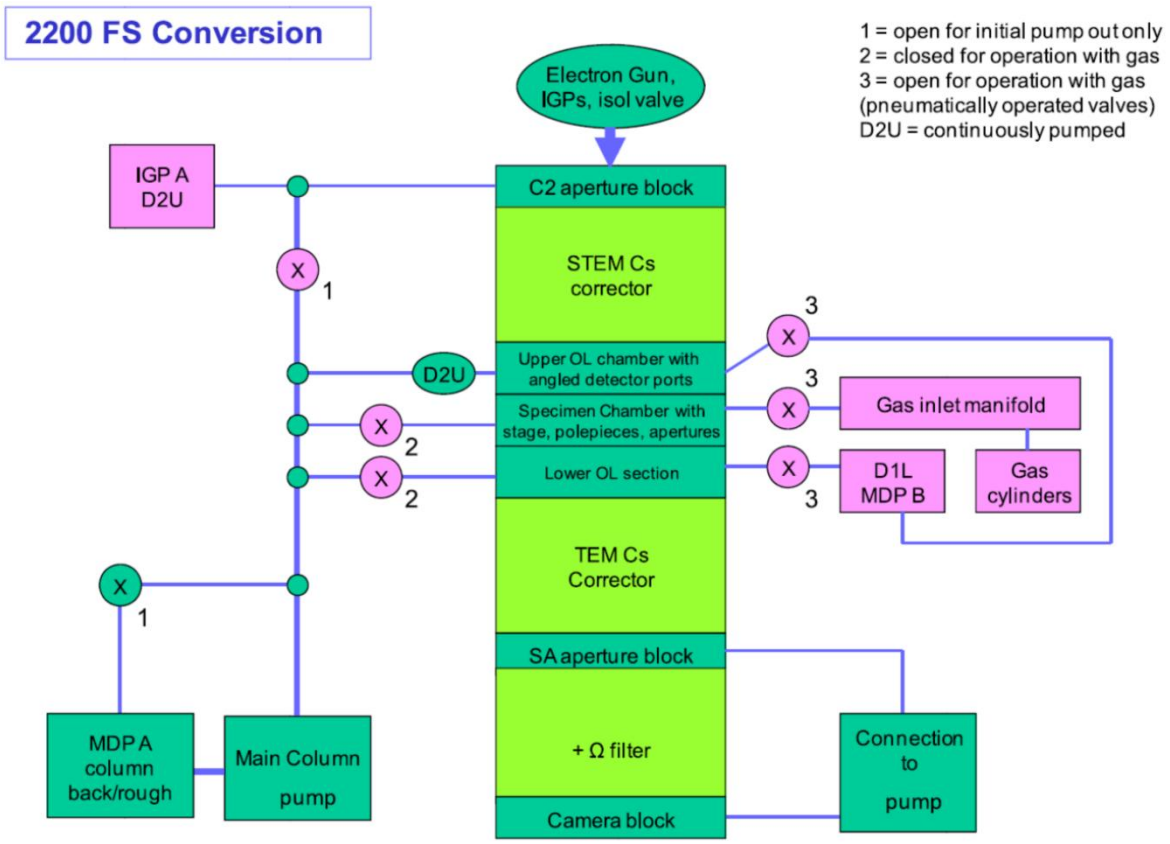

Figure 3. 11: Schematic diagram of the double aberration corrected JEOL 2200FS ESTEM system at the JEOL Nanocentre, University of York. The pink features represent the components of the vacuum system that are utilized when operating in environment (in-situ) mode. Reprinted from [17].

In a catalytic chemical reaction the first intermediate reaction step is the adsorption of gas molecules on the surface of the catalyst. By assuming that the gas molecules reach the catalyst surface and that the in-situ conditions (gas composition and temperature) are favourable for the reaction, the adsorption of gas molecules can be modelled as the formation of a Langmuir monolayer. Despite the fact that Langmuir's work focused on the formation of monolayers of amphiphilic compounds on liquid sub-surfaces, the model is applicable to the adsorption of gas molecules on metals. The average time taken for the formation of a single monolayer of adsorbate gas on a surface is given by equation 3.16.

$$t_{mono} = \frac{3 \times 10^{-4}[Pa\ s]}{P[Pa]} \tag{3.16}$$

Where t_{mono} is the monolayer formation time and P is the pressure in Pascals. Equation 3.16 is accurate if the sticking coefficient (fraction of incident adsorbate molecules that adsorb on the surface for the same time period) is unity. This is a reasonable assumption for nanoparticles given the high surface-area-to-volume ratio. The reciprocal of equation 3.16 gives the number of monolayers formed per second. The continuous flow gas

pressures that can be effectively utilized in the modified JEOL 2200FS ESTEM used for this thesis are on the order of Pascals. Thus, a pressure of 3 Pa is equivalent to ten thousand monolayers per second and at 2 Pa (used in chapters 5 and 6) is greater than six thousand monolayers per second. While this is indeed lower (by 5-6 orders of magnitude) than the pressures typically employed in real world catalytic reaction vessels, it is more than enough to drive a chemical reaction in-situ for the purposes of studying nanoparticle based catalysts [140]. Critically, the E(S)TEM pressures are well above the definition of "high pressure" used in the surface science context [141].

3.6 Supplementary Techniques

In this section contains a very brief overview of the supplementary techniques used in later chapters. These techniques are used add context or to compliment the electron microscopy data.

3.6.1 Energy Dispersive X-ray Spectroscopy (EDS)

When electrons from the incident TEM beam in-elastically scatter from electrons in the specimen energy is transferred to the specimen. When core shell electrons of the sample are scattered in this way they can be excited into higher energy states. Upon returning to the ground state electrons transition to lower energy levels to fill the hole. These transitions release photons with energy equal to the energy difference between electronic states. These photons are usually in the X-ray region with energy 0.2-20KeV. With a 200 KV beam of electrons the entire spectrum of transitions can be excited for the entire periodic table of elements.

Due to the fact that the X-ray energy is determined by the energy level transition within the atoms of the sample, these X-rays are characteristic of the elements that compose the sample [142]. In this way EDS gives information about the chemical composition of the sample. EDS can be used as quantitative technique when high purity calibration materials are used and the thickness of the specimen (and so the interaction cross-section) are known to a high precision. However, it can be used qualitatively for determination of the local distribution of chemical species, especially when used in STEM.

The X-ray background in an EDS spectrum is caused by continuum X-rays. These X-rays are produced by Bremsstrahlung radiation during elastic scattering events. The X-ray counts integrated by the detector are moderated by the take-off angle i.e. the angle between the specimen surface and the axis of the detector and the collection solid angle. These are determined by the geometry of the microscopy around the specimen. Improved X-ray collection can be gained by tilting the sample towards the detector.

3.6.2 X-ray Diffraction (XRD)

An X-ray diffractometer (XRD) consists of an optical bench which is divided into three parts: the X-ray source, the sample stage and the detector. Similar to electrons, X-ray photons have a wavelength less than the crystal inter-atomic distances and so diffract from crystal planes within the sample. X-rays are absorbed and re-emitted by the atoms in the sample as spherical wavelets leading to constructive and destructive interference according to Bragg's law.

In XRD the detector, source and stage move independently and many different scans are possible. The most basic scan is the θ-2θ scan in which the sample, usually a solid (in this case a powder) is held stationary. The detector and source are moved together such that they share a common angle relative to the sample surface. In this way the intensity of scattered X-rays can be measured as a function of angle which is characteristic of the diffraction crystal.

The width of the diffraction peaks is related to the average size of the diffracting element within the sample. The Scherrer equation [143] (equation 3.17) can be used to quantify the crystallite size of a sample. Where τ is the average crystalline size, K is a shape factor, Δ(2θ) is the full width at half maximum of the peak at the selected Bragg angle.

$$\tau = \frac{K\lambda}{\Delta(2\theta)\cos\theta_B} \tag{3.17}$$

3.6.3 X-ray Photoelectron Spectroscopy (XPS)

X-ray photoelectron spectroscopy (XPS) uses a high energy, monochromatic beam of X-rays to irradiate a solid sample causing the emission of photoelectrons from the surface.

The photoelectron kinetic energy is then measured. Since the incident X-ray energy is known, the kinetic energy of the ejected electrons is dependent on the binding energy of the electrons within the sample. By measuring the number of photoelectron counts as a function of electron kinetic energy a binding energy spectrum can be constructed. The peaks within an XPS spectrum are characteristic of the material and can yield information about the material composition and the chemical and electronic state of the elements within the specimen. Due to the short mean free path of photoelectrons in a solid: photoelectron emission is principally from the specimen surface and decreases exponentially with increasing depth. Thus, XPS is a surface-sensitive technique.

Chapter 4

Experimental Methods

This chapter describes the procedures and analysis tools used for the collection and processing of experimental data presented in the subsequent chapters of this thesis. By the end of this chapter, the reader will be familiar with the experimental methods that are common to chapters 5, 6 and 7. Together with any specific considerations mentioned in those chapters, any reader should be able to -with the necessary experimental equipment- reproduce the results found herein.

4.1 Sample Preparation

The samples used in this thesis came in two forms: powders and sputtered nanoparticles. The powders were: a nickel (II) oxide nanopowder purchased from Sigma-Aldrich (chapter 5) and catalyst samples made by JM. The composition and synthesis of each catalyst sample is described in chapters 6 and 7. The targets used for sputter deposition were Ni (99.95% pure), Pt (99.99% pure) and Pd (99.99% pure), all purchased from Testbourne Ltd. Both types of sample needed to be prepared as specimens suitable for (S)TEM observations. The (S)TEM supports used were either, 3 mm TEM grids (300 mesh Cu grid with holey carbon film or SiO_2 film) from Agar Scientific or MEMS chips (carbon or SiN_x coated) from DENS Solutions.

4.1.1 Powder Samples

For powder samples, a small amount of dry powder was transferred to a 20 mL glass sample vial with a Chattaway spatula. The vial was then filled with ethanol and sonicated for 15 minutes to disperse the sample in the solvent. One drop (4 µL) of the suspension was deposited onto TEM grids or MEMS chips using a micro-pipette and left to air dry. Drying was done under a clean, up-turned beaker to prevent dust contamination. The NiO powder was prepared in the manner described but crushed with a pestle and mortar in ethanol prior to sonication. Since finely divided Ni is known to be carcinogenic, powder samples containing Ni were prepared in a fume hood. Other samples were prepared while wearing a dust mask.

4.1.2 Sputtered Samples

Nanoparticles of Ni, Pt and Pd were made using magnetron sputtering. Deposition was performed using a JEOL JFC-2300HR fine coater. MEMS chips were placed on the base plate at the bottom of the deposition chamber. TEM grids, on the other hand, were mounted in an aluminium holder (normally used for SEM observations of TEM grids).

The deposition chamber was evacuated with the onboard molecular drag pump. The gas lines were purged with Ar gas and then evacuated again. The chamber was brought to an Ar gas pressure of ~0.02 mbar and left to stabilise for several seconds before the deposition began. A plasma current of 80 mA was used for all samples.

First, the target was blank sputtered with the shutter closed to remove any surface contamination or native oxide. Then, the shutter was opened and deposition was monitored using a quartz crystal thickness monitor. Sputtering ceased when a thickness of 0.5 nm (or 0.2 nm for Pt) was displayed. The chamber was evacuated after deposition and specimens were left under vacuum to cool before venting the chamber. This procedure was found to reliably produced metal nanoparticles in the sub-10 nm size range and with very high coverage of the support.

4.1.3 Ex-situ Treatments

The silica and carbon supported Pd samples used in chapter 7 were given ex-situ treatments prior to TEM analysis. These treatments were performed inside a stainless steel tube furnace. The 3 mm TEM supports were loaded into a Cu sample holder with a high thermal mass, this ensured a consistent temperature treatment across all of the samples. The sample holder allowed up to 10 samples to be mounted at once. When different samples were to be given the same ex-situ treatment, the samples were treated in batches to ensure that a reliable comparison could be made.

The tube furnace was evacuated using a scroll pump to a base pressure of 10^{-2} mbar. Gases (H_2 or O_2) were introduced and regulated to a pressure of 5 mbar using a needle valve. Once the pressure had stabilised the samples were brought up to temperature using a heating strip and Variac autotransformer. The temperature was monitored using a thermocouple placed adjacent to the samples. The temperature was held constant at 300 °C for 2 hours. After which, the samples were cooled in the gas environment and then removed from the furnace.

4.2 Electron Microscopy Methods

In-situ TEM and STEM experiments were performed on a double aberration corrected JEOL JEM-2200FS with a Schottky FEG operating at 200 kV accelerating voltage. This particular microscope is modified for in-situ exposure to gaseous environments (see chapter 3). A JEOL JEM-2011 TEM was also used for TEM imaging and electron diffraction. This microscope also operated at 200 kV accelerating voltage but with a LaB_6 filament.

In-situ heating was performed using a DENS Solutions Wildfire MEMS heating system. The electrical connections of the MEMS chips were checked before being inserted into the TEM. This was done using the supplied resistance monitor and an optical microscope, this ensured that the chips had not been damaged during sample preparation. The heating chips were controlled using the DENS heating software which automatically regulated the temperature at the desired set-point.

4.2.1 (S)TEM Alignment

At the start of every TEM experiment, the microscope alignment was checked and realigned when necessary. The purpose of the TEM alignment procedure was to ensure the brightest possible image, ensure that the same area of the sample was illuminated when changing the magnification and to reduce the aberrations to achieve the highest imaging resolution. A useful and concise text describing both TEM and STEM alignment procedures is given by D. Chescoe and P.J. Goodhew [73]. However, the basic (day-to-day) alignment for most modern TEMs consists of the following steps.

1) Raise the filament current so that electron emission can be seen on the phosphor screen (not needed for a FEG).
2) Select and align the condenser aperture.
3) Alignment of the electron gun with the condenser lenses.
4) Correct for condenser astigmatism.
5) Set the objective lens to its standard focus and bring the specimen into focus using the sample stage.
6) Alignment of the illumination system with respect to the objective lens (beam tilt correction) and tilt-shift compensation.
7) Select and align the objective aperture (if used, see chapter 3).
8) Correct for objective astigmatism.
9) Centre diffraction pattern and adjust intermediate lens focus.
10) Correct for higher order aberrations with aberration-corrector software interface.

In TEM mode, an alignment sample consisting of a continuous carbon film with Au nanoparticles was used. The Au nanoparticles were useful for the beam tilt alignment. The amorphous carbon produced high contrast Thon rings in the FFT, these are required for the aberration correction software to accurately measure the focus and 2-fold astigmatism. These measurements are used to calculate and correct the higher order aberrations.

In STEM mode, the alignment sample consisted of Au nanoparticles on a holey carbon film. This sample had a much higher coverage (number per square nm) of Au nanoparticles. The greater number of nanoparticles allowed for high contrast HAADF-STEM images to be acquired. These images are used to obtain under and over focused images of the electron probe for the aberration correction.

The image (scale) calibration of the microscopes used in this thesis was performed using lattice spacings in Au. Diffraction patterns were calibrated using a sample of polycrystalline Al.

4.2.2 In-Situ Procedures with the E(S)TEM

Preparation for gas injection into the E(S)TEM required approximately 10 minutes and so the beam was always blanked during gas injection, changing and removal. Additionally, closing the beam valve protected the electron gun from the sharp pressure change which occurs during gas injection. To prepare the TEM for gas injection a gate valve is used to redirect the sample vacuum system through a bypass valve. In this way flow rate of the spent gas exiting the sample chamber of the E(S)TEM could be regulated.

The high pressure gas bottles are connected to the E(S)TEM via a gas injection manifold equipped with a scroll pump. The scroll pump is used to evacuate any existing gas from the manifold. The manifold was evacuated to a pressure of ~10^{-3} mbar. Next, the gas lines were purged with gas from the bottles. The lines were purged for ~5 minutes while the gas pressure in the lines stabilised. Needle valves were used to set the pressure in the lines.

There is a pressure drop associated with gas travelling from the manifold to the TEM sample chamber. The reason for the pressure drop is due to the change in pumping rate between the gas manifold (scroll pump) and the TEM column (multiple turbo pumps). The pressure drop has been found experimentally to be 2 orders of magnitude. Therefore, 2 mbar pressure in the gas manifold resulted in 0.02 mbar (2 Pa) at the sample.

A further consideration was that, immediately upon injection, the gas enters a high vacuum environment. This resulted in a sharp decrease in the gas pressure, followed by a slow rise up to equilibrium. To compensate for this the gas pressure in the manifold was always made to stabilise at 0.5 mbar higher than required before injection. In other words, by setting the manifold gas pressure to 2.5 mbar before injection, the system would come to equilibrium at 2.0 mbar during operation (equal to 2 Pa at the sample). When ready, the gas was allowed into the microscope using electrically operated valves and the scroll pump was isolated. In this way the gas molecules are moved through the microscope (and over the specimen) by the TEM vacuum system.

The gases used for the in-situ experiments were H_2 (99.9995% from BOC UK) and O_2 (99.999% from BOC UK). During operation the gas pressure was regulated using the needle valves on the gas manifold. The removal of the gas at the end of the experiments followed the same procedure but in reverse.

At the low gas pressure used in the experiments presented in this thesis, (S)TEM imaging could be performed with gas in the microscope, without impact to the resolution. At higher pressures (>10 Pa), the beam valve is locked automatically to protect the electron gun. When using high pressure in-situ treatments the gas pressure must be lowered before imaging can resume.

4.2.3 Imaging

In order to limit the exposure of the sample to the electron beam, the beam valve was used to block the beam when imaging was not being performed. Likewise, the beam was blocked during in-situ heating and gas treatments. Beam blanking helped to ensure that the beam was minimally invasive. Preliminary calibration experiments were performed to test the effect of the electron beam on the samples. By understanding the amount of exposure (dose and dose rate), it was possible to design the experiments such that the nanoscale transformations were driven by the in-situ chemistry and not the electron beam.

TEM images were recorded using a CCD camera. Images were recorded at either 1024x1024 or 2048x2048 pixel resolution, with an exposure time of 2.0 seconds. Diffraction patterns were recorded for 5.0 seconds. It should be noted that the second condenser lens excitation was set such that the electron beam could be considered parallel across the region of interest for SAED (see chapter 3). By spreading out the electron illumination, the electron intensity on the CCD was reduced, requiring longer exposure of the CCD for a diffraction pattern with suitable signal-to-noise ratio. Care should be (and was) taken to avoid over-saturating the CCD when taking diffraction patterns.

HAADF-STEM and BF-STEM images were acquired at a pixel resolution of 1024x1024 or 2048x2048. A pixel dwell time of 19.5 µs was used for the majority of the STEM images

used in this thesis. This shorter dwell time was preferred so as to limit the exposure of the sample to the electron beam.

4.2.4 EDS Acquisition

The EDS spectra presented in this thesis were acquired in STEM mode using a retractable Thermo Scientific UltraDry EDS detector. The detector was calibrated using a Cu calibration sample. Spectra were acquired using the point-and-shoot mode in the NSS software package. EDS scans were performed on regions with a diameter <10 nm, with a 60 second acquisition time. Materials such as the alumina used in chapter 6 are particularly sensitive to long exposures with the STEM probe. An acquisition time of 60 seconds produced X-ray counts well above the noise level without altering the structure of the sample. In order to check that the sample remained unaffected, STEM images were taken before and after EDS acquisition for comparison.

4.3 Analysis

Gatan Digital Micrograph software was used for the acquisition of both TEM and STEM images. This software was also used for calibrating and measuring lattice fringes in images. The real-space lattice measurements presented in this thesis are the average of 10 measurements and quoted to a precision determined by the magnification (nm per pixel). The Digital Micrograph software was also used for FFT analysis and indexing of diffraction patterns.

Particle sizes were measured using ImageJ software. Particle size distributions were determined using measurements from >100 particles to ensure statistically relevant results. Binning of the size histograms and the fitting of appropriate curves were performed in Origin.

JEMS software was used to create the simulated diffraction patterns found in chapter 5. This software was also useful for visualisation of the lattice structure of the materials used herein.

4.4 Supplementary Methods

This section gives a brief overview of the experimental parameters used for the supplementary experiments presented in later chapters. A theoretical description of these supplementary experimental techniques is given at the end of chapter 3.

4.4.1 Powder XRD

XRD measurements were performed on a Bruker D8 Advance. The powder samples were pressed into a sample holder and loaded into the instrument. Parallel beam (Gobel mirror) optical conditions were used. Bruker EVA software was used for phase identification and Topas software for pattern refinement. The X-ray source produced Cu Kα radiation with a wavelength of 0.15406 nm (X-ray voltage: 40 kV and current: 40 mA) and a Lynxeye detector was used. The 2θ scans went from 10° to 130° (2θ) with a step size of 0.044° and step time of 2 seconds.

4.4.2 XPS Experiments

XPS measurements were performed using an in-house XPS system (mostly from Scienta Omicron). Powder samples were stuck to the sample holder using silver paint. X-ray radiation was produced by an Al Kα source with photon energy 1486.7 eV. Survey scans were performed over a photoelectron energy range of 0.0 eV to 1000 eV in steps of 0.5 eV. High resolution scans of the Ni 2p region ranged from 864.0 eV to 908.0 eV in steps of 0.1 eV. For both the survey and high resolution scans, two scans were made and the counts averaged. Sample charging effects were observed during the scans, these were accounted for and energy calibration was performed using the carbon peak (see chapter 6).

4.4.3 Scanning Electron Microscope

SEM images were acquired on a JEOL JSM-7800F Prime with a Schottky FEG. Powder samples were stuck to an aluminium stub with an adhesive carbon tab. Secondary electron SEM images were acquired with an Everhart-Thornley detector. The SEM was

used for wide area EDS scans of powder samples. EDS spectra were acquired with a Thermo Scientific UltraDry EDS detector. Scans were recorded for 30 minutes with an electron accelerating voltage of 10 kV and scan size of 10x10 µm.

Chapter 5

Dynamics of Nickel Nanoparticle Oxidation

Oxidation reactions are a fundamental part of chemistry and were arguably the first reaction ever harnessed by mankind. Many elements are found as oxides in the Earth and most transition metals can undergo oxidation, as such, an understanding of oxidation reaction kinetics and mechanisms are crucial in fields such as: metallurgy, smelting, corrosion prevention and catalysis (to name but a few). Fundamentally, oxidation is the loss of electrons and the increase in the oxidation state of an atom or ion. Given the ambient conditions around us, oxidation of materials is almost inevitable and at the nanoscale such reactions can lead to profound structural and chemical changes. In this chapter, E(S)TEM is used to investigate the nanostructural changes that occur during the oxidation of Ni. A combination of continuous and stepwise acquisitions is performed under in-situ gas and temperature conditions in order gain insights into the dynamics of Ni nanoparticle oxidation. Ni and NiO nanoparticles are known to be catalytically active, consequently a fundamental understanding of the oxidation mechanism is important for the production and stabilization of these active phases. Industrially relevant catalysts based on Ni are the focus of chapter 6.

5.1 Theory of Metal Oxidation

Before presenting the experimental findings of this work, it is useful to discuss relevant models for Ni oxidation and for metals in general. Over the years, many models have been proposed to describe the growth of continuous oxide films on a metal surface. The assumptions made about the rate limiting process for the oxide growth have led to various rate laws, including: linear, parabolic, cubic and both direct and indirect

logarithmic [144]. Overwhelmingly, these rate laws are valid only for a limited thickness of oxide. The combined literature suggests a complex matrix of interacting processes based on the formation of an oxide generating species, the movement of metal with respect to oxygen, the solubility of oxygen in the metal, the structure of the metal surface and the presence of impurities in any of the material phases involved. Some of these processes are dependent on the reaction conditions and even change with time as the oxide grows. The objective of this work is not to derive -yet another- rate law for metal oxidation that is only applicable to a given set of reaction conditions. An attempt is made to deduce an outline of the nano-structural transformations of Ni during oxidation to inform future high-resolution models, especially of nanoparticles.

The convention in the literature is to describe oxide films as being in one of three regimes: thick films (>600 nm), thin films (10-600 nm) and very thin films (<10 nm). The use of small nanoparticles inherently suggests “very thin films” as the thickness regime. The most widely known theory for the growth of very thin films is the work of Cabrera and Mott [145], “Theory of the Oxidation of Metals.” To describe the formation of oxides at low temperatures, Mott proposed that a strong field is set up in the oxide due to a contact potential difference between the metal and adsorbed oxygen. Oxygen is thought to be dissociatively adsorbed leading to oxygen ions at the surface of the oxide (or metal during initial oxidation). This strong field enables metal ions to traverse the oxide layer without the need for increased temperatures. For metals like Ni, which can dissolve excess oxygen (like defect semi-conductors), the concentration gradient of oxygen is dependent on the partial pressure of oxygen at the oxide-gas interface. This would affect the oxidation rate (change in oxide film thickness with time) for an anion diffusion mechanism. However, it is the metal which diffuses [146] through the oxide lattice. Oxygen is taken up in such a way as to form vacant cation sites which diffuse away from the oxide-gas interface. When the metal dissolves into the oxide at the metal-oxide interface, the metal is completely dissociated into ions and electrons. The concentrations of electrons and ions are unequal in very thin films and electrons move quickly across the film to the oxide-gas interface. Here they interact with adsorbed oxygen to form oxygen ions and thereby create a contact potential difference and a strong electrostatic field.

Practically all theories of oxidation start with the presupposition that for a metal ion to transition from the metal surface and into a stable position in the oxide, work must be

done to overcome some form of energy barrier. The influence of the strong field suggested by Cabrera and Mott is to lower the energy barrier for ions moving toward the oxide surface and retard the reverse motion by increasing the barrier by the same amount. Assuming that all cations leaving the metal surface reach the oxide surface and none recombine with the metal, the oxidation rate is then proportional to the rate of ions leaving the metal. The Cabrera and Mott oxidation rate for very thin films is given by equation 5.1.

$$\frac{dX}{dt} = N\Omega\nu \, exp\left(\frac{qa'V}{KTX} - \frac{W}{KT}\right) \tag{5.1}$$

Where X is the oxide thickness at time t, N is the number of metal ions per unit surface area at the metal surface, Ω is the volume of oxide generated by metal ion, ν is the atomic vibration frequency, q is the charge on the cation, a' is distance from an energy minimum position in the metal to a similar position in the oxide, V is the contact potential difference, K is the Boltzmann constant, T is temperature and W is the height of the energy barrier. Using the values in table 5.1 for Ni, figure 5.1 shows oxidation rate as a function of oxide thickness for different temperatures.

Parameter	Value	Comments
N	$8.07 \times 10^{18}\ m^{-2}$	Max value at $1/a_{Ni}^2$.
Ω	$1.81 \times 10^{-29}\ m^3$	Rock-salt structure of NiO.
ν	$4.27 \times 10^{12}\ s^{-1}$	Based on harmonic oscillator, with Young's modulus from [147].
a	$a' = a_{Ni}$	-
W	$1.08 \times 10^{-19}\ J$	[148]
V	$1.19\ V$	Contact potential difference, Ni and NiO work functions from [147] and [149].

Table 5. 1: Constants used for Cabrera-Mott estimation of Ni oxidation rate.

Note that the value of N used here is its maximum value and would be lower at under coordinated sites such as step edges, kinks or at surface dislocations.

Figure 5.1 shows that the oxidation rate is initially very large and is followed by a rapid decrease. The asymptotic levelling off of the curve suggests that the oxidation process is independent of temperature but the rate at which the reaction proceeds to a certain thickness of oxide is dependent on the temperature. Using the Cabrera-Mott theory as a

starting point, an estimate for a stable (over the course of a TEM experiment) oxide thickness would be in the range 2-4 nm (dX/dt=8 µm s^{-1} at room temperature). Equation 5.1 has been differentiated to produce both an inverse logarithmic law. Although Cabrera-Mott theory is a popular model for very thin films of metal oxide, it assumes a bulk metal surface. A nanoparticulate form of metal imposes constraints and alters the boundary conditions for oxidation models such as Cabrera-Mott. As such many studies have been performed on the oxidation of Ni nanoparticles using different experimental techniques. It should be noted, that while morphology can vary drastically between bulk and nano-scale materials, the crystallographic lattice parameter only changes by ~0.14% for nano-scale NiO [150].

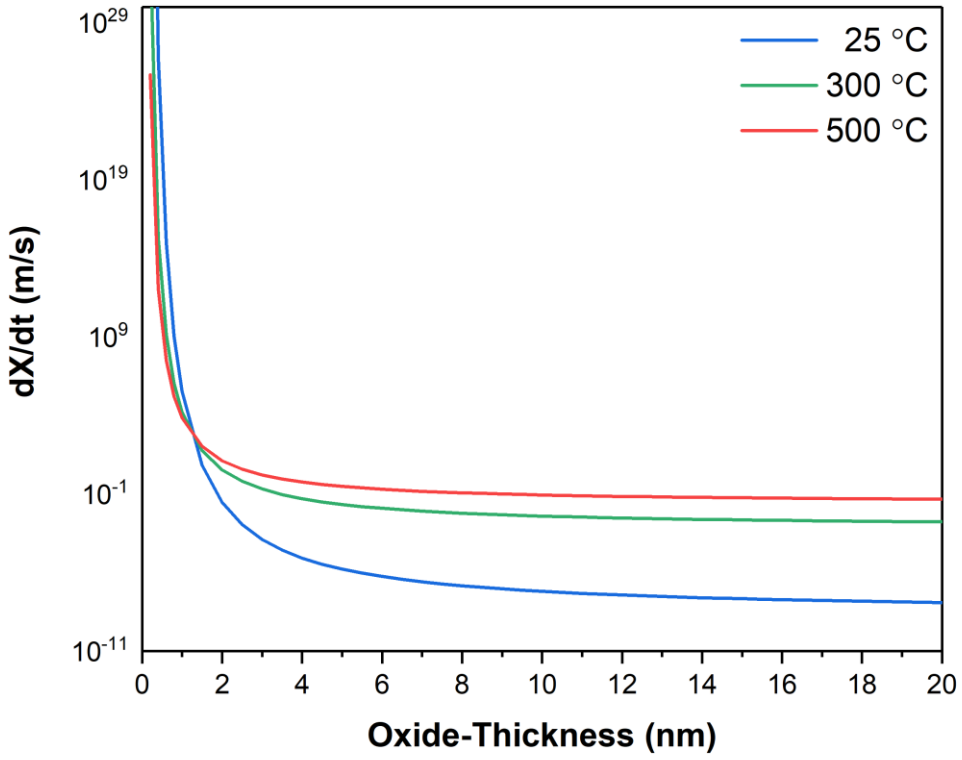

Figure 5. 1: Oxidation rate as a function of oxide layer thickness for Ni at 25, 300 and 500 °C, as described by Cabrera-Mott theory (note the log scale on the y-axis).

Zhou et al [151] reviewed twenty solid-state kinetic models for reduction and oxidation of Ni-based oxygen carriers for chemical-looping combustion. The models were tested for their applicability to the reduction (in H_2) of supported and un-supported NiO and the oxidation (in air) of supported Ni. Experimental data from the literature (mostly of scanning electron microscopy (SEM) and thermo-gravimetric analysis (TGA)), as well as

data from Zhou et al (TGA) were fitted to the kinetic models studied and a statistical analysis performed. They found that geometrical contraction models gave the best fit to the data sets explored for Ni oxidation. Geometrical contraction models suggest that the surface of the Ni particle reacts and the internal, unreacted zone shrinks, leading to a phase-boundary controlled reaction. These models suggest a reaction rate proportional to the thickness raised to a power of two-thirds. It should be noted that the conditions used in these tests were at high temperatures (800-1000 °C) for chemical-looping combustion, a comparatively harsh reaction environment.

Recently, TEM has been used to investigate the changes in morphology of Ni nanoparticles during oxidation, both ex-situ and in-situ using ETEM. These studies invariably show that after complete oxidation, hollow NiO nanoparticles are formed [148, 152-157]. These nanoparticles consist of an outer layer of NiO around a central void. The formation of such structures is usually attributed to a Kirkendall-like process.

Diffusing element	Diffusion medium	D (cm^2 s^{-1})	Temperature (°C)
Ni	Bulk Ni	10^{-25}	400
Ni	Bulk NiO	10^{-23} (10^{-19})	400 (500)
Ni	Bulk NiO (single crystal)	10^{-17}	610
Ni	NiO grain boundaries/dislocations	10^{-12}-10^{-13}	500
Ni	NiO surface	10^{-11}	500
O	Bulk Ni	10^{-19} (10^{-16})	400 (500)
O	Bulk NiO	10^{-30}	400
O	NiO grain boundaries	10^{-21}	400

Table 5. 2: Diffusion coefficients for the ionic transport pathways relevant to Ni oxidation.

To summarise the existing literature on the oxidation of Ni nanoparticles, a schematic representation of the processes described is given in figure 5.2.

The Kirkendall effect [158-160] describes the movement of an interface caused by inequalities in the diffusion rates of different materials. This was discovered by Kirkendall during observations of copper and zinc in brass; a historical overview can be found in [161]. More recently, the term "nanoscale Kirkendall effect" has been used to describe the formation of hollow nanocrystals by means of differential diffusion [162]. While NiO is not the only oxide structure to show the formation of Kirkendall voids (e.g. copper oxide

[163] and iron oxide [164]), the phenomenon has also been observed frequently in bimetallic nanoparticle systems. For example, in-situ TEM has revealed that, the oxidation of Ni-Cr [165], Pt-Ni [166], Ni-Co [167] and galvanic replacement in Ag-Au nanocubes [168], all exhibit the nanoscale Kirkendall effect.

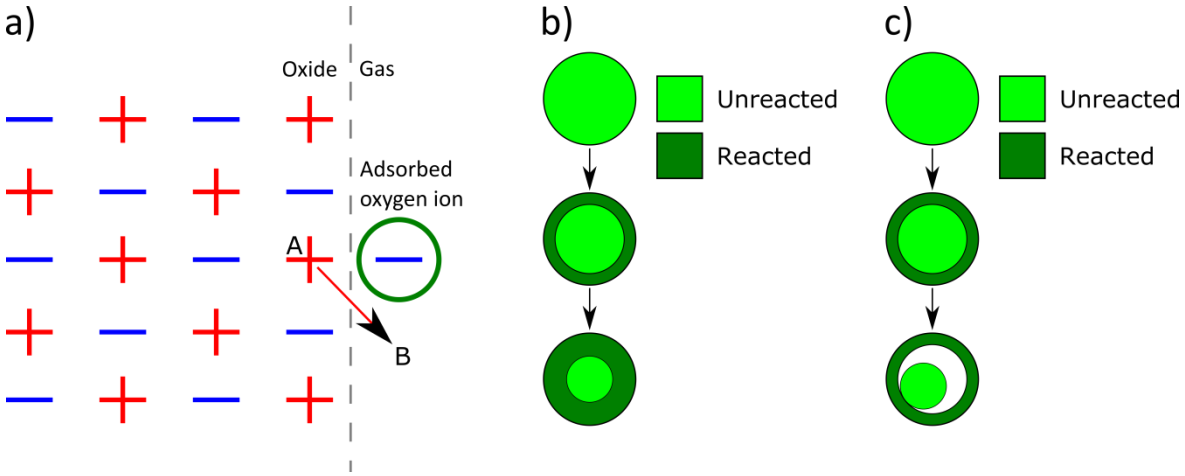

Figure 5. 2: Schematic showing: a) the creation of a cation vacancy at the oxide-gas interface [145], b) oxidation via a geometric contraction model [151], and c) oxidation by the nanoscale Kirkendall effect. b) Reprinted from International Journal of Hydrogen Energy, 39, Z. Zhou, L. Han, G.M. Bollas, Kinetics of NiO reduction by H2 and Ni oxidation at conditions relevant to chemical-looping combustion and reforming, 8535-8556, Hydrogen Energy Publications, LLC. Published by Elsevier Ltd (2014), with permission from Elsevier.

In Ni oxidation, the nanoscale Kirkendall effect describes the formation of voids by differential diffusion rates of Ni ions and O ions. In keeping with the Cabrera-Mott description, the outward diffusion of Ni ions is dominant and the concurrent inward diffusion of cation vacancies lead to the formation of a void at the metal-oxide interface. While a consensus has been reached that the metal diffusion through the oxide layer is dominant, the diffusion pathway is understood to a lesser extent. Ni can diffuse through NiO by two paths: 1) bulk diffusion through the NiO lattice (via interstitial sites or by a vacancy mechanism) or 2) short circuit diffusion along grain boundaries or along dislocations. Usually the latter is chosen as the diffusion coefficient, given by equation 5.2, is many orders of magnitude higher than for bulk diffusion. These values are usually determined via tracer diffusion [169].

$$D = D_0 \, exp\left[\frac{-E}{KT}\right] \tag{5.2}$$

Where D is the diffusion coefficient (usually quoted in $cm^2\ s^{-1}$), D_0 is the maximal diffusion coefficient at infinite temperature, E is the energy barrier to diffusion, K is the Boltzmann

constant and T is the absolute temperature. For reference, some of the relevant diffusion coefficients are given in table 5.2 [146, 169-173].

5.2 Sample Preparation

The Ni nanoparticles used in this investigation came from a nickel(II) oxide nanopowder purchased from Sigma-Aldrich. The powder was crushed using a pestle and mortar and then suspended in ethanol. An ultrasonic bath was then used to further break up any clumps of powder. The suspension was then pipetted onto a MEMS heating chip with an amorphous carbon film for E(S)TEM analysis. Figure 5.3 shows that the as-prepared specimen consists of agglomerations of crystals of various sizes and shapes. SAED shows that the sample is made of NiO. However, HR-TEM does show the presence of some Ni metal nanoparticles within the agglomerations; this was expected as the powder received was black in colour and indicative of a non-stoichiometric oxide.

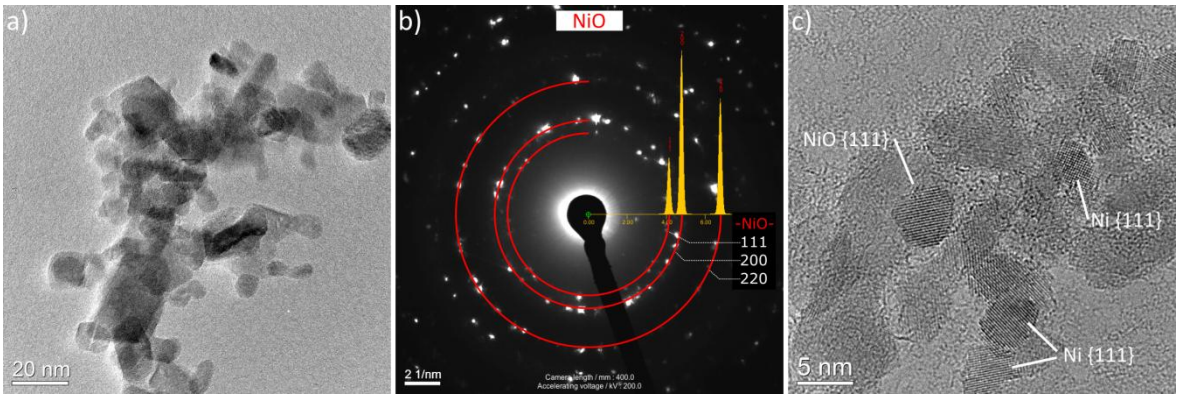

Figure 5. 3: TEM image a), SAED pattern b), and high-magnification Image c) of a typical area of the as-prepared NiO powder sample. The overlay in the SAED pattern shows that the rings correspond to NiO.

In order to create Ni nanoparticles the sample was reduced in-situ. Reduction was performed using H_2 gas at ~2 Pa pressure at 500 °C. Samples were initially reduced for 2 hours to ensure complete reduction to the metallic phase. Figure 5.4 shows that complete reduction was achieved. Since the sample initially consisted of agglomerates of oxide the reduced sample contained nanoparticles of varying size and shapes ranging from spherical and ellipsoidal to irregular where sintering had occurred during the reduction treatment.

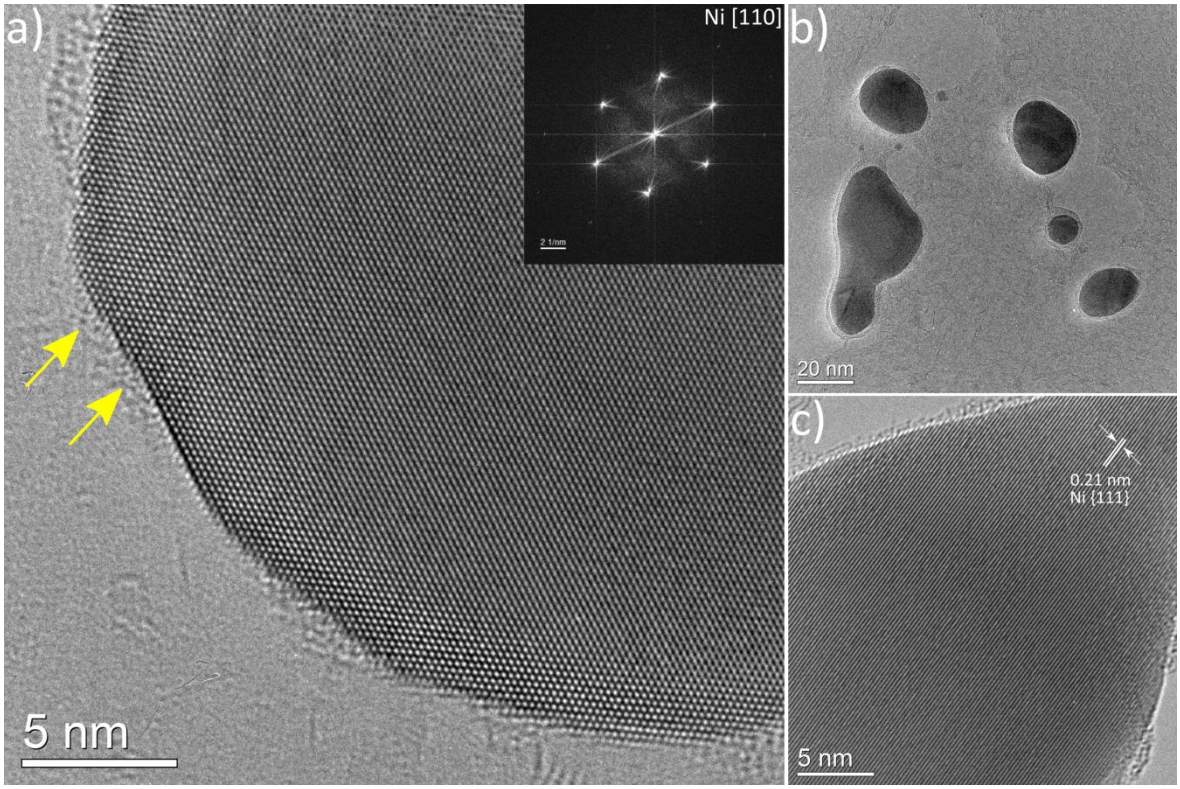

Figure 5. 4: Under exposure to H_2 at 500 °C the sample is fully reduced to Ni metal. a) Is a HR-TEM image of a Ni nanoparticle with associated FFT showing the material is Ni in the [110] zone axis. b) Illustrates the varying shapes and sizes of the nanoparticles within the sample and c) shows a portion of a very large irregular nanoparticle with lattice fringes corresponding to Ni metal.

The yellow arrows in figure 5.4 confirm the presence of step edges on the surface of some of the nanoparticles. Under-coordinated sites such as these are known to be highly active in catalysis. The sample described here was deemed an appropriate system for investigations into Ni oxidation because it provided a source of Ni in the nanometre size range while still providing enough variation in morphology and size to be applicable to real Ni catalysts.

A second model system was produced using magnetron sputtering (JEOL JFC-2300HR) from a 99.95% pure Ni target. Ni was sputtered onto MEMS chips to an indicated thickness of 0.5 nm which produced small spherical nanoparticles rather than a thin film. This system was used for comparison and to provide a smaller and narrower particle size distribution than the powder system. This will be introduced later in this chapter.

5.3 Oxidation Sequence

In the following oxidation sequence the temperature was lowered to 60 °C after the reduction process detailed above and the gas was changed to O_2 at a pressure of 2 Pa. At each temperature interval the temperature was raised and left for 15 minutes with the electron beam blanked and then the temperature lowered to 300 °C for imaging. 15 minutes was found to be adequate time for the reaction to progress to quasi-equilibrium. In other words, the oxidation rate (dX/dt) became negligible over the period required for imaging. 300 °C was found to be low enough to quench any further reaction at higher temperature but still high enough to keep carbonaceous contamination from forming.

5.3.1 Oxidation at 300 °C

After 15 minutes at 300 °C the surface of the Ni nanoparticles appear to have oxidised forming a core-shell structure of Ni-NiO. The core region remains as metallic Ni and retains its shape. The oxide layer was identified as nickel(II) oxide (NiO) from lattice and FFT analysis and no evidence of nickel(III) oxide (Ni_2O_3) was observed. Examples of these core-shell morphologies are shown in figure 5.5.

There is an 18% lattice expansion going from Ni (a= 3.52 Å) to NiO (a= 4.17 Å). From figure 5.5 it can be seen that the oxide shell is polycrystalline and therefore takes on its own unstrained lattice parameter. Rather than forming a pseudomorphic form with a lattice parameter similar to the underlying substrate [174-176], the transition between these two states is at a lattice mismatch of approximately 14%. The polycrystalline shell gives rise to grain boundaries across the oxide layer; these grain boundaries could provide a pathway for the movement of ions during oxidation i.e. a short-circuit diffusion mechanism.

The polycrystalline nature of the oxide layer gives a rough outer surface to the nanoparticle and no preferential exposure of specific surface facets. The average oxide layer thicknesses shown in figure 5.5 (a-c) are the average of 20 points around the perimeter of the nanoparticle. The shell thickness varies from 2-6 nm measured from the metal-oxide interface and individual grains of NiO vary by more than 1 nm in relation to the Ni surface due to their shape and orientation.

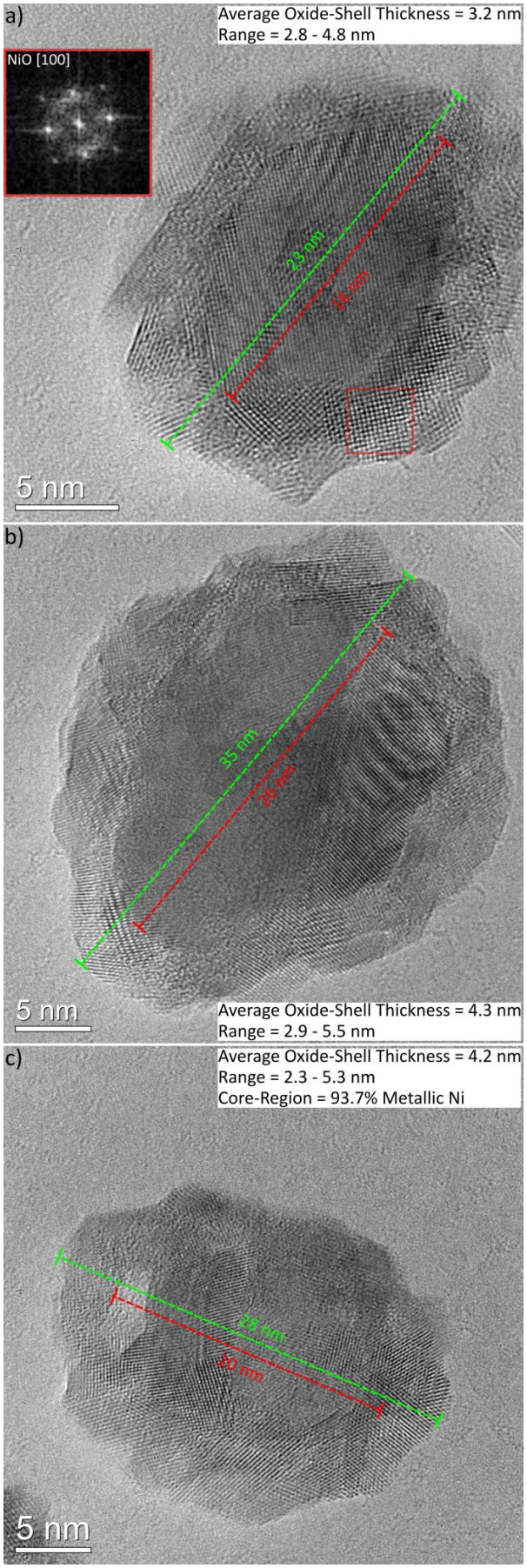

Figure 5. 5: ETEM images a-c) of core-shell (Ni-NiO) nanoparticles at 300 °C in O_2. The maximum size of the metallic core and the full nanoparticle are shown along with the average oxide shell thickness.

Finally, figure 5.5c shows the formation of a void region at the metal-oxide interface. The formation of this void is due to differential diffusion as cation vacancies diffuse from the oxide surface to the metal-oxide interface and Ni ions diffuse in the reverse direction. This will be discussed in more depth later in this chapter, for now it is interesting to note that formation of a void without complete oxidation of the nanoparticle is a stable structure at 300 °C. In other words, during the first 15 minutes, the oxidation progresses to the point where a complete oxide shell has formed (and thickened, such that diffusion processes become relevant) but complete oxidation has not yet occurred. After 15 minutes, the oxidation rate decreases to the point where negligible oxide growth is observed on the time scale of these TEM experiments (<1 hour). While this is true for all of the nanoparticles observed, figure 5.5c highlights that this is the case with or without internal void formation. Overall, the majority of nanoparticles, as well as large agglomerates of Ni have an oxide shell like those indicated. Only some of the nanoparticles show void formation at the interface.

5.3.2 Oxidation at 400 °C

Upon heating to 400 °C for 15 minutes the oxidation of the nanoparticles progresses further. All nanoparticles show the formation of voids at the metal-oxide interface and this “hollowing” of the nanoparticles proceeds by the growth of these voids. The core Ni metal continues to diffuse resulting in the core region shrinking and the oxide shell continuing to increase in thickness.

Figure 5.6 shows the transformation of two nanoparticles as the oxidation process continues. At this stage it becomes clear that there is a size dependence for the oxidation. The smaller nanoparticles (e.g. on the right of figure 5.6b) have fully hollowed and there is no Ni metal in the core region. This hollow NiO structure marks the end of the oxidation reaction for the nanoparticles. However, larger nanoparticles still have some Ni metal remaining in the core. This is also the case for the large agglomerate regions.

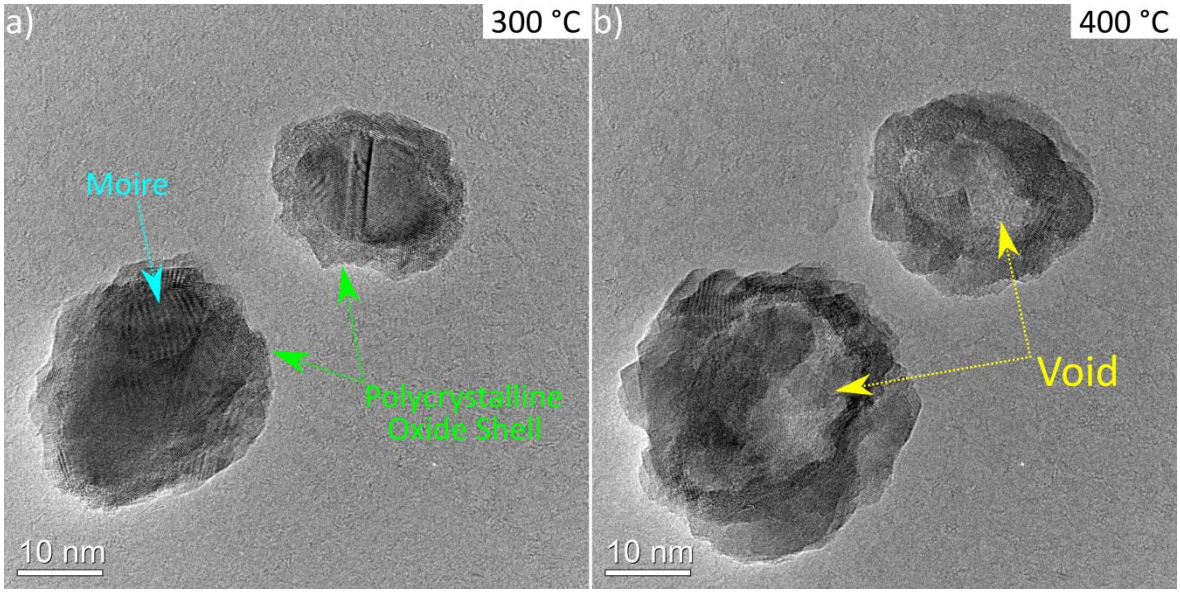

Figure 5. 6: ETEM images of two Ni-NiO nanoparticles after 15 minutes at a) 300 °C and b) 400 °C in O_2. The Moiré fringes show that the top surface of the nanoparticles are covered by oxide. Void formation in the core region can be seen in b) at 400 °C.

5.3.3 Oxidation at 500 °C

At 500 °C the differential diffusion mechanism was observed in the larger and more complex structures of the specimen. Figure 5.7a and b show an agglomerated nanoparticle at 400 °C and 500 °C respectively. Once again a single large void was formed beneath an oxide shell and the NiO grains grew in thickness in an outward direction.

Figure 5.7c and d show that the hollow NiO structure is stable at 500 °C since the side walls and top surfaces (highlighted in yellow in figure 5.7c) remain intact. Furthermore, this confirms that it is the original NiO crystallites that continue to grow during the oxidation rather than the formation of new ones. In the example of figure 5.7c the highlighted NiO crystallite has grown to take up more than one quarter of the projected surface area. The outward growth of the oxide combined with a tendency to preserve -to a certain extent- the original oxide grain structure allows for nanoparticles oxidised in this way to retain a semblance of their original shape. This has applications for the recyclability of shape controlled nanoparticles.

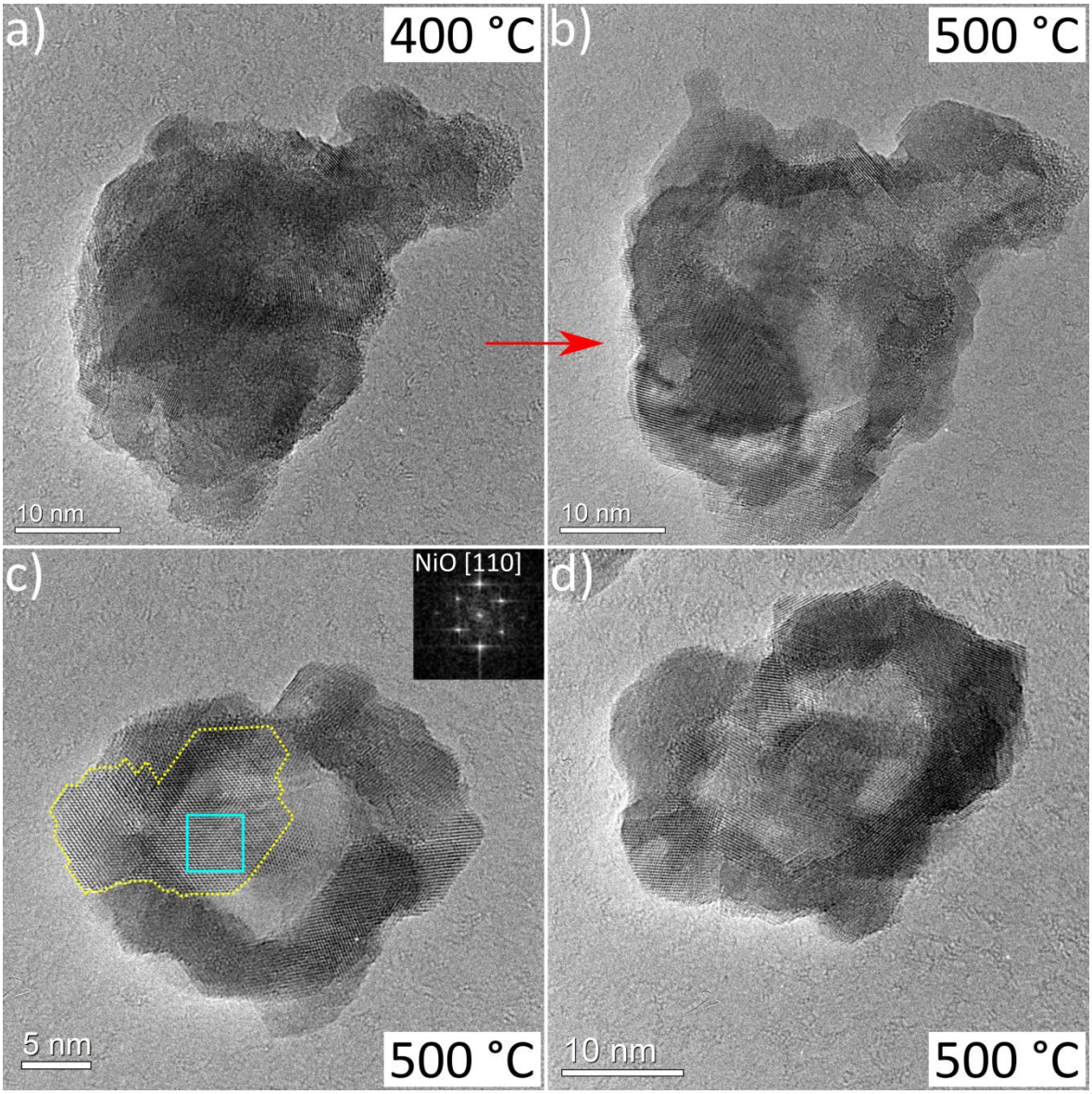

Figure 5. 7: ETEM images of Ni oxidation at 500 °C. Figures a) and b) show the same agglomerate region at 400 °C and 500 °C respectively. Figures c) and d) show fully hollowed nanoparticles. The FFT inset is taken from the area marked by the blue square.

5.3.4 Oxidation at 600 °C

After 15 minutes at 600 °C the entire specimen had been completely oxidised. SAED of an area >100 nm showed no reflections from metallic Ni (see figure 5.8a and b). As shown in the previous sections, vacancy diffusion appears to be the dominant mechanism for the oxidation.

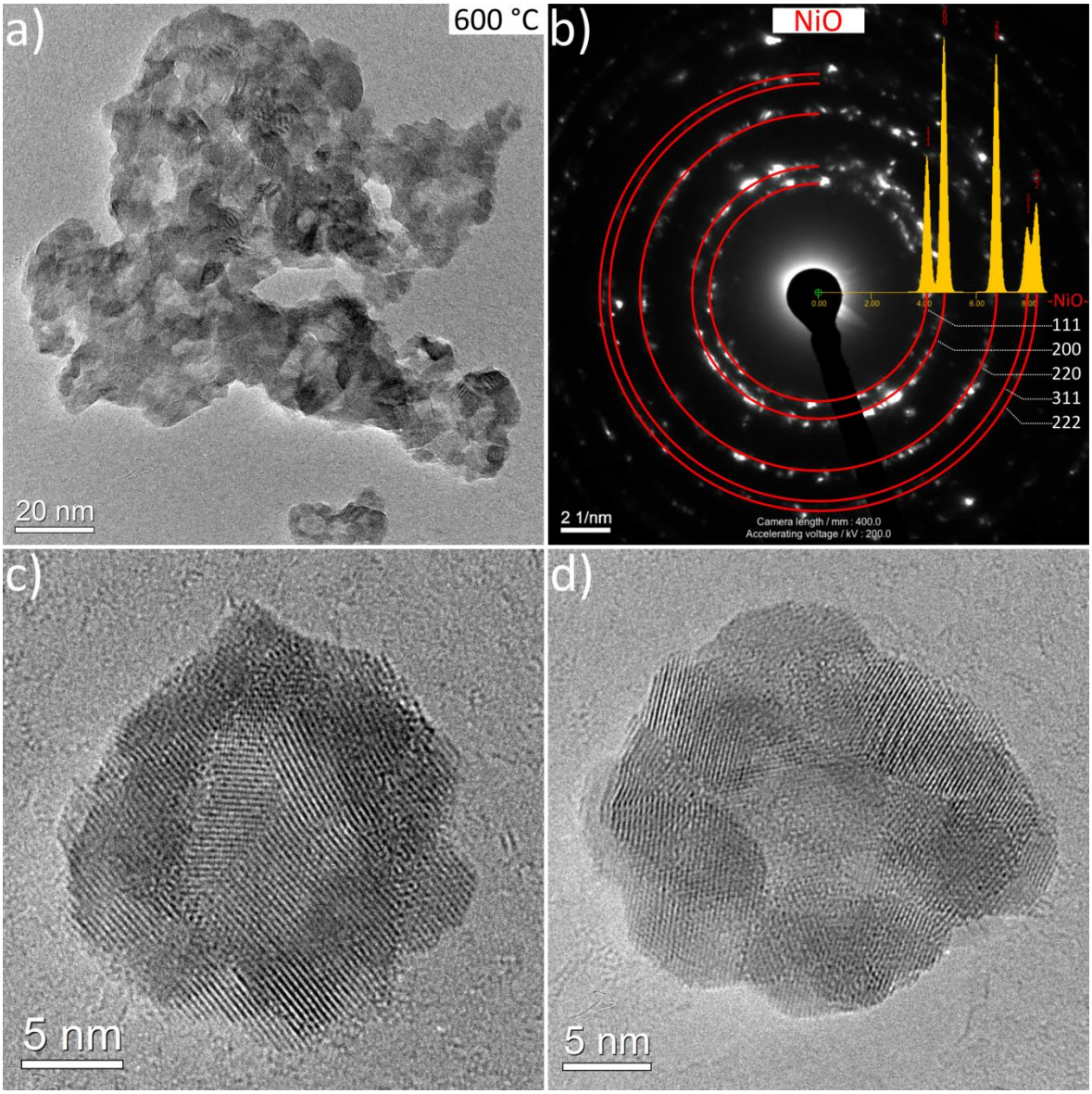

Figure 5. 8: ETEM images of Ni oxidation at 600 °C. The large agglomerate region a) has been fully oxidised, as confirmed by SAED b). Nanoparticles c) and d) retain their hollow structure.

Figures 5.8c and d demonstrate the stability of the hollow oxide structure. 600 °C at this O_2 pressure does not provide a driving force or mechanism for the collapse of this structure and the polycrystalline nature is still present in the smaller nanoparticles.

5.4 Comparison with Sputtered System

To ensure that the phenomena observed thus far were consistent across sample preparation methods, a second model system was made using sputter deposition. This method produced spherical Ni nanoparticles with a narrower size distribution than the

powder system. Since the nanoparticles were partially oxidised upon transfer in air from the deposition system to the TEM: an in-situ reduction was performed at 500 °C in H_2.

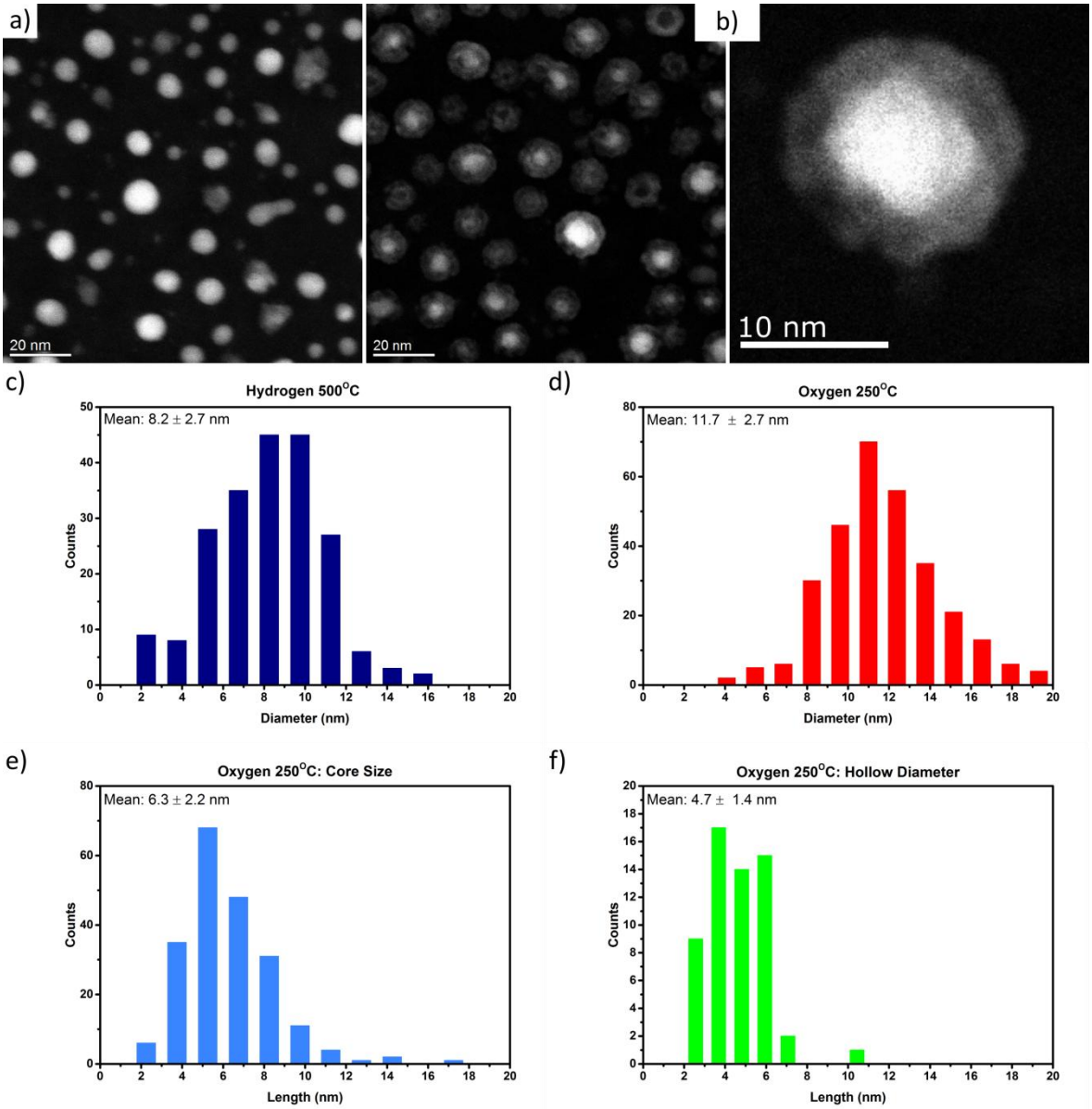

Figure 5. 9: HAADF-ESTEM images of the sputtered Ni system after a) reduction in H_2 and b) oxidation at 250 °C. The right hand image in b) shows an example of the core-shell nanoparticle structure. The size distributions (c-f) show the sizes of the various structures present under c) reducing and (d-f) oxidising in-situ conditions.

Due to the difference in atomic number density between Ni and NiO, HAADF imaging was used to probe the structures of these smaller nanoparticles. HAADF-ESTEM images and statistical distribution are presented in figure 5.9. Upon reduction the Ni nanoparticles were 8.2 ± 2.7 nm in diameter and were mostly spherical in shape. The sample was exposed to O_2 at 250 °C (P=2 Pa) for 15 minutes and the nanostructural changes were consistent with those discussed so far. All of the nanoparticles underwent a surface

oxidation leading to an increase in the average size to 11.7 ± 2.7 nm. Nanoparticles containing sufficient Ni material formed core-shell structures while the smallest nanoparticles formed hollow NiO structures containing a void at their centre. The oxide shells were polycrystalline as before and the average remaining core diameter was 6.3 ± 2.2 nm. The average void size for the fully oxidised nanoparticles was 4.7 ± 1.4 nm and would seem to be the approximate critical size for complete oxidation at this temperature.

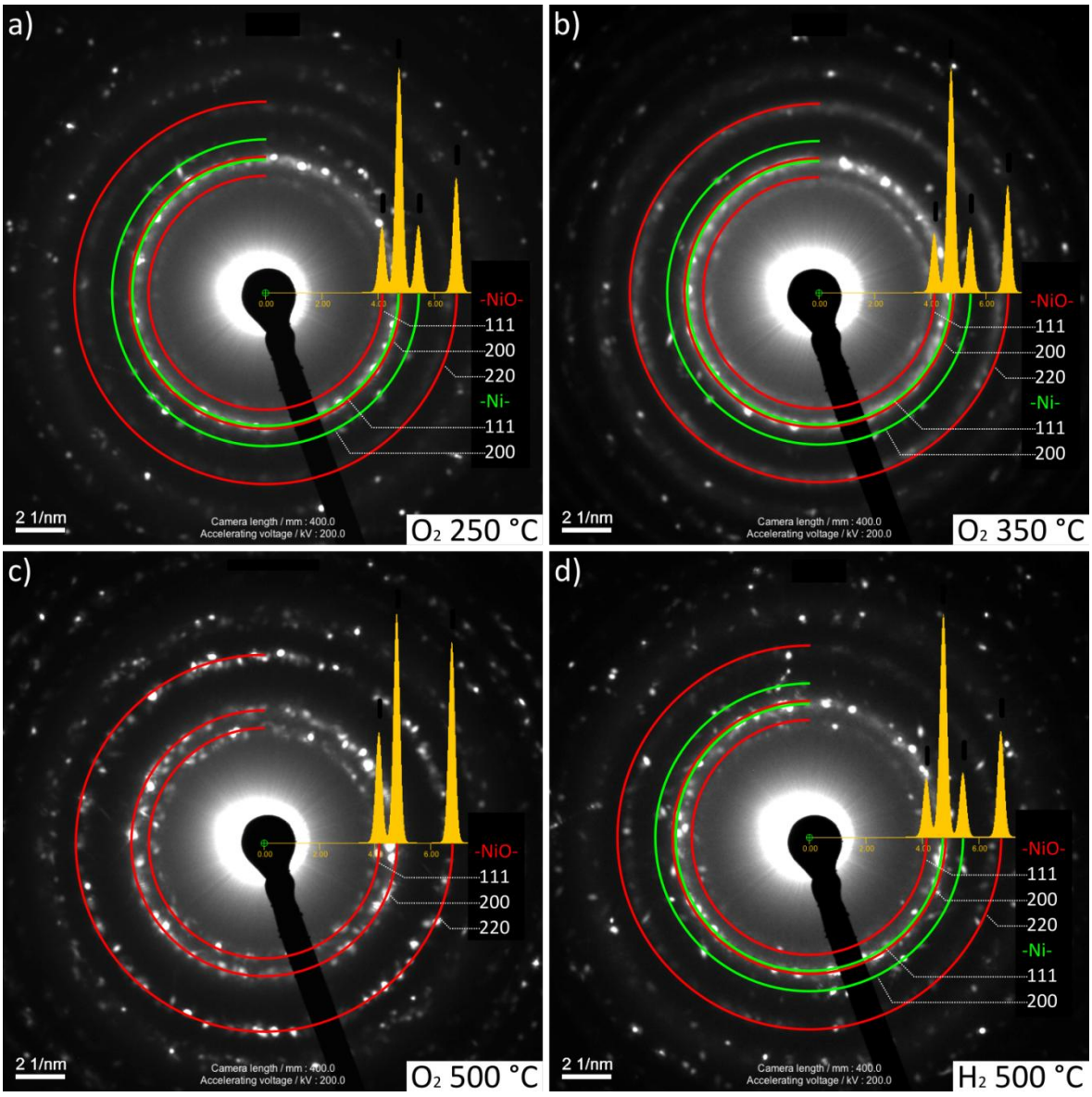

Figure 5. 10: In-situ SAED patterns of the sputtered Ni sample, taken under O_2 at a) 250 °C, b) 350 °C, c) 500 °C and d) under H_2 at 500 °C. The overlays are simulated diffraction patterns generated in JEMS. The simulations show Ni metal is present in all patterns apart from the 500 °C oxidation.

SAED was also performed on this sample using ETEM at different temperatures. Diffraction patterns are shown in figure 5.10. As expected, both Ni metal and NiO were

observed at 250 °C, this persisted until complete oxidation at 500 °C. The sample could undergo repeated redox cycling events, in which Ni metal was observed as soon as 15 minutes under reducing conditions.

Consistent with the previous sections the hollow NiO are relatively stable at the moderate temperatures discussed so far. It was only when the temperature was raised to 700 °C (above the operating temperature of most Ni based catalysts) that the hollow structures degraded. As seen in figure 5.11 the NiO has enough mobility to restructure itself. Very few hollow structures remain at this temperature. The majority of nanoparticles collapse to solid NiO particles with flat sides. This new morphology with surface facets at right angles shows an energetically favourable promotion of the [100] surface, known to be the most stable surface for the rock-salt crystal structure [177].

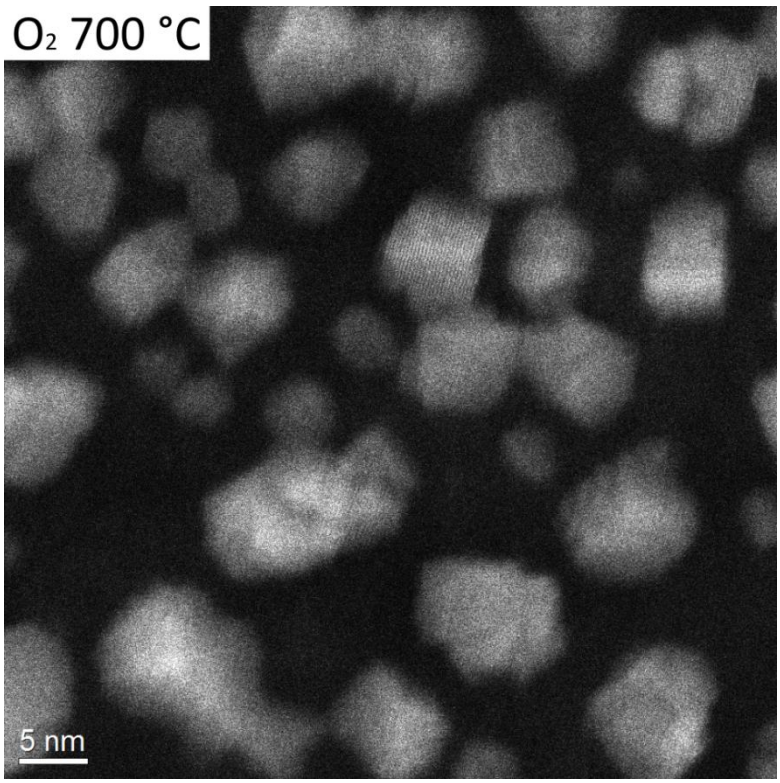

Figure 5. 11: HAADF-ESTEM image of the highly faceted NiO structures that are present at 700 °C under O_2 for the sputtered Ni sample.

5.5 Dynamic ETEM of Oxidation Reactions

Based on the observations detailed in the previous two sections, it was clear that the oxidation of Ni nanoparticles could be divided into two distinct stages. The first: a surface oxidation in which the nanoparticle adopts a core-shell structure. Followed by a diffusion

process in which Ni ions move outward from the core to the oxide surface. This deletion of the metal core results in the formation and growth of a void at the metal-oxide interface. Eventually a hollow NiO nanoparticle remains. In order to study these two stages of oxidation, continuous acquisition was combined with appropriate experimental in-situ conditions to track these phases in real-time.

The standard TEM imaging camera (Gatan UltraScan) was upgraded to fast frame OneView camera (Gatan). This camera allowed for 4096 x 4096 pixel resolution, a wider field of view and continuous acquisition at 25 frames per second. The larger CMOS chip and higher pixel density meant that lower magnifications could be used during imaging whilst retaining sufficient resolution for phase contrast imaging. Since the electron beam is more spread out at lower magnifications the total electron dose per unit time was reduced. This was beneficial as continuous acquisitions naturally require prolonged exposure to the electron beam.

5.5.1 Surface Oxide Formation

To study the formation of oxide on the Ni surface a large surface area was required, thus the powder system studied in section 5.3 was used. A large nanoparticle, clearly produced from the sintering of three smaller nanoparticles, provided the best data set and is the focus of this section. Since the surface NiO crystallites were small, the specimen needed to be mechanically stable for useful imaging. Therefore, the temperature was raised first to 250 °C and allowed to settle before the gas was introduced (O_2 at P=2 Pa). An overview time sequence is shown in figure 5.12.

At approximately 1 minute after exposure to the gas crystallites are observed to grow on the nanoparticle surface. These initially form at discrete locations on the periphery rather than as a “bulk” thin film covering the entire surface. Expanded views of the first two crystallites to form are presented in figures 5.13 and 5.14. As the reaction continues, more and more of these discrete crystallites grow on the surface. With time the areal density of these oxide crystallites increases and they begin to overlap with each other. Some crystallites are seen to merge when their growth direction, orientation relative to the metal surface and proximity are similar.

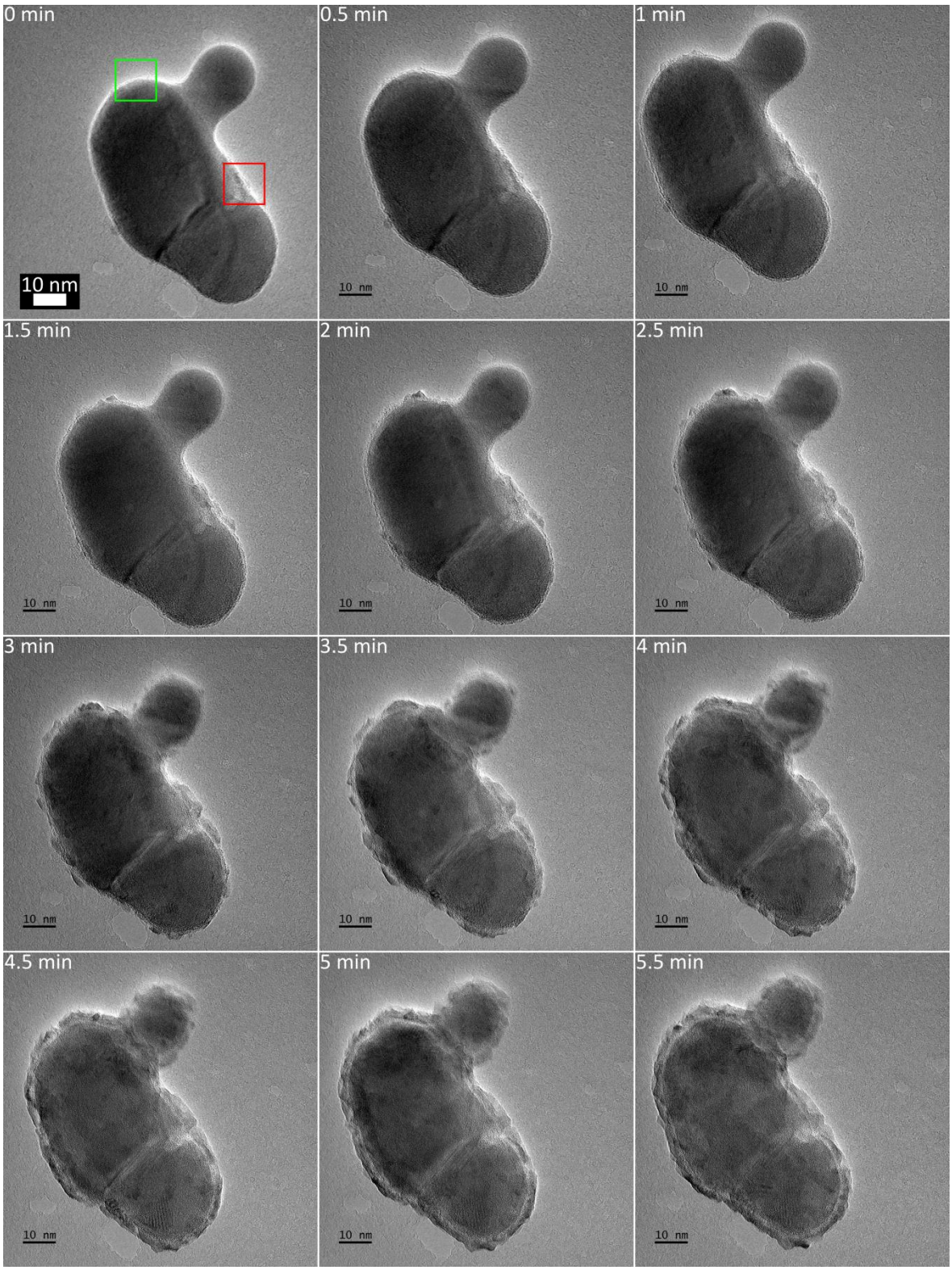

Figure 5. 12: ETEM time sequence showing the formation of the NiO shell at 250 °C in 30 second intervals. The full sequence was recorded using continuous video acquisition. The green and red squares in the first image highlight the areas used in figures 5.13 and 5.14 respectively.

After ~3.5 minutes the areal density (packing density) of the crystallites is great enough that it constitutes a continuous oxide layer over the entire surface. After 5 minutes little

change in the oxide layer is observed with time. This core-shell structure is consistent with the step-wise oxidation described in section 5.3.1.

It should be noted at this point that while NiO crystallite formation on the top surface is certain they are hard to detect here due to the thickness of the nanoparticle. Additionally, sufficient long range crystal order is required before Moiré fringes can be observed (seen at 3 minutes). Furthermore, oxide crystallites are observed only after one minute of exposure to gas. Most oxidation models predict an immediate reaction upon adsorption of oxygen on the surface. The observed lag in noticeable oxide formation here could be due to the relatively low O_2 partial pressure in the ETEM during gas injection when the microscope base pressure is lower and equilibrium gas pressure not established.

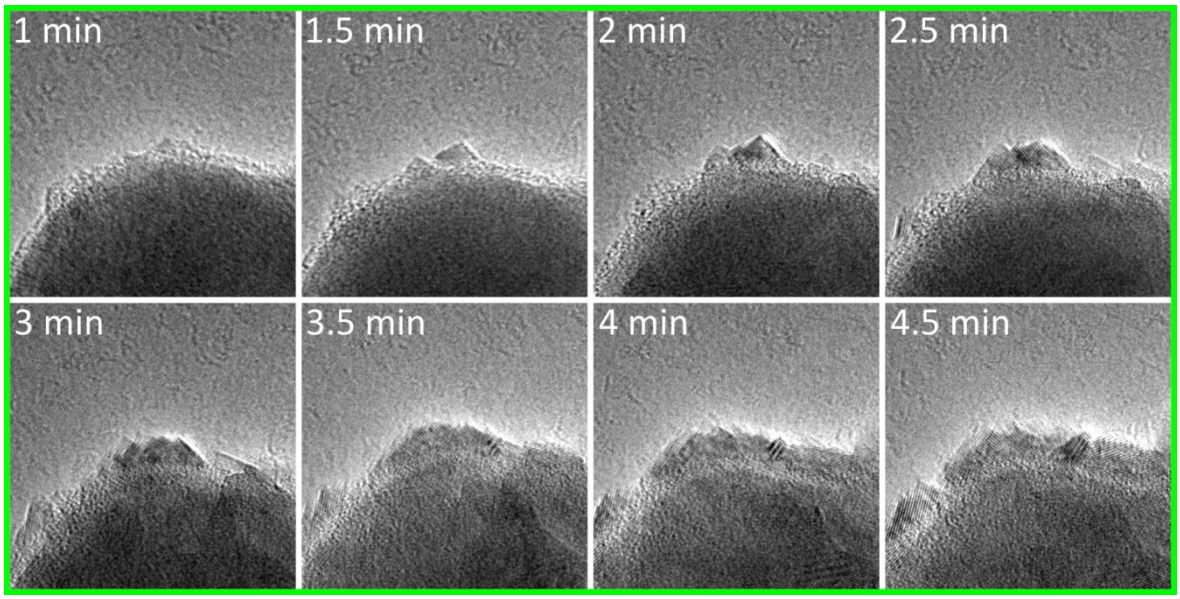

Figure 5. 13: Expanded view of the NiO crystallite on the top of the Ni nanoparticle, as highlighted in figure 5.12.

The oxide crystallites at the surface appear to have a triangular shape. Bearing in mind that this is a 2D projection of a 3D object, the symmetry axis of these triangles is normal to the metal surface. This is most obviously demonstrated in figure 5.13. The crystal facets exposed by these shapes are (200). The triangle shape and exposure of (200) facets seem to agree with the observations of MacRae using LEED to observe the growth of NiO on (111) Ni surfaces [178]. MacRae observed a growth mechanism in which triangular pyramids of NiO grow on the Ni surface exposing (100) surfaces and having their (111) planes parallel to each other. These pyramids are thought to grow at dislocations or steps on the Ni surface. Interestingly, the grain boundaries in the Ni nanoparticle do not seem to be preferential sites for the formation of NiO.

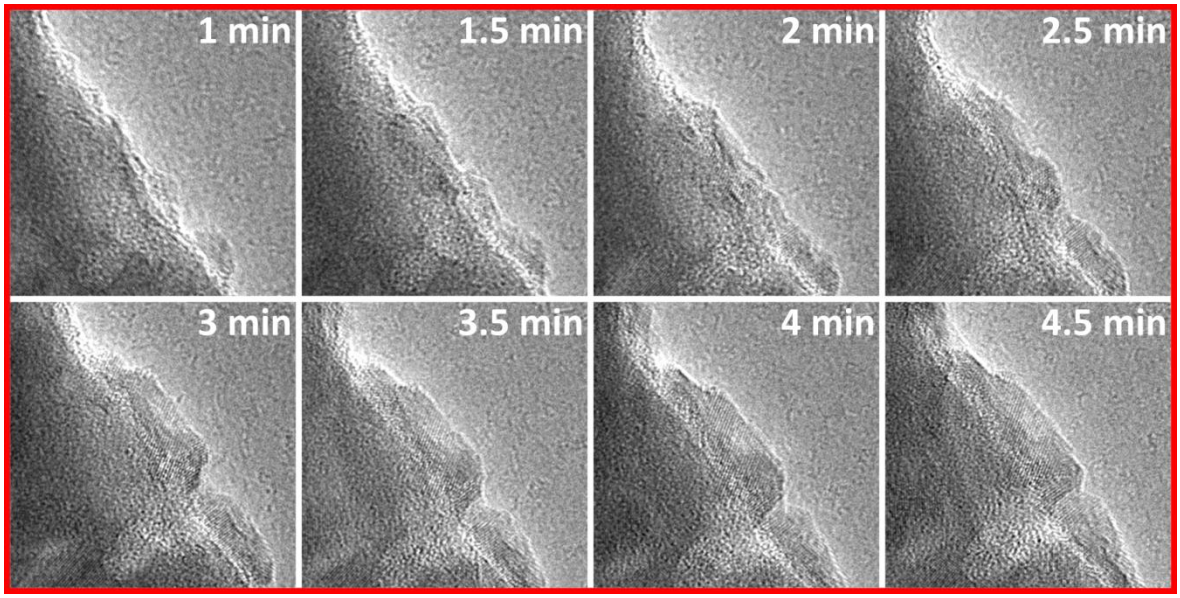

Figure 5. 14: Expanded view of the NiO crystallite on the right of the Ni nanoparticle, as highlighted in figure 5.12.

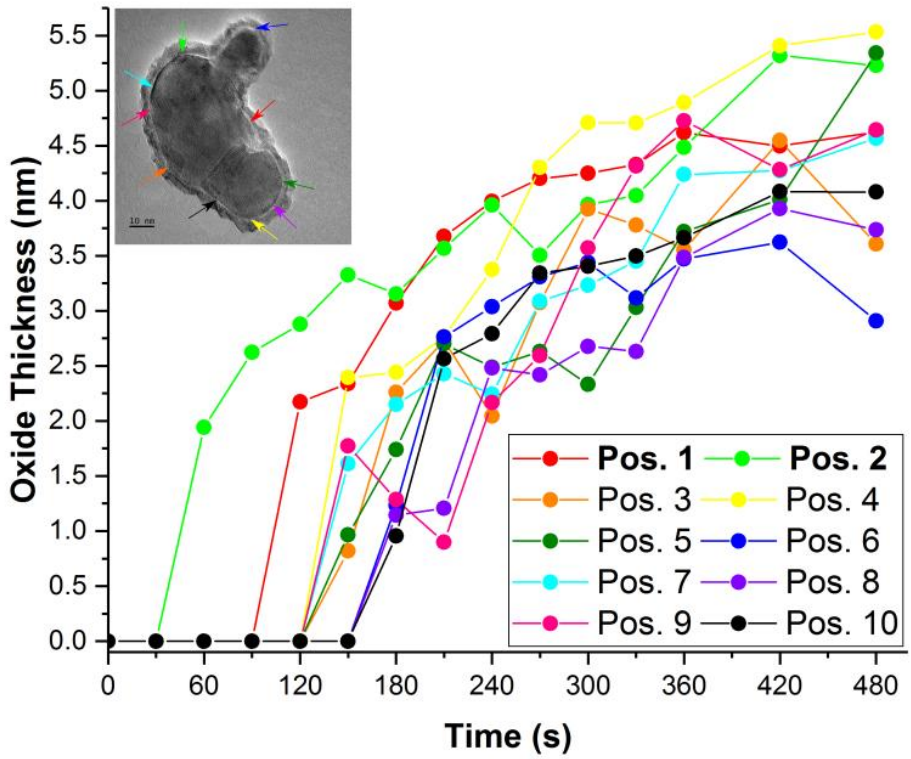

Figure 5. 15: Graph showing the change in the oxide layer thickness with time for 10 points along the perimeter of the nanoparticle shown in figure 5.12. The inset shows the positions of the data points. Position 1 and 2 correspond to the areas highlighted in figure 5.12.

Figure 5.15 illustrates the growth of the oxide layer with time by measurement of specific crystals along the perimeter of the nanoparticle as it oxidised. Position 1 and 2 show the

growth of the first two NiO crystallites to form, while the others were points on the surface chosen such that they would be identifiable across the images used for analysis. Although, different regions of the nanoparticle surface begin to oxidise at different times, most likely due to the number of point defects or nucleation sites present, the oxidation rates level off at approximately 5 minutes when a stable layer 3-5 nm thick is established. This layer thickness is consistent with that seen at 300 °C in section 5.3.1. While a critical thickness is proposed by oxidation models such as Cabrera and Mott, the oxidation rate here is much lower than that proposed by the models in section 5.1. This may be due to the low O_2 pressure of 2 Pa. It should be noted that the uncertainty in figure 5.15 come from an error in the thickness measurement due to artefacts (like Fresnel fringes) that occur at the edges of objects due to changes in defocus that occur over time.

5.5.2 Core Oxidation- Ni Cation Diffusion

In order to observe the movement of the Ni cations that lead to the formation of hollow structures like those seen in the previous sections, continuous acquisition in ETEM was once again employed. HR-ETEM images were acquired as a movie (25fps) during oxidation using the OneView fast-frame camera.

O_2 (P=2 Pa) was introduced into the microscope at 60 °C in order to allow an initial oxide shell to form on the Ni nanoparticles. For the powder system, none of the observed nanoparticles were small enough for void formation to occur at this temperature. Once an equilibrium state was reached, such that the oxide layer did not appear to thicken, the temperature was raised to 500 °C. Continuous acquisition was started just before the temperature increase. Figure 5.16 shows a time sequence over the course of the reaction (extending out to partial completion after 100 seconds).

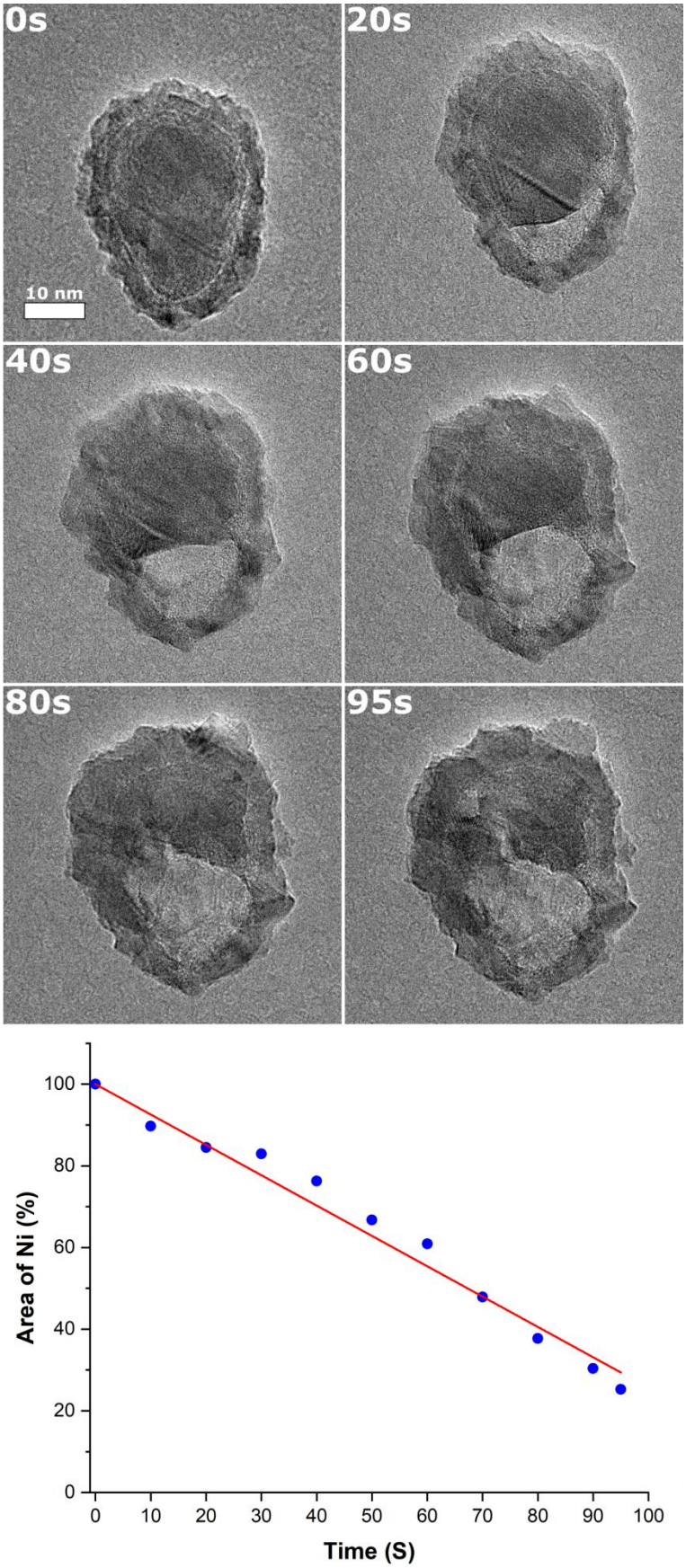

Figure 5. 16: ETEM time sequence showing the oxidation of a Ni-NiO nanoparticle at 500 °C. The full sequence was recorded using continuous video acquisition. The graph plots the normalised area of the metallic core as a function of time. The red line is a linear fit to the data.

For the particle shown in figure 5.16 there are initially two voids formed at the metal-oxide interface (bottom right and bottom left). These very quickly coalesce into a single large void and the majority of the reaction proceeds with the growth of this single void. This was also seen to be the case with other nanoparticles observed during initial void formation. The reaction proceeds quickly at this temperature, indeed half of the initial metallic Ni had diffused out of the core region by t= 1 minute. The metal-void boundary is convex with respect to the metal but becomes almost flat at the mid-line of the nanoparticle before becoming convex again; this has previously been observed for the metal-oxide interface in small Cu nanoparticles [179].

The graph shown in figure 5.16 shows the area fraction of metal remaining in the core region measured from an extended time sequence. This nanoparticle was suitable for this as the internal metal-void interface was parallel to the electron beam. While only a 2D projection of a 3D object this gives at least a qualitative idea of the volume of metal atoms (or more appropriately ions) diffusing across the metal-oxide boundary per unit time. Two immediate observations can be taken from this. Firstly, the rate of removal of material from the core region is linear with time. It is clear that the metal-oxide interface area is decreasing with time but the oxidation rate does not change. Therefore, the interface area is not a rate limiting factor in the reaction. Secondly, the loss of material is not noticeably affected by the presence of Ni grain boundaries or stacking faults observed in the nanoparticle (see figure 5.17). This is reasonable considering that ionic diffusion rates are normally independent of the crystal direction. It can also be stated that as the metal-oxide interface moves, the loss of interfacial area between Ni and NiO grains is at least an order of magnitude higher than the area loss between Ni and NiO grain boundaries. This is because the interfacial area between the Ni surface and NiO grain boundaries is proportional to the width of these grain boundaries, which is typically on the order of Angstroms —compared to the width of NiO grains, typically 1-10 nm (refer to figures 5.5 and 5.15).

Figure 5.17 shows the same particle as in figure 5.16 before and after oxidation. There appears to be no preferred orientation of the NiO crystallites compared to the underlying Ni metal. However, this could be due to the morphology of the nanoparticles observed in this system, whether or not this would be the case for highly faceted shaped nanoparticles remains to be seen.

Certain NiO grains on the surface preferentially oxidise compared to others leading to an increase in the surface roughness of the nanoparticle. This can easily be seen in figure 5.16 and figure 5.17 towards the end of the reaction in the top right region of the oxide shell. An explanation for this could be that the uptake of metal ions per unit time by a single grain of oxide is proportional to contact area between the oxide and the metal surface. This would cause more metal ions to transition into that particular grain of NiO, causing it to grow at a faster rate than the surrounding oxide grains. This seems reasonable as the internal shape of the nanoparticle (internal oxide surface) is preserved over the course of the reaction. This phenomenon may be aided (or hindered), to a certain extent, by merger of adjacent oxide grains with similar crystal orientations. A consequence of this would be that the final grain structure of the hollow NiO nanoparticle is determined by the grain size distribution in the initial surface oxide.

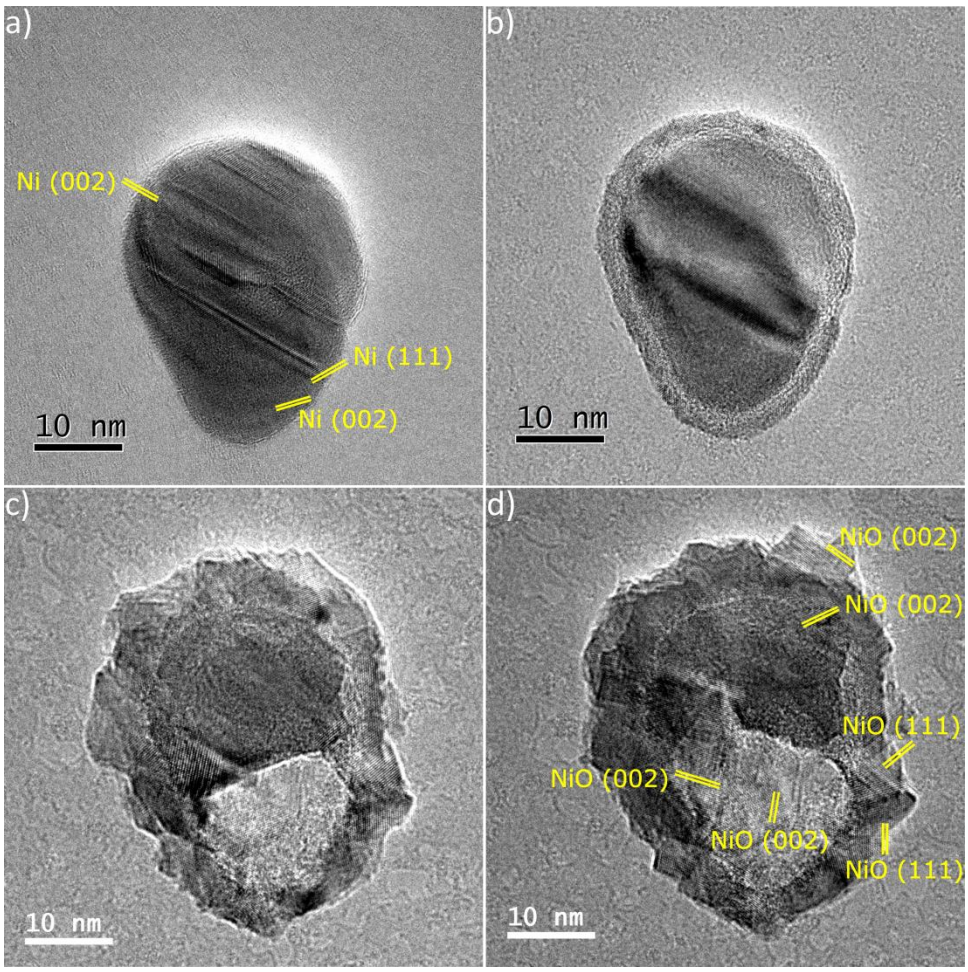

Figure 5. 17: a) Reduced nanoparticle of Ni metal (the fringes in the image and streaking seen in FFT indicate the presence of stacking faults at the grain boundaries). b) Formation of the oxide shell at low temperature (60 °C) after gas change. At 500 °C in O_2 the nanoparticle shows void formation and hollowing, the lower images show the structure of the nanoparticle c) 50 seconds and d) 90 seconds after the temperature increase.

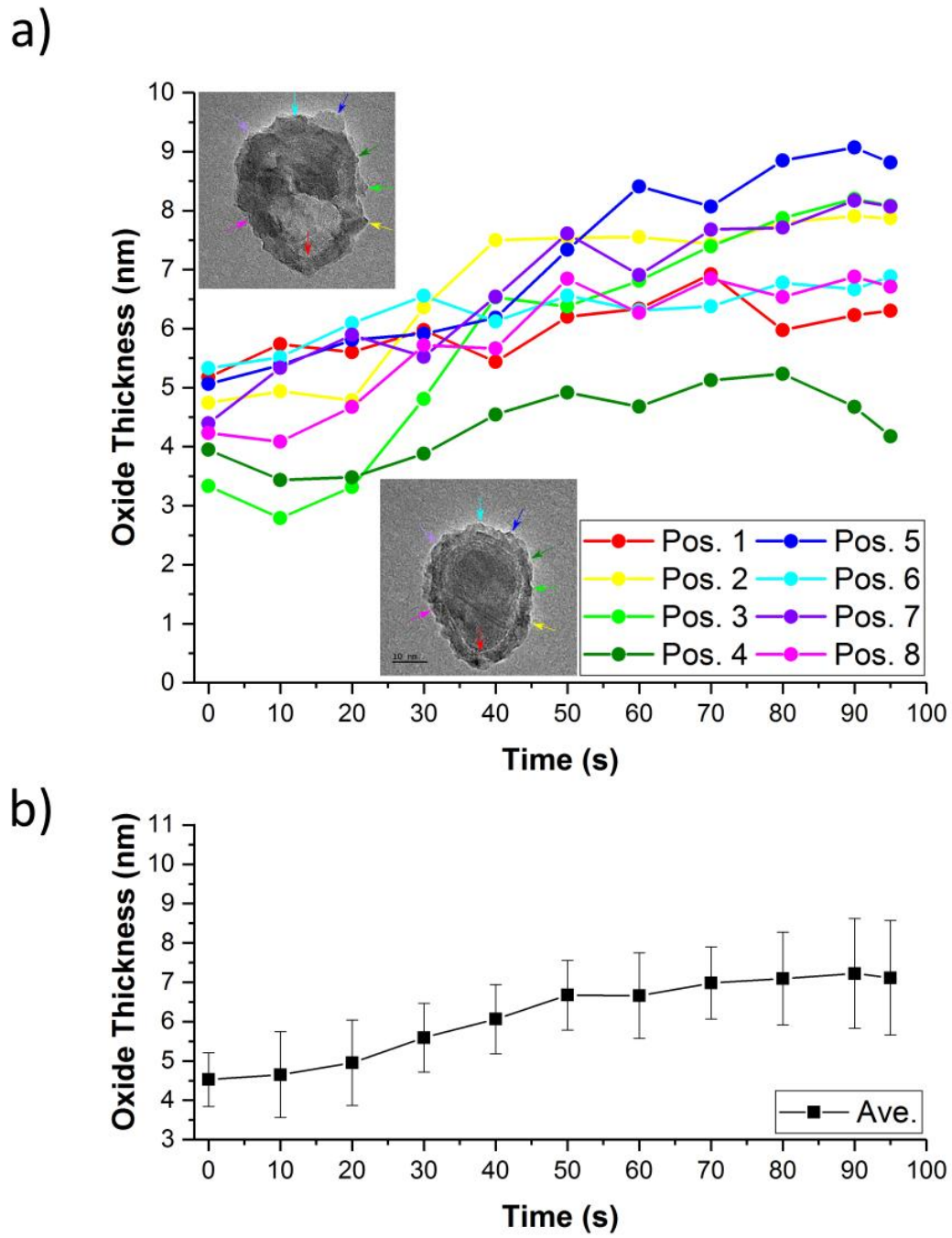

Figure 5. 18: Oxide thickness versus time for the nanoparticle shown in figure 5.17. Position specific measurements are shown in a) and the mean oxide thickness in b). The errors in b) are one standard deviation.

The thickness of the oxide shell was measured at 8 points around the periphery of the nanoparticle and the average thickness was found to increase from 4.5 nm at the start to 7.1 nm after 95 seconds. Figure 5.18 shows the average oxide thickness together with specific measurements taken from around the periphery. The errors shown in figure 5.18b are one standard deviation in either direction as standard error is inaccurate for low sample sizes. The uncertainty in figure 5.18a is due to the fact that the Ni-NiO interface has a finite size due to the Ni surface being curved. Additionally, changes in the

sample height (due to the recent temperature increase) result in defocus artefacts at the edge of the oxide.

A curious observation, highlighted by figure 5.18 but easily seen in figure 5.16 is that some of the oxide grains continue to grow for a time after the adjacent metal has diffused away. There are a few possible mechanisms for this. First, there could be a lateral component to the ion diffusion, causing Ni ions to propagate along the oxide layer parallel to the surface. This seems unlikely as the component normal to the surface is much higher. Additionally, any lateral movement of Ni would certainly mean that grain boundaries are crossed. Since short circuit transport of Ni along oxide grain boundaries is known to be several orders of magnitude higher than lattice diffusion, it is unlikely that any long range lateral transport could occur. A second possibility is that a single monolayer of Ni remains on the internal surfaces of the oxide. However, this would be a stable configuration if the internal surface of the NiO was (111), as these planes are single element terminated in the rock-salt structure i.e. alternating planes of Ni and oxygen. This would not lead to the outward growth of the oxide. An alternate possibility for the continued slow oxidation of these NiO grains could be that, as the ion and electron concentrations in the oxide layer begin to come to equilibrium, the electric field (or contact potential) breaks down resulting in a lower oxidation rate. In other words, the loss of the underlying metallic surface causes the loss of any surface potential that would otherwise enhance the movement of charge carriers across the oxide layer.

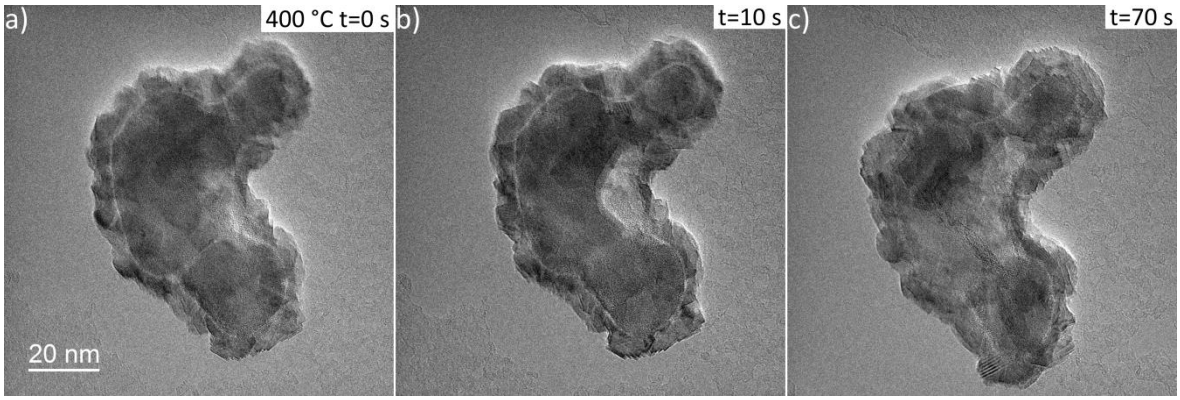

Figure 5. 19: Nanoparticle featured in figure 5.12 at 400 °C after a) 0 seconds, b) 10 seconds and c) 70 seconds.

Figure 5.19 is included here to show that the examples given in sections 5.5.1 and 5.5.2 are self-consistent. The nanoparticle from section 5.5.1 does indeed hollow out at elevated temperatures (400 °C). In this example however, the metal-void interface is not

parallel to the electron beam and is at an angle. This can be seen in the centre of figure 5.19b.

5.6 Chapter Discussion

In this chapter, in-situ E(S)TEM has been used to investigate the changes in nanoscale structure of Ni nanoparticles during oxidation in pure O_2. Before discussing the results of this chapter it is worth stating that microscopy techniques are not merely useful but essential for the study of solid state reaction kinetics and transport processes at the nanoscale. Indeed the consequences of the nano Kirkendall effect for fine structures such as nanoparticles can only be probed in a useful manner by (S)TEM.

The first stage of the reaction involves the oxidation of the exposed surface of the Ni metal. This results in core-shell structures for both small nanoparticles and larger polycrystalline structures. However, the formation of the oxide shell is not homogeneous. The shell is comprised of many pyramidal NiO crystallites which grow outward from the metal surface. As more of these crystallites are formed on the metal surface they begin to overlap with each other until the entire surface is covered by a complete shell. The pyramidal crystallites expose predominately (100) surface facets, this observation is consistent with the literature on NiO thin films [178, 180] and is reasonable considering that this surface is the most stable for the rock-salt structure. Depending on the local curvature or roughness of the underlying Ni surface, adjacent crystals may have similar crystal orientations and can merge with each other.

The formation of these individual crystallites across the surface means that the oxide shell is always polycrystalline. In other words, the shell does not become polycrystalline in order to accommodate the volume expansion that accompanies the Ni-NiO transition. Thus, the NiO will form with its unstrained lattice parameter and does not need to break away from the surface by plastic deformation or re-crystallisation, as suggested by Cabrera-Mott.

The crystallite formation is itself inhomogeneous. Some areas of the Ni surface are oxidised before others. This suggests that there are certain surface features that promote rapid adsorption of oxygen. The initial formation does not appear to coincide with grain boundaries in the Ni metal. This indicates that sites such as point defects i.e. dislocations

or steps are responsible for this rapid oxide formation. Lateral diffusion of these crystallites is not observed, only outward growth. This demonstrates that, although existing defects at the surface promote rapid NiO formation, they are not required for oxide formation. While TEM is unable to reveal the occurrence of any reconstruction of the Ni surface, the shape of the metal-oxide phase boundary is preserved during the oxidation.

Once the surface sites of the Ni nanoparticle are covered by NiO, the reaction mechanism shifts to a diffusion limited regime. The nano Kirkendall effect is observed during this stage of the oxidation. Oxygen atoms are dissociatively adsorbed on the NiO surface in the form of oxygen ions. A new layer of oxide is grown on the surface as Ni ions diffuse outward. This introduces a singly or doubly charged cation vacancy in the subsurface layer. To compensate for the Ni outward diffusion, the cation vacancies diffuse inward to the metal-oxide interface. In a thin film or bulk structure the metal-oxide interface would be replenished from the bulk, i.e. the bulk structure acting as a reservoir of Ni atoms (which dissociate to ions and electrons upon reaching the interface). In nanoparticles the metallic core can only provide a finite number of atoms before it is depleted.

As vacancies arrive at the metal-oxide interface, Ni ions are removed and the vacancies propagate into the core region creating voids. In small (<100 nm) nanoparticles the self-diffusion of Ni metal is fast enough that these voids can move along the interface and agglomerate into a single large void. The preservation of a single large void is more energetically favourable than sustaining multiple smaller voids. However, multiple voids are seen in larger nanoparticles and in Ni clusters. In such cases, the agglomeration and transport of voids is opposed by the arrival of new voids.

Continued oxidation results in the void growing and the metal-oxide interface area decreasing. The rate at which the core material is depleted does not appear to change with decreasing metal-oxide contact area. This suggests that it is the formation rate of new NiO layers that is the kinetic rate limiting process. It seems obvious then that the rate limiting process is controlled by the rate at which the Ni ions are removed from the metallic surface. Nevertheless, an interplay between this process and the rate at which oxygen ions become stable on the NiO surface cannot be ruled out. This may introduce a pressure dependence of the oxidation rate. The narrow range of operating pressures for

the E(S)TEM used in this work, limit the degree to which this dependence can be explored.

The oxidation is complete when the metallic core is fully depleted. The end result is a hollow shell of NiO. Using the sputtered Ni system, it was shown that hollow NiO structures are formed, even for nanoparticles ~4 nm in diameter and that the same model of oxidation applies. Since all of the nanoparticles involved form similar structures upon complete oxidation, it can be stated that the reaction pathway is independent of temperature. The reaction rate on the other hand is dependent on temperature and the degree of oxidation after a given reaction time is dependent on both temperature (reaction rate) and nanoparticle size (abundance of oxidisable material). It has been shown in this work as well as others [163] that the hollow NiO structures are very stable and require higher temperatures to cause collapse by atomic rearrangement.

So far, the exact pathway for the transport of Ni ions and vacancies has not been discussed. Based purely on the diffusion coefficients presented earlier, it would be reasonable to assume that Ni ions traverse the NiO shell via a short circuit diffusion pathway along grain boundaries. However, as already discussed, the oxidation does not seem to slow down as metal-oxide interface area is reduced. The reduced interface area means that the number of short circuit diffusion pathways available also decrease. Therefore, it is impossible to state with absolute certainty that one pathway is dominant. It is also reasonable to assume that across oxide layers this thin, especially at the start of the reaction, that both diffusion mechanisms are in competition.

During the oxidation of the core-shell nanoparticles, it could be seen that different NiO grains grew at different rates. The oxidation rate of each NiO grain depends on a number of factors. For example, the character of the metal-oxide interface, the crystallographic orientation of the two materials, the surface area upon which new oxide is growing and any differences in diffusion rates along certain crystalographic directions (not fully understood yet). Additionally, the movement of the metal-void interface adds an additional layer of complexity. The number of voids depends on the size of the nanoparticle and the point of formation of the first void will depend on the location of (initially) greatest oxidation rate.

In order to model the oxidation rate of such a complex system it would be necessary to take into account all of the position dependent oxidation events. In principle this could be

done by taking the metal-oxide interface at a certain time as an idealised surface, s. This surface could be broken up into a number, N, of infinitesimally small surface area elements of area ds, over which the oxidation rate (dX/dt) is constant. Then the effective, or rather average, oxidation rate for the nanoparticle (ΔX/Δt) would be the integral over all surface area elements. This is given ideally by equation 5.3 and would form the basis of simulation for such a system. If lattice diffusion were the principle diffusion pathway, then the area over which the oxidation rate is constant is equal to the area taken up by a single grain of NiO at the metal-oxide interface and the rate itself would depend on the interfacial area, the current thickness of the oxide layer and the crystal orientation relative to the surface. In this case equation 5.3 becomes a summation over i, oxide grains, which could be measured statistically for a system using HR-TEM of the initial oxide shell. The summation is given by equation 5.4, where the oxidation rate of a single NiO grain by lattice diffusion is given by $\delta X_i/\delta t$.

$$\frac{\Delta X}{\Delta t} = \frac{1}{N} \oiint_N \frac{dX}{dt} ds \tag{5.3}$$

$$\frac{\Delta X}{\Delta t} = \frac{1}{i} \sum_i \frac{\delta X_i}{\delta t} \tag{5.4}$$

To the best of the author's knowledge this is the only study that has observed the in-situ growth of the oxide shell and nanostructural evolution of its morphology. Additionally, this work is unique in that it follows both the shell formation and the core depletion with equal focus and resolution. Finally, the choice of in-situ conditions (temperature and pressure) and the choice of sample (size) meant that the reaction could take place over a suitable time period such that the changes could be observed without the ambiguity involved with second or even millisecond reaction time scales.

Chapter 6

In-Situ Redox Reactions of Ni Methanation Catalysts

Synthesis gas (or syngas) is a mixture of hydrogen and carbon monoxide (and often carbon dioxide); it is used as the feedstock in the Fischer-Tropsch (FT) process. The Fischer-Tropsch process represents a number of industrial chemical reactions that involve the conversion of syngas to create a variety of hydrocarbon alkanes and alcohols. The exact composition of the FT product mixture is governed by the reaction temperature, pressure and the type of catalyst employed. This is usually a transition metal, in nanoparticle form, on a ceramic support. The products can be further upgraded and refined to form many important chemicals including: gasoline, kerosene and diesel fuels [181]. The production of methane (CH_4) as a substitute natural gas (SNG) using this process is called: methanation. In this chapter, a number of Ni catalysts appropriate for the methanation reaction are studied using in-situ E(S)TEM. Experiments were performed to investigate changes in the catalytic activity caused by both the catalyst support and the use of an oxide promoter. The evolution of the nanostructure was observed in-situ, under both reducing and oxidising conditions. The catalyst samples were provided by Johnson Matthey Plc (JM).

6.1 Methanation Catalysis and Reactors

Oil and natural gas are the primary feedstocks for the production of fuels and commercial chemicals in most countries. However, the current projections for the reserves of these resources show that they will last approximately 50 years [182]. As a consequence,

alternative feedstocks are being explored including: coal with reserves of approximately 150 years and organic biomass which is renewable. These domestic resources present opportunities for decreased reliance on imported fuel sources, lower cost and reduced greenhouse emissions (through carbon capture). Coal and biomass can be converted to synthetic natural gas (SNG) as a substitution for natural gas with high conversion efficiency. The production of SNG is made more attractive by its applicability to established technologies such as cars, heating and power stations, as well as the existing gas pipelines and distribution network.

The production of SNG is a chemical process involving many steps which require separate reactors, catalysts and reaction conditions. These steps are summarised in figure 6.1. In general, the coal or biomass undergoes gasification, a process in which the carbon containing feedstock is made to react with oxygen and steam without combustion to create a producer gas consisting of hydrogen, carbon oxides, hydrocarbons and impurities such as sulphur and chlorine compounds (and amine species in the case of biomass). The cleaning step is a multi-stage process that aims to remove undesirable products of gasification as well as the impurities such as sulphur and chlorine which (even in relatively small concentrations, ~0.1%) can poison/deactivate the catalysts used in the fuel synthesis. The producer gas is then conditioned such that the composition is suited to the methanation technology being employed for the fuel synthesis. Finally, the fuel is upgraded by the removal and recycling of non-fuel components such that the SNG is in compliance with the required quality standards.

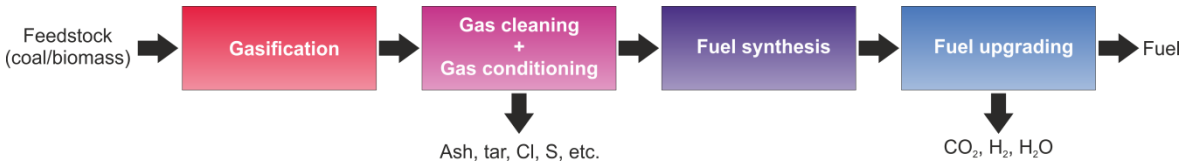

Figure 6. 1: General process flow for the industrial conversion of coal or biomass to SNG [183]. Adapted from Fuel, 89, J. Kopyscinski, T.J. Schildhauer, S.M.A. Biollaz, Production of synthetic natural gas (SNG) from coal and dry biomass - A technology review from 1950 to 2009, 1763-1783, Elsevier Ltd (2010), with permission from Elsevier.

It is interesting to note that the processes described by figure 6.1 cannot be considered in isolation and are interlinked. The gas cleaning design is based on the output of the gasification. The type of fuel synthesis determines the acceptable inlet composition and the resultant output gas. For example, coal gasification produces unwanted hydrocarbons

which can be converted into usable syngas by the steam reforming reaction (equation 6.1).

$$C_xH_y + xH_2O \rightleftharpoons xCO + \left(x + \frac{y}{2}\right)H_2 \quad \Delta H_R^o > 0 \tag{6.1}$$

The fuel synthesis concerned here is the conversion of syngas to methane (methanation). The methanation reaction proceeds by three possible reactions shown by equations 6.2, 6.3 and 6.4. These reactions are exothermic and so increase the temperature of the surroundings [184, 185]. More so in the case of methanation where high CO concentrations are present, compared to the removal of small amounts of CO via methanation from the producer gas in ammonia production. This exothermic effect can be exploited as a method for determining a catalyst lifetime by probing the temperature profile along the length of a reactor. However, this heating must be considered and mediated as excessive temperatures can lead to catalyst deactivation or shifts in the reaction dynamics which in turn impact the methane yield.

$$3H_2 + CO \rightleftharpoons CH_4 + H_2O \quad \Delta H_R^o = -206\ kJ/mol \tag{6.2}$$

$$2H_2 + 2CO \rightleftharpoons CH_4 + CO_2 \quad \Delta H_R^o = -247\ kJ/mol \tag{6.3}$$

$$4H_2 + CO_2 \rightleftharpoons CH_4 + 2H_2O \quad \Delta H_R^o = -165\ kJ/mol \tag{6.4}$$

It should be noted that for equations 6.2, 6.3 and 6.4, CO methanation prevails over CO_2 methanation in a mixed CO/CO_2 feedstock [186] and that its reaction route is determined by the stoichiometry of the syngas being used. Equation 6.2 can only occur with H_2/CO ratios of three or higher. Since this is optimistic, the methanation process is often combined in the reactor with the water gas shift reaction (equation 6.5) which increases the H_2/CO ratio. Indeed methanation catalysts also display activity for water gas shift.

$$CO + H_2O \rightleftharpoons CO_2 + H_2 \quad \Delta H_R^o = -41\ kJ/mol \tag{6.5}$$

From the 1970's up until today a number of methanation processes have been designed and tested for the methanation of syngas for the purposes of creating SNG [183, 187]. The majority of these involve the use of one of two reactor designs: the adiabatic fixed bed reactor and the fluidised bed reactor. The fixed bed design consists of a reaction vessel packed with catalyst pellets or monoliths with the gas being forced through the stationary catalyst bed. The fluidised bed reactor contains fine catalyst pellets or powder and the input gas is introduced at a velocity capable of suspending the catalyst and causing it to behave as a fluid for better mixing and for operation at almost isothermal temperatures. Both designs place different demands on the catalyst, the fluidised bed

reactor requires attrition resistance and the fixed bed reactor requires good thermal stability and removal of reaction heat to reduce sintering of the catalyst.

In general, all of the metals in groups 8-10 of the periodic table could be used to catalyse the methanation reaction; these include Ru, Fe, Ni, Co, Rh, Pd, Pt and Ir. Nickel shows the highest selectivity to methane, has high activity (although not the highest) and is low in price compared to noble metals like Pt or Pd [187]. Therefore, Ni is almost universally used as the active catalyst for industrial methanation. Normally, when a Ni catalyst is synthesised the Ni is in an oxidised state and reduction is required. The reduction is normally performed under operating conditions because the formation of metallic Ni starts the methanation reaction, the heat of which, accelerates the reduction of the rest of the catalyst bed [188]. Methanation reaction conditions involve high temperatures (300-700 °C) and pressures up to 30 bar. The conditions used are more than just a compromise to maximise the methane yield, they are a compromise to mitigate the various, often competing, catalyst deactivation mechanisms [189].

The methanation activity is dependent on the surface area of the Ni. For this reason, smaller catalyst particles are favoured and the Ni is usually dispersed on an oxide support to reduce sintering. To produce the required amounts of catalyst required for an industrial reactor and to achieve the desired mix, chemical impregnation methods are used, the choice of which determines the character of the synthesised catalyst [190, 191]. Different oxide supports have been tested over the years including silica (SiO_2), alumina (Al_2O_3), titania (TiO_2) and combinations thereof [192], as well as other compounds. However, alumina is known to have very good thermal stability and reduces sintering in Ni based catalysts [193, 194], especially high surface area transition aluminas such as γ and δ [195-197]. Alumina supported Ni catalysts have been the focus of many studies for methanation catalyst enhancement.

In addition to the variety of catalyst and support materials, promoters may also be included during catalyst synthesis. A promoter is an additional compound that can augment the activity of a catalyst. For example, promotion of a Ni/γ-Alumina catalyst with zirconia (ZrO_2) has been shown to increase the Ni dispersion [198, 199]. Ceria (CeO_2) has been presented in the literature as a highly effective promoter for Ni-based methanation catalysts. H.Z. Liu et al [200] showed that ceria promotion led to better reducibility of Ni in a Ni/γ-Alumina catalyst for CO_2 methanation. That study showed that 2 wt% was the

optimal ceria loading. Q. Liu et al [201] presented a method for ceria promotion (also of Ni/γ-Alumina) which limited Ni sintering and stopped coke formation. Wang et al [202] reported similar enhancement of the catalyst for the reverse reaction. Zeng et al [203] showed that Ce promotion of a Ni/γ-Alumina catalyst led to better dispersion of the Ni and a shift in the binding energy of the Ni atoms through interaction with Ce^{3+}/Ce^{4+} redox couples, leading to better low temperature activity. Similarly, binding energy shifts have been observed in Au nanoparticles supported on various shapes of ceria support [204]. Furthermore, ceria has been shown to stabilize transition aluminas and prevent transformations to less desirable phases such as α-alumina [205]. This stabilization has been attributed to the formation of Ce^{3+} in the form of $CeAlO_3$ on the alumina surface, which inhibits surface diffusion of species required for the formation of α-alumina.

Ding et al [206] prepared a Ni/Al_2O_3-CeO_2 catalyst which showed higher reducibility and lower coke formation when compared with other single and mixed oxide supports of silica, alumina, zirconia and ceria. Nematollahi et al [207] showed that a 50 wt% Ni/ceria catalyst, made by co-precipitation, was highly active for selective CO methanation (CO_2 methanation suppressed). Nematollahi suggested the oxygen vacancies in the ceria accelerated CO methanation and that CO adsorbed in dissociative form on the catalyst surface. Pan et al [208] demonstrated the effectiveness of impregnation methods for creating a Zr-Ce mixed-oxide Ni catalyst in which higher activity was ascribed to: higher Ni surface area, increased presence of oxygen vacancies, Ce^{3+} ions and basic reaction sites.

The literature seems to present a consensus that hydrogen activation (adsorption and dissociation) requires an exposed metallic Ni surface. Thus, NiO is not an active catalyst for methanation. However, the exact routes for CO and CO_2 activation are less clearly defined. With respect to the Ni species, it has been suggested that the active sites for CO/CO_2 are under-coordinated Ni atoms at the edges of particles [209] or at the Ni-alumina interface [210]. Many sources suggest that in ceria-promoted catalysts, the activation of CO/CO_2 is via an oxygenated intermediate species. Aldana et al [211] used IR spectroscopy on a Ni/CeO_2-ZrO_2 catalyst to suggest that CO_2 adsorbs onto basic sites provided by oxygen deficient ceria. Adsorption would form carbonates which would be hydrogenated into formates ($HCOO^-$ containing compounds) and then to methoxy species. Westermann et al [212] came to a similar conclusion using a Ce-Zr impregnated zeolite catalyst. They suggested that formate formation is a kinetically relevant step in

CO_2 methanation and that these reaction intermediates are formed at sites provided by a ceria supported phase in their sample.

In this chapter, Ni based catalysts relevant to the methanation reaction are investigated under redox conditions using E(S)TEM. The aim is to correlate the nano-structure of the samples with the various observations presented in the literature. In summary, the literature observations show (separately or together) that ceria promotion affects: morphology, dispersion and reducibility of the Ni to facilitate higher activity [213].

6.2 Sample Preparation and Summary

In the following sections Ni based catalysts prepared by JM[1] are investigated using in-situ E(S)TEM. The main catalysts used are: Ni/Alumina, Ni-Ceria/Alumina and Ni/Ceria. The alumina based sample was chosen because it is the most commonly used support in the industrial methanation process. It also allowed for a direct comparison with an oxide promoted sample, in this case ceria, at wt% consistent with those previously studied in the literature. In order to compare the role of ceria as a promoter versus as a catalyst support, a Ni/Ceria sample was also prepared. Finally, a series of comparison samples were prepared in order to test the effect of increased promoter crystallite size. The samples used herein are summarised in table 6.1.

Notation	Catalyst	NiO (wt%)	Crystallite size[a] (nm)	CeO_2 (wt%)	BET surface area[b] (m^2g^{-1})
Ni/Ceria	NiO/CeO_2	19	20.4: NiO 5.1: CeO_2	-	127
Ni/Alumina	NiO/Al_2O_3	39	<3: NiO	-	136
Ni-Ceria/Alumina	$NiO\text{-}CeO_2/Al_2O_3$	29	<3: NiO	3	148
Ni-Ceria(L)/Alumina	$NiO\text{-}CeO_2(large)/Al_2O_3$	31	<3: NiO 11: CeO_2	3	136

Table 6. 1: Summary of catalyst samples used in this chapter. [a]= Crystallite size determined via XRD using the Scherrer equation. [b]= Brunauer-Emmett-Teller (BET). The L in the notation denotes the presence of large (detectable using XRD) crystalline ceria.

The samples were prepared by incipient wetness impregnation on powder supports of δ/θ-alumina and ceria. Samples containing ceria promoter were impregnated with the promoter precursor first and then dried at 110 °C and calcined in air at 450 °C for 4 hours before impregnation with Ni. In the case of the Ni-Ceria(L)/Alumina sample, impregnation

[1] Catalyst samples, activity tests and XRD were provided by Dr. L. Van de Water and JM.

was performed using a cerium nitrate solution (pH= 1). This allows for formation and aggregation of CeO_2 during drying and calcination. However, in the case of the Ni-Ceria/Alumina sample a cerium citrate solution (pH= 10) was used instead. The citrate ($C_3H_5O(COO)_3^{3-}$) ligands form a complex with the Ce^{3+} ions which inhibit aggregation of the ceria during drying and calcination. For all samples Ni was loaded via excess liquid impregnation using a Ni ammonia solution (pH= 12) which converts to NiO during drying and calcination. The Ni precursor drying was performed at 110 °C and calcination at 350 °C. This impregnation method leads to high NiO dispersions.

The preparation methods described all produce samples with Ni in an oxide phase. However, given that the active catalyst phase is metallic Ni, the catalysts will be referred to using the notation shown in table 6.1. The final NiO and ceria loadings, as well as BET surface area, are also shown in table 6.1. It should be noted, that the samples containing ceria promoter material which are not denoted with an 'L' have ceria crystallite sizes below the limit required for identification by X-ray diffraction (XRD). The mixed phase alumina used for the catalyst-supports leads to peak broadening in XRD spectra. Since peak broadening can have multiple causes, it is not accurate to use Scherrer analysis to determine the crystallite size of the alumina. Thus, the alumina crystallite size is not included in table 6.1.

6.2.1 Methanation Activity

The current JM methanation technology splits the process into two stages. First, a bulk stage using high temperatures and gas recycling to facilitate the majority of the feedstock conversion. Second is a trim stage where 1-3 reactors are ran at lower temperatures to convert residual feedstock to maximise the methane content of the output stream.

Before shipping, the ceria, alumina and promoted samples were tested for their methanation activity. For the tests, 25 mg of catalyst powder (300-500 µm sieve fraction) was reduced in-situ (540 °C in 10% H_2/N_2 for 4 hours) and then exposed to the gas feed described in table 6.2. The catalyst was then aged under simulated trim temperature conditions shown in figure 6.2.

Feedstock Element	Composition (vol. %)
CO	0.1
CO_2	3
H_2	10
N_2	86.9
H_2O (steam)	+5% (relative to the dry gas)
Process pressure	20 bar
Feed temperature	250 °C

Table 6. 2: Gas composition used in the methanation activity test.

The methanation activity was evaluated at the end of the 5 day aging process at 250 °C; the results are shown in figure 6.3. The y-axis in figure 6.3 represents the volume fraction of the outlet gas composed of methane. As discussed the selectivity for methane of these catalysts is very high and only negligible amounts of methanol were found in the output. The JM commercial NiO/Al_2O_3 methanation catalyst: KATALCO 65-3, prepared by co-precipitation (~45 wt% NiO), is also presented in figure 6.3 as a reference.

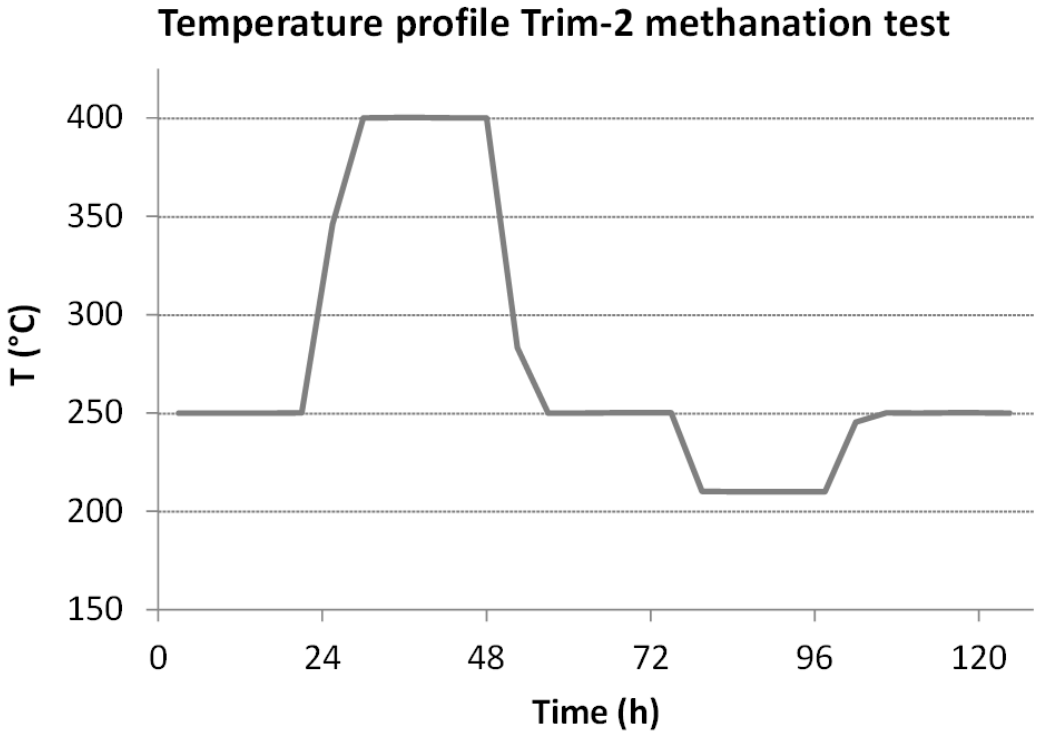

Figure 6. 2: Aging temperature steps used in the methanation activity test under conditions described in table 6.2.

From figure 6.3 it can be seen that there was a 109% increase in the production of methane from the Ni/Alumina sample to the Ni-Ceria(L)/Alumina sample. Furthermore, the increase in methane production from the unpromoted sample to the promoted sample containing very small crystallites of promoter ceria was 205%. By contrast the use

of ceria as a support material was characterised by a poor methanation performance compared to alumina.

The two and three-fold increase in the methane formation rate of the promoted catalysts is of major industrial significance. The inclusion of only 3 wt% ceria promoter has a huge effect on the catalytic activity. However, it is clear that the modified catalytic activity is heavily dependent on the crystallite size of the promoter. Nanostructural characterisation of these samples by electron microscopy is presented in the following sections.

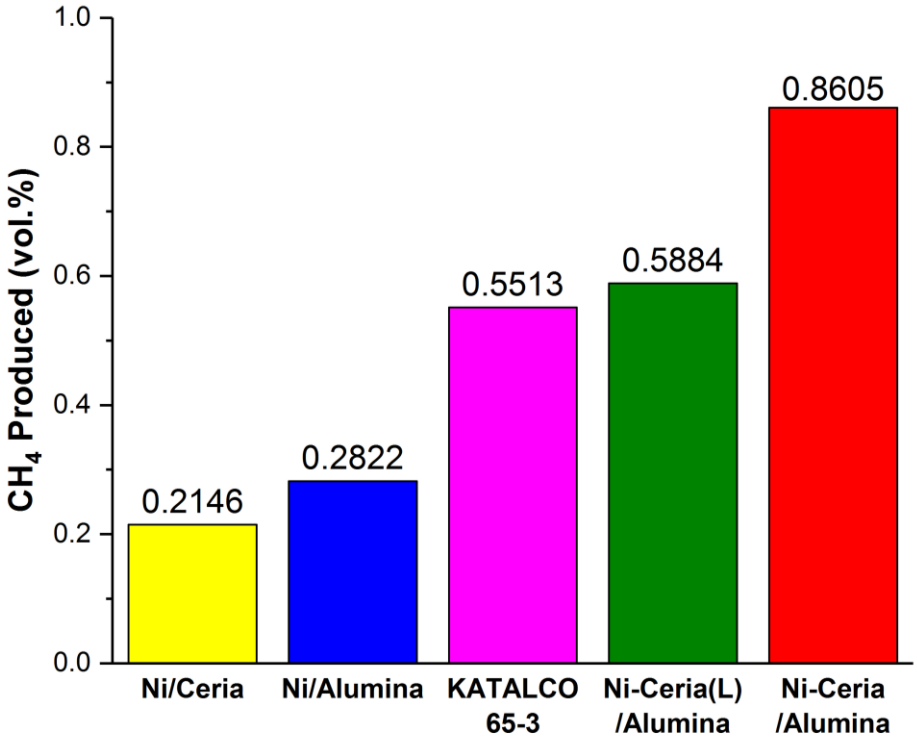

Figure 6. 3: Methanation activity test results for the catalyst samples used in this chapter. The uncertainty in the yield is approximately +/- 3%.

6.3 Ni/Alumina

Owing to the fact that all of the alumina-supported catalysts presented in figure 6.3 (except the Katalco industrial catalyst) are made using the same support material and metal impregnation method, the Ni/Alumina sample is able to serve as reference for direct comparison to the other samples. As such, this system is presented first.

All of the samples discussed in this chapter were delivered as powders; to prepare them for E(S)TEM analysis they were dispersed in ethanol and drop-cast (4 µL) onto MEMS

heating chips supporting an amorphous carbon film. The electron beam was blanked during in-situ heating, gas injection and withdrawal. The samples were only exposed to the electron beam during image preparation and acquisition. Furthermore, care was taken to minimise beam exposure to areas used for repeated imaging.

6.3.1 Initial Characterisation

The sample was initially heated to 300 °C for 10 seconds to bake off any carbonaceous contamination that may have been introduced during sample preparation. The temperature was then maintained at 60 °C to avoid contamination build up during imaging without driving any significant change in the sample itself. XRD analysis and TEM micrographs of the initial sample are shown in figure 6.4. Together they reveal that the support is comprised of mixed phase delta-theta alumina crystallites in various orientations. The alumina crystallites overlap without epitaxy. While this can make interpretation of TEM images difficult, the uneven topography is closer to an industrial catalyst than would be seen with a model system using an amorphous support or a single crystal support. The delta and theta alumina phases are good choices for catalyst supports due to their high surface areas, porosity and stability.

The TEM micrographs in figure 6.4 reveal the initial dispersion of the metal species. It is expected that the Ni is in an oxide phase due to the sample preparation method and the continued exposure to air during delivery. The NiO appeared to be highly dispersed across the alumina support. Small nanoparticles of NiO, approximately 3 nm, can be seen on the alumina. However, the high NiO loading (39 wt%) would presumably lead to many more of these nanoparticles than were observed. As such, NiO in the form of layers, disordered clusters and atomic species cannot be ruled out. This assumption is reasonable as demonstrated in the next section.

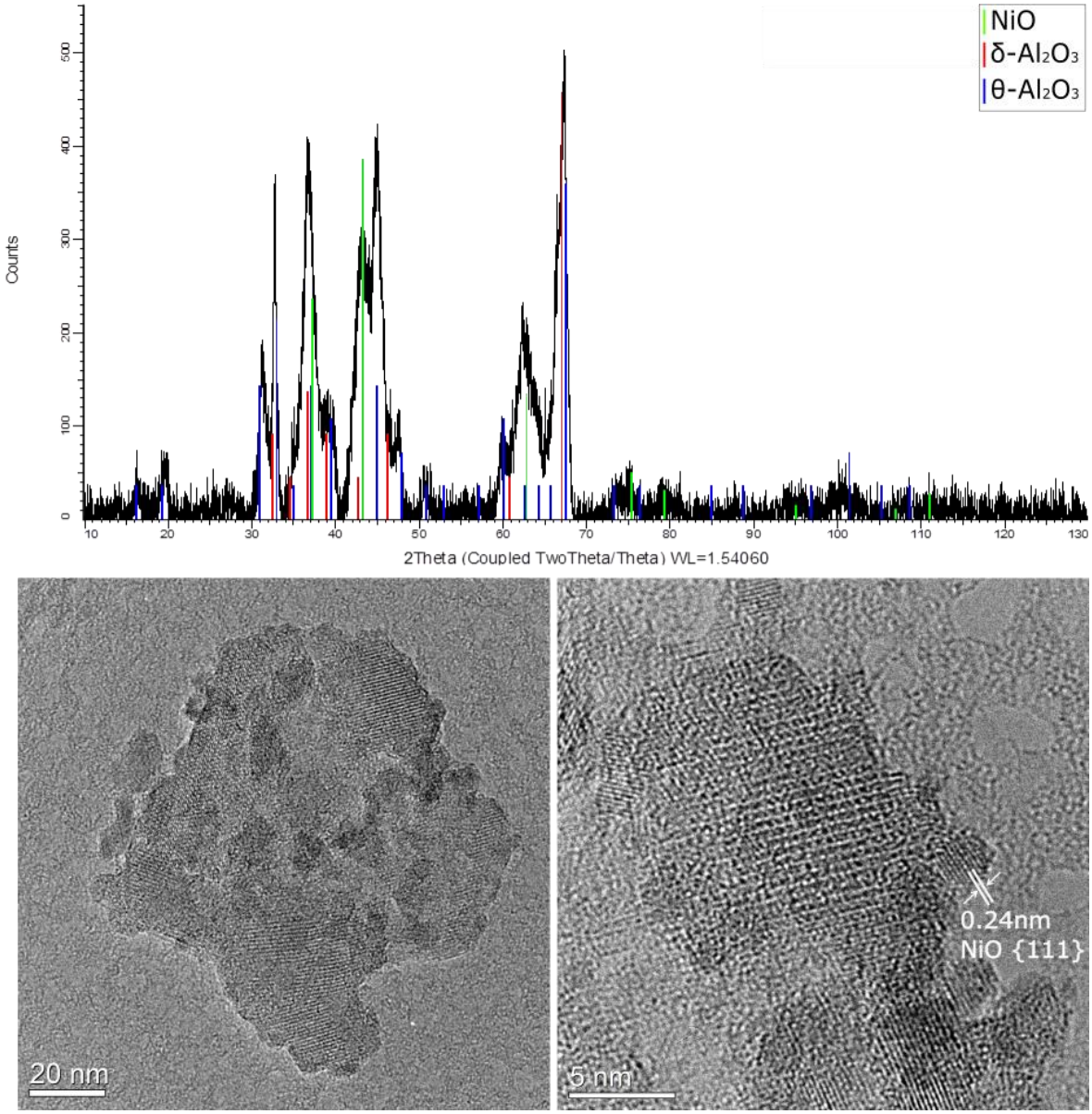

Figure 6. 4: XRD analysis (top) of the Ni/Alumina sample, provided by JM, identified the support material as a mixed phase delta-theta alumina. The TEM micrographs (bottom) show the varying size and overlap of the alumina crystallites and the high dispersion of NiO on the support.

6.3.2 In-situ Reduction and Characterisation

As discussed in previous chapters, before a catalyst can be brought online it has to undergo a pre-treatment to expose the catalytically active phase. In this case the NiO species must undergo a reduction to form a metallic phase. This can be done in two ways: a thermal decomposition (equation 6.6) or directly using a reducing agent such as hydrogen (equation 6.7).

$$2NiO \rightleftharpoons 2Ni + O_2 \quad (6.6)$$

$$NiO + H_2 \rightleftharpoons Ni + H_2O \quad (6.7)$$

In this study 500 °C was chosen as the reduction temperature. There are many factors that decide the operating temperature in large scale catalysis operation, including the system thermodynamics, reaction kinetics and catalyst life-time considerations. However, a rule of thumb for nanoparticle catalysts is that the temperature should be kept as low as possible to reduce the amount of deactivation by sintering. Methanation is usually run in the temperature range 300 to 500 °C. Indeed 500 °C reduction steps are used for co-precipitated Ni/Alumina catalysts to remove spinel type $NiO.Al_2O_3$ compounds. Therefore, 500 °C is a reasonable choice and is able to drive the reduction reaction on a time scale applicable to TEM operation times.

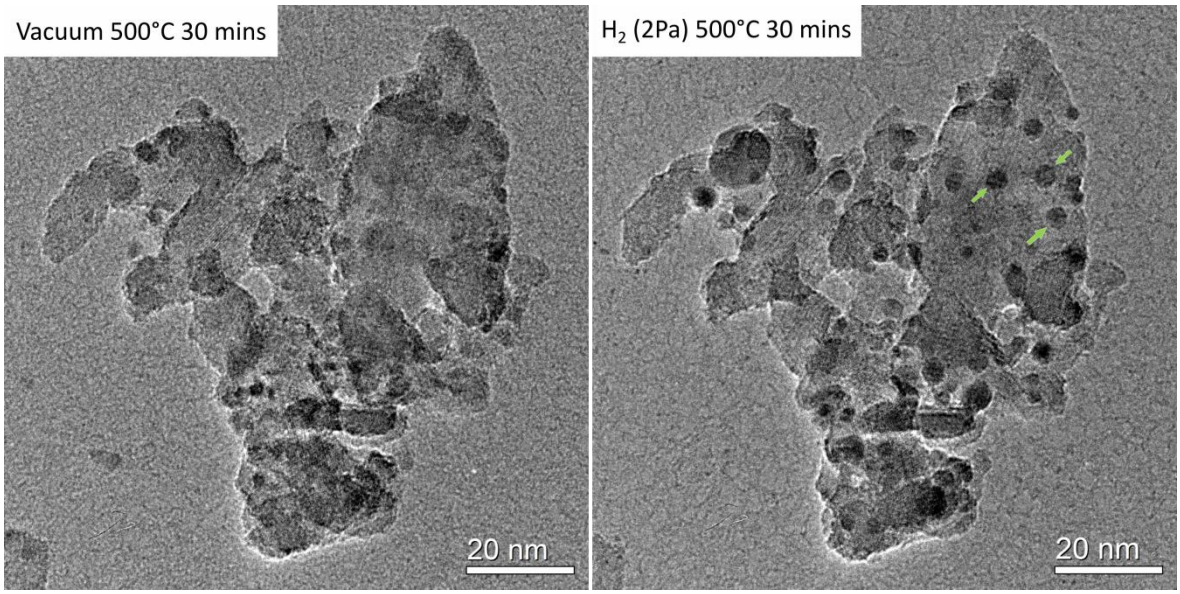

Figure 6. 5: Ni/Alumina sample after in-situ heating at 500 °C for 30 minutes in vacuum (left) and at 500 °C for 30 minutes under 2 Pa of hydrogen gas (right). Green arrows highlight the formation of Ni nanoparticles during reduction with hydrogen.

Reduction of NiO via thermal decomposition requires higher temperatures and longer time frames than are explored here. On the other hand, reduction using hydrogen gas is energetically favourable and proceeds quickly. Figure 6.5 shows the same area after in-situ heating for 30 minutes in vacuum and under hydrogen gas exposure. The Ni/Alumina sample showed high thermal stability and limited sintering of the Ni species was observed in vacuum at 500 °C. By contrast, hydrogen reduction leads to complete reduction of the NiO species and the formation of Ni nanoparticles (see figure 6.6). It should be noted that the sample was cooled to 60 °C during imaging in figures 6.5 and 6.6 to prevent localised heating from the beam that would exceed 500 °C.

Despite the low gas pressure (2 Pa), there is sufficient interaction between the NiO and the gas phase to fully drive the reduction reaction. Figures 6.5 and 6.6 show that the reducing conditions used here provide the Ni with a means of transformation to the metallic phase but also a mechanism for increased mobility across the support. The spatial distribution of the Ni nanoparticles suggests that the sintering mechanism observed during reduction is Ostwald ripening. Atomic migration has previously been suggested to be part of the reduction mechanism for NiO/α-Alumina catalysts [214].

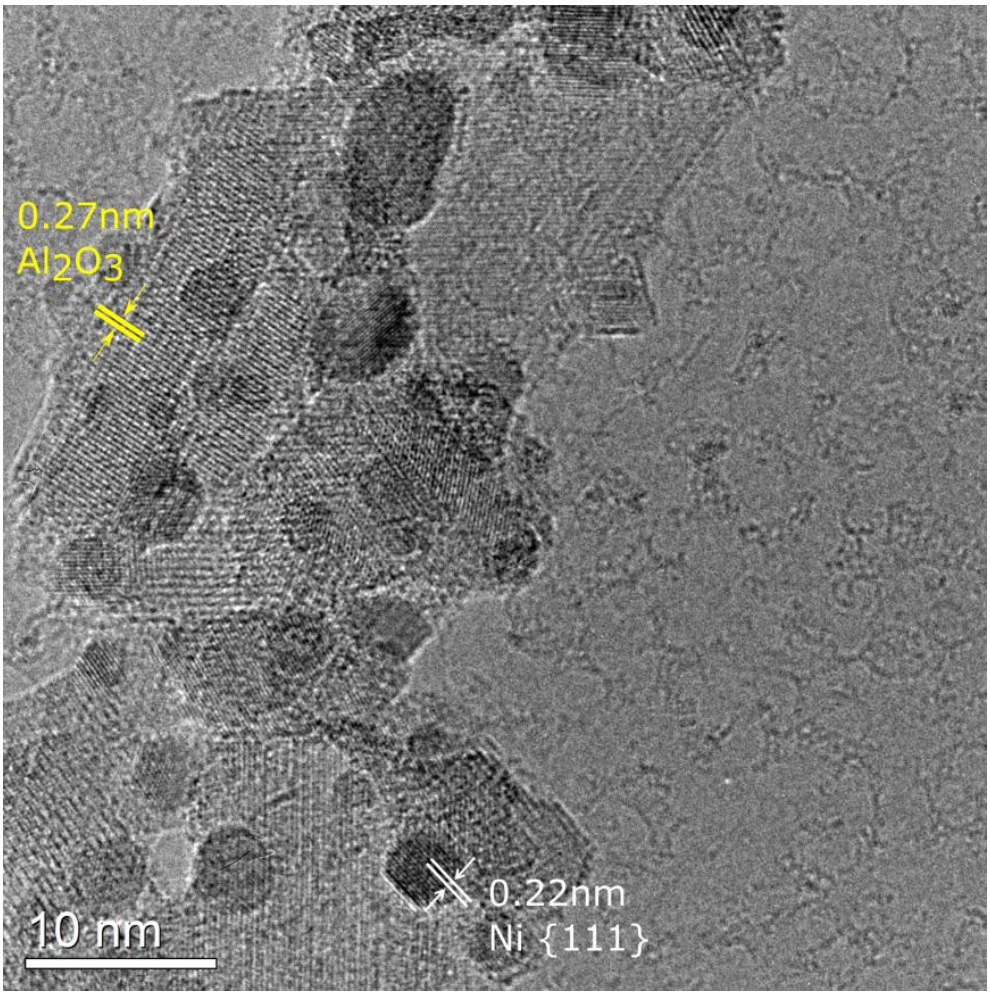

Figure 6. 6: HRTEM micrograph of the Ni/Alumina sample after in-situ reduction at 500 °C. The formation of a Ni nanoparticle species can be easily seen. The alumina support is polycrystalline and the crystallites appear to be randomly orientated with respect to each other.

In order to determine the extent of this combined sintering-reduction event, a sample of the Ni/Alumina was exposed to the same reducing conditions and was imaged multiple times at 30 minute intervals with the sample only being exposed to the beam during image acquisition. Figure 6.7 shows little change in the size and distribution of the Ni nanoparticles after the first 30 minutes. Here HAADF-STEM was chosen as the imaging

technique since the Z-contrast provides enhanced contrast between the heavy Ni atoms and the light Al and O atoms. This comes with trade off that the crystallinity and structure of the alumina support is much harder to observe.

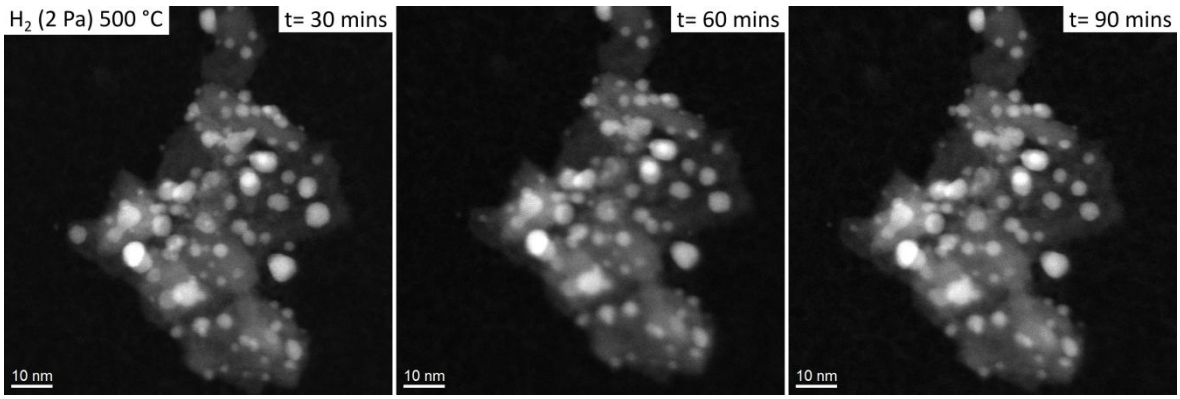

Figure 6. 7: Ni/Alumina sample under 2 Pa H_2 at 500 °C after 30 minutes (left), 60 minutes (centre) and 90 minutes (right). Little change in the Ni species is observed after the first 30 minutes.

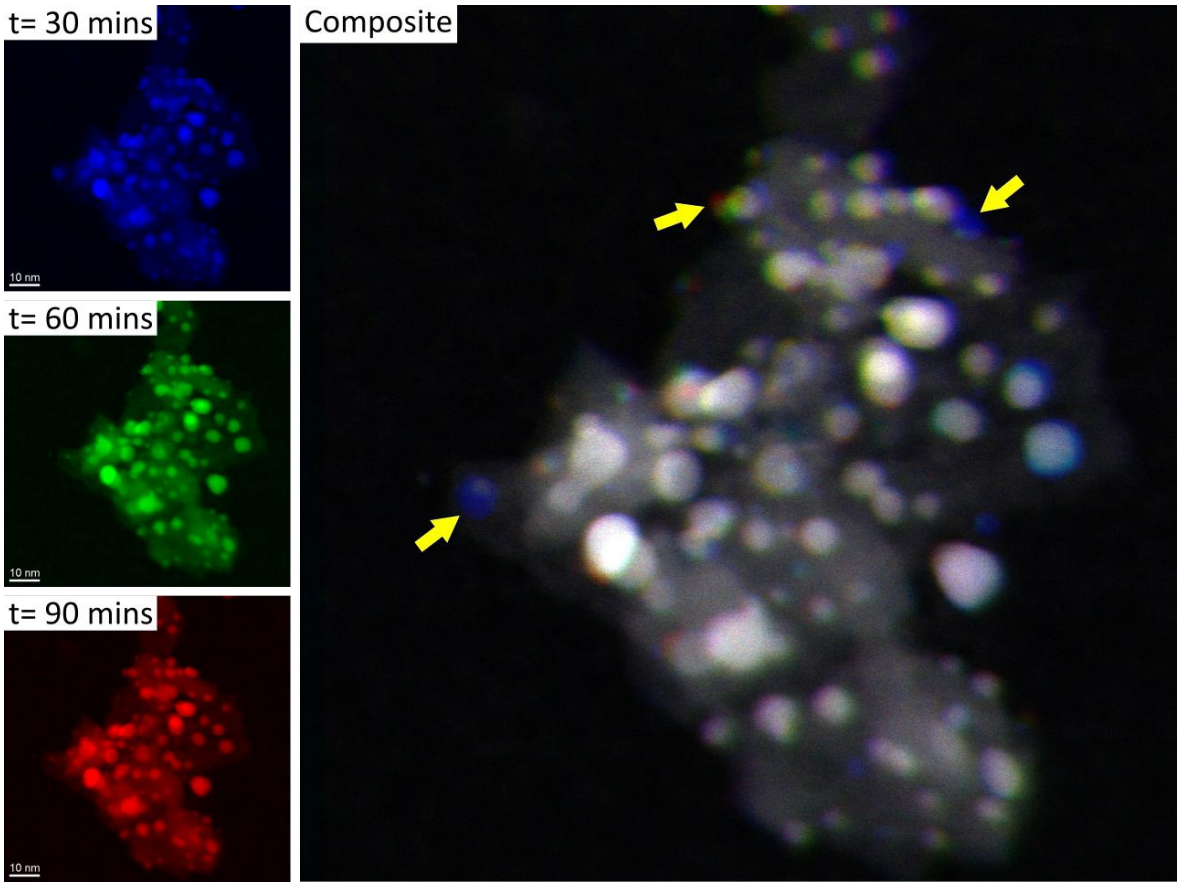

Figure 6. 8: Colourised and composite micrographs of the Ni/Alumina sample after 30, 60 and 90 minutes exposure to reducing conditions. Yellow arrows highlight the few instances of mass transfer during prolonged exposure to H_2.

Figure 6.8 shows a composite of the images shown in figure 6.7. The remaining colour in the composite image corresponds to changes with respect to time. The yellow arrows in

figure 6.8 highlight that, while some migration of the Ni species is observed after 30 minutes, it does not lead to the formation of larger particles.

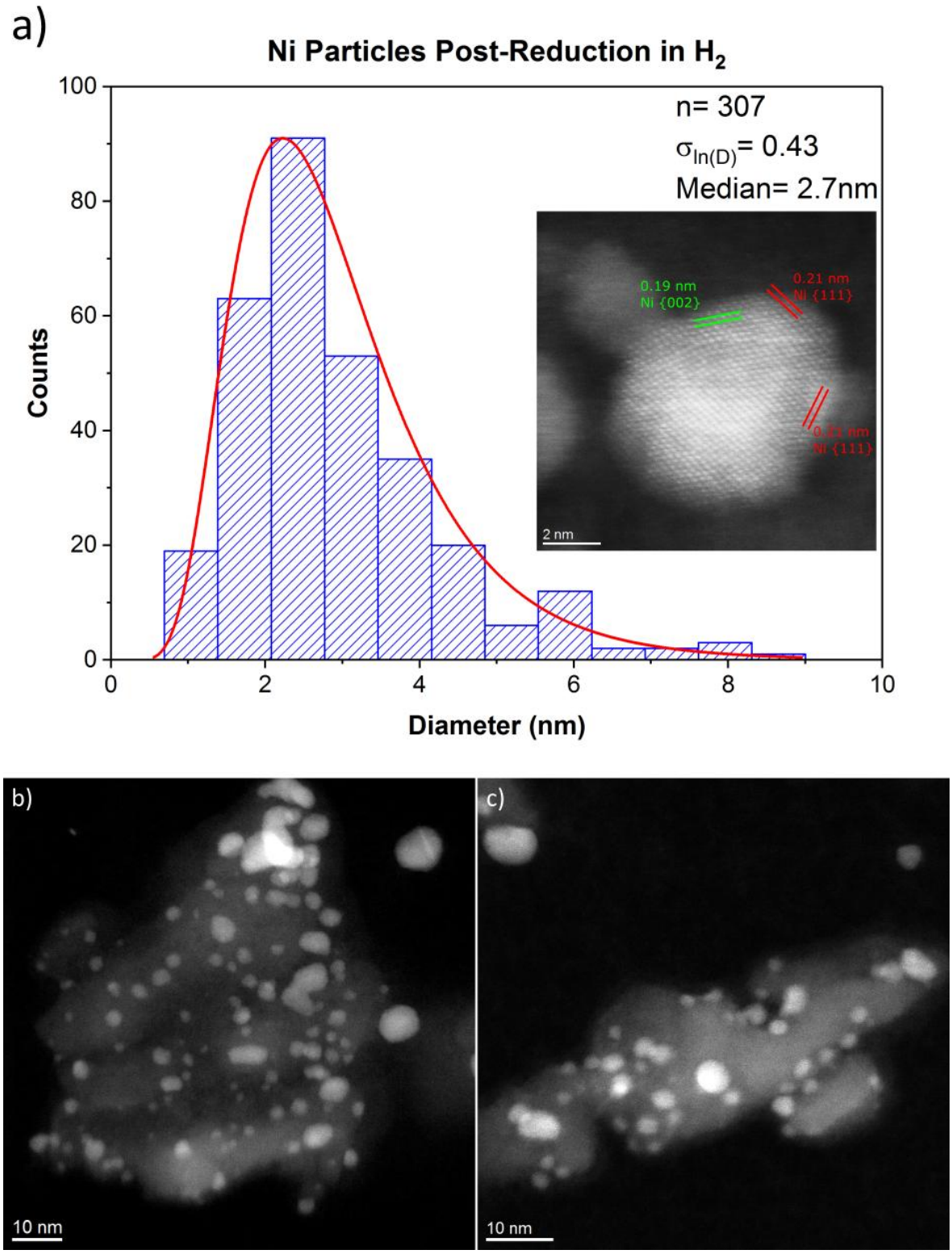

Figure 6. 9: a) nanoparticle size distribution after reduction at 500 °C, b) and c) in-situ HAADF-ESTEM micrographs of the reduced Ni/Alumina catalyst. The inset in a) shows a larger supported Ni particle partially tilted in the [011] orientation with inter-planar spacing consistent with metallic Ni.

Once it was confirmed that the Ni species had reached stability under the in-situ conditions the sample was cooled to 100 °C and the Ni size distribution was measured. The median Ni particle size was found to be 2.7 nm and followed a lognormal distribution. The inset in figure 6.9 shows that even the larger supported Ni nanoparticles have been fully reduced to the metallic active phase. Figure 6.9b and c give an overview of the Ni/Alumina system after reduction.

6.3.3 In-situ Oxidation

Under operating methanation conditions it is unlikely that the catalyst will be exposed to an oxidising environment. However, during plant maintenance exposure to air is difficult to avoid. As such it is of interest to see how the catalyst responds to oxidising conditions.

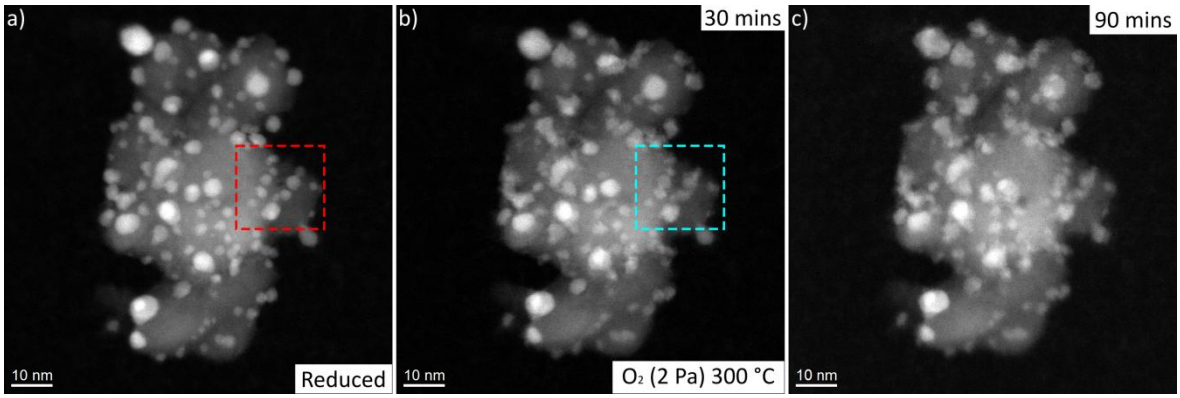

Figure 6. 10: HAADF-ESTEM image sequence of the Ni/Alumina sample after a) reduction and after exposure to O_2 at 300 °C for b) 30 minutes and c) 90 minutes. The coloured boxes highlight changes to the nanoparticle morphology during oxidation.

After the reduction detailed in the previous section samples were exposed to O_2 inside the E(S)TEM. From figure 6.10 it can be seen that the overall structure of the support remains unchanged. Meanwhile the Ni is oxidised and deformation of the nanoparticle shape is seen. This is consistent with the volume expansion that accompanies the Ni-NiO transition (discussed in chapter 5). Under 2 Pa of oxygen at 300 °C some of the particles show void formation and hollowing (see figure 6.11). This is consistent with observations of unsupported Ni given in the previous chapter.

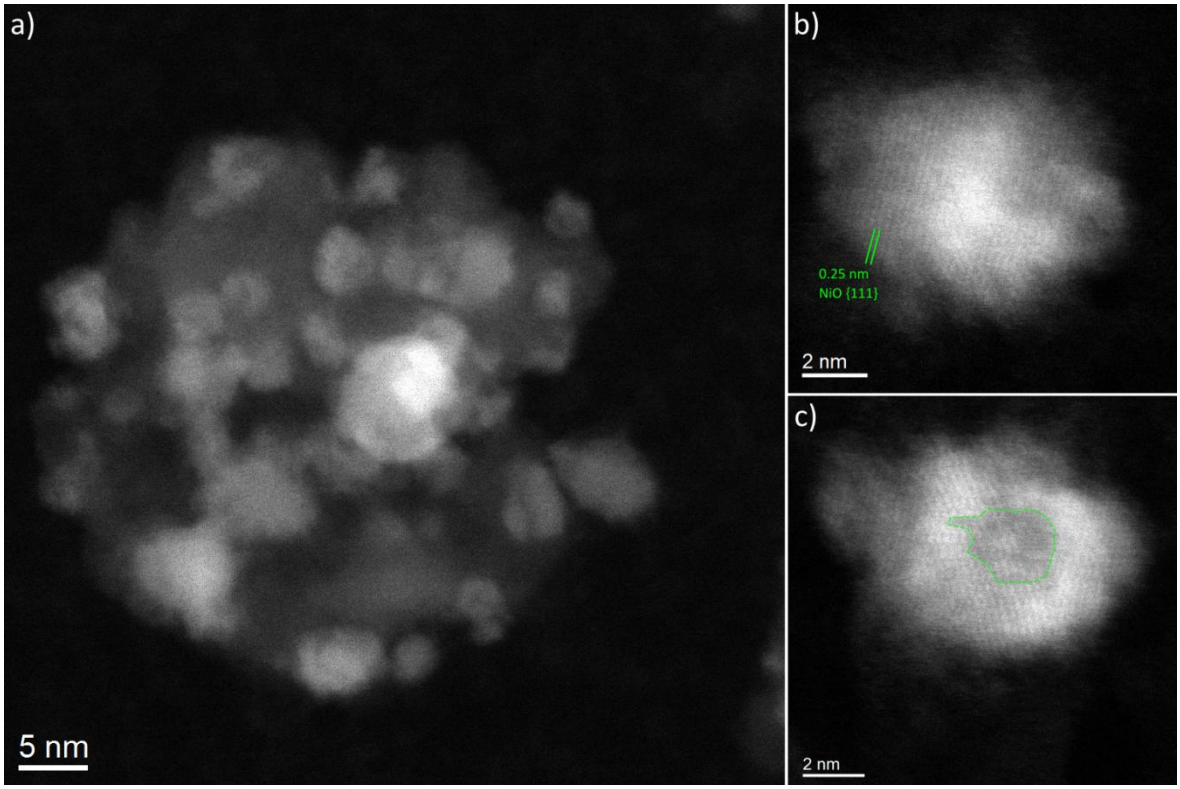

Figure 6. 11: After exposure to oxidising conditions at 300 °C void formation and hollowing can be observed in the oxidised Ni nanoparticles of the Ni/Alumina sample. a) Shows an overview while b) and c) show solid and hollow NiO nanoparticles respectively.

6.4 Ceria Promoted Ni/Alumina

As shown previously in figure 6.3, the crystallite size of the ceria promoter has a marked effect on the performance of the catalyst. The sample with the larger ceria size (Ni-Ceria(L)/Alumina) will be discussed first, followed by the smaller (Ni-Ceria/Alumina).

6.4.1 Ni-Ceria(L)/Alumina

The sample was prepared for ESTEM in the same way as the Ni/Alumina sample, as described in section 6.3, and given the same anti-contamination thermal treatment. Figure 6.12 shows XRD analysis, along with HAADF-STEM images of the as-prepared sample. The XRD scan shows the crystal features for NiO supported on delta-theta alumina with the additional peaks attributed to the ceria. STEM observations show the randomly orientated and overlapping crystals of alumina and a highly dispersed NiO species across the support. This is similar to figure 6.4 in section 6.3.1.

Upon in-situ reduction in H_2 at 500 °C for 30 minutes the NiO is converted to its metallic form and noticeable ripening is observed. A stable population of Ni nanoparticles is formed on the alumina support. This is highlighted in figure 6.13, showing an area of the sample pre and post-reduction. The transition observed here is directly comparable to that seen with the Ni/Alumina sample (figure 6.5).

The Z-contrast provided by the HAADF-STEM technique and the comparatively large lattice parameter of ceria aid in the identification of the ceria on the support. Figure 6.14 shows examples of ceria crystallites together with the supported Ni nanoparticles (identified by lattice spacing and EDS).

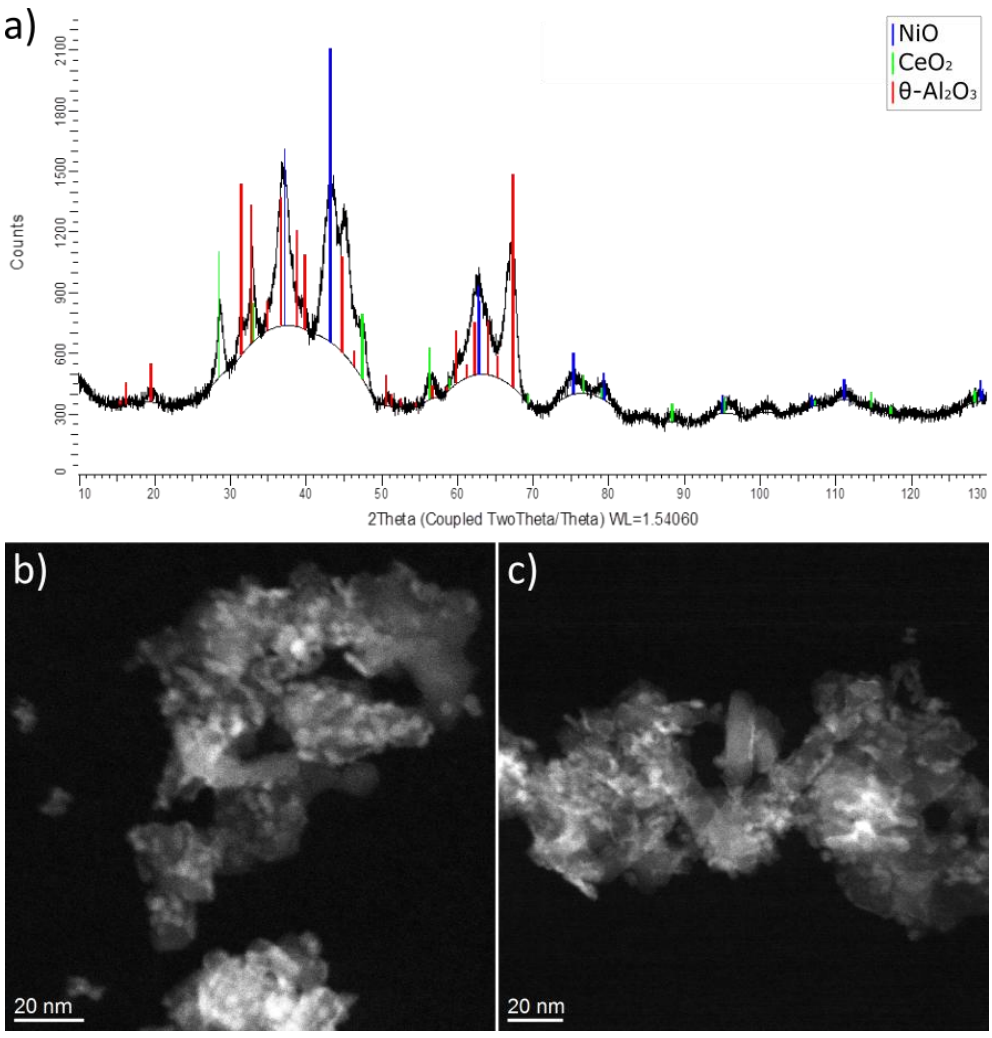

Figure 6. 12: Powder XRD analysis (a) showing additional peaks attributed to crystal planes in ceria. HAADF-STEM micrographs b) and c) showing the structure of the as-deposited Ni-Ceria(L)/Alumina sample. Note that the broad peaks below the XRD spectrum in a) are due to background from the powder sample holder.

The frequency of the ceria crystallites is consistent with the loading given in table 6.1, with only one or two ceria crystallites found per agglomeration of supported sample, and

many were observed without ceria promotion. Interestingly, the ceria-Ni contact is very low, such that the sample can be more appropriately described as a Ni/Alumina catalyst with instances of Ceria/Alumina rather than Ni-Ceria/Alumina. In other words, the ceria does not support the Ni species. Despite this apparent lack of interaction the methane yield is twice that of the sample without promotion.

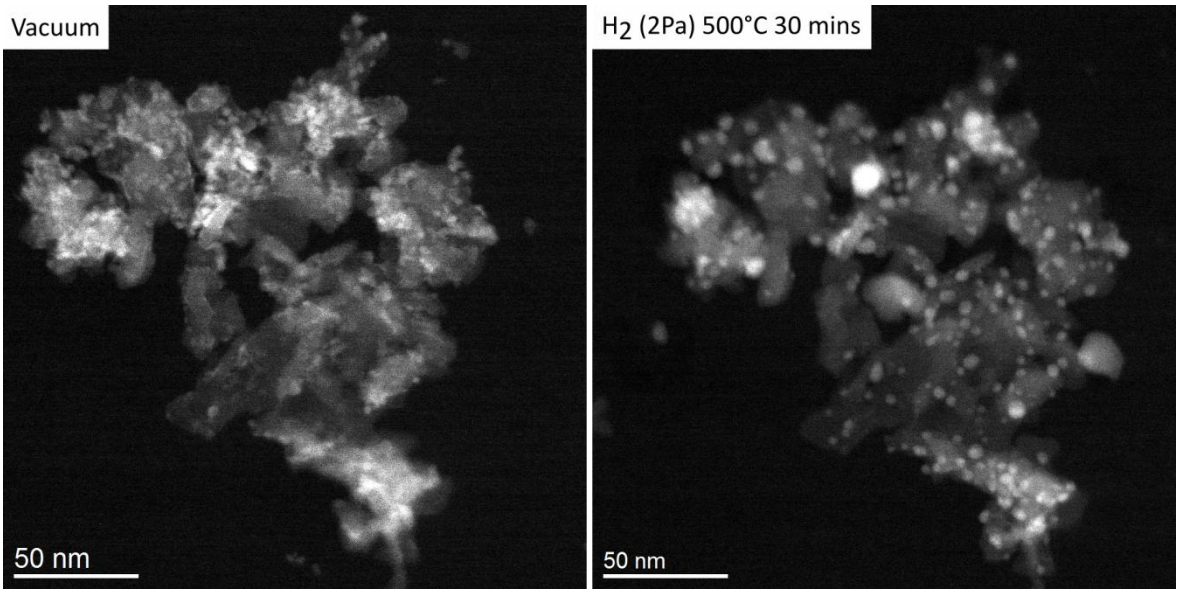

Figure 6. 13: HAADF-ESTEM micrographs from the same area of the Ni-Ceria(L)/Alumina sample before (left) and after (right) reduction at 500 °C for 30 minutes in H_2.

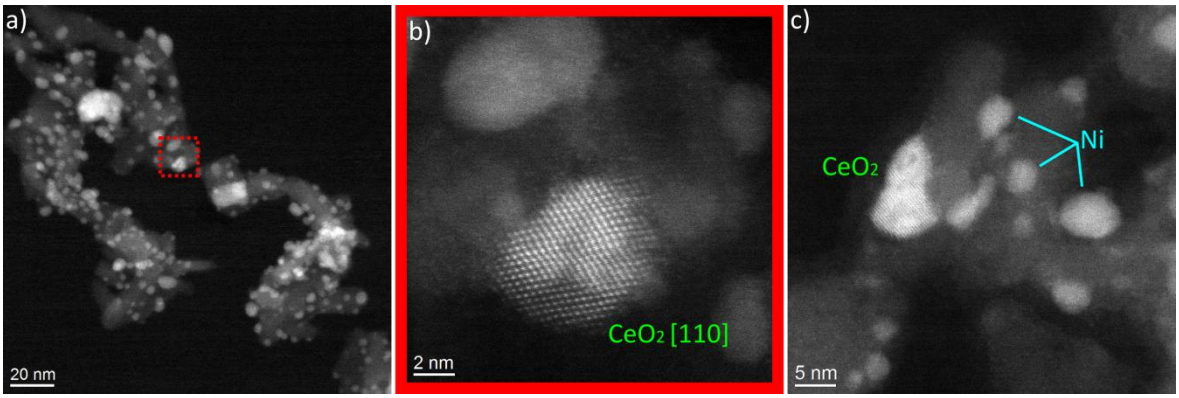

Figure 6. 14: HAADF-ESTEM micrographs of the reduced Ni-Ceria(L)/Alumina sample at low a) and high b-c) magnification. Figure b) is the area highlighted in a). Note the low contact between the ceria nanoparticles and Ni nanoparticles.

6.4.2 Ni-Ceria/Alumina

By changing the ceria precursor the form of the ceria species within the sample changed dramatically despite the same loading. XRD analysis, shown in figure 6.15, reveals the same NiO and alumina features that are common to the samples discussed thus far.

However, the characteristic peaks from the ceria are absent. A long (30 minute) EDS scan of a small area using an SEM of the powder sample confirms the presence of cerium.

Initially, the absence of the ceria peaks in the XRD analysis would suggest that either: the ceria crystallites are too small to be detected by the XRD or the ceria is amorphous in nature. The HAADF-STEM images in figure 6.16 of the as prepared sample show the same highly dispersed NiO species on the support.

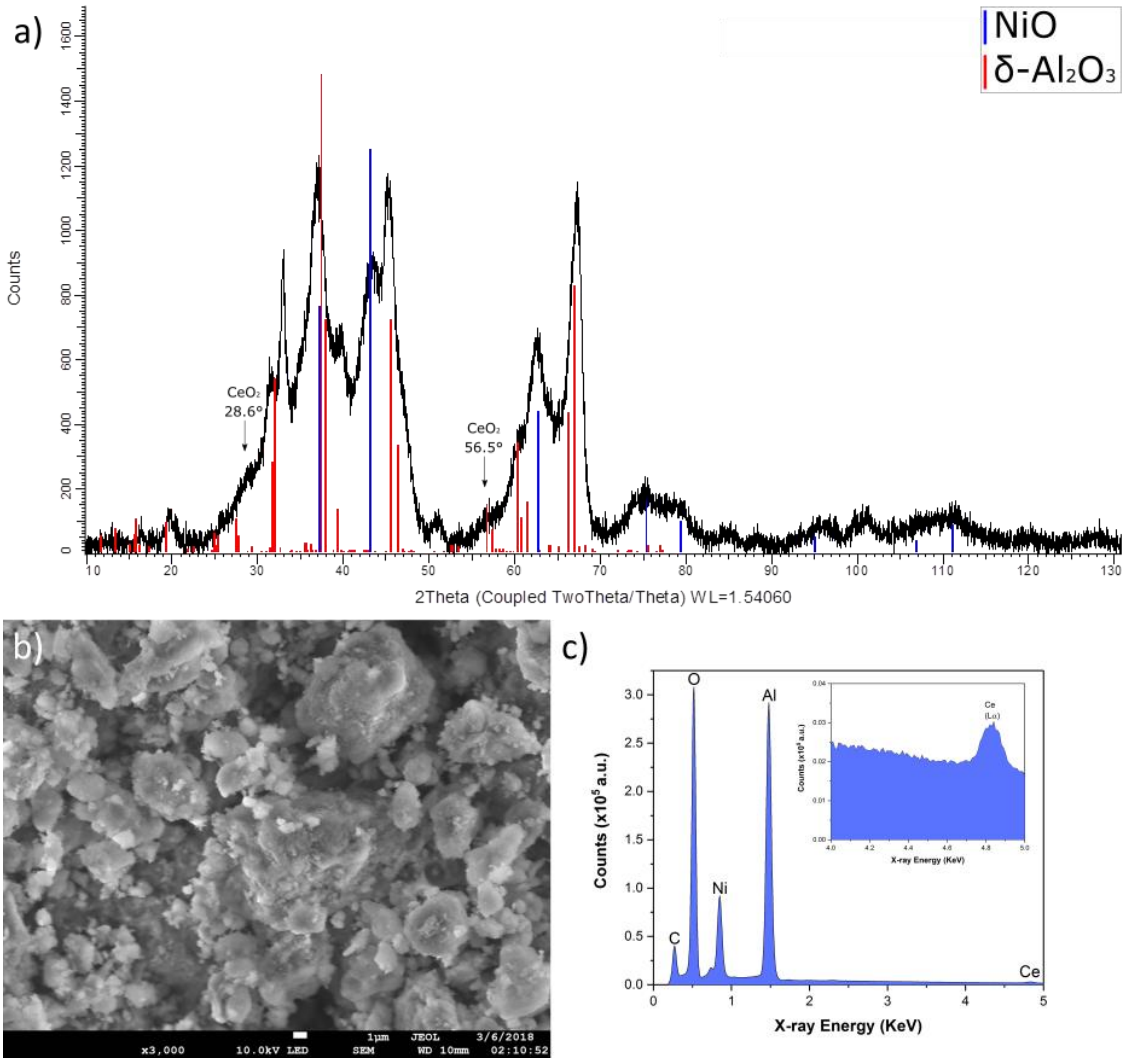

Figure 6. 15: a) XRD scan of the Ni-Ceria/Alumina sample; the missing reflections of ceria are marked for reference. SEM was used to confirm the presence of a cerium containing species, where b) shows a secondary-electron image and c) a 30 minute EDS acquisition (the inset shows the energy range of the Ce L-alpha line).

Upon reduction (H_2 500 °C for 30 minutes) the Ni species reduced to its metallic phase and ripened to create a stable population of nanoparticles. This behaviour seems common to all of the alumina supported catalyst samples studied here. Indeed the Ni particle size distribution (see figure 6.17) is not dissimilar to that of the Ni/Alumina sample.

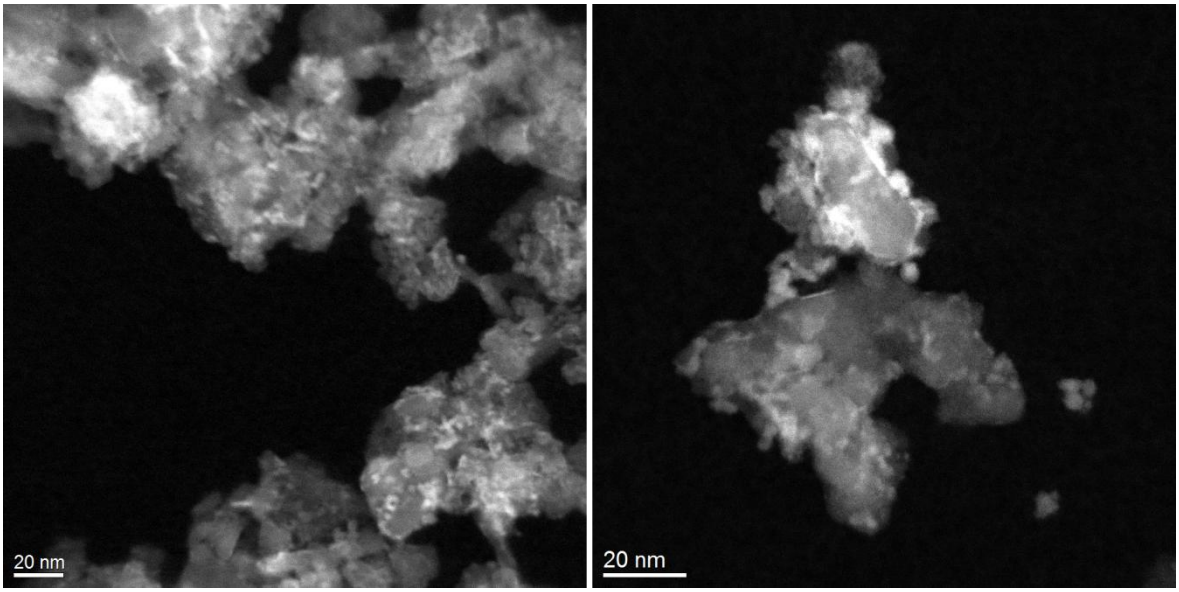

Figure 6. 16: HAADF-STEM micrographs of the as-deposited Ni-Ceria/Alumina sample.

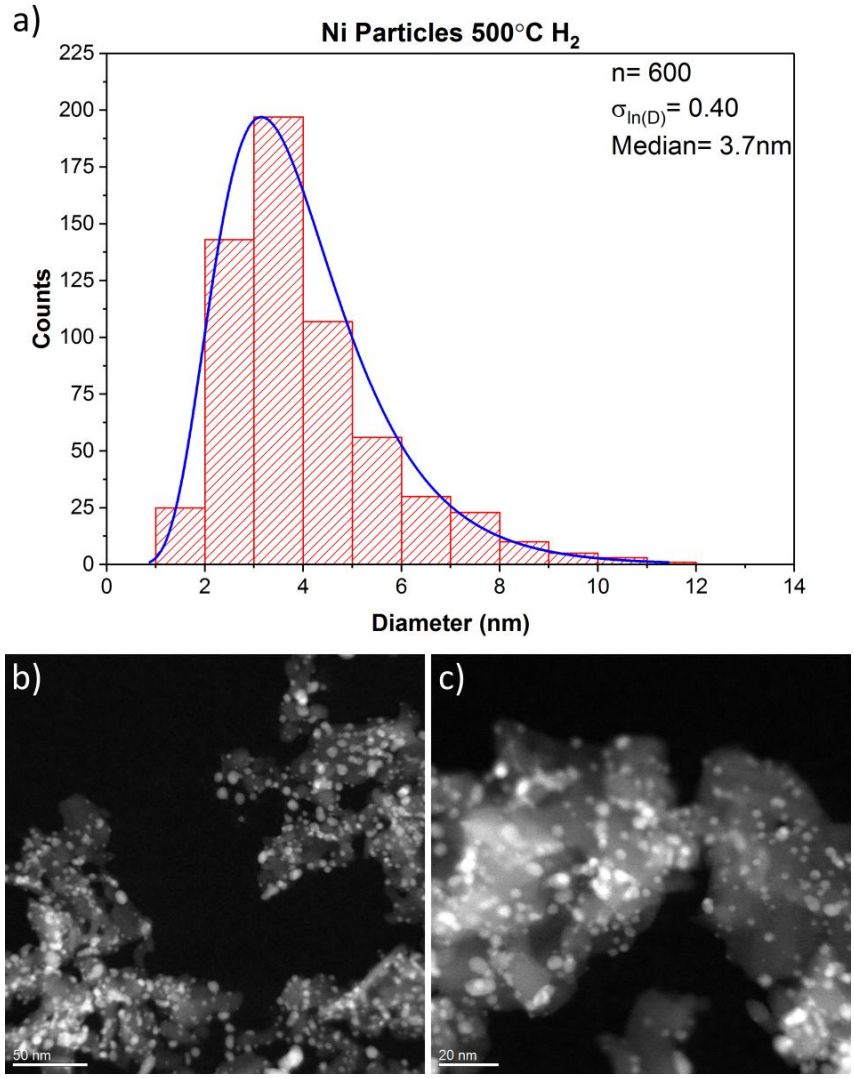

Figure 6. 17: Ni particle size distribution a) and HAADF-ESTEM micrographs b) and c) of the Ni-Ceria/Alumina sample, post-reduction.

In contrast to the previous sample (Ni-Ceria(L)/Alumina), ceria nanoparticles were not observed. This was despite checking many sample areas across different windows of the MEMS chips (equivalent to ~10^2 μm^2 search area). High magnification HAADF-ESTEM was able to resolve a population of ~0.2 nm species on the surface of both alumina and Ni. Figure 6.18 shows false coloured images to highlight this atomic-scale population on the sample. This species appeared to be evenly distributed across the sample (not on the carbon support).

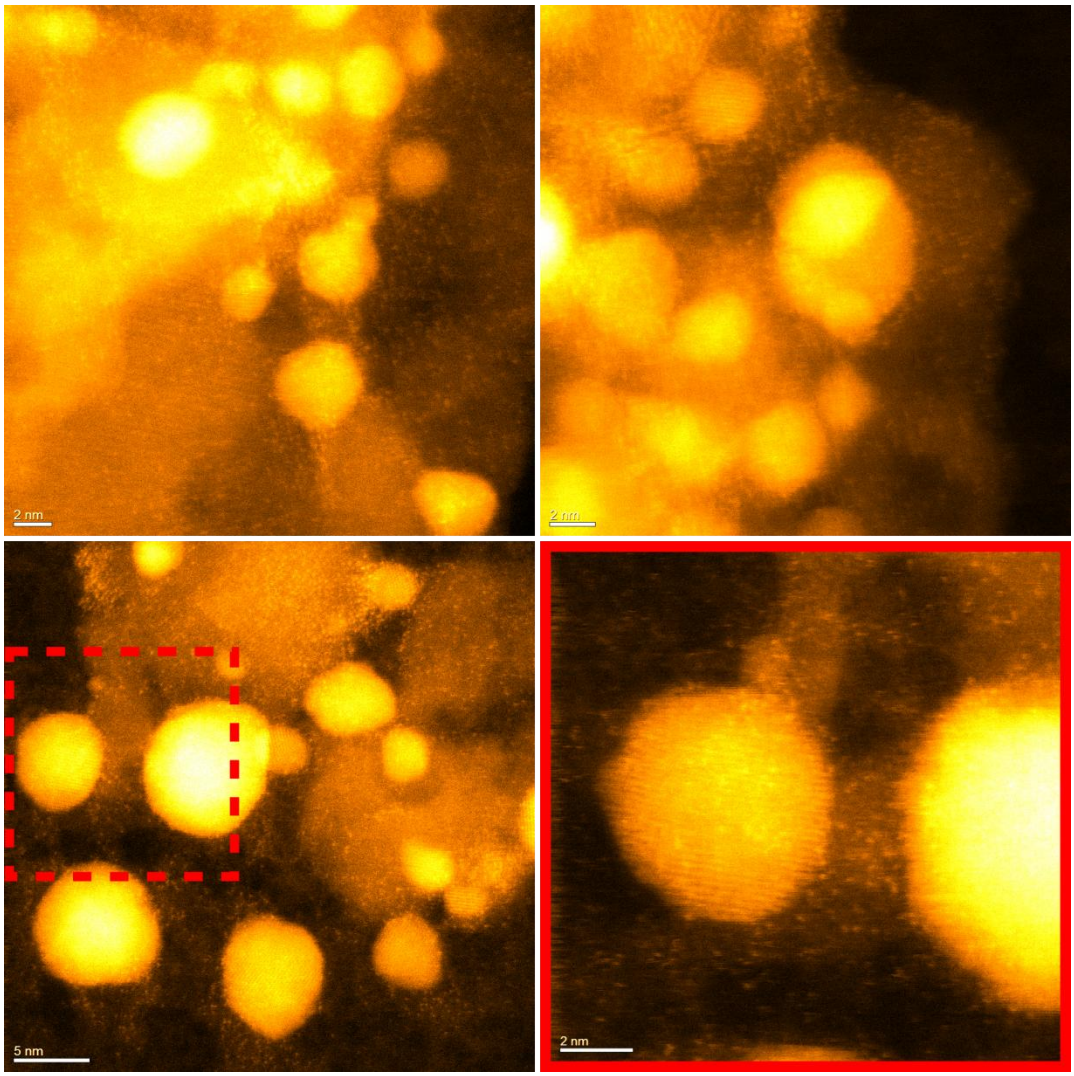

Figure 6. 18: False coloured HAADF-ESTEM micrographs of the reduced Ni-Ceria/Alumina sample with a population of ~0.2 nm species visible on the support. The bright image intensity of this species is due to high Z-contrast compared to the surrounding material.

The atomic-scale species highlighted in figure 6.18 are present in the sample pre-reduction and appear to remain constant despite the ripening of the Ni species under reducing conditions. Observations of the Ni/Alumina and Ni-Ceria(L)/Alumina samples

after reduction at atomic resolution do not show a similar population. A comparison between the samples is given in figure 6.19.

Combining the observations that: a cerium containing species is present in the sample, any ceria species is too small or too disordered to appear during XRD observation, an atomic scale species unique to this sample and no obvious ceria nanoparticle species even using HAADF-STEM suggests that the ~0.2 nm species is composed of ceria. Due to the close proximity to the alumina it is reasonable to conclude that it is indeed ceria (albeit oxygen deficient and possessing uncertain stoichiometry (CeO_{2-x})) and not metallic cerium. This is because of the abundance of oxygen at the surface of the alumina and the high temperatures (~730 °C) required to begin the reduction of ceria [215]. Furthermore, at this size the cerium atoms are almost certainly in the Ce^{3+} [216] state which is much more reactive than the Ce^{4+} state of the filled CeO_2 lattice. In further discussions (at the end of the chapter) this species will be referred to as "atomic scale ceria" since the terms atomic, amorphous or clusters are not necessarily true in this case.

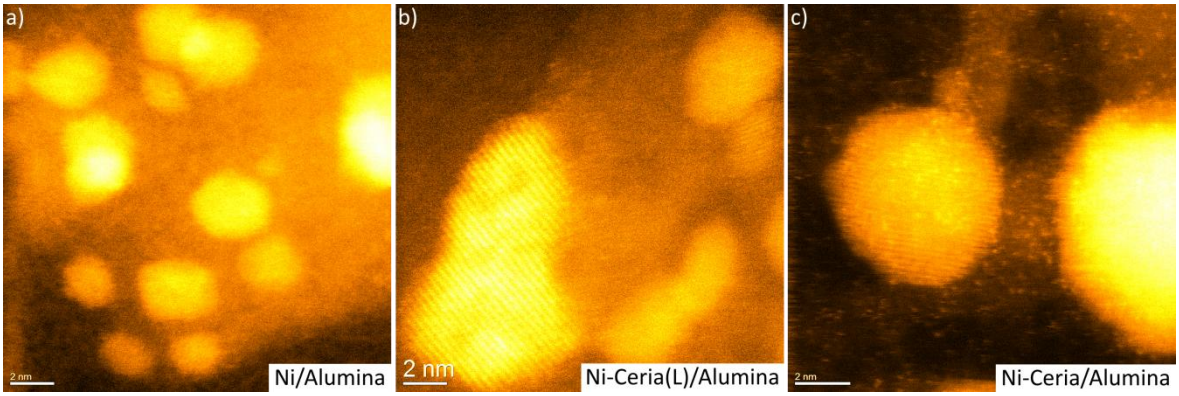

Figure 6. 19: False coloured HAADF-ESTEM micrographs of the a) Ni/Alumina, b) Ni-Ceria(L)/Alumina and c) Ni-Ceria/Alumina samples after the same reduction treatment. The ~0.2 nm dispersed species only appears in the Ni-Ceria/Alumina sample.

6.5 Ni/Ceria

From the methanation activity data (figure 6.3) it is clear that the Ni/Ceria sample performed the worst of all of the samples tested. Figure 6.20 shows the XRD analysis and TEM images of the as-deposited sample. The support consisted of ~5 nm crystallites of ceria. However, the closely packed ceria crystallites made it almost impossible to determine, with any certainty, the form of the Ni species. The images in figure 6.20 clearly

show that the phase contrast is dominated by the ceria, which has a larger lattice parameter.

In order to study the interaction of the Ni species with the ceria support, a simplified model system was created. The new sample was prepared in exactly the same way as the Ni/Ceria sample, except that the ceria was calcined at 1000 °C for 6 hours prior to impregnation with the Ni precursor. This treatment led to extensive sintering of the ceria crystallites such that the ceria size was much larger than the Ni nanoparticle size.

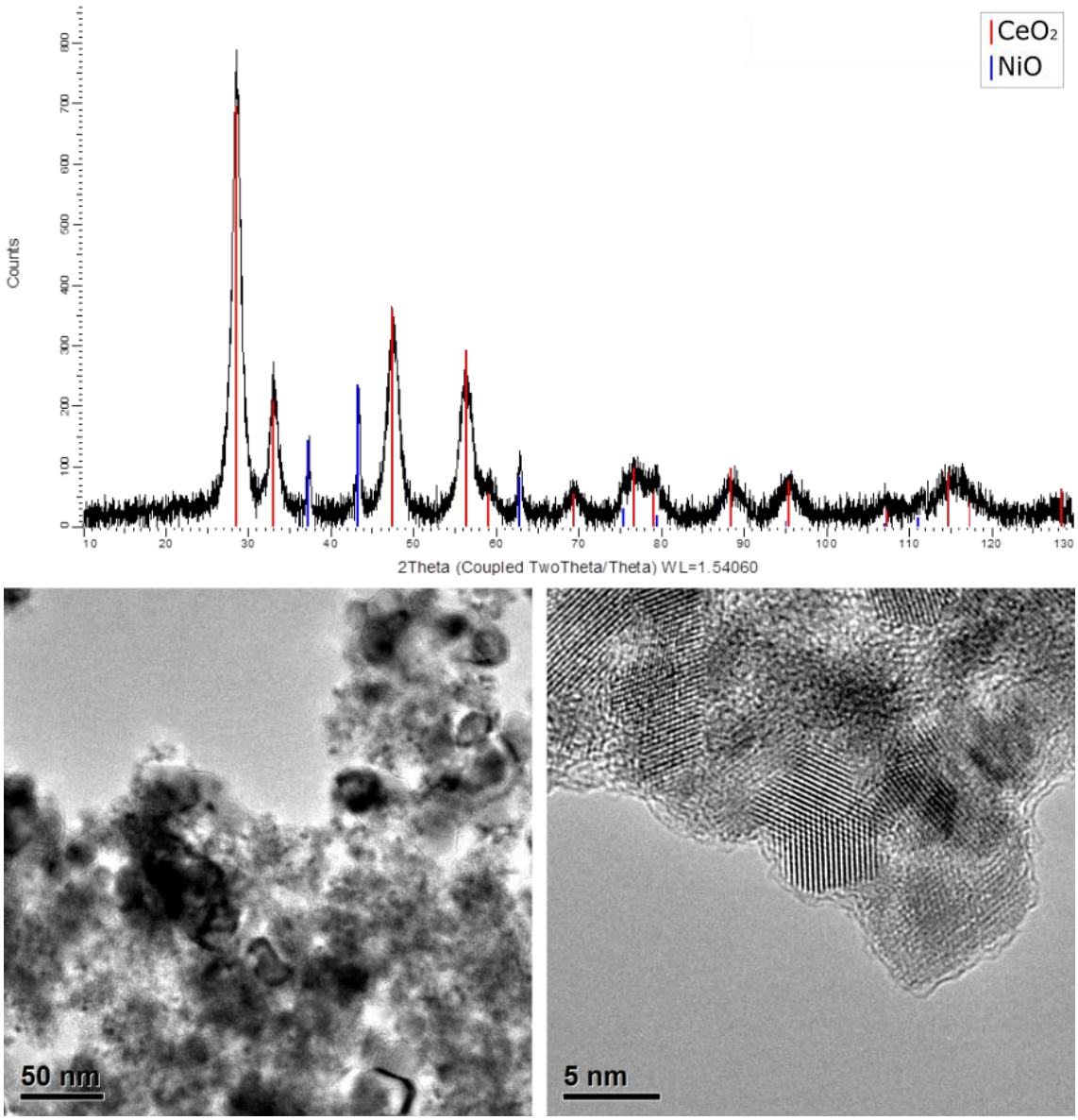

Figure 6. 20: XRD analysis (top) and TEM micrographs (bottom) of the as-deposited Ni/Ceria sample.

The new sample was reduced under H_2 (P=2 Pa) at 500 °C for 30 minutes. HAADF-ESTEM images are shown in figure 6.21. The calcined ceria crystallites took the form of quadrilateral polyhedra and exposed large (111) surface facets. The observed

morphologies and exposed facets agree with the results presented by Agarwal et al [217] for ceria octahedra. This shape preferentially exposes (111) surfaces which show the highest stability and least reactivity for the cubic fluorite structure.

Under these reducing conditions the NiO is reduced to Ni metal. However, the Ni nanoparticles are larger than those shown on the alumina based samples presented in the earlier sections. Furthermore, a large proportion of the Ni appears to de-wet the ceria and instead form Ni nanoparticles (larger than those supported by the ceria) on the carbon support. This can be seen at the left and right of figure 6.21 where there is Ni in close proximity to the ceria support. Figure 6.22 shows EDS spectra of the different regions of the specimen.

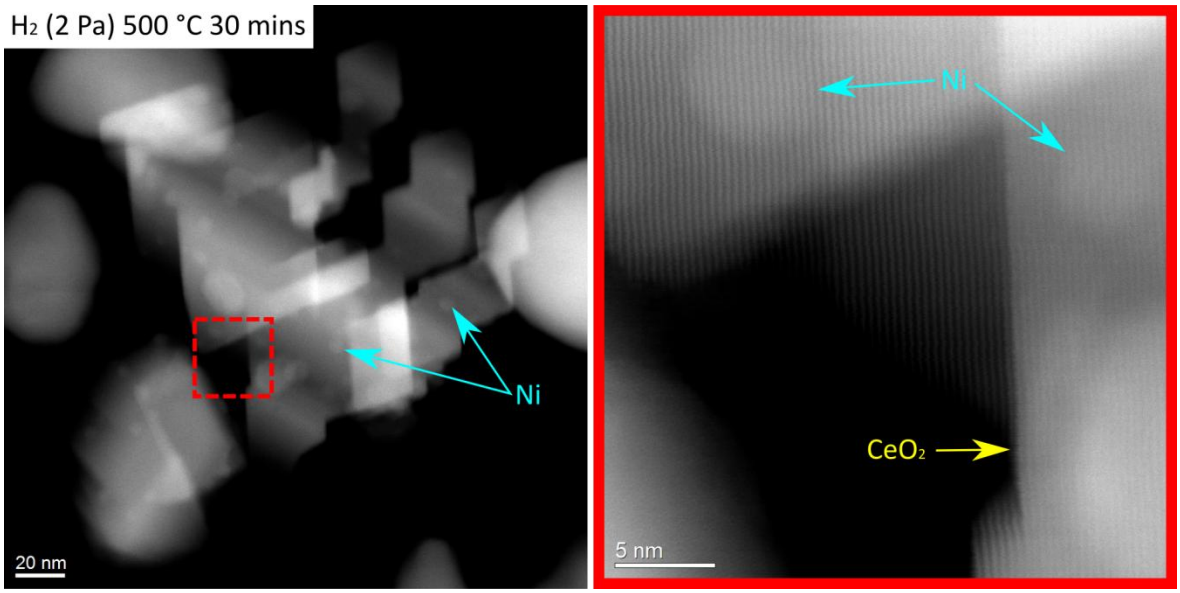

Figure 6. 21: HAADF-ESTEM micrograph showing crystallites of ceria. Ni nanoparticles can be seen on the support but there is also a large amount of un-supported Ni present in the sample. The right hand image is from the red area highlighted showing the (111) surfaces of the ceria.

The large amount of unsupported Ni and the larger Ni nanoparticle size appear to be the cause of the poor catalytic activity of the Ni/Ceria sample. Additionally, the larger ceria crystallites probably contain less oxygen vacancies than the smaller ceria species seen in the previous samples. In order to check if oxidising conditions altered the Ni-ceria interaction, the sample was exposed to O_2 (P=2 Pa) at 300 °C for 40 minutes. HAADF-ESTEM images and EDS spectra, see figure 6.23, show that the Ni nanoparticles on the surface behave in a similar way to unsupported and alumina supported Ni. The majority of the nanoparticles form core-shell Ni-NiO, while the rest show void formation, see figure 6.24. Some research groups suggest that under similar conditions the ceria support

can cover the surface of the Ni and prevent oxidation [218, 219]. However, no evidence of this can be seen from these experiments.

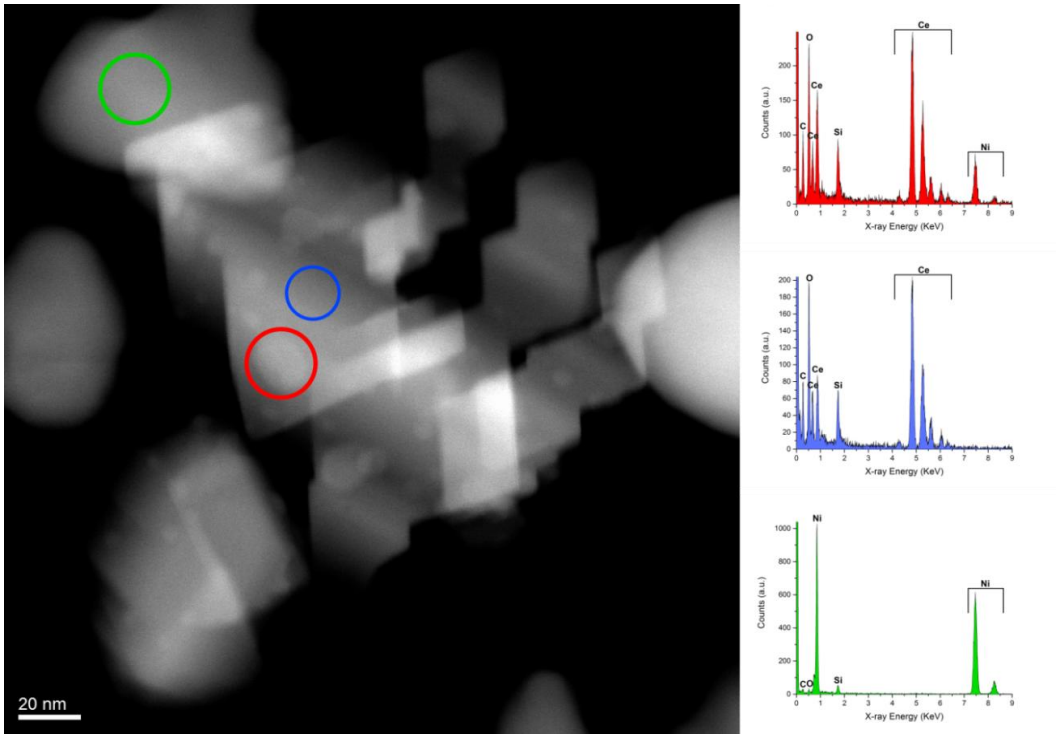

Figure 6. 22: HAADF-ESTEM micrograph of the reduced sample. The coloured circles mark the areas for the corresponding EDS spectra. The large un-faceted regions are made of Ni supported on the carbon film.

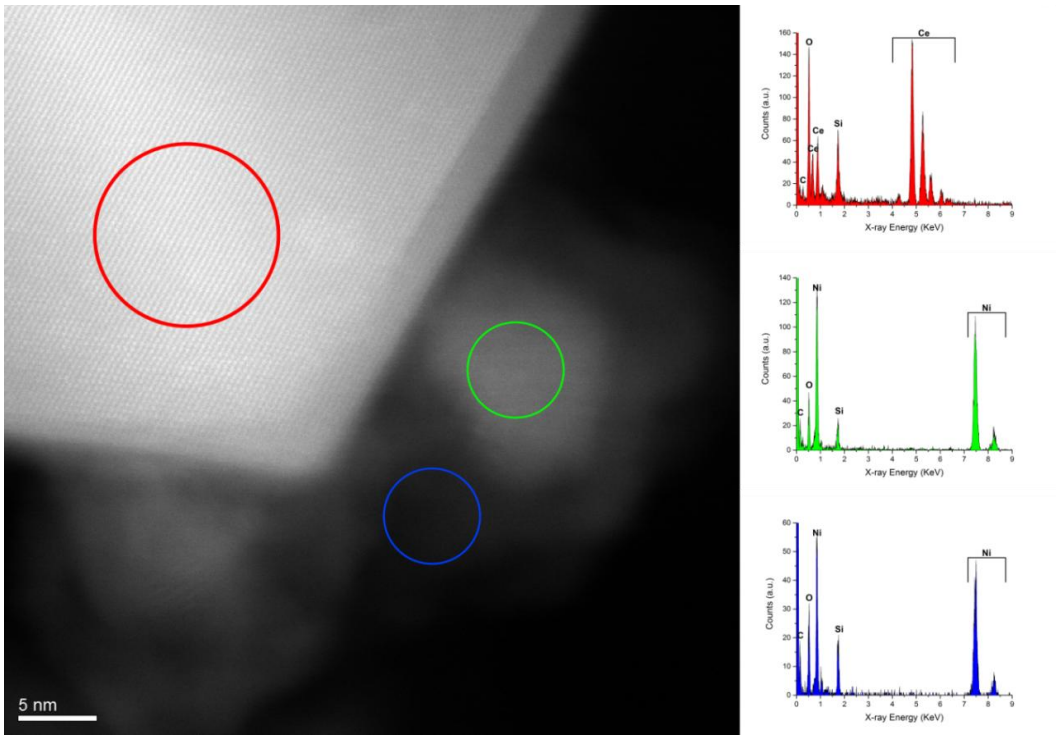

Figure 6. 23: HAADF-ESTEM micrograph of the oxidised sample. The coloured circles mark the areas for the corresponding EDS spectra. Red marks the ceria support, green the Ni nanoparticle and blue the NiO shell. No ceria is observed at the nanoparticle surface.

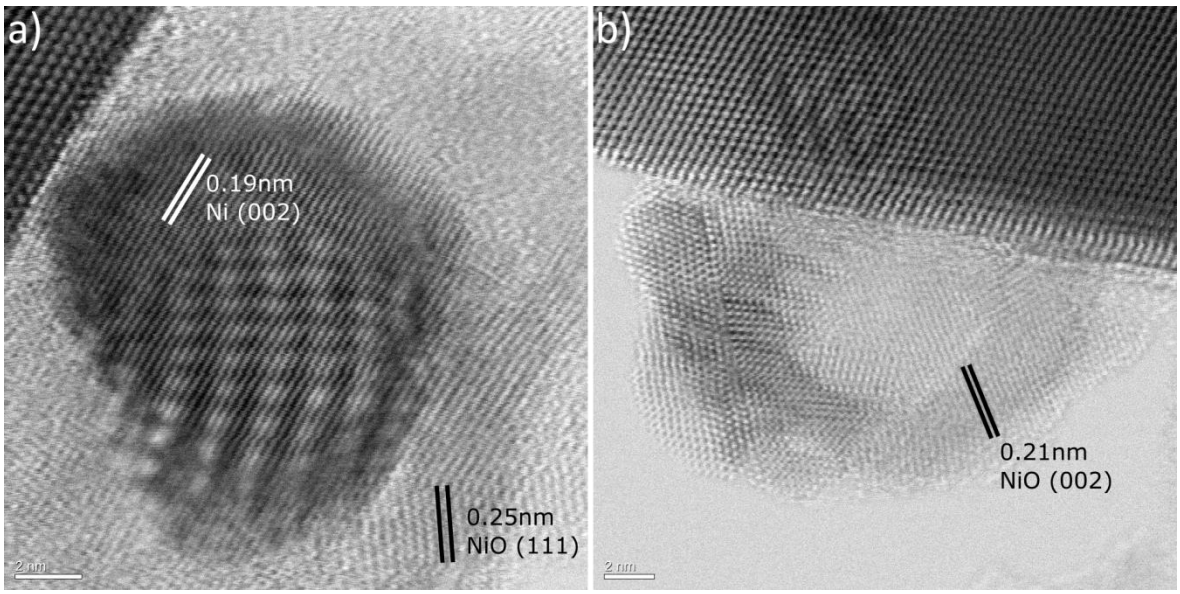

Figure 6. 24: BF-ESTEM micrographs of core-shell a) and hollow b) nanoparticles supported by the ceria. The Moiré fringes in a) are due to overlap of Ni and NiO lattice fringes.

6.6 XPS- Electronic Effects of Ceria Promotion

In order to determine whether or not the ceria promoter affected the electronic properties of the Ni (and by extension affect the interaction between adsorbed species) XPS measurements were performed on the Ni/Alumina and Ni-Ceria/Alumina samples[2].

The powder samples were placed in separate ceramic boats and inserted together into a stainless steel tube furnace. The samples were baked at 200 °C for 1 hour under 10 mbar of H_2 and then cooled under vacuum. The XPS system used for the measurements described here was not an in-situ system and this baking treatment was performed to replicate the sintering of the Ni species observed in-situ.

Binding energy calibration was performed with reference to the C1s peak at 284.8 eV and energy scale verified with the Al_2O_3 O1s peak at 531.1 eV. Both samples showed charging effects that varied with time and so repeated scans (survey and high resolution) were aligned before averaging and correction. A high resolution scan of the Ni 2p range is shown in figure 6.25.

[2] XPS measurements were provided by Mr. P. Bentley and Dr. A. Pratt, University of York.

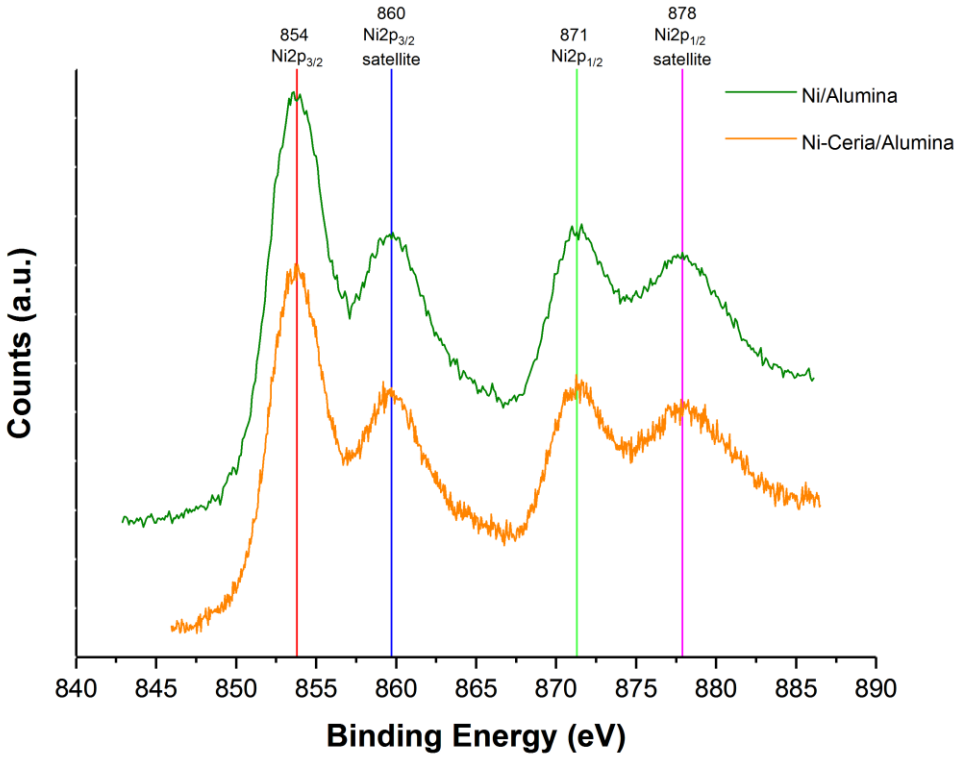

Figure 6. 25: XPS scan showing the Ni 2p peaks for the Ni/Alumina and Ni-Ceria/Alumina samples. The red, blue, green and purple lines show the peak positions of the Ni-Ceria/Alumina sample.

The XPS spectra show the spin-orbit splitting of the Ni 2p orbital. Pronounced satellite peaks are observed, these are indicative of oxidised Ni (either NiO or $Ni(OH)_2$) and are expected due to exposure to air. Figure 6.25 clearly shows that the Ni peak separation and FWHM are consistent between the two samples. While a more rigorous and, ideally, in-situ investigation is needed for a fully quantitative analysis, the results presented here suggest that there is no significant change to the electronic character of the Ni between promoted and un-promoted samples.

6.7 Chapter Discussion

The production of highly active, selective and long lasting catalysts for industrial chemical processes is a highly complex endeavour. Even for a single chemical reaction under predefined reaction conditions, the catalyst design is a highly complicated matrix of inter-dependent parameters that have huge implications. The catalyst synthesis, pre-treatment, metal loading, promoter, active surface area and thermal stability greatly affect the yield, efficiency and efficacy of a particular catalyst system. However, the origin

of these catalytic augmentations lie at the nanoscale and as such the importance for in-situ techniques that probe the structure-property relationships at this scale cannot be over stated. In this chapter, a number of Ni based catalyst samples were investigated using in-situ E(S)TEM to correlate their enhanced methanation activity with changes in the nanostructure.

To simulate the activation process of commercial catalysts, the samples were reduced using H_2 gas. During the in-situ reduction at 500 °C all of the samples studied show fast (< 30 minute) reduction to the metallic phase. The reduction was accompanied by sintering of the Ni species which was not observed when heated under vacuum. This suggests an enhanced mobility of the Ni atoms when exposed to H_2. This is most likely due to a combination of: a change in the metal support interaction during reduction as anion vacancies are introduced during the reduction, and Ostwald ripening of the highly dispersed Ni species.

The high surface area of the alumina and its ability to preserve a small particle size distribution in the Ni mean that it is a far superior catalyst support compared to the ceria. However, the promoter effects of ceria are significant even at low weight percentages. Using the un-promoted Ni/Alumina sample as a reference it was found that the ceria had no significant effect on Ni reducibility or size. All of the samples showed complete reduction of the Ni to the metal phase within 30 minutes and the size variation of the Ni was not significant between the un-promoted and promoted samples. Indeed a much smaller size distribution would be required of the promoted system if the catalytic enhancement were due purely to Ni surface area or density of surface sites. Furthermore, the sample containing large ceria crystallites showed minimal contact between the Ni and ceria species while still presenting a significant increase in the methane yield.

By eliminating the effect of ceria on the reducibility, stability and Ni-CeO_2 interaction, it is reasonable to suppose that the ceria provides its own active sites during the methanation reaction. It has been shown previously [216] that, as the size of ceria nanoparticles decrease, the surface density of oxygen vacancies increases. This leads to a higher concentration of Ce^{3+} cations (compared to Ce^{4+}). Given that the promoter effect of the ceria appears to increase as the ceria crystallite size decreases it is proposed here that it is the Ce^{3+} ions that are the active species. The atomic scale ceria observed in the Ni-Ceria/Alumina sample providing a higher number of Ce^{3+} sites per unit area of the catalyst

surface. The mechanism that these observations support is that CO_2 can form reaction intermediates by bonding with a Ce^{3+} and filling the oxygen vacancy. This preferential adsorption of the carbon oxides (CO and CO_2) onto the ceria allows the Ni to more effectively adsorb and dissociate the H_2 to form $2H^+$ [211, 212]. The migration of the activated hydrogen species across the support can then be explained by hydrogen spill-over [220, 221]. The hydrogen spill-over effect also explains the promoter effect on the sample containing larger ceria, where there is less direct contact between the Ni and the ceria. Indeed hydrogen spill-over and transport has been demonstrated on spatially separated Co and Pt nanoparticles on a silica support [222, 223].

Chapter 7

Nanoparticle Evolution Using E(S)TEM

Having investigated the effect of redox conditions on Ni catalysts supported by alumina and ceria, it is useful to compare a different metal species on a common support. In this chapter, an alumina supported Pd catalyst is investigated using ESTEM. These results are compared with other supported Pd systems and then contrasted against the Ni/Alumina system presented in the previous chapter. The chapter ends with a note on the continued modification of the York JEOL 2200FS ESTEM. The benefits of nano-diffraction are highlighted in the context of probing the nanostructure of nanoscale features in a low dose/ low signal regime. Hopefully, this note will encourage development along these lines for future projects with this instrument.

7.1 Palladium Based Catalysts

Catalyst systems based around Pd and PdO nanoparticles are used for a number of industrial chemical reactions [224]. Pd and PdO are used in methane oxidation [225], supported Pd/Silica catalyses the hydrogenation of cyclic compounds such as benzene and cyclohexene [226] and of aromatic ketones[227]. Pd/Alumina (with and without Ceria promotion) is known to be an active catalyst for NO reduction with CO [228]. The interaction of Pd with Pt produces unique nanostructures such as Pt surface clusters on PdO for diesel oxidation catalysis [229, 230] and Pt-Pd core shell nanoparticles for the oxygen reduction reaction in proton-exchange membrane fuel cells [231]. A key area of investigation concerning Pd and PdO catalysts is deactivation through loss of catalytic surface area due to sintering. ETEM has already been employed to good effect to

investigate the sintering of Pd/Silica-Alumina catalysts [232] and supported Pd model systems [32, 233].

Pd metal takes on the FCC structure with lattice parameter a=0.38898 nm, while the most common oxide, PdO, is tetragonal with lattice parameters a=0.3043 nm and c=0.5337 nm. Thus, any transition between the two phases requires a significant rearrangement of atoms within the crystal. Reduction of PdO is thought to occur via the growth of a Pd core inside of PdO particles, although many studies have suggested that metallic surface species play a significant role [225]. Oxidation of Pd is generally agreed to take place via a surface nucleation process. Oxygen is adsorbed on the surface of the metallic Pd, the restructuring of the crystal lattice is facilitated by the formation of intermediate Pd-O structures at the surface which then transition to the PdO phase. Intermediate structures include amorphous PdO and ordered Pd_2O [234].

7.1.1 Pd/Alumina- Model Catalyst

In this section in-situ ESTEM is used to investigate the evolution of Pd nanoparticles in a supported Pd/Alumina catalyst[3] relevant to JM. The catalyst was created by incipient wetness impregnation of a powder alumina (delta/theta) support using a palladium-nitrate ($Pd(NO_3)_2$) solution. The resulting powder was then dried and calcined in a manner outlined in chapter 6. The catalyst, which contained 3 wt% Pd metal, was dispersed in deionised water and drip cast onto a carbon MEMS chip for ESTEM analysis.

In order to remove carbonaceous contamination and mitigate its occurrence the sample was briefly heated in vacuum similar to the ESTEM samples described in chapter 6. Figure 7.1 shows the fresh sample. XRD analysis confirms that the support is mostly delta alumina and that the Pd is present as palladium(II) oxide (PdO). The BF-STEM image shows that the support is composed of large overlapping crystallites with no obvious epitaxial relationship, similar to the Ni/Alumina catalyst from chapter 6. The corresponding HAADF-STEM images reveal that well defined nanoparticles are already present.

The presence of nanoparticles on the support sets the Pd-based sample in stark contrast to the Ni-based samples discussed earlier, in which nanoparticle formation was

[3] Catalyst sample and XRD were provided by Dr. L. Van de Water and JM.

concurrent with (and dependent upon) metal-oxide reduction. EDS (figure 7.2) of small selected areas was used to confirm that the nanoparticles observed in figure 7.1 were Pd/PdO and that no additional Pd-containing species were present on the support. The high magnification HAADF-STEM images in figure 7.3, confirm that the nanoparticles are indeed PdO and appear to be spherical in shape.

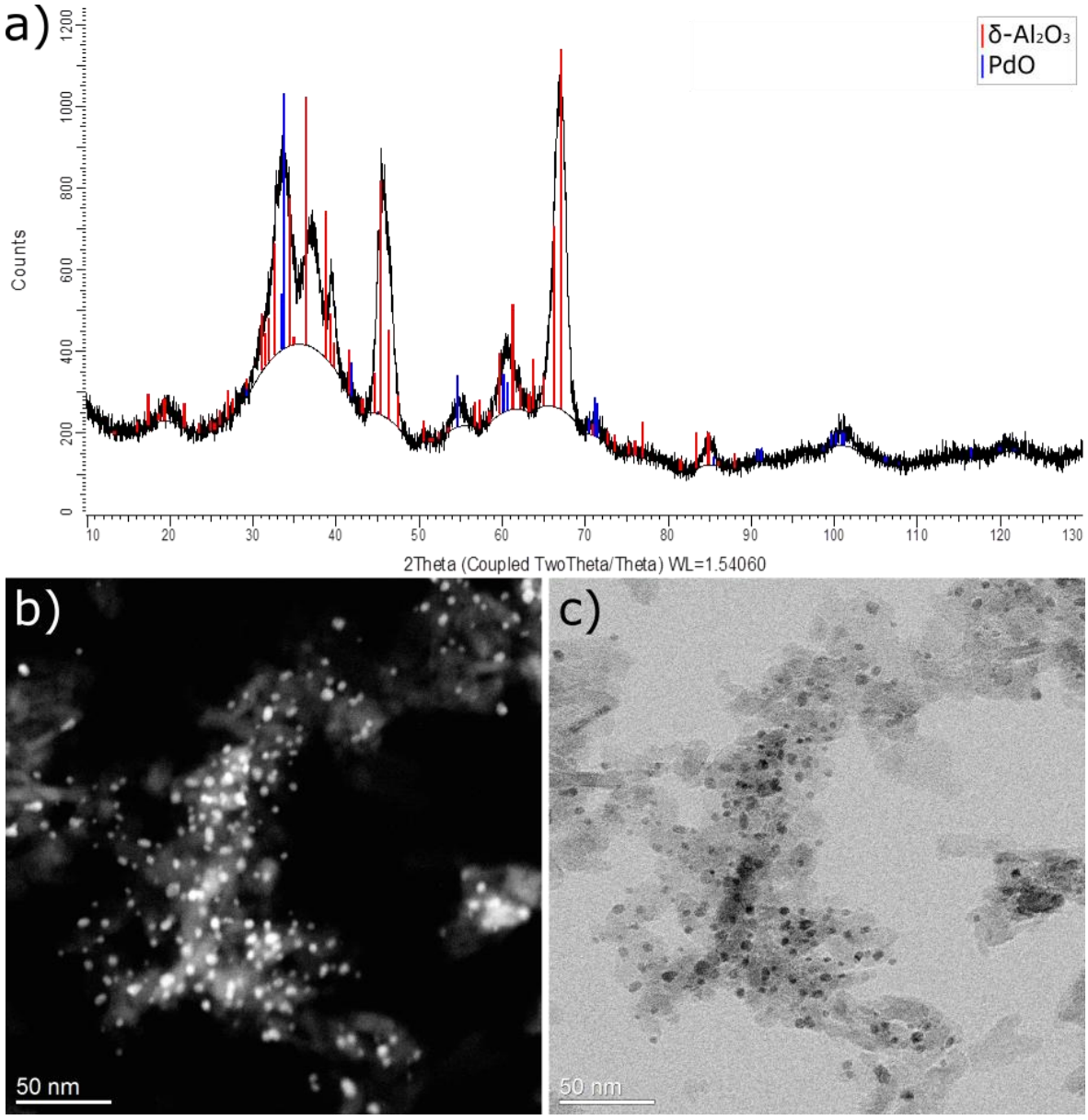

Figure 7. 1: XRD analysis a) of the fresh Pd/Alumina sample confirming the presence of delta alumina and PdO. The HAADF b) and BF c) STEM images show an overview of the fresh sample and that nanoparticles are already present.

The reduction was performed in-situ using H_2 at a pressure of 2 Pa. The specimen was heated to 500 °C for 30 minutes and then cooled prior to imaging and exposure to the electron beam. After 30 minutes negligible change was observed in the structure of the sample. The sample was left in a reducing environment for a further 30 minutes and the

temperature increased to 600 °C. Once again, no changes to the sample morphology were detected. Figure 7.4 shows an area of the specimen before reduction and after reduction at 500 °C and then 600 °C.

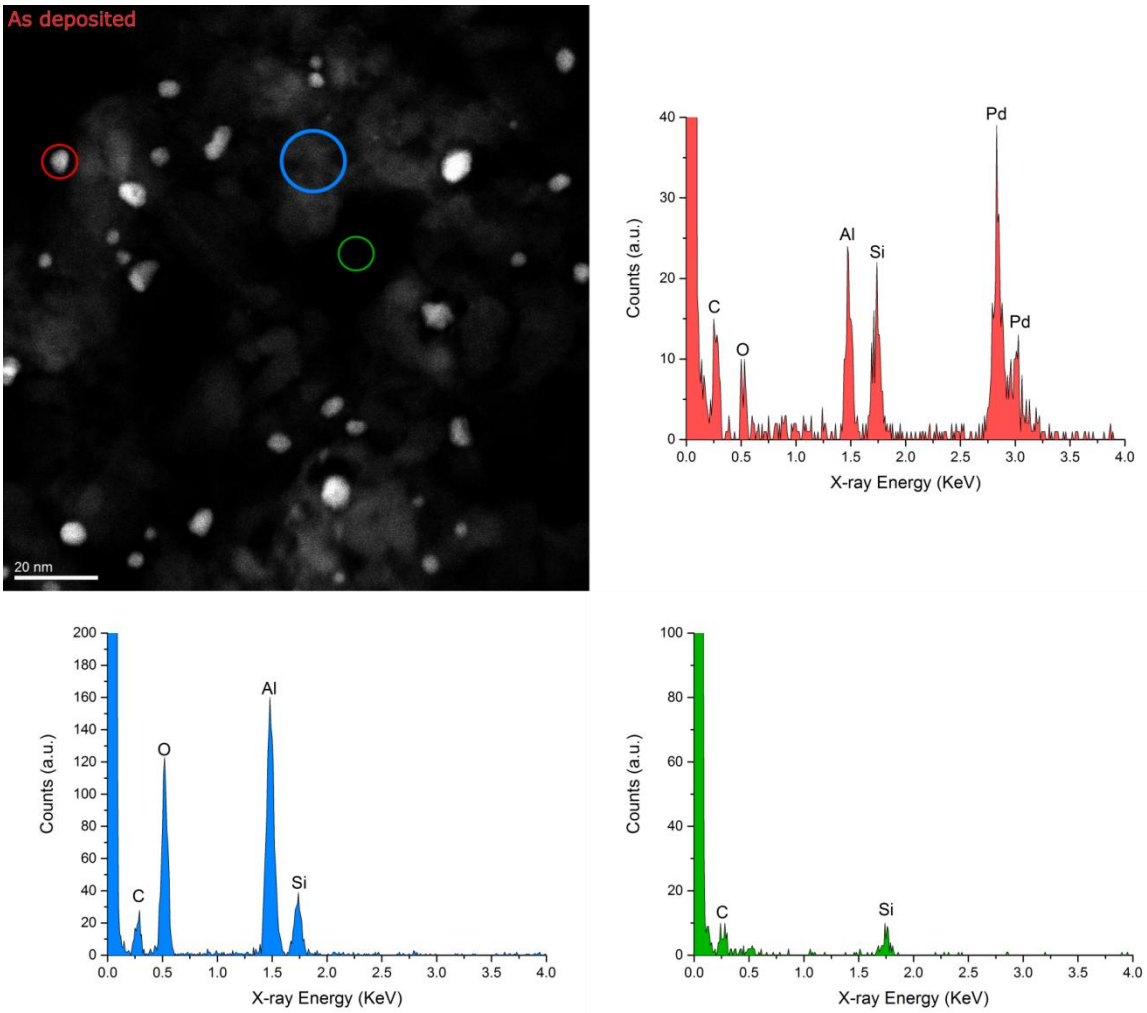

Figure 7. 2: HAADF-STEM micrograph of the fresh Pd/Alumina sample (scale bar= 20 nm). The EDS spectra are colour co-ordinated to the circles in the micrograph. EDS reveals that the Pd species is confined to the nanoparticles. Note that the Si peaks in the EDS spectra are produced by the MEMS chip.

Lattice measurements (see figure 7.5) and electron diffraction show that the PdO nanoparticles are not reduced to Pd metal under these conditions. The stability of both the oxide phase and spatial distribution of the nanoparticles on the support demonstrate the ability of alumina to preserve the surface area of PdO nanoparticles under reducing conditions.

Having confirmed that reducing environments at moderate reaction temperatures (500-600 °C) have no significant effect on the catalyst sample, an in-situ oxidation was attempted. The specimen was cooled to 60 °C and the beam blanked during gas changes.

O_2 was introduced into the microscope at a pressure of 2 Pa and the specimen heated to 300 °C for 30 minutes. The specimen was cooled to 60 °C prior to imaging.

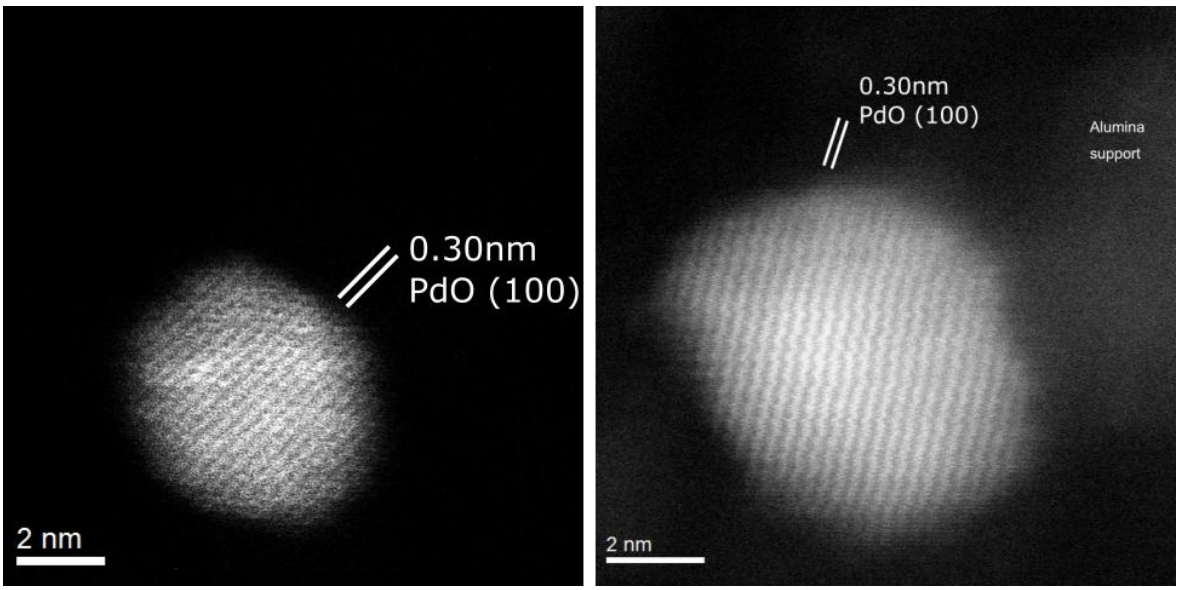

Figure 7. 3: High magnification HAADF-STEM micrographs of the nanoparticles in the Pd/Alumina sample; analysis of the lattice fringes confirms that they are PdO.

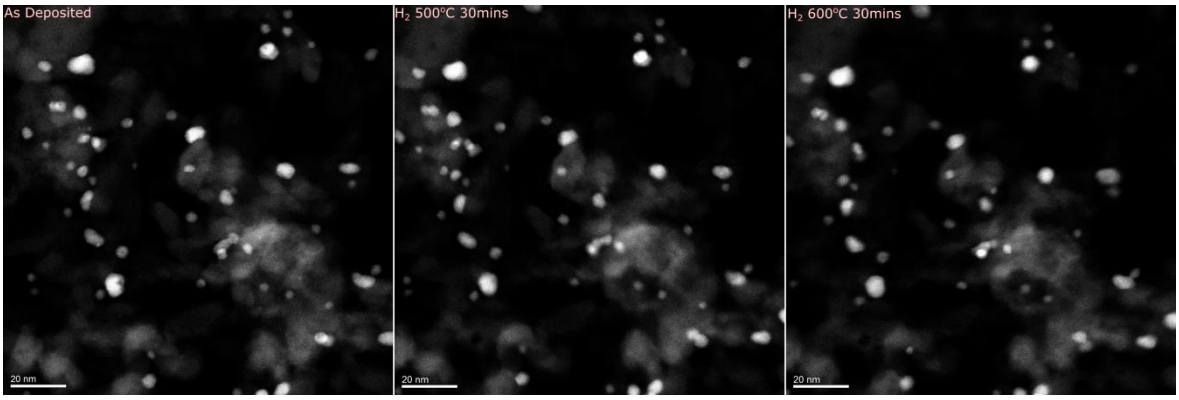

Figure 7. 4: HAADF-ESTEM micrographs showing an area of the PdO/Alumina sample pre-reduction (left), post-reduction at 500 °C (centre) and after subsequent reduction at 600 °C (right). The scale bar is 20 nm.

Figure 7.6 shows the state of the specimen after the in-situ oxidation. Large (>20 nm) agglomerates of PdO form on the alumina. No changes to the morphology of the alumina crystallites were detected. Interestingly, the sintering observed does not extend to all of the PdO nanoparticles and the majority of the original nanoparticles remain intact after oxidation. Particle size distributions for the fresh sample and post reducing/oxidising treatments are presented in figure 7.7. It should be noted that the agglomerates (PdO species greater than 20 nm in size) were discounted from the particle size distribution of the specimen post-oxidation. This was done because the nanoparticles that have not undergone any sintering are still representative of a catalytically active species. While the

formation of agglomerates is commensurate with a loss in turn-over frequency or general catalytic activity due to loss of surface area. Furthermore, the agglomerates range from ~20 nm to 60 nm across and are too infrequent to be counted with the same statistical accuracy as the data presented in figure 7.7.

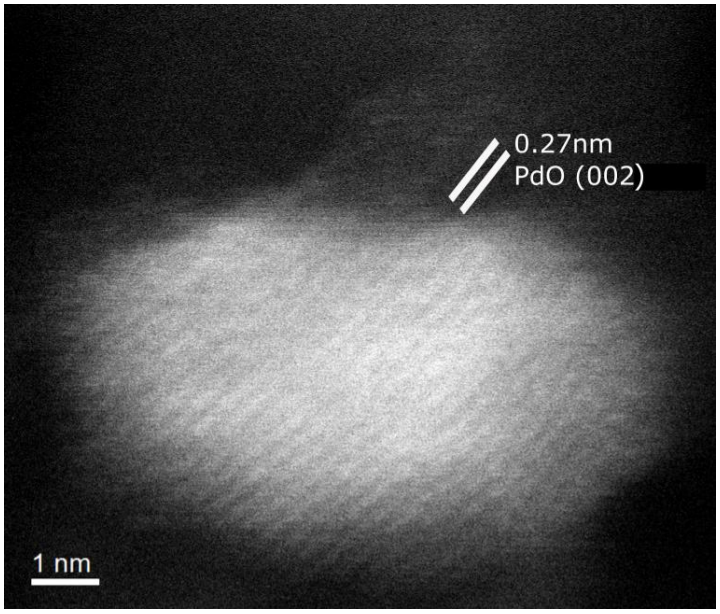

Figure 7. 5: High magnification HAADF-ESTEM micrograph of a nanoparticle on the alumina support after reduction at 600 °C. Lattice measurements confirm the nanoparticles have not undergone significant reduction.

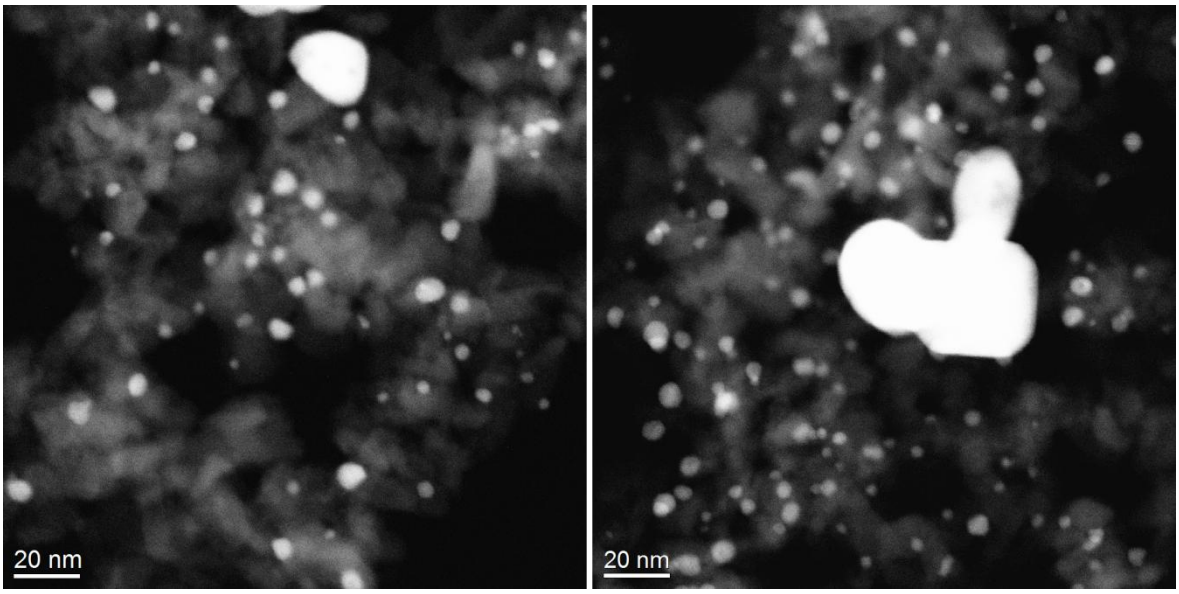

Figure 7. 6: HAADF-ESTEM micrographs of the PdO/Alumina sample after in-situ oxidation at 300 °C. Agglomerates of PdO can easily be seen on the alumina support.

Figure 7.7 reveals that the fresh sample contained PdO nanoparticles of median size 4.3 nm. Upon in-situ exposure to a reducing environment the nanoparticles did not reduce to Pd metal and the size only increased to 4.6 nm. After exposure to an oxidising

environment at an increased temperature, the majority of the nanoparticles remained unchanged and median size of 4.5 nm was calculated. In all cases the range of sizes that the distributions cover are very similar. After the oxidative treatment there is a discontinuity in the sizes after approximately 10 nm until around 20 nm which represent the agglomerates.

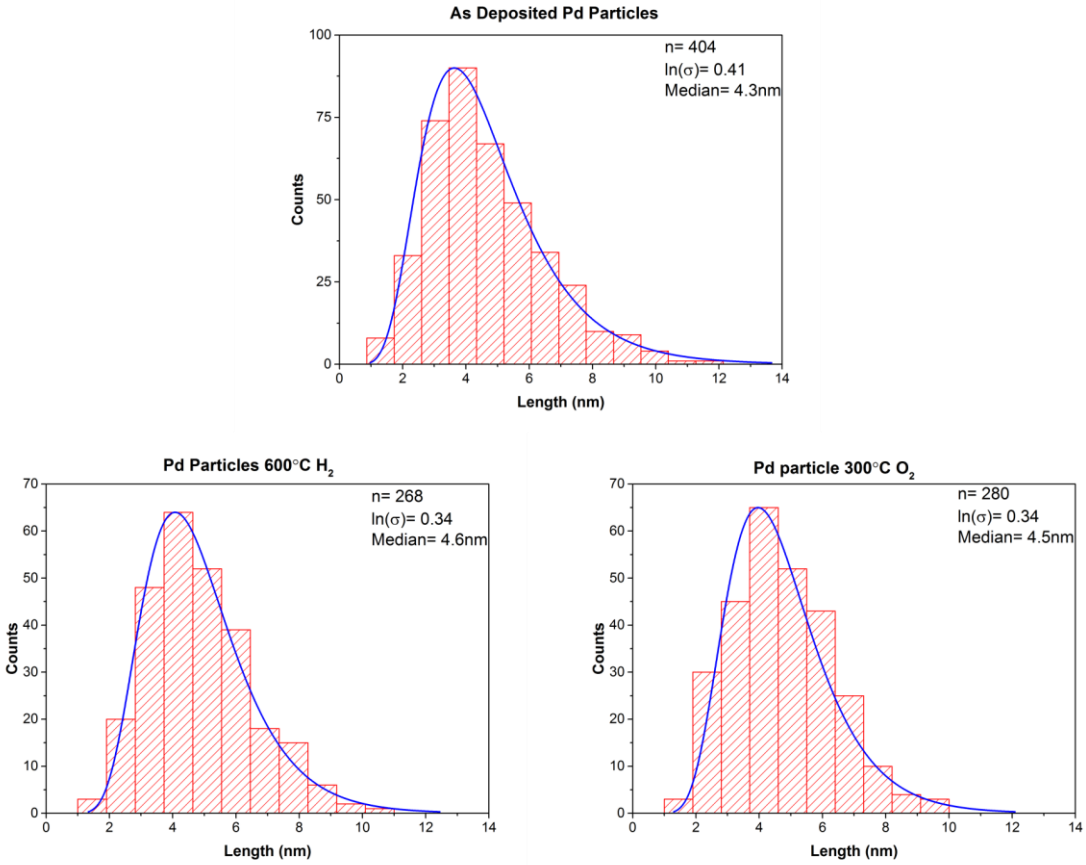

Figure 7. 7: Size distributions of the Pd-based nanoparticles in the PdO/Alumina sample. Distributions correspond to the fresh (top), 600 °C reduced (left) and 300 °C oxidised (right) sample. It should be noted that agglomerates are not represented in the oxidised particle size distribution (right).

Given that Pd metal is never observed, it is unlikely that any chemical or crystallographic change in the nanoparticles led to the sintering observed during O_2 exposure. Therefore, it is suggested that it is the interaction between the alumina support and the gas that leads to the deactivation of the PdO nanoparticles. It is possible that anion deficient sites, for example, Al terminated surfaces on the alumina support provide anchoring sites for the PdO species. This would increase the stability of the oxide phase of Pd and necessitate higher temperatures for reduction. This would also retard movement of the PdO along the alumina surface. However, these sites would become blocked when exposed to O_2 and thereby allow for increased mobility of the Pd species.

To conclude, the alumina support has proved to be a very effective catalyst support for PdO nanoparticles. The metal oxide-support interaction inhibits both reduction of the Pd species and deactivation by sintering under reducing conditions at moderate temperatures. Exposure to O_2 at these temperatures causes sintering and agglomeration of the PdO. While this effect is minor after a few cycles and with relatively low reaction times, it will nevertheless lead to significant loss of catalytic activity after prolonged exposure to oxidative reaction environments.

7.1.2 Pd/Carbon and Pd/Silica- Comparison

In the previous section, and to a lesser extent in previous chapters, the mobility of nanoscale species is affected by the reaction conditions and the interaction of the mobile species with the support. Here Pd nanoparticles on amorphous carbon and silica supports are presented for comparative purposes.

The carbon support that was used was a standard Cu mesh TEM grid with a 3.5 nm thick amorphous holey carbon film. The silica (SiO_2) support was an 8 nm thick amorphous silica membrane supported on a silicon nitride mesh (shaped as a 3 mm diameter disc for a standard TEM sample rod). Both supports were purchased from Agar Scientific. The Pd nanoparticles were deposited by magnetron sputtering using a JEOL JFC-2300HR fine coater with a Pd metal target. Pd was sputtered until the piezoelectric thickness monitor indicated 0.5 nm. To ensure consistency, all of the samples were batch sputtered i.e. all of the supports had Pd deposited onto them at the same time. All supports were at the same lateral distance from the sputter head and separated from each other by less than 2 cm. Theoretically this meant that Pd material arrived at each support surface in the same form.

Figure 7.8 shows BF-TEM images of the Pd/C and Pd/Silica samples after Pd had been deposited. The images were taken at the same magnification and the difference in the size of the nanoparticles is striking. Despite the fact that both samples were grown at the same time in identical conditions the Pd nanoparticles were larger on the silica substrate than on the carbon. During the sputtering process, metal atoms (or atomic clusters) are released from the metal target by momentum transfer from the plasma and travel ballistically to the substrates. This means that the Pd should arrive at the carbon and silica

surfaces in the same form. The difference in size is then due to the initial interaction between metal and support. Clearly significant rearrangement of Pd atoms occur on the silica support to produce larger, more rounded nanoparticles. This rearrangement is presumably driven such that the surface free energy per particle is minimised. At high magnification the contrast between the Pd and the support was poor and no useful phase contrast features were observed. This fact, coupled with the low signal acquired during SAED, made Pd/PdO phase determination inconclusive. While oxidation of Pd is usually achieved at ~350 °C the possibility of a surface oxide layer at this size cannot be ruled out.

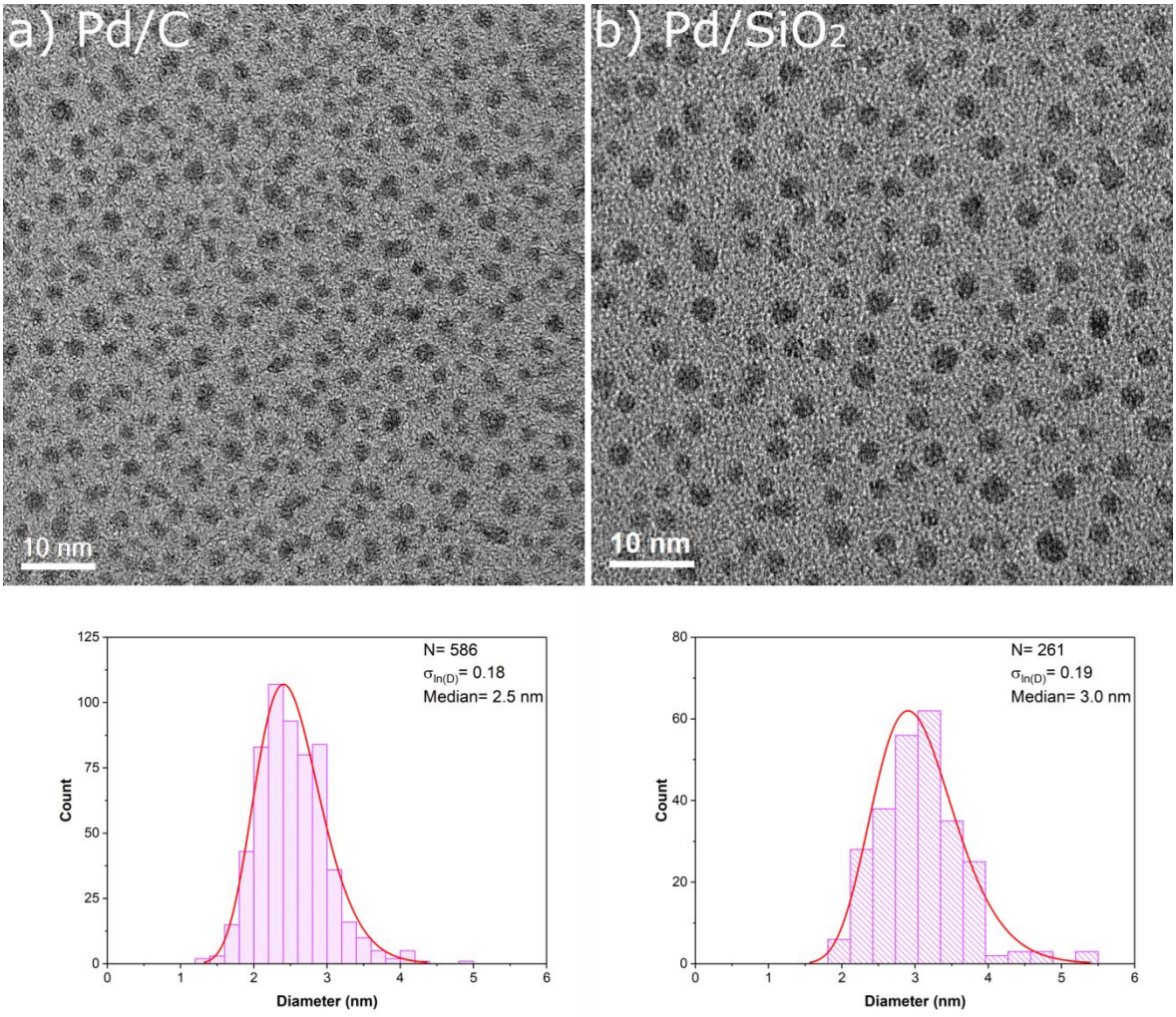

Figure 7. 8: TEM bright field micrographs and associated particle size distributions of Pd nanoparticles on the a) carbon and b) silica support.

In order to test for changes driven by different gas reaction environments the two samples were exposed to oxidising and reducing conditions. The samples were heated together in a stainless steel tube furnace. The samples were heated to 300 °C for 2 hours. One pair of samples was exposed to O_2 at a pressure of 5 mbar. Another pair were

exposed to H_2 at the same pressure. The samples were heat treated in pairs to ensure consistency for a direct comparison. Cooling took place under the same gas conditions.

Figure 7.9 shows the carbon and silica supported nanoparticles after exposure to O_2 at 300 °C. The nanoparticles in the Pd/C system underwent a clear change in size from 2.5 nm to 3.8 nm. Comparison of figures 7.8a and 7.9a reveals that the number (or areal density) of nanoparticles had decreased; this suggests that the increase in size is due to coalescence of the nanoparticles rather than simply a volume expansion caused by oxidation. Indeed high magnification imaging revealed lattice fringes corresponding to the (111) and (002) crystal planes in Pd metal.

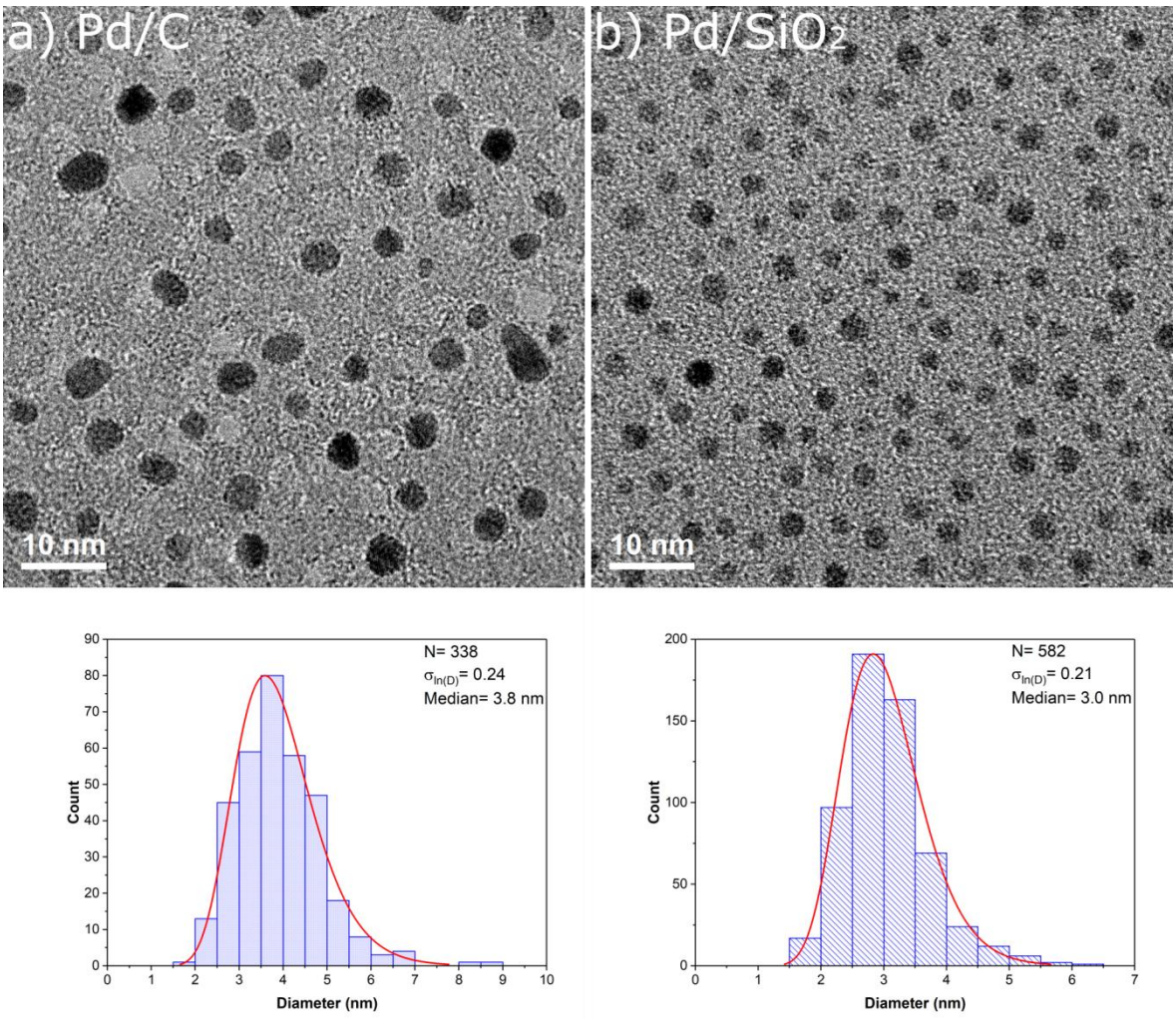

Figure 7. 9: TEM bright field micrographs and associated particle size distributions of Pd nanoparticles on the a) carbon and b) silica supports after oxidation.

In contrast, the Pd/Silica showed negligible sintering. The particle size distributions are very similar and indicate the same median size (3.0 nm). Additionally, comparison of the BF-TEM images indicates that the coverage of nanoparticles across the support has

remained unchanged. The preservation of the nanoparticle size distribution points to no significant change in the chemical state of the Pd during the oxidation treatment.

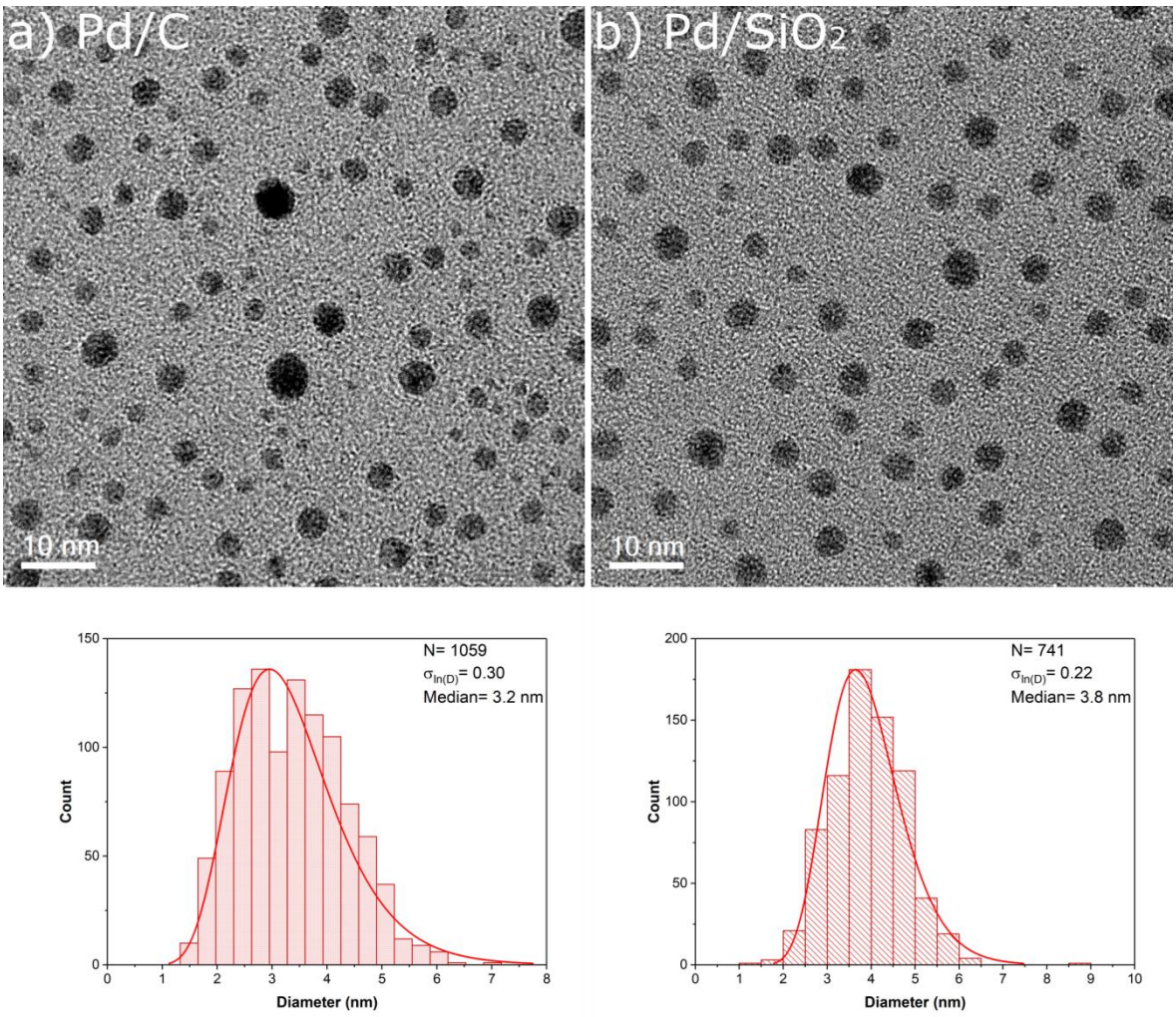

Figure 7. 10: TEM bright field micrographs and associated particle size distributions of Pd nanoparticles on the a) carbon and b) silica supports after reduction.

Figure 7.10 shows representative BF-TEM images and size distributions for the set of samples exposed to H_2 at 300 °C. The Pd/C sample displayed similar behaviour under reducing conditions. The Pd nanoparticles increased in size from 2.5 nm to 3.2 nm and a similar decrease in the number of nanoparticles on the support was observed. Despite the fact that the reaction temperature and initial nanoparticle size was the same for the oxidation and reduction treatments the character of the particle size distribution has changed. The reducing environment clearly resulted in smaller nanoparticles but a wider size distribution. This could be evidence for a different sintering mechanism under different gas environments. The broadening of the distribution is likely a result of Ostwald ripening rather than particle migration and coalescence. However, size distributions alone

cannot unambiguously confirm the dominant sintering mechanism at work. This was highlighted in a review by DeLaRiva [235].

The Pd/Silica sample manifested an increase in the size of the Pd nanoparticles under reducing conditions. In this case the nanoparticles sintered from 3.0 nm to 3.8nm. Once again, a decrease in the number of nanoparticles suggests a ripening process over a change in chemical state of the Pd. Indeed SAED of both the reduced Pd/C and Pd/Silica sample suggest that the majority of the nanoparticles are Pd metal. It should also be noted that reduction using N_2 gas produced the same results as those stated herein for H_2 gas.

In summary, Pd nanoparticles were deposited onto amorphous carbon and silica supports. The interaction between metal and support is immediately apparent without any exposure to a reaction environment. Nanoparticles form with a larger size and a more rounded shape on the silica support than on the carbon. At elevated temperatures, it is the interaction with the gaseous environment that drives changes at the nanoscale. Regarding the carbon support, Pd nanoparticles show a loss of surface area-to-volume ratio when exposed to either H_2 or O_2, with increased sintering in the case of O_2 gas. On the contrary, silica inhibits the sintering of Pd under an O_2 atmosphere but not when exposed to H_2 gas.

7.2 Dynamic Nano-Diffraction in ESTEM

The single most advantageous aspect of the (S)TEM is the ability of the electron beam to produce multiple (detectable) signals via interaction with the specimen. This feature makes electron microscopy unique amongst the diverse range of materials characterisation techniques. However, as science progresses the challenges to materials scientists grow ever higher. In recent years there has been an increase in the popularity of TEM techniques such as cryo-TEM and low dose imaging, often with software assisted analyses, for the study of soft materials. In addition, the fields of nanotechnology and catalysis are becoming more interested in comparatively small features such as atomic/single atom species, sub-nanometre layers and interfaces. All of these areas have one thing in common: low signal. Whether in relation to the background signal or with respect to time, such materials only grant a finite amount of useful, electron driven, signal

before the specimen is damaged. Therefore, it is the opinion of this author that the future of electron microscopy lies in the selection, and acquisition, of simultaneous signals for more efficient use of the incident electrons.

The results presented in this thesis are subject to the same problem described above. An example of the low signal problem was given in the previous section. In that discussion, low phase contrast and weak signal for SAED made phase identification of the fresh samples unattainable. In order to overcome such problems in the future, the ESTEM was further modified with a small (~10 μm) condenser aperture for the purposes of STEM nano-diffraction [236-238].

In STEM, a convergent beam of electrons is brought to a focus on the specimen. Provided that a crystal or periodic feature is present, a diffraction pattern will be formed. With the use of an aberration corrector and a FEG the incident electron probe can be made very bright (high beam current) and very small (high current density). By inserting a limiting aperture into the condenser system, the convergence angle of the beam can then be limited. An appropriate choice of condenser aperture will produce a diffraction pattern in which the size of the diffracted discs are smaller than their separations. This diffraction pattern originates from the region of the specimen that is illuminated by the electron probe (in modern instruments this area can be <0.5 nm in diameter). For a very thin specimen the diffraction pattern can be interpreted in the same fashion as a SAED pattern. Dynamical diffraction effects will become stronger in thicker samples and features common to CBED patterns will begin to emerge. Finally, the diffraction pattern can be captured using a CCD camera (or similar).

The area chosen for nano-diffraction can be selected with high precision using the STEM scan coils. In this way the nano-diffraction technique can be combined with other STEM information to provide a variety of data sets. Position-dependent diffraction information e.g. phase and structural insights can be added to imaging. Nano-diffraction combined with in-situ techniques could reveal time-resolved structural evolution at the single nanoparticle level. The crystal nature along 1-dimensional structures like interfaces could also be probed with nano-diffraction. In this section, some preliminary data is presented using the nano-diffraction technique with the York ESTEM. As Cowley [237] noted, the nano-diffraction technique was under represented in the literature and this continues to

be the case today. If this technique were to be properly utilised, the capability of the York ESTEM and similar future developments could be improved to dramatic scientific benefit.

7.2.1 Nano-Diffraction Results

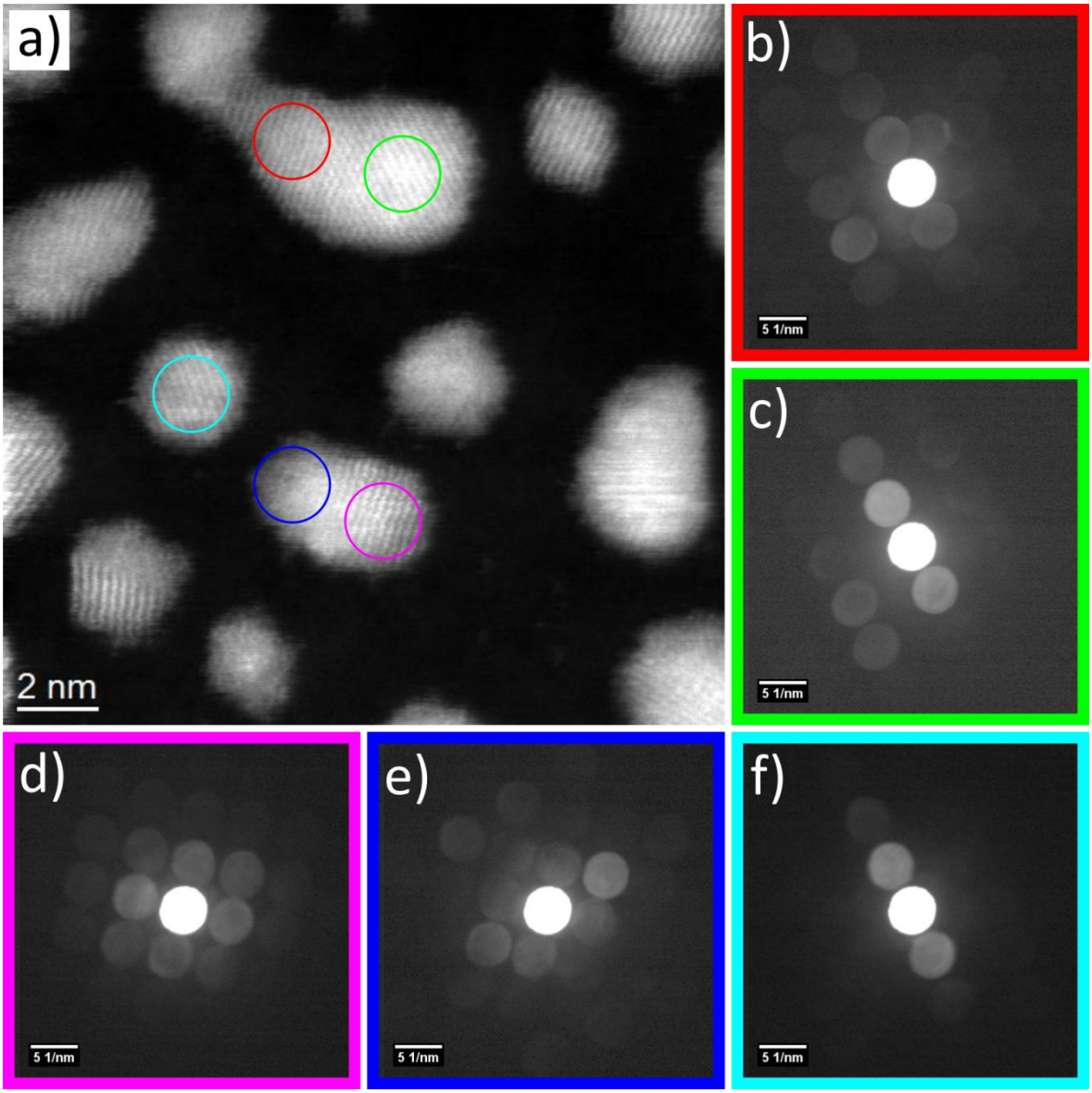

Figure 7. 11: a) HAADF-STEM micrograph of Pt nanoparticles supported on amorphous carbon. The coloured circles represent the areas from which the corresponding nano-diffraction patterns b-f) were taken. The dark-blue e) and purple d) patterns both show Pt <100> zone axis patterns, while the dark-blue region of the HAADF image appears amorphous due to the shape and orientation of the nanoparticle. The red b) area shows the overlap of two patterns produced from the sintering of two nanoparticles (see image).

Initially the nano-diffraction capabilities of the ESTEM were tested on a Pt/C model system. Pt was sputtered onto a carbon MEMS chip in exactly the same manner as the Pd

nanoparticles in section 7.1.2. This produced a sample composed of single Pt atoms, small clusters and nanoparticles. The Pt provided good Z-contrast when observed using HAADF-STEM.

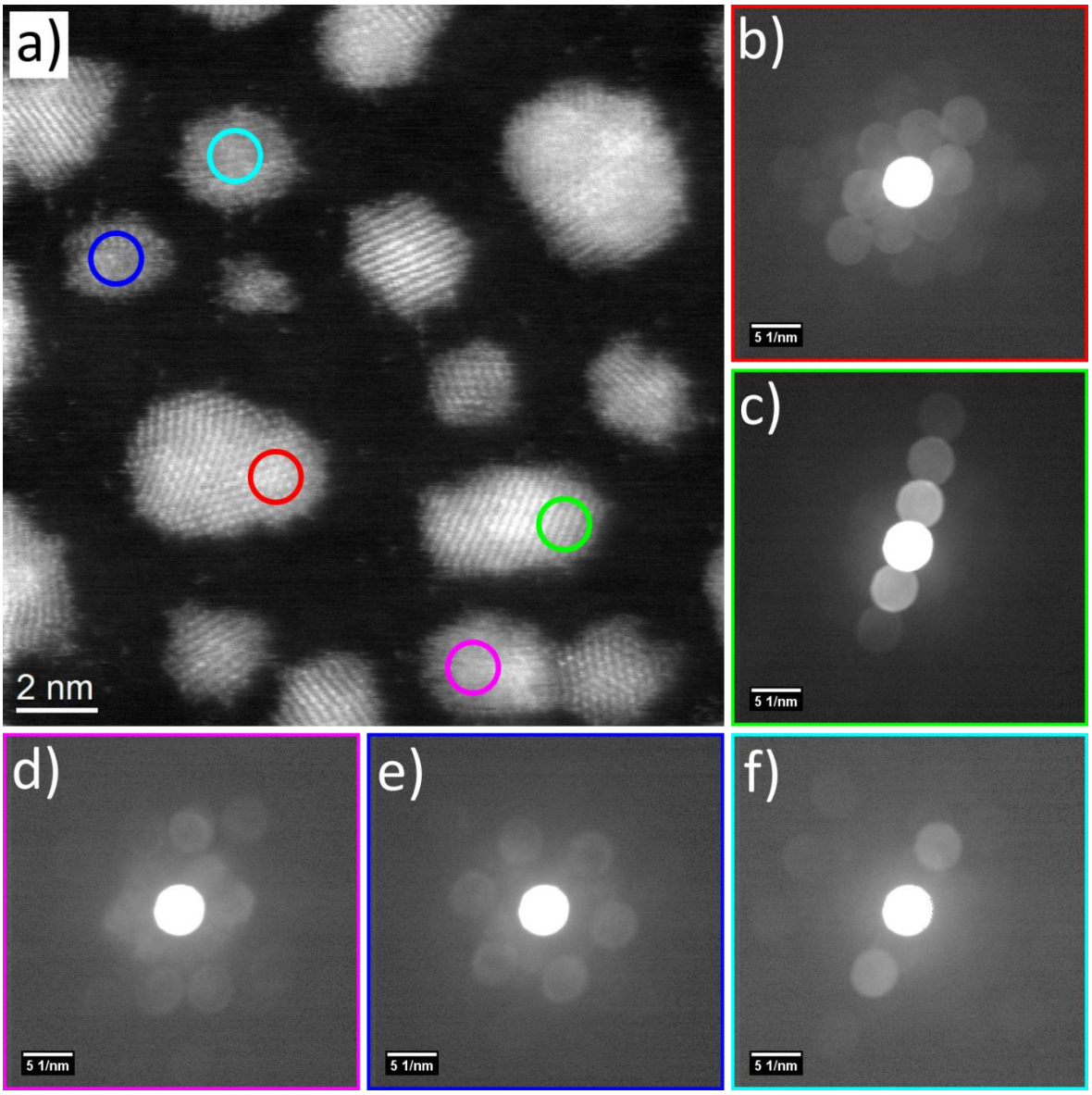

Figure 7. 12: a) HAADF-STEM micrograph of Pt nanoparticles supported on amorphous carbon. The coloured circles represent the areas from which the corresponding nano-diffraction patterns b-f) were taken. The red b) and dark-blue e) patterns show Pt <110> and Pt <111> zone axis projections respectively. The red b) and green c) patterns are from obviously crystalline areas. However, the light-blue f), dark-blue e) and purple d) patterns reveal ordered crystalline character while the atomic resolution HAADF-STEM image a) is absent of these features. The purple pattern d) contains overlapping diffraction information.

Figures 7.11 and 7.12 show atomic resolution HAADF-STEM images of the Pt/C sample. Figure 7.11 demonstrates that the shape of a nanoparticle can lead to certain areas being tilted off a zone axis with respect to other parts of the nanoparticle. In the HAADF-STEM image this led to a loss of resolvable crystallographic information, where as in the nano-

diffraction pattern, this information was preserved. Figure 7.12 contains examples of small nanoparticles which show no crystalline features and very little change in contrast across the nanoparticle. If viewed in isolation these could be, incorrectly, interpreted as amorphous small clusters. However, with the aid of nano-diffraction crystallographic and orientation information can be extracted from these regions.

Additional observations, using STEM nano-diffraction, were taken from a sample of Au nanoparticles. The specimen was made using a colloid containing Au nanoparticles, bought from Agar Scientific. The colloid contained larger particles than were present in the Pt sample.

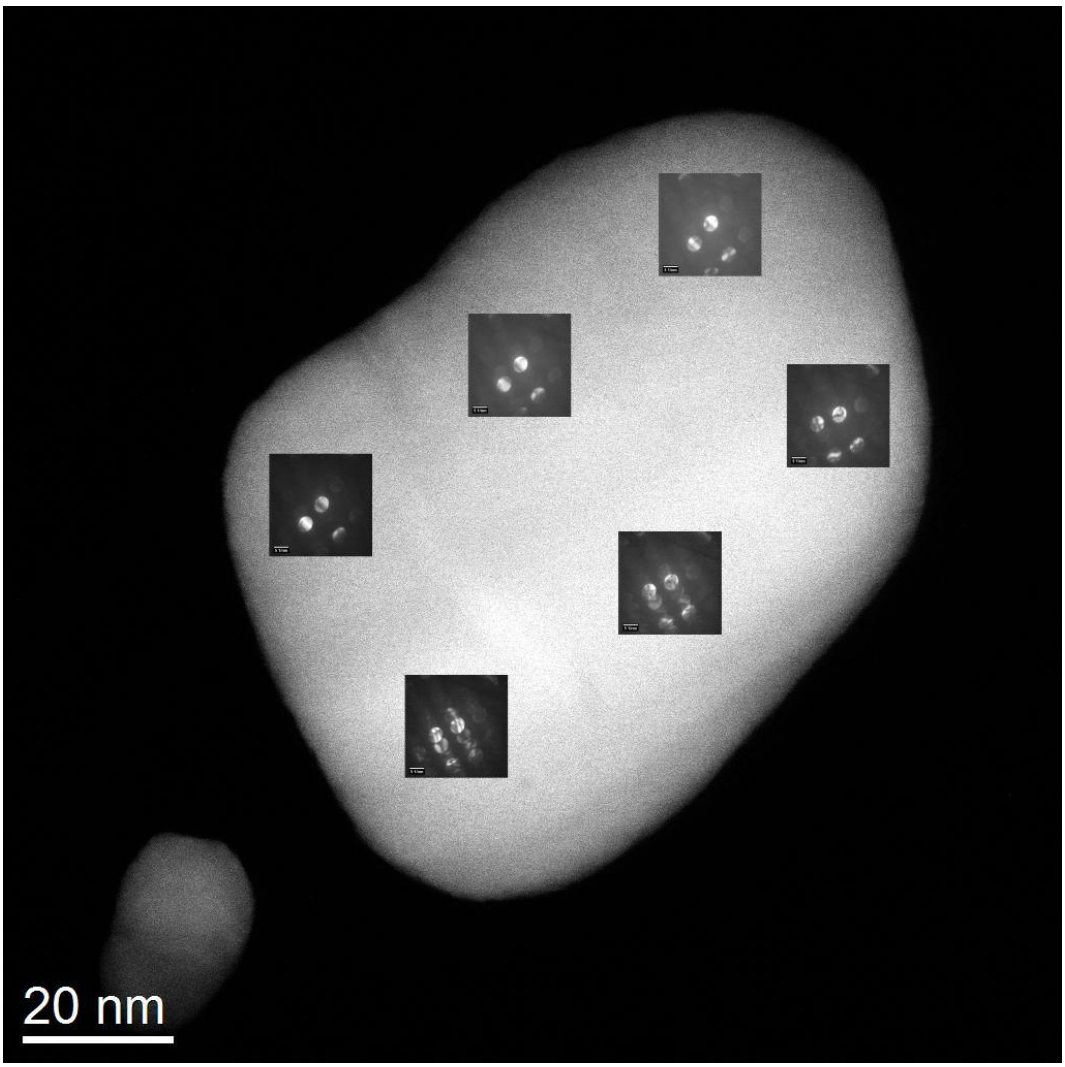

Figure 7. 13: HAADF-STEM micrograph of a large Au nanoparticle on an amorphous carbon support. The nanoparticle is not orientated to a high symmetry zone axis and so no crystallographic information can be gained from imaging alone. The insets are nano-diffraction patterns acquired from that specific area of the nanoparticle and reveal crystallographic information that is not present in the image.

The large Au nanoparticle in figure 7.13 is not tilted into a high symmetry crystallographic orientation. This fact, along with its size (projected thickness) has led to an absence of crystal features in both BF-STEM and HAADF-STEM. Recording the nano-diffraction patterns as a function of position reveals crystallographic information about the nanoparticle. In this case the diffraction patterns are equivalent to TEM-CBED patterns. While CBED simulations would be required for an in depth characterisation of this specific nanoparticle, the patterns clearly show the superposition of reflections from multiple diffracting elements. This suggests that the nanoparticle in figure 7.13 is not a single crystal; an insight which would be invisible with an imaging-only approach, regardless of the microscope resolution.

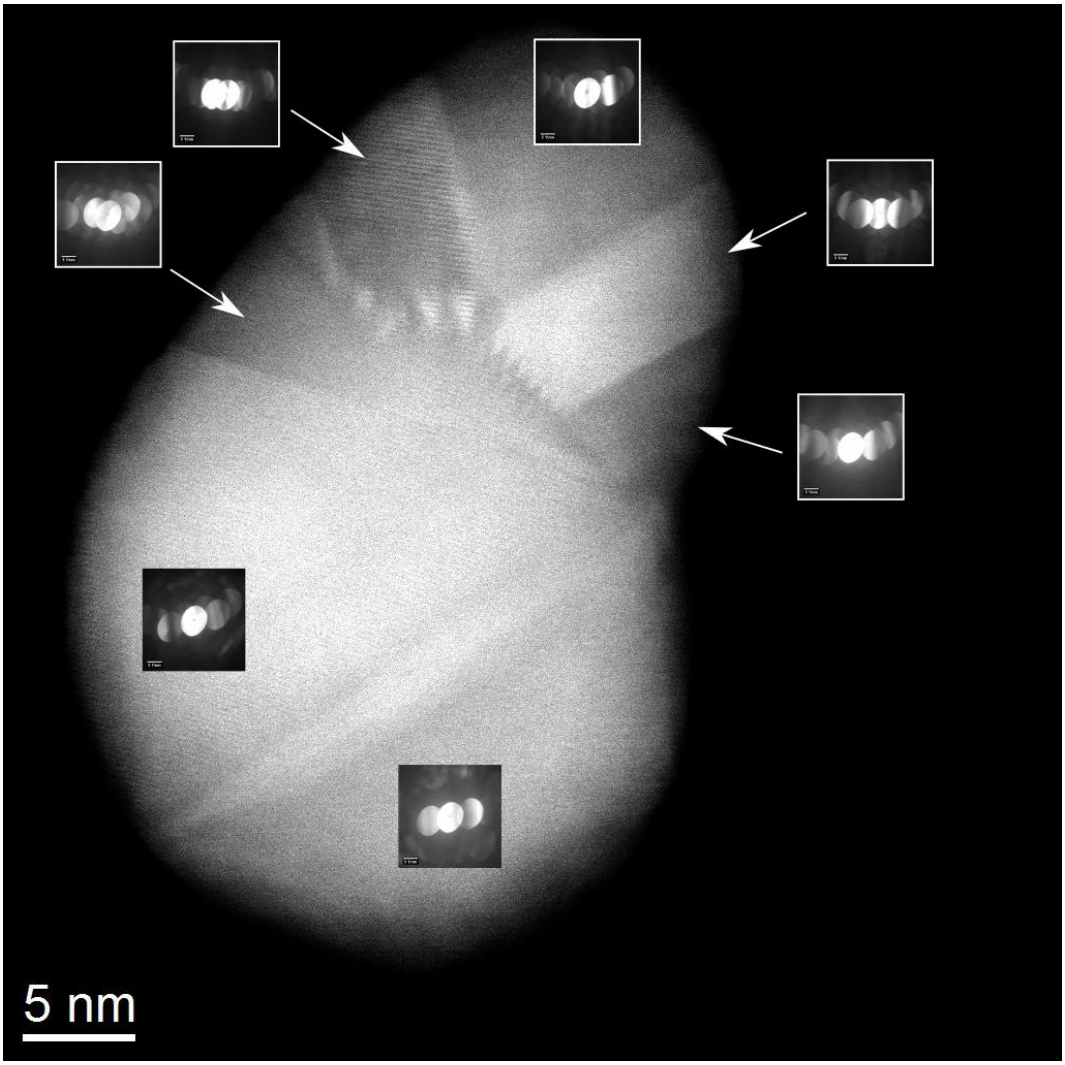

Figure 7. 14: HAADF-STEM micrograph of a Au nanoparticle on an amorphous carbon support. The structure of the nanoparticle is complex and contains many nanoscale features such as grain boundaries and twin planes. The insets show nano-diffraction patterns taken from the areas indicated.

Finally, figure 7.14 demonstrates how nano-diffraction could be used to simplify the analysis of complex nanoscale structures. The Au nanoparticle in figure 7.14 is complex to say the least. Many grain boundaries and twin planes can readily be observed in the HAADF image which lead to significant changes in contrast. The small size of the STEM electron probe provides the opportunity to take positional diffraction information, through which the components of complex nanostructure can be deconvolved.

7.3 Chapter Discussion

In this chapter, a Pd/Alumina catalyst provided by JM was investigated using in-situ ESTEM. The preparation method, using a Pd nitrate solution resulted in the formation of PdO nanoparticles on the alumina support. These nanoparticles were not reduced to Pd under temperature conditions relevant to industrial applications. Indeed the PdO nanoparticles remained stable and resisted sintering. However, during oxidation, agglomerates of PdO were observed to form. Therefore, it can be proposed that if significant levels of oxygen are present during reaction, this catalyst would show significant loss in catalytic activity caused by sintering.

This investigation into Pd/Alumina provides a comparison to the Ni/Alumina catalyst presented in chapter 6. In the case of the Ni/Alumina catalyst, the initial reduction is a unique step which leads to the reduction of NiO and the formation of a nanoparticle population which forms the active catalyst. The PdO nanoparticle distribution on the other hand is determined during the catalyst synthesis phase. Ni is observed to oxidise and reduce across cycles in which the change in nanoparticle size is negligible. By contrast, PdO is shown to lose surface area in relation to volume over repeated oxidations.

A series of Pd model systems were made to further observe the support-dependent evolution of nanoparticle size under different reaction environments. The carbon support showed the lowest interaction with the Pd nanoparticles and sintering was observed under both reducing and oxidising conditions. Silica, on the other hand, inhibited sintering under oxidising conditions but enabled it under a reducing environment.

The Pd nanoparticles supported on carbon produced very low image contrast and weak diffraction contrast in TEM. This highlighted a limitation to an imaging-only approach with

electron microscopy, a problem all to poignant in the advancing field of materials science. Continued modification to the York ESTEM presented an opportunity to explore the applicability of STEM nano-diffraction to ESTEM. Pt and Au nanoparticles supported on carbon were used. Nano-diffraction was shown to provide diffraction information, especially relating to crystallographic orientation, where atomically resolved Z-contrast HAADF imaging proved less-than adequate. Finally, during testing of the nano-diffraction capability, no impact to performance was noticed when used with hydrogen gas or at elevated temperatures.

Chapter 8

Summary and Future Work

Catalysts are ubiquitous in the chemical manufacturing economy of the modern world. Industries as diverse as fuel production, materials synthesis, food and pharmaceuticals all benefit from the use of catalytically active materials. Clean and efficient synthesis of chemicals by catalysis is a common interest world-wide and has major economic implications. For this reason there is significant financial investment by chemical companies into the materials science world for new research into catalyst materials. This thesis is a product of such investment and interest.

Since precious metals, such as the platinum group metals, are catalytically active for a broad range of chemical reactions, research has been driven by a need to make more efficient use for these materials. Using nanoparticles maximises the catalytically active surface whilst reducing the amount of inert material buried in the bulk. By going down to the nanoscale, the complexity of catalysis research increases many-fold. However, so do the opportunities for new fundamental scientific discoveries. Transmission electron microscopy is uniquely equipped to investigate the interaction of the nano and atomic scale species that are fundamental to all chemical reactions.

Traditional electron microscopy along with other metrological techniques have, to date, produced an impressive library of literature on the nature and behaviour of catalyst systems (both model and real). In-situ techniques add dynamic information to the existing knowledge by identifying the mechanisms that drive the observations of chemically dead (inactive) samples. The environmental scanning transmission electron microscope at the University of York enables researchers to observe changes happening at the atomic scale while being exposed to simulated reaction environments of temperature and pressure.

This allows fundamental dynamic processes to be investigated which would otherwise be lost via ex-situ methodologies.

In this work, the ESTEM was used to investigate supported Ni catalysts relevant to industrial methanation reactions. Methanation involves the conversion of syngas to produce methane. Methane is used as a substitute natural gas, therefore maximising the methane yield is of substantial interest. The addition of a 3 wt% ceria promoter to a Ni/Alumina catalyst increased the methane yield by more than two-fold under trim methanation conditions. ESTEM was used to investigate the origin of enhanced catalytic activity caused by the addition of a promoter.

Careful observation of structural changes under simulated reaction conditions revealed that oxygen vacancies on the ceria surface were highly active sites for the adsorption and activation of carbon oxides during reaction. Ceria is known to become more oxygen deficient as its crystallite size decreases. This correlated with observations made here, in which the enhancement of catalytic activity was found to be inversely proportional to the ceria crystallite size. The best enhancement was found to occur using a novel cerium citrate precursor which produced atomic scale (~0.2 nm) clusters of ceria which remained intact under reducing and oxidising conditions at industrially relevant temperatures (500 °C). The active sites introduced by the ceria allow for more efficient chemisorption and dissociation of H_2 on the Ni active sites. Surface diffusion of H^+ is then mediated by hydrogen spill-over.

The experimental observations herein demonstrate the ability of ESTEM to image atomic scale active sites on complex specimens. The work presented in this thesis could be extended to investigate other atomically dispersed species relevant to industrial reactions such as low weight percent promoters like ZrO_2. Alternatively, the scope of this investigation could be broadened by testing the effects of synthesis method and promoter loading. Both of which are already known to impact the performance of existing catalysts.

A range of in-situ methodologies, including both ETEM and ESTEM, were used to study the oxidation of Ni nanoparticles in the size regime relevant catalysts. The reduction of NiO is well studied, however, the oxidation is less well understood and previous studies have only focused on particular stages of the reaction. Here in-situ E(S)TEM was used to follow the oxidation reaction from start to finish on minute time scales.

The oxidation was observed to begin with the formation of pyramidal crystals of NiO which grew on the Ni surface. Certain areas of the metal surface were found to oxidise before others, most likely at surface defect sites. The oxide material did not spread out over the surface, instead more and more crystallites were seen to overlap until a core-shell structure was formed. At this point the reaction proceeded via differential diffusion in which cation vacancies were found to be the dominant diffusing species. The finite amount of metallic material in the core region of these nanoparticles resulted in the formation, and time dependant propagation, of an internal metal-void interface. The outcome was the formation of hollow polycrystalline NiO nanoparticles. These nanoparticles are structurally stable and required very high temperatures (~700 °C) for restructuring to solid, highly facetted NiO to occur.

The observations in this thesis on Ni were performed using a fast-frame camera with high pixel density. The ability to perform continuous imaging under dynamic in-situ conditions with high resolution greatly enhances the functionality of E(S)TEM systems to investigate transformation pathways and metastable states in materials. As TEM camera technology improves, so do the opportunities for fundamental investigations into the redox mechanisms of metal oxide and multi-metallic compounds. For example, the complex and environmentally dependent transitions between multiple vanadium oxide phases would be of great interest.

A series of Pd model systems were made to test the effect of support material on sintering behaviour. Carbon performed the poorest, initially supporting the smallest nanoparticles, both reducing and oxidising environments caused sintering. The silica support inhibited sintering under an oxidising environment but not under reducing conditions. Finally, PdO nanoparticles on the alumina support showed a consistent size distribution under both environments. While some sintering produced large agglomerates under O_2, this was only a small fraction of the PdO, with the majority remaining unchanged.

Towards the end of this project the capability to perform nano-diffraction in STEM was added to the in-situ microscope. While the comments in this thesis on the technique are by no means exhaustive, the potential for future investigations was more than adequately demonstrated. The pioneer of the technique noted the absence of the method in the mainstream scientific literature. As nanocatalysis looks to transition closer to atomic-scale

catalysis, nano-diffraction has the potential to push the diffraction capabilities of the STEM to be on par with its current achievement in image resolution, especially in the low-dose regimes that are becoming more fashionable today.

In summary, the E(S)TEM capability at the University of York has been applied to the study of nanoparticles relevant to nanocatalysis. Having demonstrated the ability of the ESTEM to probe the living world of atoms at the nanoscale, the only decision to be made is which unique nanoscale system will be explored next and how best to observe it.

List of Abbreviations

ADF	Annular dark field
BET	Brunauer-Emmett-Teller analysis
BF-(S)TEM	Bright field (S)TEM
CBD/CBED	Convergent beam electron diffraction
CCD	Charge-coupled device
CTEM	Conventional TEM
CTF	Contrast transfer function
DF-(S)TEM	Dark field (S)TEM
DFT	Density functional theory
E(S)TEM	Environmental (S)TEM
EDS	Energy dispersive X-ray spectroscopy
EDX	Energy dispersive X-ray spectroscopy
EELS	Electron energy loss spectroscopy
EFTEM	Energy filtered TEM
FEG	Field emission gun
FFT	Fast Fourier transform
FT	Fischer-Tropsch synthesis
HAADF	High-angle annular dark field
HR-TEM	High resolution TEM
IVEM	Intermediate voltage electron microscope
JM	Johnson Matthey Plc.
NBD	Nano-beam diffraction
NCSI	Negative C_s imagine
NP	Nanoparticle
SAD/SAED	Selected-area electron diffraction

SEM	Scanning electron microscope
SNG	Substitute natural gas
STEM	Scanning transmission electron microscope
TEM	Transmission electron microscope
TGA	Thermo-gravimetric analysis
VLM	Visible light microscope
XPS	X-ray photoelectron spectroscopy
XRD	X-ray diffraction

List of Symbols

A	Atomic weight
A(**u**)	Aperture function
a’	Distance between energy minima
B	Magnetostatic field vector
B(**u**)	Aberration function
c	Speed of light
C_c,	Chromatic aberration coefficient
C_s	Spherical aberration coefficient
D	Particle diameter
d	Inter-planar distance
D	Diffusion coefficient
D_0	Maximal diffusion coefficient at infinite temperature
ds	Surface area element
e	Charge on an electron
E	Electrostatic field vector
E	Energy barrier to diffusion
E(**u**)	Envelope function
E_0	Initial (or modal) beam energy
E_{ad}	Adsorption energy
E_d	Displacement energy
E_{diff}	Diffusion activation energy
E_t	Threshold energy for knock-on damage
E_{Tot}	Total energy
F	Lorentz force
f	Focal length

F	Structure factor
f	Atomic scattering factor
h	Planck constant
H(**u**)	Contrast transfer function
I	Current
K	Pole piece shape factor
K	XRD shape factor
K	Boltzmann constant
L	Camera length
m_0	Electron rest mass
n	Number of times that a reaction turns over
n	Diffraction order
N	Number of metal ions per unit surface area
P	Pressure
q	Charge
r	Particle radius
r	Physical distance on a recorded diffraction pattern
r_{chr}	Radius of point-spread disc due to chromatic aberration
r_{sph}	Radius of point-spread disc due to spherical aberration
S_n	Number of catalytically active sites
t	Time
T	Temperature
T(**u**)	Intensity transfer function
t_{mono}	Monolayer formation time
ToF	Turnover frequency
u	Spatial frequency
V	Potential difference
v	Velocity of the electrons
V	Contact potential difference
W	Energy barrier height
X	Oxide thickness
y	Lateral displacement of diffraction aperture
β	Collection semi-angle

β	Collection semi-angle of the lens
γ_m	Surface free energy
δ	Resolution
ΔE	Energy spread of the electron beam
Δf	Defocus
Δf_{Sch}	Scherzer defocus
ΔH	Enthalpy change of reaction
ΔH_{sub}	Sublimation energy
θ	Scattering angle
θ_B	Bragg angle
λ	Wavelength of radiation
μ	Chemical potential
μ	Refractive index
μ_0	Bulk chemical potential
ν	Atomic vibration frequency
τ	Average crystalline size
$\chi(\mathbf{u})$	Phase distortion function
Ω	Atomic volume

References

[1] A.T. Bell, The impact of nanoscience on heterogeneous catalysis, Science, 299 (2003) 1688-1691.
[2] Y. Zhou, C.C. Jin, Y. Li, W.J. Shen, Dynamic behavior of metal nanoparticles for catalysis, Nano Today, 20 (2018) 101-120.
[3] K. Hemalatha, G. Madhumitha, A. Kajbafvala, N. Anupama, R. Sompalle, S. Mohana Roopan, Function of Nanocatalyst in Chemistry of Organic Compounds Revolution: An Overview, Journal of Nanomaterials, 2013 (2013) 1-23.
[4] R.M. Mohamed, D.L. McKinney, W.M. Sigmund, Enhanced nanocatalysts, Materials Science and Engineering: R: Reports, 73 (2012) 1-13.
[5] N. Raveendran Shiju, K. Yoshida, E.D. Boyes, D. Robert Brown, P.L. Gai, Dynamic atomic scale in situ electron microscopy in the development of an efficient heterogeneous catalytic process for pharmaceutical NSAIDS, Catalysis Science & Technology, 1 (2011) 413.
[6] H.S. Gandhi, G.W. Graham, R.W. McCabe, Automotive exhaust catalysis, Journal of Catalysis, 216 (2003) 433-442.
[7] A. Russell, W.S. Epling, Diesel Oxidation Catalysts, Catal Rev, 53 (2011) 337-423.
[8] G. Prieto, J. Zecevic, H. Friedrich, K.P. de Jong, P.E. de Jongh, Towards stable catalysts by controlling collective properties of supported metal nanoparticles, Nature materials, 12 (2013) 34-39.
[9] A.V. Crewe, High-resolution scanning transmission electron microscopy, Science, 221 (1983) 325-330.
[10] M.M.J. Treacy, J.M. Gibson, Coherence and Multiple-Scattering in Z-Contrast Images, Ultramicroscopy, 52 (1993) 31-53.
[11] S.J. Pennycook, P.D. Nellist, Scanning Transmission Electron Microscopy, 1 ed., Springer-Verlag New York2011.
[12] W. Zhou, I.E. Wachs, C.J. Kiely, Nanostructural and chemical characterization of supported metal oxide catalysts by aberration corrected analytical electron microscopy, Current Opinion in Solid State and Materials Science, 16 (2012) 10-22.
[13] E.D. Boyes, P.L. Gai, Environmental high resolution electron microscopy and applications to chemical science, Ultramicroscopy, 67 (1997) 219-232.
[14] P.L. Gai, Developments of electron microscopy methods in the study of catalysts, Curr Opin Solid St M, 5 (2001) 371-380.
[15] P.L. Gai, E.D. Boyes, S. Helveg, P.L. Hansen, S. Giorgio, C.R. Henry, Atomic-Resolution Environmental Transmission Electron Microscopy for Probing Gas–Solid Reactions in Heterogeneous Catalysis, MRS Bulletin, 32 (2007) 1044-1050.
[16] C. Kiely, Electron microscopy: New views of catalysts, Nature materials, 9 (2010) 296-297.

[17] E.D. Boyes, P.L. Gai, Visualising reacting single atoms under controlled conditions: Advances in atomic resolution in situ Environmental (Scanning) Transmission Electron Microscopy (E(S)TEM), Comptes Rendus Physique, 15 (2014) 200-213.
[18] T.W. Hansen, J.B. Wagner, Catalysts under Controlled Atmospheres in the Transmission Electron Microscope, Acs Catalysis, 4 (2014) 1673-1685.
[19] Y. Jiang, Z. Zhang, W. Yuan, X. Zhang, Y. Wang, Z. Zhang, Recent advances in gas-involved in situ studies via transmission electron microscopy, Nano Research, 11 (2017) 42-67.
[20] J.M. Thomas, W.J. Thomas, Principles and practice of heterogeneous catalysis, John Wiley & Sons2014.
[21] M.J. Walsh, Aberration Corrected In-Situ Electron Microscopy of Nanoparticle Catalysts, PhD Thesis, Physics, University of York, York, UK, 2012, pp. 171.
[22] P. Atkins, J. de Paula, J. Keeler, Atkins' Physical Chemistry, 11th ed., Oxford University Press, UK, 2017.
[23] B.R. Cuenya, Synthesis and catalytic properties of metal nanoparticles: Size, shape, support, composition, and oxidation state effects, Thin Solid Films, 518 (2010) 3127-3150.
[24] L.D. Marks, L. Peng, Nanoparticle shape, thermodynamics and kinetics, Journal of Physics: Condensed Matter, 28 (2016) 053001.
[25] V. Aguilar-Guerrero, B.C. Gates, Kinetics of CO Oxidation Catalyzed by Supported Gold: A Tabular Summary of the Literature, Catalysis Letters, 130 (2009) 108-120.
[26] M. Haruta, Novel catalysis of gold deposited on metal oxides, Catalysis Surveys from Japan, 1 (1997) 61-73.
[27] M. Mavrikakis, P. Stoltze, J.K. Norskov, Making gold less noble, Catalysis Letters, 64 (2000) 101-106.
[28] A. Cho, Connecting the dots to custom catalysts, Science, 299 (2003) 1684-1685.
[29] C.R. Henry, Morphology of supported nanoparticles, Progress in Surface Science, 80 (2005) 92-116.
[30] R. Xu, D. Wang, J. Zhang, Y. Li, Shape-dependent catalytic activity of silver nanoparticles for the oxidation of styrene, Chemistry, an Asian journal, 1 (2006) 888-893.
[31] R. Wang, H. He, L.-C. Liu, H.-X. Dai, Z. Zhao, Shape-dependent catalytic activity of palladium nanocrystals for the oxidation of carbon monoxide, Catalysis Science & Technology, 2 (2012) 575-580.
[32] M.A. Newton, C. Belver-Coldeira, A. Martinez-Arias, M. Fernandez-Garcia, Dynamic in situ observation of rapid size and shape change of supported Pd nanoparticles during CO/NO cycling, Nature materials, 6 (2007) 528-532.
[33] S. Shaikhutdinov, R. Meyer, M. Naschitzki, M. Baumer, H. Freund, Size and support effects for CO adsorption on gold model catalysts, Catalysis Letters, 86 (2003) 211-219.
[34] S. Laursen, S. Linic, Oxidation Catalysis by Oxide-Supported Au Nanostructures: The Role of Supports and the Effect of External Conditions, Physical Review Letters, 97 (2006) 026101.
[35] D. Pillay, G.S. Hwang, Growth and structure of small gold particles on rutile TiO2 (110), Physical Review B, 72 (2005) 205422.
[36] J.R. Croy, S. Mostafa, J. Liu, Y. Sohn, H. Heinrich, B.R. Cuenya, Support Dependence of MeOH Decomposition Over Size-Selected Pt Nanoparticles, Catalysis Letters, 119 (2007) 209-216.
[37] M. Raney, Method of Producing Finely-Divided Nickel, in: U.S.P. Office (Ed.), M. Raney USA, 1927.
[38] D. Potoczna-Petru, L. Kępiński, Reduction study of Co3O4 model catalyst by electron microscopy, Catalysis Letters, 73 (2001) 41-46.

[39] L.M. Molina, B. Hammer, Active Role of Oxide Support during CO Oxidation at Au/MgO, Physical Review Letters, 90 (2003) 206102.
[40] F. Tao, M.E. Grass, Y. Zhang, D.R. Butcher, J.R. Renzas, Z. Liu, J.Y. Chung, B.S. Mun, M. Salmeron, G.A. Somorjai, Reaction-Driven Restructuring of Rh-Pd and Pt-Pd Core-Shell Nanoparticles, Science, 322 (2008) 932.
[41] G. Zhu, Coverage of palladium by silicon oxide during reduction in H2 and complete oxidation of methane, Journal of Catalysis, 225 (2004) 170-178.
[42] J.H. Kwak, J. Hu, D. Mei, C.-W. Yi, D.H. Kim, C.H.F. Peden, L.F. Allard, J. Szanyi, Coordinatively Unsaturated Al3+ Centers as Binding Sites for Active Catalyst Phases of Platinum on γ-Al2O3, Science, 325 (2009) 1670.
[43] X.-F. Yang, A. Wang, B. Qiao, J. Li, J. Liu, T. Zhang, Single-Atom Catalysts: A New Frontier in Heterogeneous Catalysis, Accounts of Chemical Research, 46 (2013) 1740-1748.
[44] B. Qiao, A. Wang, X. Yang, L.F. Allard, Z. Jiang, Y. Cui, J. Liu, J. Li, T. Zhang, Single-atom catalysis of CO oxidation using Pt1/FeOx, Nature Chemistry, 3 (2011) 634.
[45] R. Finsy, On the Critical Radius in Ostwald Ripening, Langmuir, 20 (2004) 2975-2976.
[46] C.T. Campbell, S.C. Parker, D.E. Starr, The Effect of Size-Dependent Nanoparticle Energetics on Catalyst Sintering, Science, 298 (2002) 811.
[47] P. Wynblatt, N.A. Gjostein, Particle growth in model supported metal catalysts—I. Theory, Acta Metallurgica, 24 (1976) 1165-1174.
[48] I.M. Lifshitz, V.V. Slyozov, The kinetics of precipitation from supersaturated solid solutions, Journal of Physics and Chemistry of Solids, 19 (1961) 35-50.
[49] A.K. Datye, Q. Xu, K.C. Kharas, J.M. McCarty, Particle size distributions in heterogeneous catalysts: What do they tell us about the sintering mechanism?, Catalysis Today, 111 (2006) 59-67.
[50] F.A. Nichols, Coalescence of Two Spheres by Surface Diffusion, Journal of Applied Physics, 37 (1966) 2805-2808.
[51] M.D. Argyle, C.H. Bartholomew, Heterogeneous Catalyst Deactivation and Regeneration: A Review, Catalysts, 5 (2015) 145-269.
[52] A.P. LaGrow, D.C. Lloyd, P.L. Gai, E.D. Boyes, In Situ Scanning Transmission Electron Microscopy of Ni Nanoparticle Redispersion via the Reduction of Hollow NiO, Chemistry of Materials, 30 (2017) 197-203.
[53] J.W. Edington, Practical Electron Microscopy in Materials Science, Van Nostrand-Reinhold, New York, 1976.
[54] P.B. Hirsch, A. Howie, R.B. Nicholson, D.W. Pashley, M.J. Whelan, Electron microscopy of thin crystals, Krieger Huntington, New York, 1977.
[55] P.J. Goodhew, J. Humphreys, R. Beanland, Electron Microscopy and Analysis, Third Edition, Taylor & Francis2000.
[56] D.B. Williams, C.B. Carter, Transmission Electron Microscopy, 2nd ed., Springer2009.
[57] L.d. Broglie, The wave nature of the electron, Nobel Lecture, 1929.
[58] L. Lambert, T. Mulvey, Ernst Ruska (1906–1988), Designer Extraordinaire of the Electron Microscope: A Memoir, in: P.W. Hawkes (Ed.) Advances in Imaging and Electron Physics, Elsevier1996, pp. 2-62.
[59] M. Knoll, E. Ruska, Beitrag zur geometrischen Elektronenoptik. I, Annalen der Physik, 404 (1932) 607-640.
[60] M. Knoll, E. Ruska, Beitrag zur geometrischen Elektronenoptik. II, Annalen der Physik, 404 (1932) 641-661.
[61] M. Knoll, E. Ruska, Das Elektronenmikroskop, Zeitschrift für Physik, 78 (1932) 318-339.

[62] H. Busch, Über die Wirkungsweise der Konzentrierungsspule bei der Braunschen Röhre, Archiv für Elektrotechnik, 18 (1927) 583-594.
[63] P.W. Hawkes, Magnetic electron lenses, Springer London, Limited1982.
[64] J. Orloff, Survey of electron sources for high-resolution microscopy, Ultramicroscopy, 28 (1989) 88-97.
[65] H. Ahmed, A.N. Broers, Lanthanum Hexaboride Electron Emitter, Journal of Applied Physics, 43 (1972) 2185-2192.
[66] A.V. Crewe, D.N. Eggenberger, J. Wall, L.M. Welter, Electron Gun Using a Field Emission Source, Review of Scientific Instruments, 39 (1968) 576-583.
[67] A.V. Crewe, J. Wall, A scanning microscope with 5 Å resolution, Journal of Molecular Biology, 48 (1970) 375-393.
[68] A.V. Crewe, The Physics of the High-Resolution Scanning Microscope, Rep Prog Phys, 43 (1980) 621-639.
[69] G.Y. Fan, M.H. Ellisman, Digital imaging in transmission electron microscopy, Journal of Microscopy, 200 (2000) 1-13.
[70] P.W. Hawkes, Electron image processing: A survey, Computer Graphics and Image Processing, 8 (1978) 406-446.
[71] M.R. Ward, Aberration corrected (S)TEM of Nanoparticle and Atomically Dispersed Catalysts, PhD Thesis, Department of Physics, University of York, York, 2013, pp. 1-225.
[72] D.J. Smith, W.O. Saxton, M.A. O'Keefe, G.J. Wood, W.M. Stobbs, The importance of beam alignment and crystal tilt in high resolution electron microscopy, Ultramicroscopy, 11 (1983) 263-281.
[73] D. Chescoe, P.J. Goodhew, The Operation of the Transmission Electron Microscope, Oxford University Press1984.
[74] C. Kittel, Introduction to Solid State Physics, 8 ed., John Wiley and Sons2004.
[75] C. Hammond, The Basics of Crystallography and Diffraction, OUP Oxford2009.
[76] W.H. Bragg, W.L. Bragg, The reflection of X-rays by crystals, Proc. R. Soc. Lond. A, 88 (1913) 428-438.
[77] W.H. Bragg, The Reflection of X-rays by Crystals.(II.), Proc. R. Soc. Lond. A, 89 (1913) 246-248.
[78] A.W. Agar, Accuracy of selected-area microdiffraction in the electron microscope, British Journal of Applied Physics, 11 (1960) 185.
[79] B.J. Duggan, I.P. Jones, The Orientation and Position Accuracy of Electron Diffraction, Texture of Crystalline Solids, 2 (1977) 205-223.
[80] J.M. Cowley, A.F. Moodie, The scattering of electrons by atoms and crystals. I. A new theoretical approach, Acta Crystallographica, 10 (1957) 609-619.
[81] W.J.d. Ruijter, R. Sharma, M.R. McCartney, D.J. Smith, Measurement of lattice-fringe vectors from digital HREM images: experimental precision, Ultramicroscopy, 57 (1995) 409-422.
[82] A.V. Crewe, J. Wall, L.M. Welter, A High-Resolution Scanning Transmission Electron Microscope, Journal of Applied Physics, 39 (1968) 5861-5868.
[83] D.A. Muller, L.F. Kourkoutis, M. Murfitt, J.H. Song, H.Y. Hwang, J. Silcox, N. Dellby, O.L. Krivanek, Atomic-Scale Chemical Imaging of Composition and Bonding by Aberration-Corrected Microscopy, Science, 319 (2008) 1073-1076.
[84] K. Kimoto, T. Asaka, T. Nagai, M. Saito, Y. Matsui, K. Ishizuka, Element-selective imaging of atomic columns in a crystal using STEM and EELS, Nature, 450 (2007) 702.
[85] A.V. Crewe, J. Wall, J. Langmore, Visibility of Single Atoms, Science, 168 (1970) 1338-1340.

[86] M. Isaacson, D. Kopf, M. Utlaut, N.W. Parker, A.V. Crewe, Direct observations of atomic diffusion by scanning transmission electron microscopy, Proc Natl Acad Sci U S A, 74 (1977) 1802-1806.
[87] C. Colliex, A.J. Craven, C.J. Wilson, Fresnel Fringes in Stem, Ultramicroscopy, 2 (1977) 327-335.
[88] P.D. Nellist, S.J. Pennycook, The principles and interpretation of annular dark-field Z-contrast imaging, in: P.W. Hawkes (Ed.) Advances in Imaging and Electron Physics, Elsevier2000, pp. 147-203.
[89] O.L. Krivanek, M.F. Chisholm, V. Nicolosi, T.J. Pennycook, G.J. Corbin, N. Dellby, M.F. Murfitt, C.S. Own, Z.S. Szilagyi, M.P. Oxley, S.T. Pantelides, S.J. Pennycook, Atom-by-atom structural and chemical analysis by annular dark-field electron microscopy, Nature, 464 (2010) 571.
[90] M.J. Hÿtch, W.M. Stobbs, Quantitative comparison of high resolution TEM images with image simulations, Ultramicroscopy, 53 (1994) 191-203.
[91] A. Howie, Hunting the Stobbs factor, Ultramicroscopy, 98 (2004) 73-79.
[92] L. Jones, Quantitative ADF STEM: acquisition, analysis and interpretation, Iop Conf Ser-Mat Sci, 109 (2016) 012008.
[93] J.M. LeBeau, S.D. Findlay, L.J. Allen, S. Stemmer, Standardless atom counting in scanning transmission electron microscopy, Nano Letters, 10 (2010) 4405-4408.
[94] D.O. Klenov, S. Stemmer, Contributions to the contrast in experimental high-angle annular dark-field images, Ultramicroscopy, 106 (2006) 889-901.
[95] J.M. Cowley, Coherent interference effects in SIEM and CBED, Ultramicroscopy, 7 (1981) 19-26.
[96] H. Sawada, T. Sannomiya, F. Hosokawa, T. Nakamichi, T. Kaneyama, T. Tomita, Y. Kondo, T. Tanaka, Y. Oshima, Y. Tanishiro, K. Takayanagi, Measurement method of aberration from Ronchigram by autocorrelation function, Ultramicroscopy, 108 (2008) 1467-1475.
[97] J.M. Rodenburg, E.B. Macak, Optimising the Resolution of TEM/STEM with the Electron Ronchigram, Microscopy and Analysis, 2002, pp. 5-7.
[98] J.S. Barnard, D.N. Johnstone, P.A. Midgley, High-resolution scanning precession electron diffraction: Alignment and spatial resolution, Ultramicroscopy, 174 (2017) 79-88.
[99] D. Van Dyck, A.F. de Jong, Ultimate resolution and information in electron microscopy: general principles, Ultramicroscopy, 47 (1992) 266-281.
[100] O. Scherzer, The Theoretical Resolution Limit of the Electron Microscope, Journal of Applied Physics, 20 (1949) 20-29.
[101] O. Scherzer, Uber einige Fehler von Elektronenlinsen, Zeitschrift Physik, 101 (1936) 593.
[102] R. Brydson, Aberration-corrected analytical transmission electron microscopy, John Wiley & Sons2011.
[103] P.W. Hawkes, The geometrical aberrations of general electron optical systems I The conditions imposed by symmetry, Phil. Trans. R. Soc. Lond. A, 257 (1965) 479-522.
[104] O. Scherzer, Spharische and chromatische Korrektur von Elektronenlinsen, Optik, 2 (1947) 114-132.
[105] H. Rose, Outline of a spherically corrected semi-aplanatic medium-voltage TEM, Optik, 85 (1990) 19-24.
[106] O.L. Krivanek, P.A. Stadelmann, Effect of three-fold astigmatism on high resolution electron micrographs, Ultramicroscopy, 60 (1995) 103-113.
[107] S. Uhlemann, M. Haider, Residual wave aberrations in the first spherical aberration corrected transmission electron microscope, Ultramicroscopy, 72 (1998) 109-119.

[108] M. Haider, S. Uhlemann, J. Zach, Upper limits for the residual aberrations of a high-resolution aberration-corrected STEM, Ultramicroscopy, 81 (2000) 163-175.
[109] C. Hetherington, Aberration correction for TEM, Materials Today, 7 (2004) 50-55.
[110] M. Haider, S. Uhlemann, E. Schwan, H. Rose, B. Kabius, K. Urban, Electron microscopy image enhanced, Nature, 392 (1998) 768.
[111] M. Haider, H. Rose, S. Uhlemann, E. Schwan, B. Kabius, K. Urban, A spherical-aberration-corrected 200kV transmission electron microscope, Ultramicroscopy, 75 (1998) 53-60.
[112] O.L. Krivanek, N. Dellby, A.R. Lupini, Towards sub-Å electron beams, Ultramicroscopy, 78 (1999) 1-11.
[113] P.E. Batson, N. Dellby, O.L. Krivanek, Sub-ångstrom resolution using aberration corrected electron optics, Nature, 418 (2002) 617.
[114] A. Bleloch, A. Lupini, Imaging at the picoscale, Materials Today, 7 (2004) 42-48.
[115] R. Erni, M.D. Rossell, C. Kisielowski, U. Dahmen, Atomic-Resolution Imaging with a Sub-50-pm Electron Probe, Physical Review Letters, 102 (2009) 096101.
[116] H.H. Rose, Optics of high-performance electron microscopes, Science and Technology of Advanced Materials, 9 (2008) 014107.
[117] V.D. Beck, A hexapole spherical aberration corrector, Optik, 53 (1979) 241-255.
[118] A.V. Crewe, D. Kopf, A sextupole system for the correction of spherical aberration, Optik, 55 (1980) 1.
[119] M. Haider, G. Braunshausen, E. Schwan, Correction of the spherical aberration of a 200 KV TEM by means of a hexapole-corrector, Optik, 99 (1995) 167-179.
[120] M. Lentzen, The tuning of a Zernike phase plate with defocus and variable spherical aberration and its use in HRTEM imaging, Ultramicroscopy, 99 (2004) 211-220.
[121] K.W. Urban, C.-L. Jia, L. Houben, M. Lentzen, S.-B. Mi, K. Tillmann, Negative spherical aberration ultrahigh-resolution imaging in corrected transmission electron microscopy, Philosophical Transactions of the Royal Society A: Mathematical, Physical and Engineering Sciences, 367 (2009) 3735-3753.
[122] F. Zemlin, K. Weiss, P. Schiske, W. Kunath, K.H. Herrmann, Coma-free alignment of high resolution electron microscopes with the aid of optical diffractograms, Ultramicroscopy, 3 (1978) 49-60.
[123] R.F. Egerton, P. Li, M. Malac, Radiation damage in the TEM and SEM, Micron, 35 (2004) 399-409.
[124] L.W. Hobbs, Introduction to Analytical Electron Microscopy, 1 ed., Springer, US, 1979.
[125] L.F. Allard, W.C. Bigelow, M. Jose-Yacaman, D.P. Nackashi, J. Damiano, S.E. Mick, A new MEMS-based system for ultra-high-resolution imaging at elevated temperatures, Microscopy research and technique, 72 (2009) 208-215.
[126] H.M. Flower, High voltage electron microscopy of environmental reactions, Journal of Microscopy, 97 (1973) 171-190.
[127] R.T.K. Baker, P.S. Harris, Controlled atmosphere electron microscopy, Journal of Physics E: Scientific Instruments, 5 (1972) 793.
[128] J.F. Creemer, S. Helveg, G.H. Hoveling, S. Ullmann, A.M. Molenbroek, P.M. Sarro, H.W. Zandbergen, Atomic-scale electron microscopy at ambient pressure, Ultramicroscopy, 108 (2008) 993-998.
[129] N. de Jonge, W.C. Bigelow, G.M. Veith, Atmospheric Pressure Scanning Transmission Electron Microscopy, Nano Letters, 10 (2010) 1028-1031.
[130] S. Mehraeen, J.T. McKeown, P.V. Deshmukh, J.E. Evans, P. Abellan, P. Xu, B.W. Reed, M.L. Taheri, P.E. Fischione, N.D. Browning, A (S)TEM gas cell holder with localized laser heating for in situ experiments, Microscopy and microanalysis : the official journal of

Microscopy Society of America, Microbeam Analysis Society, Microscopical Society of Canada, 19 (2013) 470-478.
[131] F. Banhart, W. Scientific, In-situ Electron Microscopy at High Resolution, World Scientific Publishing Company2008.
[132] T.W. Hansen, J.B. Wagner, P.L. Hansen, S. Dahl, H. Topsøe, C.J.H. Jacobsen, Atomic-Resolution in Situ Transmission Electron Microscopy of a Promoter of a Heterogeneous Catalyst, Science, 294 (2001) 1508-1510.
[133] T.W. Hansen, J.B. Wagner, R.E. Dunin-Borkowski, Aberration corrected and monochromated environmental transmission electron microscopy: challenges and prospects for materials science, Materials Science and Technology, 26 (2010) 1338-1344.
[134] J.R. Jinschek, Advances in the environmental transmission electron microscope (ETEM) for nanoscale in situ studies of gas–solid interactions, Chemical Communications, 50 (2014) 2696-2706.
[135] K. Yoshida, A. Bright, N. Tanaka, Direct observation of the initial process of Ostwald ripening using spherical aberration-corrected transmission electron microscopy, Journal of Electron Microscopy, 61 (2012) 99-103.
[136] E.D. Boyes, M.R. Ward, L. Lari, P.L. Gai, ESTEM imaging of single atoms under controlled temperature and gas environment conditions in catalyst reaction studies, Annalen der Physik, 525 (2013) 423-429.
[137] T.E. Martin, P.L. Gai, E.D. Boyes, Dynamic Imaging of Ostwald Ripening by Environmental Scanning Transmission Electron Microscopy, Chemcatchem, 7 (2015) 3705-3711.
[138] P.L. Gai, E.D. Boyes, Advances in atomic resolution in situ environmental transmission electron microscopy and 1Å aberration corrected in situ electron microscopy, Microscopy research and technique, 72 (2009) 153-164.
[139] P.L. Gai, E.D. Boyes, Angstrom analysis with dynamic in-situ aberration corrected electron microscopy, Journal of Physics: Conference Series, 241 (2010) 012055.
[140] E.D. Boyes, P.L. Gai, Aberration corrected environmental STEM (AC ESTEM) for dynamic in-situ gas reaction studies of nanoparticle catalysts, Journal of Physics: Conference Series, 522 (2014) 012004.
[141] G.A. Somorjai, R.L. York, D. Butcher, J.Y. Park, The evolution of model catalytic systems; studies of structure, bonding and dynamics from single crystal metal surfaces to nanoparticles, and from low pressure (<10−3 Torr) to high pressure (>10−3 Torr) to liquid interfaces, Physical Chemistry Chemical Physics, 9 (2007) 3500-3513.
[142] H.G.J. Moseley, XCIII. The high-frequency spectra of the elements, The London, Edinburgh, and Dublin Philosophical Magazine and Journal of Science, 26 (1913) 1024-1034.
[143] A.L. Patterson, The Scherrer Formula for X-Ray Particle Size Determination, Physical Review, 56 (1939) 978-982.
[144] K.R. Lawless, The oxidation of metals, Rep Prog Phys, 37 (1974) 231.
[145] N. Cabrera, N.F. Mott, Theory of the oxidation of metals, Rep Prog Phys, 12 (1949) 163.
[146] A. Atkinson, R.I. Taylor, P.D. Goode, Transport Processes in the Oxidation of Ni Studied Using Tracers in Growing Nio Scales, Oxidation of Metals, 13 (1979) 519-543.
[147] G. Kaye, T. Laby, Tables of physical and chemical constants, 15 ed., Longman, London, UK, 1896.
[148] A.M. Kiss, W.M. Harris, S. Wang, J. Vila-Comamala, A. Deriy, W.K.S. Chiu, In-situ observation of nickel oxidation using synchrotron based full-field transmission X-ray microscopy, Applied Physics Letters, 102 (2013) 053902.

[149] M.T. Greiner, M.G. Helander, Z.-B. Wang, W.-M. Tang, Z.-H. Lu, Effects of Processing Conditions on the Work Function and Energy-Level Alignment of NiO Thin Films, The Journal of Physical Chemistry C, 114 (2010) 19777-19781.
[150] M.A. Peck, M.A. Langell, Comparison of Nanoscaled and Bulk NiO Structural and Environmental Characteristics by XRD, XAFS, and XPS, Chemistry of Materials, 24 (2012) 4483-4490.
[151] Z. Zhou, L. Han, G.M. Bollas, Kinetics of NiO reduction by H2 and Ni oxidation at conditions relevant to chemical-looping combustion and reforming, International Journal of Hydrogen Energy, 39 (2014) 8535-8556.
[152] R. Nakamura, J.G. Lee, H. Mori, H. Nakajima, Oxidation behaviour of Ni nanoparticles and formation process of hollow NiO, Philosophical Magazine, 88 (2008) 257-264.
[153] J.G. Railsback, A.C. Johnston-Peck, J. Wang, J.B. Tracy, Size-dependent nanoscale kirkendall effect during the oxidation of nickel nanoparticles, ACS Nano, 4 (2010) 1913-1920.
[154] S. Chenna, R. Banerjee, P.A. Crozier, Atomic-Scale Observation of the Ni Activation Process for Partial Oxidation of Methane Using In Situ Environmental TEM, ChemCatChem, 3 (2011) 1051-1059.
[155] S. Chenna, P.A. Crozier, In situ environmental transmission electron microscopy to determine transformation pathways in supported Ni nanoparticles, Micron, 43 (2012) 1188-1194.
[156] J.A. Medford, A.C. Johnston-Peck, J.B. Tracy, Nanostructural transformations during the reduction of hollow and porous nickel oxide nanoparticles, Nanoscale, 5 (2013) 155-159.
[157] J. Yu, W. Yuan, H. Yang, Q. Xu, Y. Wang, Z. Zhang, Fast gas-solid reaction kinetics of nanoparticles unveiled by millisecond in-situ electron diffraction at ambient pressure, Angewandte Chemie, DOI 10.1002/anie.201806541(2018).
[158] E. Kirkendall, L. Thomassen, C. Upthegrove, Rates od Diffusion of Copper and Zinc in Alpha Brass, Trans. AIME, 133 (1939) 186-203.
[159] E.O. Kirkendall, Diffusion of Zinc in Alpha Brass, Trans. AIME, 147 (1942) 104-110.
[160] A.D. Smigelskas, E.O. Kirkendall, Zinc Diffusion in Alpha Brass, Trans. AIME, 171 (1947) 130-142.
[161] H. Nakajima, The discovery and acceptance of the Kirkendall Effect: The result of a short research career, JOM, 49 (1997) 15-19.
[162] Y.D. Yin, R.M. Rioux, C.K. Erdonmez, S. Hughes, G.A. Somorjai, A.P. Alivisatos, Formation of hollow nanocrystals through the nanoscale Kirkendall Effect, Science, 304 (2004) 711-714.
[163] R. Nakamura, D. Tokozakura, J.G. Lee, H. Mori, H. Nakajima, Shrinking of hollow Cu2O and NiO nanoparticles at high temperatures, Acta Materialia, 56 (2008) 5276-5284.
[164] Y. Sun, X. Zuo, S. Sankaranarayanan, S. Peng, B. Narayanan, G. Kamath, Quantitative 3D evolution of colloidal nanoparticle oxidation in solution, Science, 356 (2017) 303-307.
[165] C.M. Wang, A. Genc, H. Cheng, L. Pullan, D.R. Baer, S.M. Bruemmer, In-situ TEM visualization of vacancy injection and chemical partition during oxidation of Ni-Cr nanoparticles, Sci Rep, 4 (2014) 3683.
[166] L. Dubau, J. Nelayah, S. Moldovan, O. Ersen, P. Bordet, J. Drnec, T. Asset, R. Chattot, F. Maillard, Defects do Catalysis: CO Monolayer Oxidation and Oxygen Reduction Reaction on Hollow PtNi/C Nanoparticles, Acs Catalysis, 6 (2016) 4673-4684.
[167] L. Han, Q. Meng, D. Wang, Y. Zhu, J. Wang, X. Du, E.A. Stach, H.L. Xin, Interrogation of bimetallic particle oxidation in three dimensions at the nanoscale, Nature communications, 7 (2016) 13335.

[168] S.W. Chee, S.F. Tan, Z. Baraissov, M. Bosman, U. Mirsaidov, Direct observation of the nanoscale Kirkendall effect during galvanic replacement reactions, Nature communications, 8 (2017) 1224.
[169] A. Atkinson, R.I. Taylor, The diffusion of63Ni along grain boundaries in nickel oxide, Philosophical Magazine A, 43 (1981) 979-998.
[170] G.J. Lloyd, J.W. Martin, The Diffusivity of Oxygen in Nickel Determined by Internal Oxidation of Dilute Ni–Be Alloys, Metal Science Journal, 6 (1972) 7-11.
[171] A. Atkinson, R.I. Taylor, The self-diffusion of Ni in NiO and its relevance to the oxidation of Ni, Journal of Materials Science, 13 (1978) 427-432.
[172] A. Atkinson, D.P. Moon, D.W. Smart, R.I. Taylor, Tracer diffusion studies in NiO bicrystals and polycrystals, Journal of Materials Science, 21 (1986) 1747-1757.
[173] R. Peraldi, D. Monceau, B. Pieraggi, Correlations Between Growth Kinetics and Microstructure for Scales Formed by High-Temperature Oxidation of Pure Nickel. II. Growth Kinetics, Oxidation of Metals, 58 (2002) 275-295.
[174] F.C. Frank, J.H. van der Merwe, One-Dimensional Dislocations. I. Static Theory, Proceedings of the Royal Society A: Mathematical, Physical and Engineering Sciences, 198 (1949) 205-216.
[175] F.C. Frank, J.H. van der Merwe, One-Dimensional Dislocations. II. Misfitting Monolayers and Oriented Overgrowth, Proceedings of the Royal Society A: Mathematical, Physical and Engineering Sciences, 198 (1949) 216-225.
[176] F.C. Frank, J.H. van der Merwe, One-Dimensional Dislocations. III. Influence of the Second Harmonic Term in the Potential Representation, on the Properties of the Model, Proceedings of the Royal Society A: Mathematical, Physical and Engineering Sciences, 200 (1949) 125-134.
[177] M. Yan, S.P. Chen, T.E. Mitchell, D.H. Gay, S. Vyas, R.W. Grimes, Atomistic Studies of Energies and Structures of (Hk0) Surfaces in NiO, Philos Mag A, 72 (1995) 121-138.
[178] A.U. Macrae, The Epitaxial Growth of NiO on a (111) Nickel Surface, Applied Physics Letters, 2 (1963) 88-90.
[179] A.P. LaGrow, M.R. Ward, D.C. Lloyd, P.L. Gai, E.D. Boyes, Visualizing the Cu/Cu2(O) Interface Transition in Nanoparticles with Environmental Scanning Transmission Electron Microscopy, J Am Chem Soc, 139 (2017) 179-185.
[180] B. Warot, E. Snoeck, P. Baules, J.C. Ousset, M.J. Casanove, S. Dubourg, J.F. Bobo, Epitaxial growth of NiO layers on MgO(001) and MgO(110), Applied Surface Science, 177 (2001) 287-291.
[181] M.E. Dry, Catalytic Aspects of Industrial Fischer-Tropsch Synthesis, Journal of Molecular Catalysis, 17 (1982) 133-144.
[182] BP Statistical Review of World Energy 2017, 2017, pp. 1-49.
[183] J. Kopyscinski, T.J. Schildhauer, S.M.A. Biollaz, Production of synthetic natural gas (SNG) from coal and dry biomass - A technology review from 1950 to 2009, Fuel, 89 (2010) 1763-1783.
[184] L. Seglin, R. Geosits, B.R. Franko, G. Gruber, Survey of Methanation Chemistry and Processes, 146 (1975) 1-30.
[185] L. Kiewidt, J. Thoming, Predicting optimal temperature profiles in single-stage fixed-bed reactors for CO2-methanation, Chemical Engineering Science, 132 (2015) 59-71.
[186] T. Van Herwijnen, H. Van Doesburg, W.A. De Jong, Kinetics of the methanation of CO and CO2 on a nickel catalyst, Journal of Catalysis, 28 (1973) 391-402.
[187] S. Rönsch, J. Schneider, S. Matthischke, M. Schlüter, M. Götz, J. Lefebvre, P. Prabhakaran, S. Bajohr, Review on methanation – From fundamentals to current projects, Fuel, 166 (2016) 276-296.

[188] G.W. Bridger, C. Woodward, Formulation and Operation of Methanation Catalysts, Methanation of Synthesis Gas, AMERICAN CHEMICAL SOCIETY1975, pp. 71-86.
[189] T.T.M. Nguyen, L. Wissing, M.S. Skjoth-Rasmussen, High temperature methanation: Catalyst considerations, Catalysis Today, 215 (2013) 233-238.
[190] Y.-L. Du, X. Wu, Q. Cheng, Y.-L. Huang, W. Huang, Development of Ni-Based Catalysts Derived from Hydrotalcite-Like Compounds Precursors for Synthesis Gas Production via Methane or Ethanol Reforming, Catalysts, 7 (2017) 70.
[191] J. Chen, R. Wang, J. Zhang, F. He, S. Han, Effects of preparation methods on properties of Ni/CeO2–Al2O3 catalysts for methane reforming with carbon dioxide, Journal of Molecular Catalysis A: Chemical, 235 (2005) 302-310.
[192] C. Mebrahtu, S. Abate, S. Perathoner, S. Chen, G. Centi, CO 2 methanation over Ni catalysts based on ternary and quaternary mixed oxide: A comparison and analysis of the structure-activity relationships, Catalysis Today, 304 (2018) 181-189.
[193] J. Lif, I. Odenbrand, M. Skoglundh, Sintering of alumina-supported nickel particles under amination conditions: Support effects, Applied Catalysis A: General, 317 (2007) 62-69.
[194] F.B. Rasmussen, J. Sehested, H.T. Teunissen, A.M. Molenbroek, B.S. Clausen, Sintering of Ni/Al2O3 catalysts studied by anomalous small angle X-ray scattering, Applied Catalysis A: General, 267 (2004) 165-173.
[195] H.S.S. P.S. Santos, S.P. Toledo, Standard Transition Aluminas. Electron Microscopy Studies, Mat. Res., 3 (2000) 104-114.
[196] I. Levin, D. Brandon, Metastable alumina polymorphs: Crystal structures and transition sequences, J Am Ceram Soc, 81 (1998) 1995-2012.
[197] H.P. Rooksby, C.J.M. Rooymans, The Formation and Structure of Delta Alumina, Clay Minerals Bulletin, 4 (1961) 234-238.
[198] J. Zhang, Y. Bai, Q. Zhang, X. Wang, T. Zhang, Y. Tan, Y. Han, Low-temperature methanation of syngas in slurry phase over Zr-doped Ni/γ-Al2O3 catalysts prepared using different methods, Fuel, 132 (2014) 211-218.
[199] M.D.E. Cai, J. Wen, W. Chu, X.Q. Cheng, Z.J. Li, Methanation of carbon dioxide on Ni/ZrO2-Al2O3 catalysts: Effects of ZrO2 promoter and preparation method of novel ZrO2-Al2O3 carrier, Journal of Natural Gas Chemistry, 20 (2011) 318-324.
[200] H.Z. Liu, X.J. Zou, X.G. Wang, X.G. Lu, W.Z. Ding, Effect of CeO2 addition on Ni/Al2O3 catalysts for methanation of carbon dioxide with hydrogen, Journal of Natural Gas Chemistry, 21 (2012) 703-707.
[201] Q. Liu, J. Gao, M. Zhang, H. Li, F. Gu, G. Xu, Z. Zhong, F. Su, Highly active and stable Ni/γ-Al2O3 catalysts selectively deposited with CeO2 for CO methanation, RSC Adv., 4 (2014) 16094-16103.
[202] S.B. Wang, G.Q. Lu, Role of CeO2 in Ni/CeO2-Al2O3 catalysts for carbon dioxide reforming of methane, Appl Catal B-Environ, 19 (1998) 267-277.
[203] Y. Zeng, H. Ma, H. Zhang, W. Ying, D. Fang, Ni–Ce–Al composite oxide catalysts synthesized by solution combustion method: Enhanced catalytic activity for CO methanation, Fuel, 162 (2015) 16-22.
[204] R. Si, M. Flytzani-Stephanopoulos, Shape and crystal-plane effects of nanoscale ceria on the activity of Au-CeO2 catalysts for the water-gas shift reaction, Angewandte Chemie, 47 (2008) 2884-2887.
[205] A. Piras, A. Trovarelli, G. Dolcetti, Remarkable stabilization of transition alumina operated by ceria under reducing and redox conditions, Applied Catalysis B: Environmental, 28 (2000) L77-L81.

[206] M.-Y. Ding, J.-Y. Tu, T.-J. Wang, L.-L. Ma, C.-G. Wang, L.-G. Chen, Bio-syngas methanation towards synthetic natural gas (SNG) over highly active Al 2 O 3 –CeO 2 supported Ni catalyst, Fuel Processing Technology, 134 (2015) 480-486.
[207] B. Nematollahi, M. Rezaei, E.N. Lay, Preparation of highly active and stable NiO–CeO2 nanocatalysts for CO selective methanation, International Journal of Hydrogen Energy, 40 (2015) 8539-8547.
[208] Q.S. Pan, J.X. Peng, T.J. Sun, D.N. Gao, S. Wang, S.D. Wang, CO2 methanation on Ni/Ce0.5Zr0.5O2 catalysts for the production of synthetic natural gas, Fuel Processing Technology, 123 (2014) 166-171.
[209] M.P. Andersson, F. Abild-Pedersen, I.N. Remediakis, T. Bligaard, G. Jones, J. Engbæk, O. Lytken, S. Horch, J.H. Nielsen, J. Sehested, Structure sensitivity of the methanation reaction: H2-induced CO dissociation on nickel surfaces, Journal of Catalysis, 255 (2008) 6-19.
[210] G. Garbarino, P. Riani, L. Magistri, G. Busca, A study of the methanation of carbon dioxide on Ni/Al2O3 catalysts at atmospheric pressure, International Journal of Hydrogen Energy, 39 (2014) 11557-11565.
[211] P.A.U. Aldana, F. Ocampo, K. Kobl, B. Louis, F. Thibault-Starzyk, M. Daturi, P. Bazin, S. Thomas, A.C. Roger, Catalytic CO2 valorization into CH4 on Ni-based ceria-zirconia. Reaction mechanism by operando IR spectroscopy, Catalysis Today, 215 (2013) 201-207.
[212] A. Westermann, B. Azambre, M.C. Bacariza, I. Graca, M.F. Ribeiro, J.M. Lopes, C. Henriques, The promoting effect of Ce in the CO2 methanation performances on NiUSY zeolite: A FTIR In Situ/Operando study, Catalysis Today, 283 (2017) 74-81.
[213] F.H. Meng, Z. Li, J. Liu, X.X. Cui, H.Y. Zheng, Effect of promoter Ce on the structure and catalytic performance of Ni/Al2O3 catalyst for CO methanation in slurry-bed reactor, Journal of Natural Gas Science and Engineering, 23 (2015) 250-258.
[214] J.T. Richardson, R.M. Scates, M.V. Twigg, X-ray diffraction study of the hydrogen reduction of NiO/α-Al2O3 steam reforming catalysts, Applied Catalysis A: General, 267 (2004) 35-46.
[215] P.A. Crozier, R. Wang, R. Sharma, In situ environmental TEM studies of dynamic changes in cerium-based oxides nanoparticles during redox processes, Ultramicroscopy, 108 (2008) 1432-1440.
[216] R.K. Hailstone, A.G. DiFrancesco, J.G. Leong, T.D. Allston, K.J. Reed, A Study of Lattice Expansion in CeO2 Nanoparticles by Transmission Electron Microscopy, J Phys Chem C, 113 (2009) 15155-15159.
[217] S. Agarwal, L. Lefferts, B.L. Mojet, D.A. Ligthart, E.J. Hensen, D.R. Mitchell, W.J. Erasmus, B.G. Anderson, E.J. Olivier, J.H. Neethling, A.K. Datye, Exposed surfaces on shape-controlled ceria nanoparticles revealed through AC-TEM and water-gas shift reactivity, ChemSusChem, 6 (2013) 1898-1906.
[218] A. Caballero, J.P. Holgado, V.M. Gonzalez-delaCruz, S.E. Habas, T. Herranz, M. Salmeron, In situ spectroscopic detection of SMSI effect in a Ni/CeO2 system: hydrogen-induced burial and dig out of metallic nickel, Chem Commun (Camb), 46 (2010) 1097-1099.
[219] L.P. Matte, A.S. Kilian, L. Luza, M.C.M. Alves, J. Morais, D.L. Baptista, J. Dupont, F. Bernardi, Influence of the CeO2Support on the Reduction Properties of Cu/CeO2and Ni/CeO2Nanoparticles, The Journal of Physical Chemistry C, 119 (2015) 26459-26470.
[220] W. Karim, C. Spreafico, A. Kleibert, J. Gobrecht, J. VandeVondele, Y. Ekinci, J.A. van Bokhoven, Catalyst support effects on hydrogen spillover, Nature, 541 (2017) 68-71.
[221] R. Prins, Hydrogen spillover. Facts and fiction, Chem Rev, 112 (2012) 2714-2738.
[222] S.K. Beaumont, S. Alayoglu, C. Specht, N. Kruse, G.A. Somorjai, A nanoscale demonstration of hydrogen atom spillover and surface diffusion across silica using the

kinetics of CO2 methanation catalyzed on spatially separate Pt and Co nanoparticles, Nano Lett, 14 (2014) 4792-4796.
[223] S.K. Beaumont, S. Alayoglu, C. Specht, W.D. Michalak, V.V. Pushkarev, J. Guo, N. Kruse, G.A. Somorjai, Combining in situ NEXAFS spectroscopy and CO(2) methanation kinetics to study Pt and Co nanoparticle catalysts reveals key insights into the role of platinum in promoted cobalt catalysis, J Am Chem Soc, 136 (2014) 9898-9901.
[224] Z. Hui, X. Younan, L. Byungkwon, X. Yujie, J. Mingshang, Shape-controlled synthesis of Pd nanocrystals and their catalytic applications.(palladium)(Report), Accounts of Chemical Research, 46 (2013) 1783-1794.
[225] D. Ciuparu, M.R. Lyubovsky, E. Altman, L.D. Pfefferle, A. Datye, Catalytic Combustion of Methane over Palladium-Based Catalysts, Catalysis Reviews, 44 (2002) 593-649.
[226] O. Domínguez-Quintero, Silica-supported palladium nanoparticles show remarkable hydrogenation catalytic activity, Journal of Molecular Catalysis A: Chemical, 197 (2003) 185-191.
[227] A. Quintanilla, J. Bakker, M. Kreutzer, J. Moulijn, F. Kapteijn, Tuning the support adsorption properties of Pd/SiO2 by silylation to improve the selective hydrogenation of aromatic ketones, Journal of Catalysis, 257 (2008) 55-63.
[228] J.H. Holles, R.J. Davis, T.M. Murray, J.M. Howe, Effects of Pd Particle Size and Ceria Loading on NO Reduction with CO, Journal of Catalysis, 195 (2000) 193-206.
[229] T.R. Johns, R.S. Goeke, V. Ashbacher, P.C. Thune, J.W. Niemantsverdriet, B. Kiefer, C.H. Kim, M.P. Balogh, A.K. Datye, Relating adatom emission to improved durability of Pt-Pd diesel oxidation catalysts, Journal of Catalysis, 328 (2015) 151-164.
[230] C. Carrillo, T.R. Johns, H. Xiong, A. DeLaRiva, S.R. Challa, R.S. Goeke, K. Artyushkova, W. Li, C.H. Kim, A.K. Datye, Trapping of Mobile Pt Species by PdO Nanoparticles under Oxidizing Conditions, The journal of physical chemistry letters, 5 (2014) 2089-2093.
[231] X. Wang, S.I. Choi, L.T. Roling, M. Luo, C. Ma, L. Zhang, M. Chi, J. Liu, Z. Xie, J.A. Herron, M. Mavrikakis, Y. Xia, Palladium-platinum core-shell icosahedra with substantially enhanced activity and durability towards oxygen reduction, Nature communications, 6 (2015) 7594.
[232] J.G. McCarty, G. Malukhin, D.M. Poojary, A.K. Datye, Q. Xu, Thermal coarsening of supported palladium combustion catalysts, The journal of physical chemistry. B, 109 (2005) 2387-2391.
[233] S.B. Simonsen, I. Chorkendorff, S. Dahl, M. Skoglundh, S. Helveg, Coarsening of Pd nanoparticles in an oxidizing atmosphere studied by in situ TEM, Surface Science, DOI 10.1016/j.susc.2015.11.003(2015).
[234] J. Kumar, R. Saxena, Formation of Nacl-Type and Cu2O-Type Oxides of Platinum and Palladium on Carbon and Alumina Support Films, Journal of the Less-Common Metals, 147 (1989) 59-71.
[235] A.T. DeLaRiva, T.W. Hansen, S.R. Challa, A.K. Datye, In situ Transmission Electron Microscopy of catalyst sintering, Journal of Catalysis, 308 (2013) 291-305.
[236] J.M. Cowley, Electron nanodiffraction, Microscopy research and technique, 46 (1999) 75-97.
[237] J. Cowley, Applications of electron nanodiffraction, Micron, 35 (2004) 345-360.
[238] D. Alloyeau, C. Ricolleau, T. Oikawa, C. Langlois, Y. Le Bouar, A. Loiseau, STEM nanodiffraction technique for structural analysis of CoPt nanoparticles, Ultramicroscopy, 108 (2008) 656-662.